National Library
of Canada

Acquisitions and
Bibliographic Services Branch

395 Wellington Street
Ottawa, Ontario
K1A 0N4

Bibliothèque nationale
du Canada

Direction des acquisitions et
des services bibliographiques

395, rue Wellington
Ottawa (Ontario)
K1A 0N4

Your file Votre référence

Our file Notre référence

NOTICE

The quality of this microform is heavily dependent upon the quality of the original thesis submitted for microfilming. Every effort has been made to ensure the highest quality of reproduction possible.

If pages are missing, contact the university which granted the degree.

Some pages may have indistinct print especially if the original pages were typed with a poor typewriter ribbon or if the university sent us an inferior photocopy.

Reproduction in full or in part of this microform is governed by the Canadian Copyright Act, R.S.C. 1970, c. C-30, and subsequent amendments.

AVIS

La qualité de cette microforme dépend grandement de la qualité de la thèse soumise au microfilmage. Nous avons tout fait pour assurer une qualité supérieure de reproduction.

S'il manque des pages, veuillez communiquer avec l'université qui a conféré le grade.

La qualité d'impression de certaines pages peut laisser à désirer, surtout si les pages originales ont été dactylographiées à l'aide d'un ruban usé ou si l'université nous a fait parvenir une photocopie de qualité inférieure.

La reproduction, même partielle, de cette microforme est soumise à la Loi canadienne sur le droit d'auteur, SRC 1970, c. C-30, et ses amendements subséquents.

Canada

UNIVERSITY OF ALBERTA

THE DEVELOPMENT OF A PHARMACOKINETIC AND RADIATION DOSIMETRIC MODEL FOR SELECTED ^{99m}TC LABELLED MONOCLONAL ANTIBODIES

BY

STEPHEN ANDREW MCQUARRIE ©

A Thesis submitted to the Faculty of Graduate Studies and research in
partial fulfillment of the requirements for the degree of DOCTOR OF PHILOSOPHY

In

RADIOLOGY AND DIAGNOSTIC IMAGING

DEPARTMENT OF MEDICAL SCIENCES,

EDMONTON, ALBERTA

SPRING, 1995

National Library
of Canada

Acquisitions and
Bibliographic Services Branch

395 Wellington Street
Ottawa, Ontario
K1A 0N4

Bibliothèque nationale
du Canada

Direction des acquisitions et
des services bibliographiques

395, rue Wellington
Ottawa (Ontario)
K1A 0N4

Your file Votre référence

Our file Notre référence

THE AUTHOR HAS GRANTED AN IRREVOCABLE NON-EXCLUSIVE LICENCE ALLOWING THE NATIONAL LIBRARY OF CANADA TO REPRODUCE, LOAN, DISTRIBUTE OR SELL COPIES OF HIS/HER THESIS BY ANY MEANS AND IN ANY FORM OR FORMAT, MAKING THIS THESIS AVAILABLE TO INTERESTED PERSONS.

L'AUTEUR A ACCORDE UNE LICENCE IRREVOCABLE ET NON EXCLUSIVE PERMETTANT A LA BIBLIOTHEQUE NATIONALE DU CANADA DE REPRODUIRE, PRETER, DISTRIBUER OU VENDRE DES COPIES DE SA THESE DE QUELQUE MANIERE ET SOUS QUELQUE FORME QUE CE SOIT POUR METTRE DES EXEMPLAIRES DE CETTE THESE A LA DISPOSITION DES PERSONNE INTERESSEES.

THE AUTHOR RETAINS OWNERSHIP OF THE COPYRIGHT IN HIS/HER THESIS. NEITHER THE THESIS NOR SUBSTANTIAL EXTRACTS FROM IT MAY BE PRINTED OR OTHERWISE REPRODUCED WITHOUT HIS/HER PERMISSION.

L'AUTEUR CONSERVE LA PROPRIETE DU DROIT D'AUTEUR QUI PROTEGE SA THESE. NI LA THESE NI DES EXTRAITS SUBSTANTIELS DE CELLE-CI NE DOIVENT ETRE IMPRIMES OU AUTREMENT REPRODUITS SANS SON AUTORISATION.

ISBN 0-612-01728-1

Canada

UNIVERSITY OF ALBERTA

RELEASE FORM

NAME OF AUTHOR: Stephen Andrew McQuarrie

TITLE OF THESIS: The Development of a Pharmacokinetic and Radiation Dosimetric Model for Selected ^{99m}Tc Labelled Monoclonal Antibodies

DEGREE: Doctor of Philosophy

YEAR THIS DEGREE GRANTED: Spring, 1995

Permission is hereby granted to the University of Alberta Library to reproduce single copies of this thesis and to lend or sell such copies for private, scholarly or scientific research purposes only.

The author reserves all other publication and other rights in association with the copyright in the thesis, and except as hereinbefore provided neither the thesis nor any substantial portion thereof may be printed or otherwise reproduced in any material form whatever without the author's prior written permission.

241 Colonial Estates
Sherwood Park, Alberta
T8E 1C1

DATED: 14 MARCH , 1995

UNIVERSITY OF ALBERTA

FACULTY OF GRADUATE STUDIES AND RESEARCH

The undersigned certify that they have read, and recommend to the Faculty of Graduate Studies and Research for acceptance, a thesis entitled The Development of a Pharmacokinetic and Radiation Dosimetric Model for Selected ^{99m}Tc Labelled Monoclonal Antibodies by Stephen Andrew McQuarrie in partial fulfillment of the requirements for the degree of Doctor of Philosophy in Medical Sciences (Radiology and Diagnostic Imaging).

Dr. A.J.B. McEwan (Supervisor)

Antoine Noujaim

Dr. A.A. Noujaim (Co-supervisor)

Dr. L.J. Filipow

Dr. S. Poppema

Dr. S.A. Jackson

David A. Goodwin M.D.

Dr. D.A. Goodwin (External Examiner)

Date: 2 March , 1995.

DEDICATED TO

My wife Joyce and our children Robert and Carolyn
for their unlimited tolerance, understanding and love.

ABSTRACT

The affects of circulating versus non-circulating antigen on the serum biodistribution in cancer patients were measured for several ^{99m}Tc labelled monoclonal antibodies (MAbs). These included MAb-170H.82 (pan adenocarcinoma), MAb-174H.64 (pan-squamous cell carcinoma), MAb-B43.13 (ovarian cancer) and MAb-B80.3 (prostate cancer). A two-compartment model describing the serum pharmacokinetics was found to best fit the data for these MAbs; yielding a distribution phase half-life (T_1) of 2-4 h and a terminal elimination phase half-life (T_2) of 22-40 h. For selected MAbs, HPLC, RIA and ELISA techniques were utilized to confirm that the unlabelled MAb followed similar distribution patterns. These results were augmented with data obtained from normal, non-tumor bearing rabbits where T_1 » 3-5 h and T_2 » 15-28 h.

In addition to serum and urine measurements, gamma camera region-of-interest data were used to develop a radiation dosimetry model for two of the ^{99m}Tc labelled MAbs (MAb-170H.82 and MAb-B43.13). Primary source organs were identified as the heart liver and kidneys, and in addition for MAb-B43.13, the spleen. Dose estimates based on the rabbit studies were in agreement with those obtained from patients.

Patient studies with MAb-B43.13 provided information on both the MAb and the antigen, CA 125. A drop in the CA 125 level was observed following injection, possibly through the formation of a MAb/antigen complex. Spleen uptake observed for this group of patients confirmed the formation of an immune complex. Although MAb-B80.3 was also used in the presence of its antigen (PSA), immune complexes formed in this case tended to clear through the liver. A similar, though more modest drop in the PSA serum level, was detected.

ACKNOWLEDGMENT

I would like to express my sincere thanks and appreciation to Dr. Sandy McEwan and Dr. Tony Noujaim for their guidance and friendship during the course of my research. Their generosity, both with their time and resources, as well as their sagacious insight into the many challenges associated with this project, were invaluable to me.

My sincere thanks are also extended to the following people who contributed to the successful completion of this research: Drs. Larry Filipow, YK Tam, Ron Sloboda, Stuart Jackson, Stamatina Stathaki, Tom Sykes, Graeme Boniface, Mr. Ken Golberg, Mrs. Lori Golberg, Mrs Connie Sykes, Mrs. Gail Hipperson, Mr. Thomas Woo, Mr. Terry Riauka and Mr. Eroll Zastre. I would also like to thank Dean Moskalyk and Dr. Bachynsky for their continued support and faith in me during the course of my studies.

Last, but by no means least, I would like to thank my wife Joyce and my children Rob and Carrie for their continuos support and encouragement during my studies.

TABLE OF CONTENTS

1. INTRODUCTION 1

1.1 Goals 4

2. BACKGROUND AND LITERATURE REVIEW 6

2.1 Overview of Monoclonal Antibody Imaging 6

2.2 Historical Perspective 7

2.2.1 Antibodies 9

2.2.2 Monoclonal Antibodies 13

2.2.3 Chimeric Monoclonal Antibodies 18

2.3 Clinical Use of Radiolabelled Monoclonal Antibodies 20

2.3.1 Radioimmunoscintigraphy: A Clinical Case-Study 25

2.3.2 Radioimmunotherapy: A Clinical Review 29

2.4 General Theory of Pharmacokinetics Related to Monoclonal Antibodies 33

2.4.1 Multicompartmental Analysis 33

2.4.2 Examples 38

2.5 Clinical Data Sources 42

2.6 Radiochemical Labelling 43

2.6.1 Choice of radionuclide 47

2.7 Factors Affecting Monoclonal Antibody Biodistribution 49

2.7.1 Physiological Factors 50

2.7.1.1 Human Anti-Mouse Antibody 50

2.7.1.2 Nonspecific Uptake 52

2.7.1.3 Glycosylation 53

2.7.1.4 Effects of Cytokines 53

2.7.1.5 Metabolism 54

2.7.1.6 Antibody Kinetics and Specific Uptake 54

2.7.1.7 Circulating Antigen 55

2.7.2 Physical Factors 56

2.7.2.1 Immunoconjugate Stability 56

2.7.2.2 Antigen Affinity 57

2.7.2.3 Modelling Assumptions 57

2.7.2.4 Molecular Weight 58

2.7.2.5 Radionuclide Location 58

2.8 Radiation Dosimetry 58

2.8.1 General Theory 60

2.8.2 MIRD Data Sources 65

2.8.3 Monoclonal Antibody Dosimetry 66

2.8.3.1 Radioimmunoimaging 67

2.8.3.2 Bladder Contents 71

2.8.3.3 Remainder of the Body 73

3. MATERIALS AND METHODS 75

3.1 Monoclonal Antibodies 75

3.1.1 MAb-170H.82 75

3.1.1.1 Clinical Trials 76

3.1.2 MAb-174H.64 77

3.1.2.1 Clinical Trials 78

3.1.3 MAb-80.3 78

3.1.3.1 Clinical Trials 79

3.1.4 MAb-B43.13 80

3.1.4.1 Clinical Trials 81

3.2 High Performance Liquid Chromatography 81

3.3 Multisample Gamma Counter 82

3.4 Gamma camera 83

3.5 Statistics 84

3.6 Software 85

3.7 HAMA 85

4. EXPERIMENTAL METHODOLOGY 86

4.1 Radionuclide Labelling 86

4.2 Radioimmunoimaging 91

4.2.1 Data Processing 92

4.2.2 Rabbit Imaging Protocol 97

4.2.2.1 Rabbit Blood-Flow 98

4.2.3 Patient Imaging Protocol 99

4.3 Sampling Methodology 101

4.3.1 Rabbits 101

4.3.1.1 Biological sampling 103

4.3.1.2 Blood-flow Measurements 104

4.3.2 Patients 105

4.3.2.1 Gamma camera imaging 106

4.3.2.2 Biological sampling 106

4.4 Phantom Studies 108

4.5 Radioimmunoassay 113

4.5.1 MAb-170H.82 RIA 115

4.5.2 MAb-174H.64 RIA 116

4.5.3 MAb-B80.3 RIA 117

4.5.4 CA 125 RIA 118

4.6 Enzyme-Linked Immunosorbent Assay - MAb-B43.13 118

4.7 Kinetic Modeling 119

5. EXPERIMENTAL RESULTS 121

5.1 MAb-170H.82 121

5.1.1 Rabbit Kinetics 122

5.1.1.1 Routes of Elimination 124

5.1.1.2 Gamma Camera Imaging 125

5.1.1.3 Tissue Sampling 128

5.1.2 Patient Kinetics 129
5.1.2.1 HPLC Analysis 135
5.1.2.2 Radioimmunoassay:MAb-170H.82 138
5.1.2.3 Dosimetry 140
5.2 MAb-m174H.64 141
5.2.1 Rabbit Kinetics 142
5.2.1.1 Routes of Elimination 144
5.2.1.2 Gamma Camera Imaging 145
5.2.1.3 Tissue Sampling 148
5.2.2 Patient Kinetics 148
5.3 MAb-c174H.64 152
5.3.1 Rabbit Kinetics 152
5.3.1.1 Routes of Elimination 154
5.3.1.2 Gamma Camera Imaging 155
5.3.1.3 Tissue Sampling 157
5.3.2 Patient Kinetics 158
5.4 MAb-B80.3 162
5.4.1 Rabbit kinetics 163
5.4.1.1 Routes of Elimination 166
5.4.1.2 Gamma Camera Imaging 167
5.4.1.3 Tissue Sampling 173
5.4.2 Patient kinetics 174
5.4.2.1 Radioimmunoassay 177
5.5 MAb-B43.13 177
5.5.1 Patient Kinetics 177
5.5.1.1 Kinetic Modeling 178
5.5.1.2 ELISA: MAb-B43.13 183
5.5.1.3 RIA: CA125 185
5.5.1.4 Dosimetry 185

6. DISCUSSION OF RESULTS 187

6.1 Monoclonal Antibodies With No Circulating Antigen 187

6.1.1 Rabbit Kinetics: MAb-170H.82 vs MAb-174H.64 188

6.1.2 Patient Kinetics: MAb-170H.82 vs MAb-174H.64 193

6.1.3 Monoclonal Antibody Dose 195

6.2 Monoclonal Antibodies With Circulating Antigen 196

6.2.1 MAb-B80.3 197

6.2.2 MAb-B43.13 200

6.3 InterMAb Kinetic Comparison 201

6.4 Kinetic Modeling 205

6.5 Dosimetry 212

7. CONCLUSIONS 217

7.1.1 Two-Compartment Model 217

7.1.2 Circulating versus Non Circulating Antigen: No Significant Difference 218

7.1.3 Dosimetry Concordance 218

7.2 Future Research 219

7.2.1 Variations in ^{99m}Tc-MAb-170H.82 Liver Uptake 219

7.2.2 Pharmacodynamic Modelling of MAb-B43.13 221

8. REFERENCES 222

TABLE OF TABLES

Table 1: A partial list of some of the radiopharmaceuticals used in nuclear medicine. 3

Table 2: Characteristics of some commonly used radionuclides used to label monoclonal antibodies (EC = electron capture, IT = internal transition). 44

Table 3: Some potentially useful radionuclides for labelling monoclonal antibodies for RIS and RIT. 48

Table 4: Organ activity obtained from quantitative conjugate-view gamma camera imaging of ^{99m}Tc-red cells expressed as a percentage of the injected dose (%ID). 98

Table 5: Rabbit tissue sample data for in vivo ^{99m}Tc labelled red cells. 99

Table 6: Phantom activity expressed in MBq and as a percent of all the activity in the phantom (whole body). The activity was decay corrected to the time of the first image. 110

Table 7: Variation in drawing wide and narrow regions for each phantom organ (expressed as a percentage). 111

Table 8: Error associated with multiple attempts at drawing the same region of interest. The data shown represents the mean of 10 trials of the geometric mean of the ROI's shown in Figure 8. 112

Table 9: Effects of background subtraction and correction for overlaying activity, expressed as a percentage of the whole body activity 113

Table 10: MAb 170H.82 serum activity measured as dpm/mL (1 x 10^6) and as a percentage of the injected dose (% ID) at various time intervals. 122

Table 11: Pharmacokinetic parameters representing a two compartment model of the form $C(t) = C_1 e^{-\lambda_1 t} + C_2 e^{-\lambda_2 t}$ following the administration of ^{99m}Tc 170H.82. 123

Table 12: SAM04 organ activity in obtained from quantitative gamma camera imaging of ^{99m}Tc-170H.82. 125

Table 13: SAM06 organ activity in obtained from quantitative gamma camera imaging of ^{99m}Tc-170H.82. 126

Table 14: SAM11 organ activity in obtained from quantitative gamma camera imaging of ^{99m}Tc-170H.82. 126

Table 15: Organ kinetic parameters from quantitative RIS data of ^{99m}Tc-170H.82 in rabbits. 127

Table 16: Kinetic parameters representing the biodistribution of ^{99m}Tc 170H.82 in the left kidney. 128

Table 17: Rabbit tissue sample data for ^{99m}Tc-170H.82. 128

Table 18: Patient data (E196766) following the injection of 1 mg of ^{99m}Tc-170H.82. 129

Table 19: Patient data (E185902) following the injection of 1mg of ^{99m}Tc-170H.82. 130

Table 20: Patient data (E193637) following the injection of 1 mg of ^{99m}Tc-170H.82. 130

Table 21: Patient data (E179268) following the injection of 2mg of ^{99m}Tc-170H.82. 130

Table 22: Patient data (E191358) following the injection of 4 mg of ^{99m}Tc-170H.82. 131

Table 23: Patient data (E192473) following the injection of 4 mg ^{99m}Tc-170H.82. 132

Table 24: Pharmacokinetic parameters obtained from a two compartment model representing the biodistribution of ^{99m}Tc-170H.82. 134

Table 25: Patient RIA data following the i.v. administration of ^{99m}Tc-170H.82. 139

Table 26: Pharmacokinetic parameters obtained from the 170H.82 RIA data. 139

Table 27: Mean radiation dose estimates following the administration of ^{99m}Tc-170H.82 for each target organ over all dosage levels. 141

Table 28: MAb 174H.64 serum activity in rabbits measured as dpm/mL (1×10^6) and as a percentage of the injected dose (% ID) at various time intervals. 142

Table 29: Pharmacokinetic parameters representing a two compartment model of the form $C(t) = C_1 e^{-\lambda_1 t} + C_2 e^{-\lambda_2 t}$ following the administration of ^{99m}Tc 174H.64. 144

Table 30: SAM 12 organ activity obtained from quantitative RIS of ^{99m}Tc-174H.64 expressed as a percentage of the injected dose (%ID). 146

Table 31: SAM 13 organ activity in obtained from quantitative RIS of ^{99m}Tc-174H.64 expressed as a percentage of the injected dose (%ID). 146

Table 32: SAM 14 organ activity obtained from RIS of ^{99m}Tc-174H.64 expressed as a percentage of the injected dose (%ID). 147

Table 33: Organ kinetic parameters from quantitative RIS data of ^{99m}Tc-m174H.64 in rabbits. 147

Table 34: Rabbit tissue sample data for ^{99m}Tc-174H.64. 148

Table 35: Patient M1 data following the injection of 2 mg of Tc-99m labelled m 174H.64 MAb. 149

Table 36: Patient M3 data (head and neck cancer) following the injection of 2 mg of Tc-99m labelled m-174H.64 MAb. 150

Table 37: Patient M2 data (head and neck cancer) following the injection of 2 mg of Tc-99m labelled m-174H.64 MAb. 150

Table 38: Pharmacokinetic parameters representing a two compartment model of the form $C(t) = C_1 e^{-\lambda_1 t} + C_2 e^{-\lambda_2 t}$ 152

Table 39: MAb c174H.64 serum activity in rabbits measured as dpm/mL (1×10^6) and as a percentage of the injected dose (% ID) at various time intervals. 152

Table 40: Pharmacokinetic parameters representing a two compartment model of the form $C(t) = C_1 e^{-\lambda_1 t} + C_2 e^{-\lambda_2 t}$ following the administration of ^{99m}Tc c174H.64. 153

Table 41: SAM 30 organ activity obtained from quantitative gamma camera imaging of ^{99m}Tc-c174H.64 expressed as a percentage of the injected dose (%ID). 155

Table 42: SAM 31 organ activity obtained from quantitative gamma camera imaging of ^{99m}Tc-c174H.64 expressed as a percentage of the injected dose (%ID). 156

Table 43: Kinetic parameters of selected organs from quantitative RIS data of 99mTc-c174H.64 in rabbits (2 compartment model, bolus input). 157

Table 44: Rabbit tissue sample data for ^{99m}Tc-c174H.64. 157

Table 45: Patient data (head and neck cancer) following the injection of 1 mg of Tc-99m labelled c-174H.64 MAb. 158

Table 46: Patient data (head and neck cancer) following the injection of 1 mg of Tc-99m labelled c-174H.64 MAb. 159

Table 47: Patient data (head and neck cancer) following the injection of 1 mg of Tc-99m labelled c-174H.64 MAb. 159

Table 48: Patient data (head and neck cancer) following the injection of 1 mg of Tc-99m labelled c-174H.64 MAb. 159

Table 49: Patient data (head and neck cancer) following the injection of 1 mg of Tc-99m labelled c-174H.64 MAb. 160

Table 50: Patient data (head and neck cancer) following the injection of 1 mg of Tc-99m labelled c-174H.64 MAb. 160

Table 51: Patient data (head and neck cancer) following the injection of 1 mg of Tc-99m labelled c-174H.64 MAb. 160

Table 52: Pharmacokinetic parameters representing a model of the form: $C(t) = C_1 e^{-\lambda_1 t} + C_z e^{-\lambda_z t}$. # Data are ill-conditioned 162

Table 53: ^{99m}Tc-B80.3 serum activity measured as dpm/mL (1 x 10^6) and as a percentage of the injected dose (% ID) at various time intervals. 164

Table 54: ^{99m}Tc-B80.3/PSA complex serum activity measured as dpm/mL (1 x 10^6) and as a percentage of the injected dose (% ID) at various time intervals. 164

Table 55: ^{99m}Tc-B80.3 pharmacokinetic parameters representing a two compartment model of the form $C(t) = C_1 e^{-\lambda_1 t} + C_z e^{-\lambda_z t}$. 166

Table 56: ^{99m}Tc-B80.3/PSA pharmacokinetic parameters representing a two compartment model of the form $C(t) = C_1 e^{-\lambda_1 t} + C_z e^{-\lambda_z t}$. 166

Table 57: SAM 7 organ activity obtained from quantitative gamma camera imaging of ^{99m}Tc-B80.3 expressed as a percentage of the injected dose (%ID). 168

Table 58: SAM 8 organ activity obtained from quantitative gamma camera imaging of ^{99m}Tc-B80.3 expressed as a percentage of the injected dose (%ID). 168

Table 59: SAM 10 organ activity obtained from quantitative gamma camera imaging of ^{99m}Tc-B80.3 expressed as a percentage of the injected dose (%ID). 169

Table 60: SAM 9 organ activity obtained from quantitative gamma camera imaging of ^{99m}Tc-B80.3/PSA complex expressed as a percentage of the injected dose (%ID). 170

Table 61: SAM 15 organ activity obtained from quantitative gamma camera imaging of ^{99m}Tc-B80.3/PSA complex expressed as a percentage of the injected dose (%ID). 170

Table 62: SAM 16 organ activity obtained from quantitative gamma camera imaging of ^{99m}Tc-B80.3/PSA complex expressed as a percentage of the injected dose (%ID). 171

Table 63: Organ kinetic parameters from quantitative RIS data of ^{99m}Tc labelled B80.3 MAb in rabbits (bolus input). 171

Table 64: Organ kinetic parameters from quantitative RIS data of ^{99m}Tc labelled B80.3/PSA complex in rabbits (bolus input). 172

Table 65: Kinetic parameters representing the biodistribution ^{99m}Tc labelled B80.3/PSA complex in the rabbit liver (first-order input). 172

Table 66: Rabbit tissue sample data for ^{99m}Tc-B80.3 in % injected dose/gm at time-of death. 173

Table 67: Rabbit tissue sample data for ^{99m}Tc-B80.3/PSA. 173

Table 68: Patient data (E201981) following the injection of 2 mg of ^{99m}Tc-B80.3, PSA: 10 ng/mL. 174

Table 69: Patient data (E127971) following the injection of 2 mg of ^{99m}Tc-B80.3, PSA: 2500nl/mL. 175

Table 70: Pharmacokinetic parameters representing the biodistribution of ^{99m}Tc-B80.3. The standard error term is shown for each data point. 176

Table 71:Patient serum and urine data (OVAREX-Gy-01-002) following the IV injection of 2 mg of ^{99m}Tc-B43.13. 178

Table 72: Patient serum and urine data (OVAREX-Gy-01-001) following the IV injection of 2 mg of ^{99m}Tc-B43.13. 179

Table 73: Patient serum and urine data (OVAREX-Gy-01-003) following the IV injection of 2 mg of ^{99m}Tc-B43.13. 179

Table 74: Patient serum and urine data (OVAREX-Gy-01-004) following the IV injection of 2 mg of ^{99m}Tc-B43.13. 180

Table 75: Patient serum and urine data (OVAREX-Gy-01-005) following the IV injection of 2 mg of ^{99m}Tc-B43.13. 180

Table 76: Patient serum and urine data (OVAREX-Gy-01-006) following the IV injection of 2 mg of ^{99m}Tc-B43.13. 180

Table 77: Model parameter values representing the serum biodistribution of ^{99m}Tc-B43.13. 182

Table 78: Patient ELISA data expressed as a percentage of the injected dose at selected times post injection of ^{99m}Tc-MAb-B43.13. 183

Table 79: Pharmacokinetic parameters obtained from MAb-B43.13 ELISA data. 184

Table 80: CA 125 levels following the injection of ^{99m}Tc-MAb-B43.13. 185

Table 81: Mean radiation dose estimates following the administration of ^{99m}Tc-MAb-B43.13 for the target organs listed in the first column. 186

Table 82: Comparison of the serum kinetic parameters representing ^{99m}Tc labelled 170H.82 and 174H.64 in rabbits. 190

Table 83: A comparison of the kinetic models describing the biodistribution of the ^{99m}Tc labelled MAbs 170H.82 and 174H.64. 191

Table 84: A comparison between rabbit tissue samples obtained at necropsy. 192

Table 85: A statistical comparison of the pharmacokinetic parameters representing biodistribution of ^{99m}Tc-170H.82 (murine) and ^{99m}Tc-174H.64 (murine and chimeric) in patient serum. 194

Table 86: A non-parametric comparison of the serum kinetic parameters (p-values) representing ^{99m}Tc labelled c174H.64 and m174H.64 in patients. 195

Table 87: A comparison of ^{99m}Tc-B80.3 serum kinetics in rabbits and patients. 198

Table 88: A comparison between ^{99m}Tc labelled B80.3 and B80.3/PSA heart and liver models in rabbits. 199

Table 89: Rabbit tissue sample data for ^{99m}Tc-B80.3 presented as the % injected dose/gm (% ID/gm) at 48 h post-injection. 200

Table 90: T-test values comparing ^{99m}Tc-MAb-B43.13 and MAb-B43.13 kinetics. 201

Table 91: Pharmacokinetic parameters describing the serum distribution of ^{99m}Tc labelled 170H.82, 174H.64, B43.13 and B80.3 in patients. 202

Table 92: Pharmacokinetic parameters describing the serum distribution of ^{99m}Tc labelled 170H.82, 174H.64 and B80.3 in rabbits. 204

Table 93: A comparison of ^{99m}Tc activity in selected tissues at 48 hours post-injection for MAbs 170H.82, 174H.64 and B80.3. 205

Table 94: Organ/heart ratios for RIS data. 206

Table 95: Comparison between the serum and organ time-dependent kinetic model coefficients (p-values for an unpaired t-test). 208

Table 96: A comparison of serum kinetic model parameters in patients and rabbits for ^{99m}Tc-170H.82. 213

Table 97: ^{99m}Tc-170H.82 radiation dose estimates based on human and rabbit data. ^{111}In OncoScint data shown for comparison. 216

TABLE OF FIGURES

Figure 1: Structure of an immunoglobulin molecule. 10

Figure 2: Production of monoclonal antibodies. 14

Figure 3: Schematic diagram of a linear multicompartmental model representing the in vivo biodistribution of a hypothetical MAb. 41

Figure 4: Decay scheme for ^{99m}Tc (from MIRD: Radionuclide Data and Decay Schemes, DA Weber et al, Society of Nuclear Medicine, 1989). 88

Figure 5: Schematic view of a ROI depth-profile. 94

Figure 6: Schematic view of patient - gamma camera orientation. 95

Figure 7: Typical whole-body imaging illustrating the placement of ROI's. This particular image is a 6h anterior view of ^{99m}Tc labelled MAb 170H.82. 100

Figure 8: Posterior image of the phantom showing ROI's drawn around the kidneys and liver. 110

Figure 9: Rabbit serum profile following the iv. bolus administration of 170H.82 MAb. 122

Figure 10: Renal elimination of ^{99m}Tc-170H.82 in rabbits. 124

Figure 11: Cummulative fecal elimination of ^{99m}Tc-170H.82 in rabbits. 124

Figure 12: Variation with time of ^{99m}Tc-170H.82 serum levels expressed as a percentage of the injected dose. 132

Figure 13: Renal excretion following the i.v. administration of ^{99m}Tc-170H.82. 133

Figure 14: HPLC of ^{99m}Tc labelled MAb 170H.82; pre-injection kit. 136

Figure 15: HPLC of ^{99m}Tc labelled MAb 170H.82; serum - 1 hr post-injection. 136

Figure 16: HPLC of ^{99m}Tc labelled MAb 170H.82; serum - 18 hr post-injection. 137

Figure 17: HPLC of ^{99m}Tc labelled MAb 170H.82; urine - 18 hr post-injection. 137

Figure 18: Serum ^{99m}Tc-170H.82 overlaid with the immunoreactive component of the MAb as identified by RIA. 140

Figure 19: Rabbit serum profile following the iv. bolus administration of ^{99m}Tc 174H.64 MAb. 143

Figure 20: Cumulative fecal elimination of ^{99m}Tc labelled MAb 174H.64 in rabbits. 145

Figure 21: Cumulative urine excretion of ^{99m}Tc labelled MAb 174H.64 in rabbits. 145

Figure 22: Patient serum radioactivity profile following the iv. administration of 2 mg of m-174H.64 MAb. 151

Figure 23: Rabbit serum profile following the iv. bolus administration of ^{99m}Tc c174H.64 MAb. 153

Figure 24: Cumulative fecal elimination of ^{99m}Tc labelled MAb c174H.64 in rabbits. 154

Figure 25: Cumulative urine excretion of ^{99m}Tc labelled MAb c174H.64 in rabbits. 154

Figure 26: Patient serum profile following the iv. administration of 1 mg of c-174H.64 MAb. 161

Figure 27: Serum biodistribution of ^{99m}Tc-B80.3 and ^{99m}Tc-B80.3/PSA illustrating the different clearance rates. 165

Figure 28: Renal elimination of ^{99m}Tc labelled B80.3 and B80.3/PSA in rabbits. 167

Figure 29: Fecal elimination of ^{99m}Tc labelled B80.3 and B80.3/PSA in rabbits. 167

Figure 30: Variation with time of ^{99m}Tc-B80.3 serum levels expressed as a percentage of the injected dose. 176

Figure 31: Renal excretion following the i.v. administration of ^{99m}Tc-B80.3. 176

Figure 32: Biodistribution of ^{99m}Tc-B43.13 in patient serum. 181

Figure 33: Urine elimination of ^{99m}Tc-B43.13 in patients. 181

Figure 34: Serum ^{99m}Tc-B43.13 overlaid with the immunoreactive component of the MAb as identified by ELISA. 184

Figure 35: Serum biodistribution of ^{99m}Tc labelled 170H.82 and 174H.64 in rabbits. 189

Figure 36: Biodistribution of ^{99m}Tc-170H.82 and ^{99m}Tc-174H.64 in patient serum. 193

Figure 37: Serum biodistribution of ^{99m}Tc labelled B80.3 in patients and rabbits. 198

Figure 38: Serum data representing the biodistribution of ^{99m}Tc labelled 170H.82, 174H.64, B43.13 and B80.3 in patients. 203

Figure 39: Possible kinetic model for ^{99m}Tc labelled 170H.82. 209

Figure 40: A comparison between patient and rabbit ^{99m}Tc-170H.82 serum data. 213

Figure 41: High liver uptake expressed as a percentage injected dose. 220

Abbreviations

Ab	antibody
Ag	antigen
dpm	disintegrations per minute
ELISA	enzyme-linked immunosorbent assay
$F(ab')_2$	antigen-binding fragment, generated by digestion of IgG with pepsin
Fab	antigen-binding fragment, generated by binding of IgG with papain
Fc	immunoglobin fragment, crystallizable
HAHA	human anti-human antibody
HAMA	human anti-mouse antibody
HPLC	high performance liquid chromatography
%ID	percentage of the injected dose
Ig	immunoglobin
IL-2	interleukon-2
i.p.	intraperitoneal
i.v.	intravenous
ITLC	instant thin layer chromatography
keV	kilo-electron volt
MAb	monoclonal antibody
MBq	megabecquerel
PBS	phosphate buffered solution
RIA	radioimmoassay
RIS	radioimmunoscintigraphy
RIT	radioimmunotherapy

1. INTRODUCTION

The theory, methodology and practical application of tracers labelled with radionuclides, which may be used to study physiological and disease processes in the human body, is the central theme of nuclear medicine. When radiotracers are used in conjunction with modern nuclear medicine imaging devices it is possible to diagnose and aid in the management of a wide variety of diseases, including cancer.

The evolution of radiotracers used in nuclear medicine over the last three decades may be divided into three distinct and separate stages of development. The first would contain the class of relatively nonspecific radiopharmaceuticals used in routine diagnostic practice. For example[1], ^{99m}Tc methylene diphosphate (MDP) is incorporated into the inorganic bone matrix and appears to reflect local osteoblastic activity[2]. Other compounds in this class would include ^{99m}Tc labelled red-blood cells used for blood-pool studies[3] as well as morphological imaging agents such as ^{99m}Tc-glucoheptonate for brain imaging and ^{99m}Tc-sulfur colloid used for liver and spleen imaging.

The next stage of development began in the early 1980's when radiopharmaceuticals began to be used to study specific pathophysiological conditions. For example, ^{131}I, and subsequently ^{123}I labelled metaiodobenzylguanidine (mIBG) was used for the diagnostic evaluation and subsequent therapy of neuroendocrine tumors such as pheochromocytoma, neuroblastoma and carcinoid. Also classed in this group is ^{123}I-Iodoazomycin arabinoside (IAZA) which appears to detect hypoxia in vivo[4]. In addition to its use in patients with peripheral vascular disease, radiolabelled IAZA compounds have been used to locate hypoxic regions in solid tumors[5,6].

The third phase of development of radiopharmaceuticals has arisen from recent advances in immunology that have provided the nuclear medicine community with exciting new compounds which are highly specific in nature. This class includes monoclonal antibodies (MAb), antibody fragments, and smaller peptide recognition units labelled with ^{131}I, ^{111}In, ^{123}I or ^{99m}Tc. These radiotracers derive their sensitivity from the immune system's native ability to design unique molecules specifically against foreign antigenic determinants. In fact, the monoclonal antibody has been proclaimed by some as a 'magic bullet', implying its exquisite specificity to recognize its target (such as an antigen associated with a tumor cell).

The next class of biological molecules which will be involved in clinical practice will be the biologically active peptide. ^{111}In Octreotide, the first of these, is already in routine clinical practise in the United States and Europe. As peptide labelling technology improves, it is likely that current investigations using monoclonal antibodies will ultimately utilize radiolabelled peptides, substituted for the larger molecules. This approach will require a rapid and rigorous strategy for preclinical and clinical evaluation of these compounds.

A selection of radiopharmaceuticals from each of these three phases currently in routine clinical practice, as well as some radiotracers now in developmental studies[7] are summarized in Table 1. For each radiopharmaceutical, it is possible to define three important parameters that will define its scope of clinical use: 1) the mechanism of uptake and elimination, 2) the physiological or pathophysiological process that is being imaged and 3) the use to which it will be put in clinical practice. Clearly, for some of the compounds under development, this latter parameter will not yet have been fully defined; however, as is clear from the table, it is possible to at least indicate those areas where it is believed clinical use of the compound may have some diagnostic or prognostic benefit.

Table 1: A partial list of some of the radiopharmaceuticals used in nuclear medicine.

Radiopharmaceutical	Radionuclide	Application
potassium analogue	Rb-86, Th-199	myocardial agent
methoxyisobutyl isonitrile (MIBI)	Tc-99m	myocardial agent
ethylhydroxy diphosphonate (EHDP)	Tc-99m	skeletal agent
methylene diphosphonate (MDP)	Tc-99m	skeletal agent
hydroxymethylene diphosphonate (HMDP)	Tc-99m	skeletal agent
dimercaptosuccinic acid (DMSA)	Tc-99m	renal morphology
(EDTA)	Cr-51	glomerular filtration rate
diethylenetriaminepentaacetic acid (DTPA)	Tc-99m	glomerular filtration rate, brain
o-iodohippuric acid (Hippuran)	I-131, I-123	renal plasma flow
mercaptacetyl triglycine (MAG-3)	Tc-99m	renal plasma flow
microspheres, macroaggragates	Tc-99m	organ perfusion, reticuloendothelial system
hexamethypropyleneamineoxine (HMPAO)	Tc-99m	brain - regional blood flow
pertechnetate	Tc-99m	brain, thyroid
glucoheptonate	Tc-99m	brain
rose bengal	I-131	hepatobiliary studies
dimethyl iminodiacetate (HIDA)	Tc-99m	hepatobiliary studies
blood cells	Tc-99m, In-111, Cr-51	organ perfusion, inflammation, reticuloendothelial system, cell kinetic studies
sodium iodide	I-131, I-123	thyroid function
iodoazomycin arabinoside (IAZA)	I-131, I-123	tissue hypoxia

A review of the extensive literature on monoclonal antibody imaging indicates that little attention has been paid to the second and third parameters discussed above or the impact of pharmacokinetics on clinical use. Many of the clinical trials that have been described are poorly planned, poorly conducted and do not give the reader a clear understanding of the way in which the compound could impact clinical practice. It is only in very recent times that the nuclear medicine community has acquired an understanding of the rigor required to develop compounds into useful clinical radiopharmaceuticals.

1.1 Goals

Several promising antibodies directed against various cancer associated antigens have been developed at the University of Alberta[8,9]. Utilizing patient and animal data this work will focus on four of those MAbs, labelled with ^{99m}Tc. These MAbs are 170H.82 (pan adenocarcinoma), 174H.64 (pan squamous cell cancer), B43.13 (ovarian cancer) and B80.3 (prostate cancer). The goal of this project may be summarized as the development of the necessary model for the rational introduction of MAbs into RIS in clinical practice. This model will be developed to comprise 8 associated procedures:

1. the development of a rigorous protocol to test MAbs,
2. the development of the methodology necessary to achieve a kinetic and dosimetric model,
3. the development of a phantom model to test the kinetic and dosimetry methodology,
4. the development of an animal model for kinetic and dosimetry estimates
5. the application of an animal model to estimate human kinetics and dosimetry,
6. a comparison of the biodistribution and dosimetry of the different MAbs tested with respect to the presence or absence of circulating antigen,
7. a comparison of murine vs chimeric formulations of a particular MAb and
8. an evaluation MAb metabolism.

Currently the optimum monoclonal antibody labelling technology for RIS utilizes ^{99m}Tc directly labelled to the antibody. Using the MAbs described in the next chapter, this dissertation will explore the requirements for the preclinical and clinical evaluation of each compound, and will provide supporting data for the development of appropriate clinical algorithms for the routine clinical use of the compounds. By developing this rigorous framework, it is hoped that future compounds may be rapidly evaluated, using comparable methodology, which in turn will take them more quickly through the necessary developmental steps to Phase I and Phase II clinical studies. The thesis will describe the development of this methodology for a number of antibodies, will outline the limitations of this methodology and will provide the necessary data to support clinical use of the compounds.

2. BACKGROUND AND LITERATURE REVIEW

2.1 Overview of Monoclonal Antibody Imaging

Radiolabelled monoclonal antibodies (MAbs) are a class of nuclear medicine imaging agents used to detect sites of disease[10,11] and also have potential as therapy agents[12]. The process of acquiring information on the distribution of radioactive MAbs by external means has been termed radioimmunoscintigraphy (RIS)[13]. The major application of RIS has been in oncology where it was first developed to identify malignant disease[14]. This same principle of disease targeting has also been exploited for treatment of cancer using a technique known as radioimmunotherapy (RIT)[15]. Although MAbs have been used in areas such as imaging myocardial infarction[16], thrombi[17] and inflammation[18] the following discussions will focus on the use of MAbs in the field of oncology.

The success of RIS and RIT depends on a multidisciplinary approach involving the fields of immunology, radiochemistry, antibody production and purification, pharmacokinetics, image processing and image analysis. This success requires an understanding of:

1. the class, normal distribution patterns, and anticipated host-antibody interactions of the MAb;
2. the target antigen (Ag) such as its structure, location(s) and distribution pattern;
3. the physical properties of the radionuclide, the nature and effects of the labelling method, and MAb-radionuclide bond stability;
4. the stability of the MAb-Ag bond and MAb metabolic pathways;
5. the effects of different routes of administration, and

6. the choice of imaging modality, and most appropriate time to measure targeted radioactivity.

The following sections will address these topics and highlight several of the important historical landmark experiments that have led to their current status in oncologic imaging. These sections will include: a historical prespective of monoclonal antibodies, radiochemical labelling techniques, clinical applications, pharmacokinetic theory, factors that affect monoclonal antibody distribution and radiation dosimetry.

2.2 Historical Perspective

Any historical discussion on the beginnings of radioimmunoimaging must include mention of Paul Erlich's "magic bullet" from his 1904 article[19]. However, it was not until 1948, that Pressman and Keighly first described the use of rabbit anti-rat kidney antiserum antibodies labelled with ^{131}I to define a population of cells in an animal model. Subsequent studies focused on localizing antibodies to other normal organs which led to the idea that labelled heteroantisera could be used to detect tumors. One of the first studies utilized antibodies to human fibrin in a lymphosarcoma rat model. Similar antibodies were used in the 1960's for tumor localization and therapy in human cancer. In the 1970's Goldenberg and co-workers used a hamster model for human colorectal cancer and demonstrated localization of goat heteroantisera to CEA. Still, there were many inherent problems associated with the use of heteroantisera, the most important being the high foreign protein content and the polyclonal nature of the immunoglobulins in the antisera. The foreign protein contamination was greatly reduced with the advent of affinity-purified antibodies but the lack of high specificity and affinity due to the polyclonal mix of the antibodies remained[20].

It was Cesar Milstein's and George Koehler's discovery of a method to produce unlimited quantities of an antibody with a single specificity and directed against a predetermined antigen that was the harbinger for modern radioimmunoimaging. An explosion in laboratory research and clinical trials took place to utilize these "magic bullets" to diagnose and cure a host of illnesses. Medical researchers now had at their disposal a molecule that had the capability to target disease. In oncology, this signified a new ability to screen and identify cancer in patients, monitor treatment protocols, aid in staging of the disease, assist in prognostic evaluations, and to treat cancer using MAbs labelled with either a toxic drug or high LET emitting radionuclide[21,22].

In current clinical practice, MAbs are primarily employed as in vitro diagnostic radioimmunoassay tests ranging from the detection of HIV-1 antibodies to over-the counter home pregnancy tests[23,24]. In vitro applications in oncology have been directed towards developing an inexpensive test as part of a general screening program to detect those cancers that shed their unique antigen into circulation[25]. MAbs have also been used as reagents for immunohistochemical staining to diagnose neoplasms in pathologic specimens[26]. Ex vivo applications of immunotoxin conjugated MAbs have been reported as an aid to bone marrow transplant therapy[27,28]. Filipovich and co-workers used a cocktail of anti-T-cell antibodies conjugated to ricin in an attempt to deplete the T-cells in the transplanted allogenic marrow to reduce the chance of graft-versus-host disease[29].

The focus of this project is the application of MAbs as an in vivo cancer diagnostic agent. Utilizing tumor markers associated with cancer, the appropriate radiolabelled MAb will concentrate at the site of the lesion resulting in an area of increased uptake that can be visualized using gamma camera scintigraphy. This targeting approach can be used to locate and monitor the presence of specific receptors or tumor-associated antigens as a diagnostic aid for patient management. The book, Immunoscintigraphy: Practical Aspects and Clinical Application by Perkins and Pimm (p178) summarizes some of the work in this field (references 169 MAbs).

2.2.1 Antibodies

Antibodies or immunoglobulins are large glycoprotein molecules of high molecular weight (IgG: 150,000 daltons) that are secreted by B lymphocytes of the adaptive immune system. Their primary function is involved with the recognition of foreign glycoproteins and their subsequent participation in the immune response mounted by the host[30].

All immunoglobulins are composed of pairs of identical light and heavy polypeptide chains linked by disulphide bonds. The smaller light chain (MW ≈ 25,000) is common to all classes and occurs in two distinct forms called kappa (κ) and lambda (λ) as distinguished by their behavior as antigens. The larger heavy chain (MW ≈ 50,000 - 70,000) is structurally distinct for each class and subclass of antibody.

Although there are several different immunoglobulin isotypes, the IgG class is the antibody most often used for MAb targeting[31]. IgG is the predominant immunoglobulin found in human serum (70% - 75%) and represents about 15% of the protein content in serum. The human IgG class is composed of the gamma (γ) chain and can be divided into four distinct subclasses, IgG1 to IgG4, dependent upon the particular γ-chain used to construct the antibody. Either light chain type may combine with any of the heavy chain types, but in any one antibody, both light chains are of the same type and all antibodies produced by a single B-lymphocyte are identical.

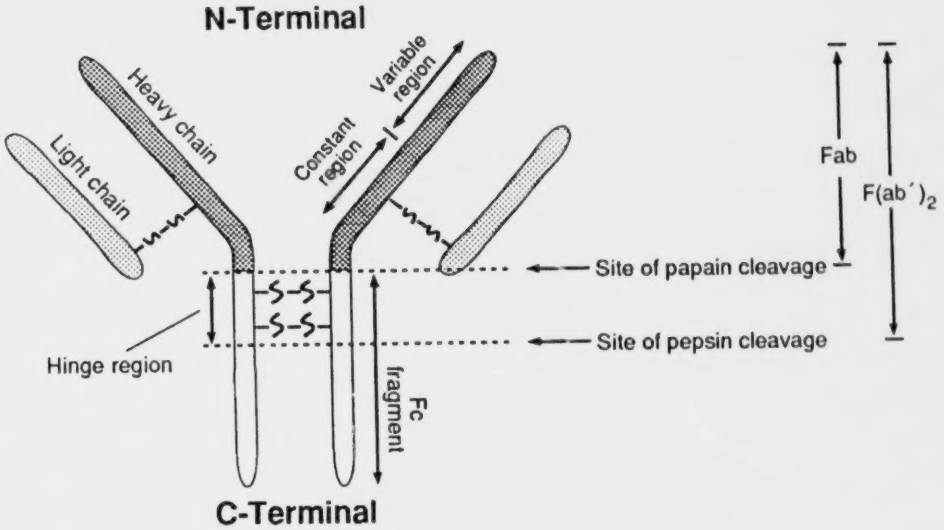
N-Terminal
Heavy chain
Light chain
Variable region
Constant region
Fab
F(ab′)$_2$
Site of papain cleavage
Site of pepsin cleavage
-S-S-
-S-S-
Hinge region
Fc fragment
C-Terminal

Figure 1: Structure of an immunoglobulin molecule.

It has been established that the light chain consists of two distinct regions[32]. The carboxy-terminal half composed of approximately 107 amino acid residues is constant except for certain allotypic and isotypic variations and is known as the Constant:Light chain (C_L) region. The amino-terminal half of the light chain is highly variable in sequence and is known as the Variable:Light chain (V_L) region. In a similar manner, the heavy chain can be divided into four regions, three constant regions (C_H1, C_H2, C_H3) and one variable region (V_H).

The heavy and light regions are linked by intra and inter-chain disulfide bonds, which in conjunction with the three-dimensional conformational folding of the antibody produce the characteristic "Y" shaped molecule with a pair of variable regions at the top and the constant region at its base

(Figure 1). There are two intra-chain disulphide bonds in the light chain and four in the heavy chain (which is twice as long). Each disulphide bond encloses a polypeptide loop of approximately 60 -70 amino acid residues to produce a series of globular regions. However, the number of inter-chain disulphide bonds varies between IgG subclasses from two (IgG1, IgG4) to four (IgG2) to fifteen (IgG3). The number of disulphide bonds is of importance for certain radiolabelling procedures as is discussed in the section on Radiochemical Labelling, page 43.

Different antigen recognition sites are created by variations in the three dimensional structure at the two tips of the Y known as the hypervariable region. It is the great diversity in the number of different ways that the antigen-recognizing region can form that makes the antibody so valuable in the immune system's fight against foreign pathogens. As a B cell prepares to make an antibody, it must first rearrange the genetic code that will specify the variable region on the light and heavy chains. There are over 10 million possible combinations, and taking into account the somatic mutations which occur in and around the V section genes[33], this number of antigen combining sites may be increased by a factor of 10 to 100. Following this rearrangement, that particular sequence of genes encoding the antibody becomes fixed and the cell produces only antibodies having that unique hypervariable region that only recognize an antigen whose shape fits, analogous to a hand fitting into a glove.

The strength of binding or affinity between the antibody and antigen can be measured by using a Scachard plot to derive the affinity constant K which can be used to assess the functional affinity of a particular antibody-antigen combination[34]. Based on the law of mass action, where the rate of complex formation is proportional to the concentration of the antibody [Ab] and antigen [Ag], the value for K at equilibrium is given by the ratio of the concentration of antibody-antigen complex [AbAg]/[Ab][Ag]. Values of K can vary from 10^5 litres/mole for low affinity complexes to 10^{13} litres/mole or greater for high affinity complexes. High affinity antibodies are desirable for diagnostic and therapeutic applications.

Each antibody has two distinct functional parts: 1) the variable region which is concerned with binding to Ag and 2) the Fc region which mediates binding of the immunoglobulin to host tissues, including various cells of the immune system, certain phagocytic cells and the first component of the classical compliment system (C1q). The antigen binding site may be split from the antibody yielding an antigen-binding F(Ab) portion (fragment for antigen binding) having a molecular weight of approximately 50,000 daltons or an $F(Ab)_2'$ portion (100,000 daltons) consisting of both binding sites. As the Fc portion of the antibody is responsible for its functional properties, including complement binding and recruitment of effector cells during an immune response of the host, it may be desirable to reduce interactions with the Fc portion by cleaving at the hinge region with papain or pepsin, leaving respectivrly, a fully functional F(Ab) or $F(Ab)_2'$ [35].

The IgG class of human immunoglobulins are normally present in the blood and lymphatic circulatory systems and have a half-life of approximately 21 days[36]. Following binding to an antigen, the antibody-antigen complex can give rise to a series of reactions. If the antigen is a soluble protein, the reaction generally results in the formation of an insoluble complex which is removed from circulation by the reticuloendothelial system. When the antigen is found on the surface of particles such as bacteria or erythrocytes, the divalent antibodies tend to form bridges between the particles, causing their aglutination. These immune complexes are then removed by a mononuclear phagocyte system, particularly in the spleen (red pulp), liver (Kupfer cells) and lungs (pulmonary alveoli). A more complete description of immunoglobulins, their function and production has been compiled by Turner and co-workers[37].

2.2.2 Monoclonal Antibodies

Monoclonal antibodies (MAbs) are homogeneous populations of antibody molecules where all the antibodies are identical and have the same unique specificity for a given epitope on an antigen. In general, normal B-lymphocytes will produce antibodies when challenged by an appropriate antigen such that all immunoglobulins secreted by a particular B-lymphocyte have the same specificity for that antigen. However, these cells are impractical for producing clones of the antibody because they can only be maintained for a short time (weeks) in tissue culture.

The technology currently used to produce MAbs was developed in 1974 by George Kohler and Cesar Milstein[38] at the Medical Research Council in Cambridge, England, for which they were later awarded the Nobel Prize in Medicine in 1984. This new technique made possible the potential for obtaining unlimited quantities of a pure antibody with a single specificity[39,40] Their technique is summarized below and illustrated in Figure 2.

The desired antigen is injected into a host species, usually a mouse, to stimulate B-lymphocytes that recognize the antigen to become antibody producing plasma cells. At this point several different plasma cells may be stimulated to produce antibodies directed against different epitopes on the antigen. Additional antigen exposure may be given to the mouse to ensure a high yield of the specific lymphocyte. The mouse is then sacrificed, its spleen removed and the splenic lymphocytes isolated. All the harvested cells are then mixed in vitro with an immortal (malignant) non-antibody-producing plasma cell line (myeloma cell) in presence of polyethylene glycol (PEG), inactivated Sendaii virus[41] or electric fields[42] to fuse the cellular membranes of the two cell types to produce a hybridoma. This fusion results in a new cell type, or hybridoma, but is present only in small amounts of the cell mixture with other components including lymphocyte-lymphocyte and myeloma-myeloma fused cells and unfused lymphocytes and myeloma cells.

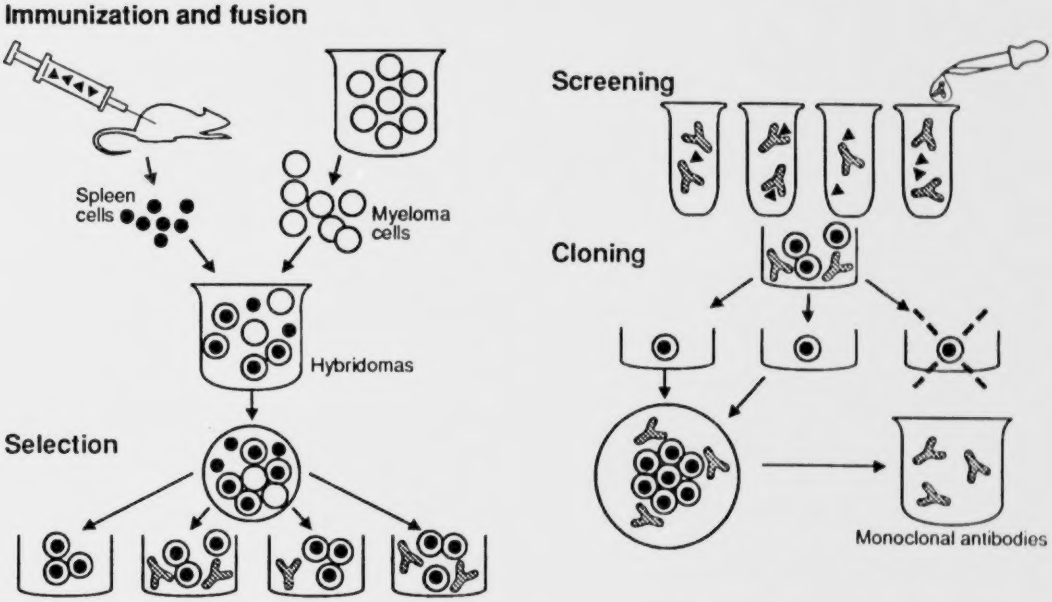
Immunization and fusion
Spleen cells
Myeloma cells
Hybridomas
Selection
Screening
Cloning
Monoclonal antibodies

Figure 2: Production of monoclonal antibodies.

The hybridoma cells must next be selected from this mixture. The mixture of lymphocytes, myeloma cells and hybridomas are transferred to a selected growth medium containing hypoxanthine, aminopterin and thymidine (HAT). The aminopterin blocks amino acid synthesis but the hypoxanthine and thymidine can be used to produce nucleic acids by the nucleotide salvage pathways in cells containing either hypoxanthine-guanine phosphoribosyl-transferase (HGPRT) or thymidine kinase (TK). The myeloma cell line that was chosen as the fusion partner lacks both of these enzymes so that all unfused myloma cells will die due to their inability to synthesize nucleic acids by either the de nova or salvage pathways. The unfused lymphocytes will also naturally die out in a few days due to poor growth in vitro. However, the hybridoma cells will continue to grow as the genes that form the lymphocytes can provide the genetic code for producing the enzymes HGPRT or TK. The surviving hybridomas are then separated and cultured in small quantities.

The next task is to locate those clones that secrete the desired antibody. This is usually accomplished by screening the harvested antibodies using radioimmunoassay (RIA) or enzyme-linked immunoabsorbent assay (ELISA) techniques. In both the RIA and ELISA assays the target antigen is fixed at the bottom of a test tube and the supernatant from the hybridoma cultures (containing the antibody) are added to each tube and incubated for a predetermined time. The contents are then washed, leaving behind only those antibodies that recognize the antigen. Radioactive or enzyme-linked antibodies specific to the primary antibodies are then added to the tubes, incubated and rewashed. Only those wells which contain radioactivity or a color reaction contain the desired activity.

The cells in the identified wells of the hybridoma cultures are then separately cloned to produce a clonal population of the hybridoma that produced the desired MAb. This cell type or hybridoma is encouraged to multiply in tissue culture and the secreted antibodies are concentrated, purified and retested for specificity against the antigen. These clones can be further tested by performing Scachard plots to identify those clones having the highest affinity to the antigen. The harvested MAbs have a unique specificity for the target antigen, and these MAbs can then be propagated indefinitely from the hybridoma.

The final step following their selection is to collect a portion of the hybridoma cells to be frozen in liquid nitrogen and preserved for future use. This is done because occasionally a hybridoma will stop secreting antibodies and the cell line will have to be retrieved from the frozen stock. Cells have been shown to be viable after several years of storage in liquid nitrogen[43].

Commercial production can yield large quantities sufficient for clinical application as drug carriers. There are several methods for producing large quantities of a desired MAb. The simplest method is to grow the hybridomas in cell culture and harvest the secreted antibodies from the supernatant. This method provides low yields compared to other methods (less than 1 mg/mL) and is relatively expensive. However, this method is useful for research purposes requiring only limited supplies.

In another technique, the hybridomas are injected into the peritoneal cavities of mice where they grow quickly due to their neoplastic properties. The antibodies are secreted into the peritoneal cavities producing an ascites fluid rich in antibody. In 2 to 3 weeks, 2 to 5 mL of ascites fluid can be harvested having concentrations in the range of 5 to 15 mg/mL. Disadvantages of this method include the cost of maintaining a large supply of mice and the contamination of the peritoneal fluid with other proteins and viruses besides the antibody[44].

Newer techniques use bioreactors consisting of a mass of semipermeable hollow fibres packaged into cylindrical cartridges. The hybridomas are grown in the extracapillary volume and the nutrients are delivered by the hollow fibres. Each cylinder contains about 10^{10} cells and continuously produces relatively pure forms of the MAb at the rate of several mg/day. A similar technique involves growing the cells inside semipermeable porous spheres with the nutrients circulating on the outside. After a period of several weeks the spheres are harvested and the MAbs collected. Purity and production rates are similar to that of the hollow fibre method.

Purification of the MAbs following production and prior to in vivo use and commercialization depends on the production method. In general, the medium containing the MAb (ascites fluid or cell culture) is clarified by either centrifugation or filtration. Purification of MAbs is usually carried out using some type of affinity chromatography[45]. Two commonly used purification techniques are: 1) the protein A column (derived from a staphylococcal protein) which non-specifically binds immunoglobulins and 2) hydroxyapatite, a non-specific adsorbent for immunoglobulins. The immunoglobulins are respectively eluted from these columns by reducing the pH or increasing the salt in buffer used to wash the column. Eluent from these columns can then be passed through a SEC-HPLC column to remove unwanted proteins and MAb aggregates. Virus contamination can be removed by heat treatment (55 - 60°C for a few minutes), or through the use of virus-antibody-free mice to produce the MAbs or cell cultures. Final testing of the MAb may employ such techniques as: protein assay, SEC-HPLC, gel chromatography, RIA, cell-line and frozen section bioassay, NR/R SDS PAGE - extended XC, extended $S^{+}L^{-}$, and reverse transcriptase. Conventional membrane filtration can be used to remove bacterial contamination. Antigen affinity and MAb stability should also be confirmed.

2.2.3 Chimeric Monoclonal Antibodies

Most of the antibodies currently in the various stages of clinical trials are derived from hybridomas of murine origin. However, when this foreign protein is injected into patients, a human antimouse antibody (HAMA) response (see page 50) is produced in about 50% of patients receiving a single dose of intact IgG[46]. The desire to reduce the antigenicity of these MAbs due to the HAMA response has lead to the development of chimeric antibodies[47].

Chimeric MAbs are immunoglobulin molecules created by recombinant-DNA techniques and gene transfection techniques in a process that creates human-mouse antibodies consisting of murine variable regions and human constant regions[48,49]. Genes from the desired variable regions from murine cell lines are spliced to the genes that code for the constant region of the human immunoglobulin. The resulting chimeric gene is then spliced into an expression vector and transfected into an appropriate cell line. The resulting transfectoma cells are then selected for stability and their ability produce the MAb of interest. Once identified, the transfectomas are amplified in culture or in the ascitic fluid of mice, similar to the techniques used for murine-derived MAbs. Using this method it is possible to combine any murine variable region to any human Fc region, where changes in the constant region will alter the MAbs ability to bind different proteins, to fix complement or be multivalent.

New advances in the production of chimeric antibodies have enabled researchers to locate the hypervariable regions that actually bind antigen within the murine F(Ab). These sequences have been cloned from the murine F(Ab) and inserted into the genes encoding intact human immunoglobulin. The resulting MAb has the same binding affinity but is now almost entirely of human composition. These chimeric hybrids should prove much less antigenic than the corresponding murine derived MAbs, thereby permitting multiple application protocols with less risk of immunological intolerance. However, it should be remembered that even entirely human MAbs may be immunogenic due to allotype and idiotype polymorphism. One of the antibodies used in this study, c174H.64, is a chimeric MAb where only the hypervariable region is of murine origin.

The future use of MAbs depends upon the ability to genetically engineer them to enhance certain properties or circumvent problems. Through recombinant and gene transfection techniques the antigen-binding properties can be optimized and the Fc effector functions can be increased, decreased or totally eliminated from the antibody[50]. Some of the next generation of MAb-like molecules might include:

1. Single-chain antigen-binding proteins (F_V) consisting of the variable-domains from the light(V_L) and heavy(V_H) chains, linked by a peptide. It would have similar antigen-binding properties as the parent MAb; however, its smaller size should aid in its ability to penetrate tumor sites while clearing from the vascular system more quickly with the net effect of enhancing target uptake with decreased background.
2. V_H -domain proteins having similar properties as the single-chain antigen-binding proteins but with reduced antigen-binding affinity compared to the parent MAb.
3. Hypervariable-region peptides or molecular recognition units have the same amino-acid sequence as the hypervariable region of the heavy chain of the parent MAb. These peptides may contain as few as 16 amino-acids (approximately 1320 residues for a MAb) and should have an even greater penetrating ability due to their small size.

2.3 Clinical Use of Radiolabelled Monoclonal Antibodies

The main feature of an antibody that is exploited for RIS and RIT is its ability to recognize and bind to a specific antigen[51]. It is this high degree of specificity and the ability to tailor that specificity to a given antigen that makes MAbs appealing as carriers when designing drug or radionuclide targeting protocols. An understanding of its role in the immune response, the mechanisms for localization, and its metabolic fate following Ag binding will assist in the recognition of the benefits and potential problems associated with RIS and RIT.

Pressman and co-workers were among the first to use polyclonal antibodies labelled with ^{131}I for tumor localization[52] in rats bearing Wagner's osteogenic sarcoma. In the mid 1960's Gold and Freemen described carcinoembryonic antigen (CEA) as a possible tumor marker for gastrointestinal malignancies[53]. Anti-CEA polyclonal antibodies labelled with ^{131}I were first successfully used by Goldenberg and co-workers to target a variety of tumors in addition to gastrointestinal cancers. Unfortunately, other investigators using polyclonal ^{131}I anti-CEA antibodies were not able to duplicate some of the early successes of tumor targeting[54]. Some of the problems have been attributed to the polyclonal nature of the antibodies as different preparations could target any of the several epitopes of the CEA antigen. Another persistent problem was related to the radionuclide used to label many of the early polyclonal antibodies. Dehalogenation of the ^{131}I from the antibody[55] and the relatively high radiation dose to the patient as a result of the associated beta emission and 8 day half-life were the main problems. A lesser, though not insignificant problem was due to the 364 keV gamma-ray which adversely affected gamma camera sensitivity and image resolution.

The problems related to polyclonal antibodies were solved with the arrival of hybridoma technology in 1975. This new technology overcame a major hurdle in the field of tumor immunology; large scale production of uniquely characterized monoclonal antibodies was now possible. Indium-111 replaced ^{131}I with improved targeting, lower radiation dose, better imaging characteristics and higher ^{111}In-MAb stability[56]. Further improvements have been made with the introduction of ^{99m}Tc as the radiolabel due to its optimal energy for imaging and low radiation absorbed dose to the patient[57]. Advances in genetic engineering have yielded many improvements in "second generation" of MAbs[55] including: increased antigen-binding specificity and affinity, chimeric and humanized MAbs as well as fragments and even smaller molecular-recognition units.

Unfortunately, a true cancer antigen has yet to be identified. It should be truly tumor-specific, uniformly and densely distributed among all cancer cells and accessible to the MAb. It should be membrane bound since circulating antigen could complex with the injected MAb before reaching the tumor. Even if a unique antigen was found, there would likely be a subpopulation of cancer cells not expressing that antigen, due to tumor heterogeneity.

Never-the-less, several antigens have been isolated that are quantitatively increased during malignancy and often circulating in the blood such as alpha-fetoprotein[58] (AFP) in germ cell and hepatocellular carcinomas and carcinoembryonic antigen[59,60] (CEA) in gastrointestinal cancers. Other antigens have been isolated that have altered glycosylation or are normally cyrptic within the cell membrane but are expressed on the cell surface of cancer cells. This type of antigen has been termed a tumor (cancer) associated antigen or TAA (CAA) as it is not usually expressed on the normal, mature cell surface. As a result of these discoveries, several generalities have emerged from the study of TAAs over the last 20 years and have aided in the design of new MAbs[61,62].

1. Truly distinct cancer antigens are not required for RIS.
2. A particular TAA will usually be associated with more than one type of cancer and these pan-carcinoma MAbs can be used to image a variety of tumor types.
3. Heterogeneity of cancer cells within a tumor-type may lead to altered or absence TAA expression. Cellular heterogeneity can be a greater problem for RIT if there are insufficient TAAs within the tumor mass to mediate a significant therapeutic response.
4. Expression of the TAA on the cell surface may change following binding with a MAb. Some TAAs are stable on the cell surface when complexed with antibody[63], while others are internalized[64].

In some cases, circulating TAAs do not neutralize the injected MAb. This is more likely to be the case for low affinity MAbs[65]. Targeting has been accomplished even when as little as 15% of the cells express the antigen[66].

These effects must be balanced against one another when designing a MAb (or bank of MAbs) for use as a delivery protocol against a particular TAA[67]. The effects of circulating antigen must also be addressed and may even preclude the use of a particular MAb in patients, as in the case of the B80.3 MAb tested in this study and further discussed on page 55.

The affinity of a MAb for a particular TAA governs its capacity to bind with antigen and will influence the target to background ratio[a] (T/B) and hence, the detectability of the target by RIS procedures. As the concentration of the TAA in a given clinical context is usual fixed, a higher affinity MAb/TAA complex will enhance tumor visualization. Alternatively, the T/B ratio can be increased by reducing the background activity (circulating MAb). This may be accomplished by decreasing nontarget binding[68] from nonspecific interactions with molecules other than the TAA or by increasing the clearance rate of the radiolabelled MAb. MAb clearance may be increased if a F(Ab) or $F(Ab)_2'$ fragment is used or through the use of bispecific MAbs[69] (as explained on page 54).

---

[a] The tumor to background ratio is defined in equation 4.

A theoretical maximum target to background ratio can be estimated from the law of mass action[70]. Assuming that the binding sites of the MAb are uniform and uncooperative in action, the following equation will describe their relationship:

$$\text{MAb} + \text{TAA} \underset{k'}{\overset{k}{\rightleftarrows}} \text{MAb}\bullet\text{TAA} \qquad (1)$$

where k = association constant and

k′ = dissociation constant of the complex MAb•TAA.

At equilibrium, the rate of formation of the immune complex is equal to the rate of dissociation so that equation (1) can be rewritten as:

$$k \times [\text{MAb}][\text{TAA}] = k' \, [\text{MAb}\bullet\text{TAA}] \qquad (2)$$

The intrinsic association constant K_a, which represents the affinity of the binding site is simply the ratio of the association and dissociation constant. Substituting for K_a and rearranging equation (2):

$$[\text{MAb}\bullet\text{TAA}]/[\text{MAb}] = K_a \, [\text{TAA}] \qquad (3)$$

Recognizing that [MAb•TAA]/[MAb] is in effect the target-to-background ratio, equation (3) becomes:

$$T/B = K_a \, [\text{TAA}] \qquad (4)$$

Equation (4) implies that RIS visualization of a tumor theoretically depends upon the concentration of the antigen in the tumor and the affinity of the MAb for the TAA. Assuming the concentration of the TAA to be constant at about 10^6 per tumor cell[71], and 10^9 cells per gram ($\approx$1 mL) of tumor, there will be approximately 10^{15} TAA per gram of tumor. Using Avogadro's number one obtains $10^{15}/6.023\times10^{23} = 1.66\times10^{-9}$ moles of TAA per gram of tissue which is equal to 1.66×10^{-6} molar. To achieve a target-to-background ratio of 10:1 for a tumor of this size, the intrinsic association constant, K_a (from equation 4) would need to be at least 6×10^6 litres/mole. This assumes that:

1. all the TAAs are bound to a radiolabelled MAb,
2. there are no conformational changes in the TAA,
3. there is no antibody clearance from the circulation and
4. that there is no limit on the number of passages that the MAb can make to the tumor.

Thus knowledge of the pharmacokinetics of the MAb and estimates of its accessibility to the tumor are necessary to predict tumor-to-background ratios. If only 1% of the antigen is available for binding and 50% of the MAb is cleared from the circulation by other means or does not reach the tumor, the K_a would need to be in the range of 10^9 to achieve a T/B ratio of 10:1.

Assuming that an appropriate TAA has been identified, there are many other factors that affect cancer radioimmunodetection and may be summarized as:

1. the character of the MAb (specificity, purity, affinity to the TAA, isotype, whole or fragment, dose to patient, species in which the MAb was raised, and patient pharmacokinetics);
2. the nature of the radiolabel (physical properties, chemical properties-immunoconjugate stability, imaging properties, radiation dose, specific

activity, effects on immunoreactivity, metabolic cleavage from the MAb, pharmacokinetics of the unbound radionuclide);

3. the tumor size and location(s), location and distribution of the TAA, TAA density, TAA modulation (shedding, capping, internalization, etc.), target/nontarget ratio, vascularization and permeability and the distribution of the TAA in other body sites or fluids;
4. the imaging system and method of interpretation (planar, SPECT, PET, image manipulation such as computer assisted background subtraction and the best time post-injection to perform RIS
5. the route of administration;
6. the presence or absence of a host anti-MAb response; and
7. the presence or absence of circulating TAA or MAb-TAA complexes.

All of these need to be addressed when designing new RIS patient protocols. Two examples from the literature are reviewed on page 25 and page 29 that illustrate the care and detail required to develop a successful MAb RIS or RIT program.

2.3.1 Radioimmunoscintigraphy: A Clinical Case-Study

Radioimmunodetection in oncology uses radioactively labelled anti-tumor antibodies which are administered to patients with malignant disease. When used as diagnostic agents, these radiolabelled MAbs are designed to find cell-surface antigens that are expressed on primary and metastatic cancer cells. Standard nuclear medicine scintigraphic procedures are then used to locate disease.

A clinical perspective of the B72.3 MAb is reviewed to illustrate its utility as a diagnostic agent for colorectal cancer. The B72.3 MAb was derived in mice immunized with a membrane enriched fraction of a human carcinoma metastasis to the liver[72]. The antigen to the murine IgG_1 was a high molecular weight glycoprotein (MW > 10^6) with the characteristics of a mucin and has been called TAG-72 (tumor-associated glycoprotein)[73]. Tag-72 is expressed in several epithelial derived cancers including colon adenocarcinomas[74], invasive ductal carcinomas of the breast[75], common epithelial ovarian carcinomas[76] as well as a large number of pancreatic, gastric and esophogeal cancers[77] suggesting its pancarcinoma nature. Varying levels of circulating TAG-72 antigen have been found in patients with these types of cancer[78]. The antigen was also found in fetal colon, stomach and esophogeal tissue, defining TAG-72 as an oncofetal antigen[79].

The work by Jeffrey Schlom, David Colcher and co-workers at the National Cancer Institute in Bethesda, Maryland illustrates the amount of effort involved in coordinating different research groups and the resulting successes obtained from a carefully planned set of clinical trials. Using the resources at the National Cancer Institute and the National Institutes of Health they were able to evaluate the ability of radiolabelled MAb B72.3 to localize in the metastatic lesions in colorectal cancer patients using a variety of radioimmunodetection modalities. Different routes of administration were also compared.

All patient groups in the following patient trials had confirmed or suspected metastatic peritoneal lesions. The first study tested the effects of varying dose. A group of twenty patients were given 0.8 to 10 mCi of ^{131}I labelled B72.3 i.v., with doses ranging from 0.16 to 20 mg[80].

Gamma camera images were taken approximately 2 hours post-injection, and daily thereafter for the following week. As part of an NCI Surgery Branch protocol, suspected carcinoma lesions and selected normal tissues were removed from each patient. All specimens were weighed and placed in a gamma counter to determine the activity per gram of tissue. The samples were then sent to pathology for routine histopathologic processing and examination, with the tissue classified as cancerous or normal, solely on the basis of histopathologic examination by two pathologists. Fixed biopsy specimens were analyzed to determine the percentage of tumor to normal cells. TAG-72 antigen positive cells were identified using radioimmunoassay (RIA) and the ABC immunoperoxidase immunohistochemical reaction. The location of the reactive antigen in relation to cellular anatomy was noted and autoradiography employed to observe the penetration and distribution of the radiolabelled MAb through the tumor mass. With this well designed protocol and abundance of data, the following observations were made for those patients receiving ^{131}I-B72.3 i.v.

1. No correlation was made between IgG dose, ^{131}I activity (Bq) or its specific activity (Bq/gm), and whether a gamma camera image was positive or negative.
2. Positive gamma images as confirmed by surgery were observed in 10 of the 20 patients.
3. Autoradiography indicated that the radioactivity was equally distributed in the medial and peripheral regions of the tumor demonstrating good penetration of the label throughout the tumor mass.
4. Histology of normal tissue samples revealed 198 of 210 had no uptake, 10 with uptake were either next to carcinoma or draining carcinoma and the final 2 uptake samples were from spleen biopsies. In both these cases, the patients had high serum levels of circulating ^{131}I-B72.3-TAG-72 complexes as identified by HPLC size exclusion chromatography. Even though immune complexes can also localize in the liver, this was not observed in the scans or biopsies. No liver biopsies were available from the patients having high levels of circulating immune complex.
5. TAG-72 levels were elevated in approximately 60% of the patients prior to injection with ^{131}I-B72.3 as identified by RIA; however, in no cases did this elevated level interfere with MAb binding to the tumor.

6. No anaphylaxis, serum sickness, indication of bone marrow suppression or other evidence of toxicity was observed at any of the MAb or ^{131}I dose levels or from the isotype identical control MAb ^{125}I-BL-3.
7. Positive uptake of ^{131}I-B72.3 was observed in 99 of 142 separately biopsied carcinoma lesions. Antigenic heterogeneity of the tumor or poor tumor vascularization was speculated for one category of patients who had both positive and negative MAb biopsies.
8. Mucinous adenocarcinomas were the histological tumor type that had the highest overall uptake of ^{131}I-B72.3.

The following observations were made for a group of four patients using the same surgical and histological protocol but receiving simultaneous administration of identical MAb mg doses of ^{131}I-B72.3 i.p. and ^{125}I-B72.3 i.v. to compare the effects of a different route of administration[81]. To compare tumor localization from the two routes of administration (0.76-1.2 mg of B72.3 labelled with 5-10mCi ^{131}I and 2 mCi or of ^{125}I). Serum pharmacokinetic parameters were measured for both the i.v. and i.p. administered radiolabelled B72.3.

1. The i.p. administered MAb localized at least two times better in terms of percent injected dose per gram than that administered by the i.v. route for 35 of 55 biopsied carcinoma lesions, 7 lesions were comparable and in 13 the i.v. administered MAb localized at least two times better.
2. The levels of i.p. and i.v. administered MAb were similar in normal tissues.
3. The most striking correlation with the differential MAb uptake occurred when the metastatic lesions were characterized as peritoneal implants or nonimplant metastases. In all 10 nonimplant lesions the i.v. route was better than the i.p., with differential uptake ratios as high as 38:1. In 35 of 40 lesions classified as peritoneal implants the i.p. route was superior.

A hand-held intraoperative gamma-probe was tested to study its utility during surgery for the radiolocalization of colorectal carcinoma in 35 patients receiving ^{125}I-B72.3 i.v. In 92% of patients there was good agreement between the techniques. None of the 50 positive probe readings were TAG-72 negative. They also noted a trend toward higher tumor to normal tissue ratios (>10:1) when there was a prolonged interval between administration of the MAb and surgery (serum half-life of ^{131}I-B72.3 was approximately 3.5 d). No correlation was noted between different degrees of tumor differentiation. Both primary and metastatic lesions were detected by the probe.

The above study has been summarized to illustrate a number of the factors involved in evaluating the clinical utility of a MAb used as a radioimmuno-diagnostic tool. The ability to link into a pre-existing surgery protocol for their patients provided the ability to image the MAb, as well as obtain histopathological data to compare the presence or absence of disease with the uptake of activity. The difficult questions of tumor penetration by the MAb and the simultaneous measurements of different routes of administration were also addressed. Although the specificity of MAb B72.3 was low compared to other Mabs currently in Phase I and Phase II testing, the researchers found that they could improve their imaging results by using a bank of MAbs to counteract some of the effects of antigen heterogeneity. Schlom and co-workers also speculated on obtaining a higher specificity using second generation MAbs designed against a purer form of TAG-72.

2.3.2 Radioimmunotherapy: A Clinical Review

As described in the introduction, monoclonal antibodies have held great promise for their ability to target disease. Unfortunately, there have been problems in bringing the successes observed in animal models and in vitro studies into the clinical milieu. One of the main difficulties is achieving easy access to the antigen. Most solid tumors frequently outgrow their blood supply and, combined with high interstitial pressures associated with the tumors, delivering sufficient MAb to the tumor site for either RIS or RIT becomes difficult.

The problem of choosing the best practical route for overall efficacy is difficult and depends on several factors as observed in the work by Schlom and co-workers discussed above. Access to the tumor sites were partially achieved by choosing an alternate route to administer the MAb.

Most antibodies used clinically are administered intravenously for both RIS and RIT to provide access to all tissues with the possible exception of those in the central nervous system. With macromolecules as large as MAbs, regional delivery may be a feasible alternative as they are more easily confined than small molecules in anatomically defined compartments and tissues. Much of the work to date on regional delivery of MAbs has delt with the lymphatic system, and to a lesser extent, intraperitoneal administration, intraarterial infusion, and injection into the cerebrospinal fluid[82]. As we have seen from Schlom's work, the decision as to the best route of administration depends upon the type and location of the tumor. In some cases a combination approach may be best to target both well-vascularized tumors (i.v.) and poorly vascularized tumors in anatomically restricted regions (i.p.).

The following work is reviewed to show the potential of this technology in locating and treating cancer. It demonstrates the importance of kinetic and dosimetric modelling to estimate tumor burden and predict a radioimmunotherapeutic response for RIT. More important, this study was designed around the hematological malignancy, acute myelogenous leukemia (AML), where the MAb access to the TAA was easy and rapid.

In a Phase I clinical trial, George Sgouros and co-workers[83] at the Memorial Slone-Kettering Cancer Center in New York used MAb ^{131}I-M195 (anti-CD33) in AML patients to estimate the tumor burden and absorbed radiation dose. These estimates, together with predictions on MAb clearance kinetics and the MAb-TAA interaction, are needed for RIT to assess the amount of MAb that should be administered and the amount of radioactivity that should accompany the MAb.

A nonlinear, two compartment model was used to fit the biodistribution data. The MAb was injected into compartment 1 (free MAb), followed by distribution in a volume (V_d) where it bound to available antigen (compartment 2: bound MAb-TAA). Their model assumed that a given number of antigen sites (10^4 per leukemia blast) were equally distributed in a volume V_d, equal the plasma volume (3 litres), plus the extracellular fluid volume of the liver, spleen and red marrow (0.48, 0.05 and 0.22 litres)[b]. Due to the near absence of a developed capillary basal lamina in the liver and spleen, tumor cells within the extracellular fluid (ECF) space of these tissues were assumed to be directly accessible to the i.v. administered MAb.

The contents of compartment 1, representing free MAb was distributed in the vascular and extravascular spaces of these tissues. Compartment 2 distributed in a similar manner according to tumor burden. The time activity curve obtained from the image data then represented the sum of these two compartments. By assuming that compartment 1 distributes according to the ECF volume and that tumor cells not in the liver and spleen were in the marrow, a biodistribution curve for the marrow was derived. The parameters of the equations describing the pharmacokinetics of MAb M195 were obtained from serial blood samples obtained over a 4 - 6 day period and from quantitative gamma camera imaging.

---

[b] Patient-specific assessments of Vd were not made but could have been using a radiolabelled irrelevant MAb or albumin.

The mean absorbed dose to the liver, spleen and red marrow was calculated according to the Medical Internal Radiation Dose Committee (MIRD) formalism (page 58) using the biodistribution data. All the unassigned activity was assumed to be uniformly distributed throughout the rest of the body. The dose to the tumor was estimated from the cumulated activity in compartment 2 representing the dose that occurred while the MAb was bound to a cell-surface TAA. This calculation was made for an isolated leukemia blast cell for the electron dose only. Although the photon dose from sources other than the target could be significant, it was not considered in the tumor cell dose calculation as it did not impact on the target to normal tissue absorbed dose ratio. This calculation provided a worst-case scenario since the only radiation delivered to the cell was from activity on its surface.

By providing an estimate of the residence time and hence the cumulated activity for the MAb/antigen complex (compartment 2), and coupling this information with standard tumor cell geometry, a standardized approach to tumor dosimetry may be adopted. This approach would permit model-based estimates of patient response and provide a quantitative intercomparison of different therapeutic strategies using the absorbed dose to an isolated cancer cell as the end-point. It also demonstrated the potential of achieving significant treatment responses when RIS and RIT are used to manage this type of disease. The favorable response was, due in part, to the rapid access of i.v. administered MAb, and the intrinsic radiosensitivity of a hematopoietic cancer. For example, in the treatment of AML, a pilot study using ^{131}I labelled MAb M195 caused significant cytoreduction, resulting in up to 99% decrease in biopsied bone marrow blasts.

2.4 General Theory of Pharmacokinetics Related to Monoclonal Antibodies

The development of a pharmacokinetic model for a monoclonal antibody may include the study of its in vivo absorption, distribution, metabolism and excretion with time. In essence, a kinetic model is a mathematical description of the time-course of a MAb within a living organism; from the time of its administration through to its ultimate disappearance via excretion or metabolism to an unreactive form. Pharmacokinetic modelling is a tool that can be used to optimize the experimental design and development of new radioimmunoconjugates and, clinically, may result in improvements in RIS and RIT with direct benefits to the patient.

The origin of pharmacokinetics has generally been attributed to Torsten Teorell for his work published in 1937 in the International Archives of Pharmacodynamics, "Kinetics of Distribution of Substances Administered to the Body". The field has since grown rapidly, due in part to the advances in analytical chemistry which made possible the measurement of drug concentrations with ever increasing sensitivity. This review will summarize the methods of multicompartmental analysis which have been successfully used to interpret the behavior of MAbs in animals and humans. Several examples from the literature will be discussed in relation to their ability to predict MAb behavior in various diagnostic and therapeutic modalities used in the clinical environment.

2.4.1 Multicompartmental Analysis

The most common approach to describing the in vivo behavior of a MAb is to represent the body as a series of compartments which may or may not correspond to an anatomical feature. The rate of transfer of the MAb between compartments and the rate of elimination from the compartments is assumed to follow first-order or linear kinetics. Nonlinear or rate-limiting kinetics may be encountered in instances of low TAA concentration or in metabolic processes that require an enzyme or carrier system. These systems are relatively specific with respect to substrate and have finite capacities.

The simplest linear model has only one compartment and the body is represented as a single, kinetically homogeneous unit. Usually the plasma or serum is taken to represent that compartment and the rate of change of MAb concentration in the serum is reflected by a similar rate of change of the MAb in other body fluids or tissues. The one-compartment model does not constrain the MAb concentration in the other fluids or tissue to be the same as that in the plasma, only that their rate of change in concentration be the same.

Elimination from a one compartment model is also assumed to conform to first-order kinetics with the elimination rate constant represented by K and having units of inverse time. The following equation can be used to describe the biodistribution of a MAb that can be described by a one compartmental model:

$$X(t) = X_0 e^{-Kt} \tag{5}$$

where

$X(t)$ = amount of MAb in the body at any time t, after administration,

X_0 = amount administered,

K = elimination rate constant and

e = base of the natural logarithm.

Several other relevant pharmacokinetic parameters can be derived from this model including the volume of distribution and plasma clearance. The reader is referred to several of the excellent texts on pharmacokinetics that cover these topics[84].

In most cases however, it takes a finite time for the MAb to fully distribute itself throughout the available body space after administration. During this distribution phase the MAb concentration will decrease more rapidly than in the post-distribution phase. As the distribution phase may last from minutes to hours, it may or may not be apparent, depending on the frequency with which the serum is sampled.

The blood and all easily accessible fluids and tissues are often treated as a common homogeneous unit and are referred to as the central compartment. As with the one-compartment model, this does not mean that all the tissues in the central compartment are the same, only that the rate of change of the MAb is equally reflected in all tissues of the central compartment. Following the administration of a MAb that exhibits multicompartment kinetics, MAb levels in the central compartment decline more rapidly during the distribution phase than in the post-distribution phase.

However, in poorly perfused tissue, MAb levels first increase, reach a maximum and then begin to decline during the distribution phase. The access of the MAb to poorly perfused tissues (i.e. muscle and fat) may occur at different rates and frequently cannot be distinguished from serum data alone. Consequently, all poorly perfused tissues are usually "lumped" into a single peripheral compartment. Peripheral compartments in a kinetic model are, at best, a hybrid of several physiological components.

At some point in time, a pseudo-equilibrium is reached between the tissues and fluids of the central compartment and the poorly perfused peripheral compartment. Once this equilibrium has been established, loss of MAbs from the serum can be described by a monoexponential process indicating a MAb kinetic homogeneity in all fluids and tissues in the body. This final phase is usually referred to as the terminal-elimination phase.

Similar to the one-compartment model, the elimination phase is assumed to follow a first order process, as is the transfer of MAb between compartments.

The number of exponential terms required to describe the MAb serum concentration with time determines the number of kinetically homogeneous compartments that may be used to describe the biodistribution of the MAb. Generally, although it need not be the case, elimination is assumed to occur from the central compartment based on the assumption that the major sites of metabolism and excretion (liver and kidney) are well perfused with blood and therefore, have rapid access to the MAb in the systemic circulation.

A two-compartment model will be developed to illustrate the kinetics following the rapid i.v. administration of the MAb with elimination from the central compartment. If adequate blood sampling is performed to capture the MAb concentration-profile with time, the following equation will represent its biodistribution in the body over time:

$$C(t) = C_1 e^{-\lambda_1 t} + C_z e^{-\lambda_z t} \qquad (6)$$

where

C(t) = MAb concentration at any time t, post-injection,
C_1 = ordinate intercept by the fastest disposition slope minus the intercept of the next fastest disposition slope,
C_z = intercept of the slowest disposition slope,

λ_1 = distribution-phase rate constant,
λ_z = terminal-elimination phase rate.

This model can be expanded further to three or more compartments, but generally if more than three compartments are used, MAb sampling at sites in addition to the serum are required. This may be accomplished in a clinical nuclear medicine environment using a gamma camera (page 67) to measure the biodistribution of MAbs labelled with a suitable radionuclide. Detailed, multicompartmental animal models may be developed using either a gamma camera or by direct tissue and organ analysis. Several examples illustrating the use of different pharmacokinetic models are described below to demonstrate the in vivo utility of MAbs in the diagnosis and management of cancer.

If the biodistribution patterns of a MAb appear to follow nonlinear or rate-limited kinetics, Michaelis-Menton formulations are used to describe these capacity limited processes using the equation:

$$-\frac{dC}{dt} = \frac{V_m C}{K_m + C}, \qquad (7)$$

where

$\frac{dC}{dt}$ is the rate of decline (biological elimination) of drug concentration (C),

V_m is the theoretical maximum rate of the elimination process and

K_m is Michaelis constant.

An inspection of equation 7 can be used to illustrate the physiological significance of the constants K_m and V_m. The Michaelis constant is equal to the drug concentration at which the rate of the process is one-half of its theoretical maximum rate. When drug concentrations are significantly greater than K_m, then the rate of decline of drug concentration occurs at a constant rate of V_m.

A combination of both linear and nonlinear kinetics may be required to describe the biodistribution and elimination of certain drugs. One such compound is salicylate which is described by two capacity-limited and three linear processes[85].

2.4.2 Examples

One of the simplest tumor models is a two compartment open model with the blood and well perfused organs as the central compartment and the tumor, together with poorly perfused tissue, as the peripheral compartment. At the other extreme, Koizumi and co-workers used a 17-compartment nonlinear parametric model to analyze the behavior of their MAb, Lym-1, in patients[86]. Numerous compartmental models of varying degrees of complexity have appeared in the literature, but the following general pattern has emerged when describing MAb concentrations in blood.

The serum biodistribution pattern of an intact MAb is bi-exponential while that of a F(Ab) fragment generally follows a tri-exponential model. Initial biodistribution half-lives are longer for an intact MAb when compared to a F(Ab), leading to the general rule that the smaller the fragment, the faster it is eliminated and usually, the higher its dissociation rate from the tumor[87].

Shani and co-workers at the School of Pharmacy, University of Southern California, studied the compartmental biodistribution of MAbs against human lung adenocarcinoma grown in athymic mice[88]. The biodistribution of the radioiodinated monoclonal antibody (KS1/4) was measured for the F(Ab), $F(Ab)_2'$ and intact antibody in tumor-bearing nude mice. Different fragments were labeled with a different radioisotope of iodine. The plasma clearance of each type of fragment was analyzed by size exclusion HPLC and compared with the radioactivity data. They showed a reasonable correlation between the expected time-course of the antibody and the experimental biodistribution data using an eight-compartment, linear radiopharmacokinetic model.

As expected[89,90], the F(Ab) and $F(Ab)_2'$ fragments were shown to clear faster than the intact MAb and the highest tumor-blood ratios were observed for the intact MAb. The presence of a significant amount of radioactivity in other organs, such as the liver, was taken into account by inclusion into this model. With the exception of the tumor, all radiolabelled molecules were lumped together in each compartment. The tumor compartment was divided into two compartments, one for free MAb and another for MAb-antigen complex. No detectable quantities of metabolites or MAb-antigen conjugates could be detected in the circulating blood.

An eight-compartment model was found to best fit their data and capture the experimental biodistribution results. Although their model was proposed using physiological compartments, it was based entirely on the data from a set of animal experiments. No assumptions were required from independent measurements and the model lent itself to analysis from data collected from a single animal. This model was validated by its ability to predict the time-course of the radiolabelled material in each organ and was superimposable over the experimental data.

From the brief summary above, it is apparent that a variety of multicompartmental models have been used to describe the in vivo distribution of different radiolabelled MAbs in both experimental animals and in humans. The number of compartments varied from 2 to as high as 17 but all were chosen to represent the biodistribution of the immunoconjugate in structurally identifiable regions that demonstrated observable uptake. In the case of the 17 compartment model, a basic structural model was expanded to specifically address the kinetics of an intact radioiodinated MAb and attempt to describe the biodistribution of its metabolic products following deiodination.

The majority of the pharmacokinetic models developed to describe the in vivo distribution of radiolabelled MAbs follow several guidelines that aid in their design. The choice of model is generally constrained to structurally identifiable regions, and compartments only used if they are determined to be observable, controllable and identifiable[91,92]. The kinetic parameters predicted by the model should also fit reasonably well with those obtained from experimental data.

For example, a simple model used to estimate the biodistribution patterns of a MAb (injected i.v.) that is excreted primarily by the kidneys and is metabolized in the liver, may be represented by the model illustrated in Figure 3. The rate constants, k_{ij}, describe the elimination from compartment i to compartment j. The accuracy of this model would be assessed using experimental data obtained from serial tissue samples in experimental animals or gamma camera image data from patients (page 42). As part of an iterative process, the kinetic model would be refined and other compartments added or removed to more accurately reflect the observed experimental data. Effects of blood-flow within an organ should be monitored during the assessment of organ activity in order to properly assess whether or not the organ should be relegated to a separate compartment (i.e. Is the organ activity due solely to the blood in its tissue?) If not, then there may be a case for the creation of a separate compartment to describe the kinetics within that organ.

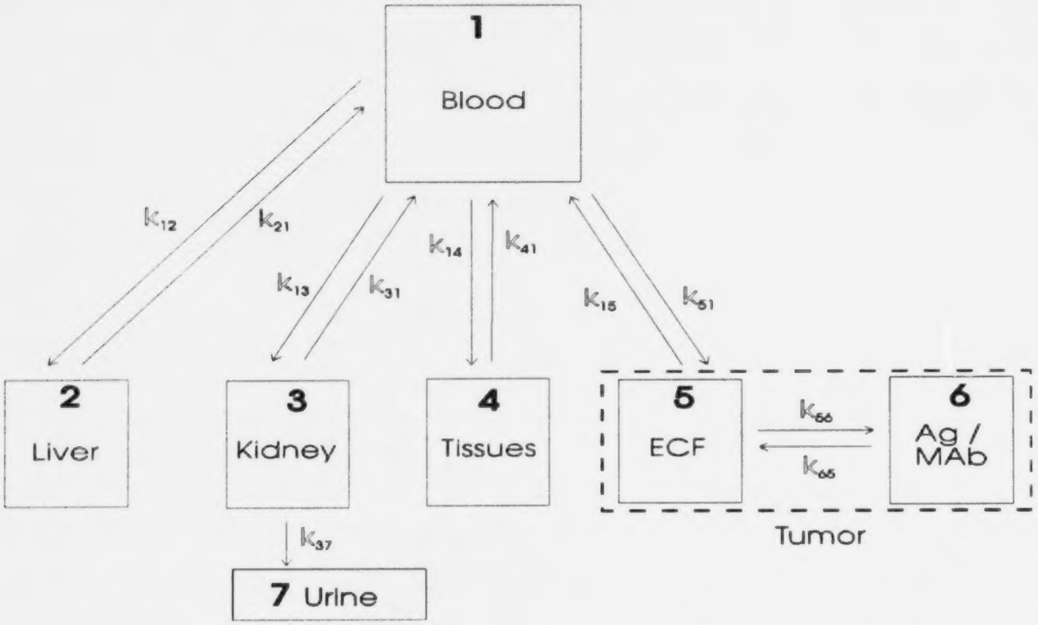

Figure 3: Schematic diagram of a linear multicompartmental model representing the in vivo biodistribution of a hypothetical MAb.

Perfusion of solid tumors can very widely depending on the type and size of the tumor. The heterogeneous blood supply of tumors may range from a well-perfused peripheral zone, through a moderately-perfused and sometimes hypoxic region, to a non-perfused and possibly necrotic interior-zone. Current research[93] has shown the uneven and changeable distribution of blood vessels and the variability of blood-flow with time, even in a single vessel. Some vessels are extremely porous or "leaky", whereas others are not. Even within a single vessel, the porosity can change from region to region. A high interstitial pressure is normally found within large solid tumors (>0.5 cm) due mainly to the absence of a functional lymphatic system. This is somewhat offset by a higher than normal blood pressure in the microvasculature of the tumor due to its abnormal geometry and compression by the tumor cells. Eventually the pressure within the vessels and interstitial matrix equalizes and small molecules in the blood can escape by diffusion (in those areas that still maintain a blood supply)[94]. Larger molecules can diffuse out into the interstitium, but at a slower rate. Thus, a variety of physiological factors can conspire to alter blood-flow in solid tumors that will in turn affect the MAb biodistribution patterns over time. This implies that, depending upon the stage of growth of a tumor, a different type of model or different rate-constants for the same model need to be used.

At some point a decision has to be made as to the significance of the amount of uptake observed in a particular compartment. If a compartment contains an insignificant amount of the radiolabelled MAb, it may be desirable to amalgamate it with a larger compartment, or possibly ignore it altogether. However, even if a small compartment was not included in the model, before dismissing it, the clinical and pharmacodynamic impact should be analyzed. For example; a small quantity of radiolabelled MAb localized in tumor tissue, may be sufficient for RIS (depending on the activity in the surrounding tissue). Alternately, a low value of tumor uptake may be sufficient for RIT if the clearance in other organs and tissues is rapid enough to spare them from the cytotoxic nature of the immunoconjugate used during therapeutic procedures. Thirdly, and possibly of greater importance, even very small amounts of MAb uptake in a particular compartment (such as the spleen or lymph nodes of the reticuloendothelial system), may be enough to trigger an immune response against the cancer[95].

2.5 Clinical Data Sources

Data collection protocols for kinetic modelling in clinical nuclear medicine utilize standard methods to monitor radiolabelled MAb levels in the serum and urine. However, problems can arise when samples are analyzed only for total radioactivity, based on the assumption that the radionuclide is still bound to the original carrier[96]. If fragmentation occurs or the radiolabel is lost from the MAb, serum analysis using size exclusion HPLC coupled to a radiation monitor may provide information on possible metabolites, free radionuclide, or antibody-antigen complexes in the serum. Radioimmunoassay techniques have also been used to monitor the serum status for free MAb or free fragment with the capacity to bind antigen.

These data can be supplimented with in vivo nuclear image data to non-invasively provide an estimate of the radioactivity within different organs and regions of the body[97]. This information can then be used to augment the pharmacokinetic model developed from the serum data. Occasionally, tissue samples may also be available, either from biopsy or following surgery, and can help in assessing the percentage of the injected dose in organs or tumors. Information obtained from gamma camera imaging is discussed in greater detail in the Materials and Methods chapter under the appropriate subheading.

2.6 Radiochemical Labelling

If a MAb is to be used routinely in RIS or RIT, a satisfactory radiolabelling procedure must be developed to form a viable radionuclide-antibody molecule or "immunoconjugate". Consideration of the method of radionuclide conjugation and its location on the MAb are of prime importance to ensure in vivo stability and to maintain the targeting capacity of the immunoconjugate. This depends on the method of attachment to the MAb and also upon its location on the molecule[98]. Placement of the radionuclide should not interfere with distribution, recognition of the antigen against which it was derived, or change the specificity of the response. The label should ideally resist both metabolic and chemical cleavage from the

MAb to reduce possible toxic effects caused by the free radionuclide[99]. An unbound radiolabel circulating in the body is undesirable because of the possible toxic effect produced in non-targeted organs due to nonspecific localization (such as bone marrow). The radionuclide will follow its own kinetic redistribution patterns once free of the MAb. For example, radioisotopes of iodine and yttrium which have been used to label MAbs for RIS and RIT will concentrate in the thyroid, stomach and gut (radioiodines)[100] and in the bone marrow (yttrium)[101].

Many methods have been developed in the last ten years to produce radiolabelled MAbs, however, a detailed discussion of the radiochemistry of MAb labelling is beyond the scope of this report and the reader is referred to several excellent reviews of the subject[102,103,104,105]. Table 2 summarizes some of the more popular labels that have been used and the method used to label the MAb. The labelling method indicates whether the radionuclide is directly attached to one of the amino-acids of the MAb or indirectly conjugated via an intermediary chelate such as diethylenetriamine-pentaacetic acid (DTPA)[106]. Of the many radionuclides listed in this table[107], the decay characteristics of ^{99m}Tc and ^{123}I are best suited for gamma camera imaging and deliver the lowest radiation absorbed dose to the patient compared to the other radionuclides. A more complete list of radionuclides that may have utility as MAb radiolabels are listed in the table on page 47.

Table 2: Characteristics of some commonly used radionuclides used to label monoclonal antibodies (EC = electron capture, IT = internal transition).

Radionuclide	Half-life	Gamma Emission (keV)	Beta Emission (MeV)	Labelling Method
^{67}Ga	78 hours	93,185,300	EC	Direct
^{90}Y	64 hours	None	2.26	Indirect
^{99m}Tc	6 hours	140	IT	Direct & Indirect
^{111}In	2.8 days	171, 245	EC	Indirect
^{123}I	13 hours	159	EC	Direct
^{131}I	8 days	637, 364, 284	0.606, 0.335	Direct

The MAbs used in this study were provided to the clinic in a pre-reduced form ready for one-step ^{99m}Tc pertechnetate labelling (see section on Radiochemical Labelling, page 86). The rest of this section will summare some of the recent work on ^{99m}Tc labelled MAbs.

The labelling of MAbs with ^{99m}Tc can be performed using 1) a direct method where the radionuclide is added to a chemically reactive site native to the MAb or 2) an indirect method where the ^{99m}Tc is coupled to the MAb by an exogenous bifunctional chelating agent. Many methods for the direct labelling of MAbs with ^{99m}Tc have been reported[108,109] where different conditions of reducing agent, pH, buffer, etc., have been used to label the MAb. The direct method of labelling entails the insertion of ^{99m}Tc between two sulphur groups endogenous to the MAb. Many of the direct labelling methods involve an initial reduction step to generate the sulphydryl groups from the MAb disulphides. Following reduction from its pertechnetate form, ^{99m}Tc is mixed with the reduced MAb to form a thiol bond with the sulphydral groups. There are approximately 35 disulphide bonds in a MAb (varies with IgG subclass) and if less than 4% of these bonds are reduced, the immunoglobulin will retain its structural integrity[110].

There has also been some discussion on weak and strong binding sites associated with this type of direct labelling method. The two endogenous binding sites for ^{99m}Tc on MAbs are: 1) a high capacity, low affinity site that accounts for 76 - 84% of the binding sites and 2) a low capacity, high affinity site which accounts for the remainder of the binding sites[111]. The low affinity sites are predominantly labelled when ^{99m}Tc pertechenetate is reduced by stannous chloride and mixed with the MAb. The low affinity sites can be blocked by the addition of diethylene triamine penta-acetate (DTPA) but labelling efficiency of the MAb is greatly reduced due to the affinity of DTPA for the ^{99m}Tc. High affinity sites on the MAb can be labelled if the disuphide bonds on the MAb are reduced prior to ^{99m}Tc labelling.

Several different methods for reducing the disulphide bonds in the MAb have been reported and their merits discussed at length in the literature[112,113]. The methods summarized below have been successfully used in the preparation of a direct-labelling kit form where the radiolabel, in this case ^{99m}Tc-pertechnetate, is added to the vial containing the MAb that has been previously prepared to accept the radionuclide. The advantages of a kit-style of labelling include: ease of labelling, speed of labelling (generally requiring only a few minutes), high specific activities and no requirements for post-labelling purification.

MAb reduction by stannous chloride or "pretinning" is a popular method and has been used in a variety of chemical conditions. When used at a strength of 1 - 2 mM, stannous chloride reduction is slow, mild and does not normally destroy the intrachain disulphide linkages of the intact MAb. $F(Ab)_2'$ fragments however appear to be more susceptible to cleavage when labelled with this method. Another common method for direct labelling MAbs with ^{99m}Tc is the Schwartz method which uses 2-mercaptoethanol or 2-aminoethanethiol to reduce the disulphide bonds. The resulting free sulphydrals are then labelled with reduced ^{99m}Tc as a phosphonate or pyrophosphate complex. A similar method uses dithioretol as the reducing agent and glucarate as the weak complexing agent[114].

The indirect methods for labelling MAbs with ^{99m}Tc use bifunctional chelates[115,116]. The chelate has a specific binding site for a preselected region on the MAb and a second designed to bind ^{99m}Tc, in effect acting as a "glue" between MAb and the radionuclide. One of the methods that has been used to label MAbs for patient use employs a diamide dimercaptide (N_2S_2) chelator which form highly stable tetradentate complexes with reduced ^{99m}Tc. In this method the ^{99m}Tc is first reduced with stannous chloride or sodium dithionite and weakly complexed to gluconate. The ^{99m}Tc is next transchelated to the ^{99m}Tc-N_2S_2 ligand. This complex is converted to the active ester form for conjugation to lysine groups on the MAb. Some of the disadvantages of this technique are relatively long labelling times (3 hours) and a low labelling efficiency of 35-50%. Post-purification is required to remove the unbound chelator. Its main advantage is its high stability as measured by in vitro cysteine challenge[117].

2.6.1 Choice of radionuclide

The choice of the drug or radionuclide conjugated to the MAb depends upon the application[118]. For diagnostic and prognostic studies using in vivo radioimmunoimaging techniques, the MAbs are labelled with gamma-emitting radionuclides. Modern nuclear medicine imaging equipment has been designed around the 140 keV gamma photon of ^{99m}Tc so that the ideal radionuclide should emit a single gamma photon with an energy of approximately 150 keV. This ideal radionuclide would have a half-life of 12 to 24 hours to permit patient scanning during the expected uptake and distribution phases of the MAb or its fragments. Some of the radionuclides that have been used for these types of studies are ^{99m}Tc, ^{111}In, ^{123}I and ^{131}I (see Table 3).

A relatively new field of nuclear medicine is positron emission tomography (PET) which utilizes the physics of positron decay to yield quantitative, attenuation corrected images of the radiolabelled MAb within the patient[119,120,121]. It is also possible to extract quantitative data from these images that would enable the pharmacokineticist to perform non-invasive, in vivo analyses of the uptake in different organs by MAbs labelled with positron-emitters[122,123,124]. This pharmacokinetic data could be compared to those of normal individuals to diagnose different disease conditions or be used to plan therapeutic MAb dose regimens for cancer patients. A list of possible PET radionuclides with application in RIS might include: ^{52}Fe, ^{64}Cu, ^{68}Ga ^{76}Br, ^{89}Zr and ^{124}I.

A Table of candidate radionuclides for RIS and RIT has been compiled by Muasner and Srivastava[125]. These and other potentially useful radionuclides are presented in Table 3.

Table 3: Some potentially useful radionuclides for labelling monoclonal antibodies for RIS and RIT.

Radionuclide	Half-life	Emissions	Application
^{18}F	1.8 h	$\beta+$	RIS
^{55}Co	17.5h	$\beta+$	RIS
^{64}Cu	12.7 h	$\beta+$	RIS
^{67}Cu	2.6 d	$\beta-, \gamma$	RIS, RIT
^{76}Br	16 h	$\beta+$ (54%)	RIS
^{77}Br	2.4 d	EC, γ	RIS
^{90}Y	2.6 d	$\beta-$	RIT
^{97}Ru	2.9 d	EC, γ	RIS
^{99m}Tc	6.0 h	IT, γ	RIS
^{105}Rh	1.5 d	$\beta-, \gamma$	RIS, RIT
^{109}Pd	14 h	$\beta-, \gamma$	RIS, RIT
^{111}In	2.8 d	EC, γ	RIS
^{117m}Sn	13.6 d	IT, $\beta-, \gamma$	RIS, RIT
^{123}I	13 h	EC, γ	RIS
^{124}I	4.2 d	$\beta+$	RIS
^{125}I	60 d	EC, X-rays	RIT
^{131}I	8.0d	$\beta-, \gamma$	RIS, RIT
^{151}Pm	1.2 d	$\beta-, \gamma$	RIS, RIT
^{153}Sm	1.9 d	$\beta-, \gamma$	RIS, RIT
^{159}Gd	19 h	$\beta-, \gamma$	RIS, RIT
^{161}Tb	6.9 d	$\beta-, \gamma$	RIS, RIT
^{166}Ho	1.1 d	$\beta-, \gamma$	RIS, RIT
^{186}Re	3.8 d	$\beta-, \gamma$	RIS, RIT
^{188}Re	17 h	$\beta-, \gamma$	RIS, RIT
^{210}Bi	5.0 d	$\beta-$	RIT
^{211}At	7.2 h	α	RIT

where:

α: alpha decay, β: beta decay,
EC: electron capture, IT: internal transformation,
γ: gamma decay with sufficient energy for external detection.

When radionuclides are used with little or no gamma emissions, preliminary biodistribution studies must be done with other, more appropriate radionuclides. Although it is possible to produce RIS images from bremsstrahlung radiation[126], scintigraphic resolution is usually poor, making quantitation for dosimetry difficult. Of interest then is choosing a pair of radionuclides with similar chemistry, where one would be used for RIS to develop the biodistribution patterns and dosimetry estimates and the other used for RIT. One of these RIS/RIT pairs that has been tested in Phase I clinical trials[127] is $^{99m}Tc/^{186}Re$.

2.7 Factors Affecting Monoclonal Antibody Biodistribution

As evident from the above reviews, there are a number of complicating factors that should be addressed when developing a pharmacokinetic model based on the biodistribution of MAbs in patients. Not the least of these is the difficulty in obtaining blood, urine and tissue samples. Due to the patient's state of health or their unavailability over part of the sampling period, it may not be possible to obtain all the samples required for a complete analysis. In general, the fewer the number of samples, the greater the error in fitting the model. Fortunately, a number of human tumors can be grown in animal models where sampling is not a problem and the data can usually be extrapolated to at least give a gross estimate of what the patient response might be.

The two greatest differences between human and mouse antibody kinetics when injected into patients are:

1. the shorter serum half-life of the mouse MAb (1 - 2 days versus approximately 21 days for human IgG) and
2. the ability of murine MAbs to produce an immune response in patients (and subsequent change in the biodistribution).

However, in spite of these limitations, positive results from animal studies have encouraged clinical evaluation of potential new products. Animal models have been developed with various pathological conditions and have proved valuable in pre-clinical evaluations to determine MAb imaging capabilities when labelled with appropriate radionuclides[128].

Several other factors that can affect the kinetic modelling procedure can be divided into those of either a physiological or physical nature. Some of these will be identified and possible solutions proposed.

2.7.1 Physiological Factors

There are many obstacles that can occur during RIS procedures that may cause the MAb to bind with something other than its intended target. Some of the physiological elements that can modify the expected biodistribution of a radiolabelled MAb are; the presence of circulating antigen, a host-mounted adaptive immune response against the foreign MAb protein, nonspecific uptake, the effects of cytokines and MAb metabolism. Some of these have been discussed elsewhere in greater detail under the appropriate subsection and are only mentioned briefly here. The main physiological factors which may alter the biodistribution of a MAb are discussed below.

2.7.1.1 Human Anti-Mouse Antibody

It is well known that foreign proteins can cause an adaptive immune response in humans that is manifest following the second contact to a given antigen[129]. Murine derived MAb infusions have been shown to induce a human anti-mouse immunoglobulin immune response which has been termed the human anti-mouse antibody (HAMA) response[130,131,132,133,134].

Anti MAbs (α–MAb) can be of either the μ or γ isotype. They are usually detectable within 14 days after the first infusion and initially directed against the Fc portion, and/or CH1 or CL region of the murine MAb[135]. Circulating HAMA may form high molecular weight complexes with the MAbs that result in rapid blood clearance of the MAb-complex by the liver and spleen, and concomitantly reduce tumor targeting[136]. An altered pharmacokinetic and radiation dose profile with reduced tumor uptake[137] are the prime effects of a HAMA response in RIS.

In order to overcome this problem either the HAMA must be removed from the patient by plasmaphoresis[138] or the MAb made less immunogenic to reduce the probability of a HAMA type response. The latter has been accomplished through the genetic manipulation of the MAb to produce a human/mouse chimeric antibody as discussed on page 18. Initial results from repeated infusions of these MAbs look promising in HAMA positive patients[139].

If humanized or chimeric MAbs are used, the HAMA response is generally lessened, but the possibility of a human antihuman antibody (HAHA) response could still occur due to allotypic variations between individuals. This leads to the question; if MAbs were chimerized from Santa Claus, would the patient develop a HOHO immune response?

It may be desirable to repeat a MAb study on a patient to test for recurrent disease or as part of a therapy program[140], whereby the MAb would carry a cytotoxic or radiotoxic moiety to the tumor (RIT). Repeated infusions of the same MAb generally lead to higher titres of the α–MAb (HAMA) with the anti-idiotypic portion of the α–MAb titre steadily increasing with each MAb infusion. This anti-idiotypic portion may even come to dominate the HAMA response[141].

One can speculate on the implications of this circulating α-MAb on the ability of a patient to mount an immune response against their cancer. Following Jerne's network hypothesis[142], once the α-MAb has been produced, the body may then produce idiotypic-antibodies against it or α-α-MAbs. These theoretically would be able to recognize the TAA's on the cell-surface of the cancer cells so that the body could marshal its own immune response[143,144] against the malignant disease.

HAMA levels in all patients in the studies contained in this report were tested by Biomira Inc. Pre-existing HAMA levels were found to be in the normal range for all kinetic patients and so, for this work, were considered to not effect the biodistribution of the MAbs.

2.7.1.2 Nonspecific Uptake

Nonspecific uptake and cross-reactivity with similar antigens will cause reduced targeting to the TAA and inappropriate targeting to other tissues. The effects of circulating TAAs or other molecules recognized by the MAb may also lead to altered biodistribution patterns and clearance patterns of the MAb complex that must be accounted for when designing RIS or RIT protocols. The problems of nonspecific uptake of MAbs in radio-immunoimaging are obvious[145]. False positive results may be incurred during diagnostic procedures and toxic radiolabelled MAb immunoconjugates might concentrate in non-target organs during therapy. Thus, although demonstrating the presence of a TAA associated with a tumor is necessary for RIS (or RIT), it is not a sufficient condition to insure adequate targeting. A new generation of MAbs, including those used in this study[146,147,148,149], have yielded images of clinically verified tumors with very little non-specific uptake evident and, in some cases, have revealed tumor masses undetectable by other diagnostic imaging procedures (X-ray, CT, ultrasound or magnetic resonance imaging).

2.7.1.3 Glycosylation

In addition to the primary MAb structure composed of the heavy and light chains, a secondary structure of glycosylated side-chains are present on the Fc region, generally attached to the CH2 domain (IgG)[150]. Glycosylated carbohydrate side chains have been shown to play an important role in its biodistribution[151]. For example, removal of the terminal sialic acid residue from the carbohydrate side chain of homologous mouse IgG1 resulted in its rapid excretion (half-life 10-20 minutes). Zuckier and co-workers have speculated that the rapid elimination might be due to exposed terminal galactose residues that mediate antibody binding to hepatatic galactose receptors[152]. Rapid intravascular clearance and hepatic uptake of an IgG-Ag complex was shown to be uniquely inhibited by the co-injection or pre-injection of galactose terminal proteins[153], thereby, comfirming a role for the hepatic galactose receptor sytem in immune clearance.

2.7.1.4 Effects of Cytokines

The effects of cytokines can modulate an increase or decrease in tumor targeting. Immunomodulators produced either as a result of the patient's disease or artificially administered (such as recombinant interferon) can overcome some of the effects of tumor cell antigenic heterogeneity and antigenic modulation to enhance MAb targeting[154].

2.7.1.5 Metabolism

If the MAb is internalized by the tumor cell, the radiolabel may be metabolically cleaved and re-enter circulation. Alternately, cleavage of the radiolabel may occur in other organs such as the liver, kidney or the reticuloendothelial system. If the radionuclide then re-enters the circulation, either as a free radionuclide or conjugated to another protein, the distribution and excretion patterns used to predict the kinetic model may be affected. This effect is of particular importance when gamma camera images are used in model development, as the only information available is that provided by the radiotracer.

2.7.1.6 Antibody Kinetics and Specific Uptake

Absolute MAb localization at the tumor site generally represents only a very small portion of the administered MAb[155], typically much less than 1%. Several factors contributing to poor localization are: inadequate MAb specificity, few antigen biding sites, low affinity binding sites, interference from circulating antigen, antigen modulation on the cell surface, loss of the radiolabel after binding to the tumor cell surface, immune complex formation, poor vascularization or permeability of the tumor, and competition for the MAb by other organs or tissues. However, on a basis of relative uptake compared to surrounding tissue, even a low-level of MAb uptake can be sufficient for RIS, if sufficient time is provided for tumor both uptake and the washout of activity from nonrelevant surrounding tissue. Optimal patient imaging times for the MAbs used in this study were approximately 24 hours post-injection.

The biodistribution[156] of a MAb injected intravenously into patients generally follows a rapid distribution phase (several hours) where the MAb redistributes into the poorly perfused tissues and partly into the extravascular tissue fluid. A slower (hours to days) elimination phase follows where the MAb is metabolized and eliminated from the patient. The best time for RIS will occur at an optimal balance of target to non-target ratio and blood clearance of the MAb and its metabolic products have been attained.

One novel approach to increase the target to non-target ratio and reduce the wait between administration of the radiolabel and patient imaging used a bispecific MAb[157]. One binding-site had an affinity for the TAA and the other an affinity for the radionuclide. The unlabeled MAb was first administered to the patient so that the slow clearance from normal tissue and uptake into the tumor could proceed. After localization of the MAb at the tumor site, the appropriate radionuclide would be given in a formulation that was rapidly distributed within the body to achieve maximum ratios of tumor to normal tissue within hours through binding to the bifunctional MAb. This procedure could potentially drastically reduce the toxic effects of radioactive MAbs in non target tissues.

2.7.1.7 Circulating Antigen

If the radiolabelled MAb is to bind to TAA's on a tumor it must first travel through the circulatory system while maintaining its antigen binding capacity. When a circulating antigen is encountered by the MAb, it may form a MAb-antigen complex and thereby compromise its ability to target the tumor[158]. Altered biodistribution patterns are also usually observed. The effects of circulating antigen resulting in altered clearance patterns of the MAb with the concomitant MAb-antigen complex localizing in non-targeted tissue (i.e. liver, spleen, lungs) have been discussed elsewhere.

2.7.2 Physical Factors

The physical factors that alter the biodistribution of a radiolabelled MAb in vivo can, for the most part, be more easily manipulated than the physiological factors. This allows the researcher to alter the MAb biodistribution patterns to enhance RIS and RIT programs. As some of these factors have been addressed in other sections, only a short summary will appear here.

2.7.2.1 Immunoconjugate Stability

Poor stability of the radionuclide-MAb immunoconjugate can result in the buildup of activity in non-target organs and reduce tumor targeting. This is an interdependent factor related to both the strength of the MAb-radionuclide bond and physiological processes that may compete for the radionuclide (e.g. dehalogenation of radioiodines[159] and transchelation of technetium[160]). Kinetics of these radiolabelled metabolites arising from this process will most likely differ from that of the MAb, thereby confusing the modelling process.

In a recent study[161], John and co-workers at the Thomas Jefferson University Hospital in Philadelphia evaluated the influence of ^{99m}Tc binding sites on monoclonal antibodies in relation to liver and tumor uptake. Direct and indirect labelling procedures were tested (see page 43). They also examined the role of native binding sites on the MAb[162] (N-terminal amino acids and the aliphatic E-amino groups of lysine) as nonspecific binding sites for ^{99m}Tc. Using these two methods of labelling, they determined the amount of ^{99m}Tc bound specifically to the intended functional groups as well as nonspecific binding to the native MAb groups and studied their influence on the tissue distribution and tumor uptake in mice.

All preparations were evaluated for embryonal carcinoma grown in Balb/c mice. The control and specific preparations permitted excellent scintigraphic visualization of the tumors (2 - 3 %/gm of tumor). Tumors were not visualized with the nonspecific preparation and less than 1% of the activity administered was observed per gram of tumor tissue. Higher liver uptake and faster blood clearance was also observed with the nonspecific preparations. They speculated that the in vivo instability of the nonspecifically bound ^{99m}Tc may contribute to its binding to the large liver glutathione pool (100-1500 μg) and suggested that liver uptake can be minimized and tumor uptake enhanced by a reduction in nonspecific binding. One method would utilize the indirect chelation labelling method; another would block the E-amino groups prior to the addition of the reduced ^{99m}Tc used in the direct labelling method.

2.7.2.2 Antigen Affinity

High affinity bonds should increase tumor uptake in the absence of circulating antigen and cross-reactivity with other tissues. However, in the presence of circulating antigen, low affinity MAbs may be able to target the tumor better as they will not complex as quickly with the circulating antigen. The affects of antigen affinity were elaborated on in the section on Clinical Use of Radiolabelled Monoclonal Antibodies, page 20.

2.7.2.3 Modelling Assumptions

Faulty modelling assumptions based on poor data, inappropriate animal or human models or unrecognized in vivo behavior of the immunoconjugate may result in the inability to adequately predict the in vivo biodistribution of the MAb. Subsequent dosimetry estimates based on this model are likely to lead to erroneous results and critical problems for RIT. Similar problems may exist in estimating the radiation dose due to ^{99m}Tc labelled MAbs during RIS procedures (see page 47).

2.7.2.4 Molecular Weight

Changes in the molecular weight of the immunoconjugate will alter clearance patterns and tumor localization. The trend to lower molecular weight immunoconjugates $F(Ab)_2'$, F(Ab), F_V or small proteins containing only the TAA recognition site has resulted their faster clearance, which in the case of RIS has resulted in earlier imaging times. In general, the use of intact MAbs (when compared to F(Ab) or $F(Ab)_2'$ fragments) has shown greater accumulation at tumor sites when measured as a per cent of injected dose[163].

2.7.2.5 Radionuclide Location

The placement of the radionuclide within the MAb structure is important so as to not compromise the conformational pattern of the antigen recognition site in the hyper-variable region of the MAb. Immunoglobulins or antibodies are relatively large protein molecules of high molecular weight (IgG: 150,000 daltons) so that the addition of the radionuclide or chelate-radionuclide complex should not greatly affect their ability to target the TAA. The effect of label placement on the smaller immunoconjugates will of course be more critical.

2.8 Radiation Dosimetry

The mathematical formulations used to assess the radiation dose to the patients in this study are based upon the Medical Internal Radiation Dose (MIRD) Committee of the Society of Nuclear Medicine[164]. This committee has provided guidance on methods for calculating radiation absorbed dose estimates[165] since 1968 with new applications and updates published in the Journal of Nuclear Medicine[c] as MIRD Pamphlets. Although the MIRD schema are valid for sizes from normal organ sizes down to the subcellular level,[d] [and] [166] this discussion will only address the macroscopic features of this formalism as they apply to this work.

The radiation absorbed dose to tissue is the energy absorbed from ionizing radiation per unit mass of tissue. However, as the absorbed dose from internally distributed radionuclides is never uniform, the MIRD equations give the average absorbed dose to a volume of tissue. These calculations are applied to an anatomical model chosen to represent the patient, where the regions in the model are uniform and homogeneous, unless macroscopic variations in composition or density are specifically included[167,168]. The radiation dose in conventional dosimetry is a macroscopic concept and microscopic fluctuations in the energy imparted per unit mass will be ignored. The target volumes used in this study are many orders of magnitude greater than the cellular components which make up the tissue.

In order to estimate the radiation dose absorbed by a patient, knowledge of specific localization and clearance of the radioactivity is required. This is usually obtained through the development a pharmacokinetic model that describes the distribution of the radionuclide in the body with time. Some of the major factors influencing the radiation dose received by a patient following the infusion of a radioactive compound are:

---

[c] Published monthly by the Society of Nuclear Medicine, 136 Madison Ave, New York, NY, 10016-6760.

[d] MIRD schema is intrinsically able to accommodate most of the complex problems associated with microdosimetry, provided that appropriate biological data are available, Kassis AI, The MIRD approach: remembering the limitation, *J Nucl Med*, 33:781-782, 1992.

1) the biodistribution of the labelled molecule, i.e.
   - a) How much activity is present in the tissues of interest?
   - b) How long does the activity remain in those tissues?

2) the type of radioactive decay, i.e.
   - a) How much energy is emitted by this activity and what form do the emissions take?
   - b) What fraction of this energy is deposited in the tissue?

A brief discussion of the central theory outlining the calculation of radiation absorbed dose to patients and some of the assumptions and inherent limitations used to develop this theory are addressed below.

2.8.1 General Theory

By definition, the absorbed dose to tissue is the energy absorbed from ionizing radiation per unit mass of tissue. For nonuniform distributions of internal radionuclides, the MIRD equations provide the average absorbed dose to a volume of tissue. The equation for calculating the absorbed dose may be written as:

$$D\ (r_k \leftarrow r_h) = \bar{A}_h \sum_i \Delta_i\, \phi_i\ (r_k \leftarrow r_h)/m_k \qquad (8)$$

where:

$D\ (r_k \leftarrow r_h)$ = mean absorbed dose in a target region r_k from activity in a source region r_h

$\bar{A}_h$ = cumulated activity (the time integral of activity in source region r_h over the time interval of interest)

Δ_i = mean energy emitted by a radionuclide per nuclear transition of type "i" radiation

ϕ_i ($r_k \leftarrow r_h$) = absorbed fraction, or the energy emitted in region r_h that is absorbed by region r_k

m_k = mass of the target r_k

Equation (8) can be summarized to express the total mean absorbed dose in a target region as a sum of the doses from all the source regions that affect that target. In order to facilitate a better understanding of the calculations involved in obtaining an estimate of the mean absorbed dose, the expression for the radiation dose from a source region can be separated into a physical and a biological component.

The physical parameter that describes the energy released during nuclear decay is the mean energy emitted per nuclear transition, Δ. Each radionuclide decays by a unique series of "i" events characterized by a mean energy per particle, n_i and an intensity related to the number of particles emitted per transition, Ei. The mean energy emitted per nuclear transition is then given as the sum of all the types of radiation emitted during its nuclear decay:

$$\Delta = k\sum_i n_i E_i \qquad (9)$$

where k is a constant that depends upon the units used. For traditional units, k = 2.13 , E is measured in MeV and the resulting Δ has units of rad g μCi^{-1} h^{-1}. When performing calculations in SI units, k = 1, E is measured in MeV and the resulting Δ has units of Gy kg Bq^{-1} s^{-1}. A compilation of 242 radionuclides showing the energies and intensities of their associated emissions has been compiled by the MIRD Committee[169].

The mean energy emitted per nuclear transition or Δ values are also provided.

The other physical parameter is the absorbed fraction, ϕ, which represents that proportion of energy emitted during a nuclear transition that is actually absorbed by the target tissue. The absorbed fraction varies with the type and energy of the radiation emitted during nuclear decay and has been subdivided into penetrating and nonpenetrating radiation. Nonpenetrating radiation has insufficient energy to exit the source region and therefore will not contribute to the radiation dose of any region other than itself. Thus, for nonpenetrating radiation, the absorbed fraction in the source region is one and the absorbed fraction to all other target regions is zero. Penetrating radiation can contribute to the dose deposited in regions other than itself and so the absorbed fraction will vary between zero and one. The specific absorbed fraction, Φ, is the absorbed fraction in the target per unit mass of the target. The specific absorbed fractions and absorbed fractions are related by

$$[\ \Phi(r_k \leftarrow r_h) = \phi(r_k \leftarrow r_h)/m_k] \tag{10}$$

and their values for photons in the organs of a standard reference man have been published by the MIRD Committee[170].

The product of Δ and Φ is a constant for a given radionuclide and a given source-target combination. It has been designated by the MIRD Committee as the S value and termed the "mean dose per cumulated activity". Equation (3) can now be rewritten as:

$$D\ (r_k \leftarrow r_h) = \bar{A}_h S(r_k \leftarrow r_h) \tag{11}$$

where

$$S(r_k \leftarrow r_h) = \sum_i \Delta_i \phi_i (r_k \leftarrow r_h)/m_k \quad (12)$$

S has units mean dose per unit of cumulated activity (Traditional units: rad μCi^{-1} h^{-1}, SI: Gy Bq^{-1} s^{-1}). Tables of S values have been published to simplify dose calculations[171].

The biological parameters are represented by the cumulated activity ($\tilde{A}_h$) which is the total number of nuclear transformations occurring over the time of interest in the source region *h* and measured in units of µCi h or Bq s. The cumulated activity in equation (11) may be calculated by expanding $\tilde{A}_h$ for the case of instantaneous uptake, with removal by both physical decay and biological elimination from source region *h* as expressed by:

$$\tilde{A}_h = A_h \int e^{-(\lambda + \lambda_h)t}\, dt \quad (13)$$

where:

λ is the physical decay constant = ln 2 / T
λ_h is the biological decay constant = ln 2 / T_h
A_h is the maximum activity in source organ h
T is the physical half life of the radionuclide and
T_h is the biological half-life.

The physical and biological half-lives can be combined as the effective half-life, T_{eff}, where:

$$T_{eff} = \ln 2 / (\lambda + \lambda_h) = T \times T_h / (T + T_h) \quad (14)$$

so that equation (13) becomes

$$\tilde{A}_h = A_h \int e^{-(\ln 2 / T_{eff})t}\, dt \quad (15)$$

Integrating this equation from the time of injection (t = 0) to complete removal of the radioactivity (t = ∞) we have:

$$\bar{A}_h = 1.443\ A_h\ T_{eff} \tag{16}$$

For the case of a multi-compartment pharmacokinetic model with j compartments, the cumulated activity in the source region *h* can be represented by:

$$\bar{A}_h = \sum_i A_i \int_0^{\infty} e^{-(\lambda+\lambda_h)t}\, dt \tag{17}$$

$$= 1.443 \sum_j A_j (T_j)_{eff} \tag{18}$$

As the cumulated activity is a function of the distribution of the radiolabelled compound within the different tissues with time, a residence time τ of a radionuclide in a source region may be defined to equal the cumulated activity in the source region divided by the administered activity:

$$\tau_h = \bar{A}_h\ /\ A_0 \tag{19}$$

Alternately, the residence time in a source region can be expanded in terms of the effective half-life so that we have

$$\tau_h = \bar{A}_h\ /\ A_0 = 1.443\ T_{eff}\ A_h / A_0 \tag{20}$$

Equation (8) can be rewritten using the expression for the residence time and the equation for the radiation dose becomes:

$$D\ (r_k \leftarrow r_h) = \tau_h\ A_0\ S(r_k \leftarrow r_h)$$

(21)

The radiation dose is usually expressed as the mean radiation dose per unit of administered activity and equation (21) then becomes:

$$D\ (r_k \leftarrow r_h)\ /\ A_0 = \tau_h\ S(r_k \leftarrow r_h) \tag{22}$$

Thus, in addition to the S values, one requires either the residence time of the activity in the source region and the administered activity (Equation 21) or the integral of the time-activity curve (cumulated activity) for the source region (Equation 11) in order to calculate the absorbed radiation dose to a target region. These values may be obtained by external measurements using scintillation cameras or inferred from data describing the clearance of radioactivity from the body using pharmacokinetic modeling techniques.

2.8.2 MIRD Data Sources

From the discussion above, it is apparent that three key pieces of information are required in order to calculate the radiation absorbed dose: 1) information on the physical characteristics of the radionuclide and absorbing medium (S value), 2) knowledge of the radioactivity distribution within the body ($\tilde{A}_h$ or τ_h) and 3) an appropriate scheme to calculate the absorbed dose estimate.

The nuclear parameters of selected radionuclides can be found in MIRD: Radionuclide Data and Decay Schemes[172]. A compilation of absorbed fractions for different source to target configurations appear in MIRD Pamphlets No 3 (1968), No 5 (revised 1978) and No 8 (1989). Values for S for a variety of radionuclides and human phantoms have been published in

MIRD Pamphlet No.11. S values can also be obtained from the computer program, MIRDOSE2[e].

As it not always possible to directly measure the radioactivity in the tissue of interest, the distribution must often be estimated indirectly. Information on the biological distribution of the radioactivity within the body can be estimated from the measurement of body fluids and excreta, external measurements from a gamma camera, compartmental modelling of the radioactive distribution and by extrapolation from animal data.

Finally, an appropriate method to calculate the absorbed dose estimate must be chosen and any limitations and assumptions used in these calculations should be addressed when interpreting the results.

2.8.3 Monoclonal Antibody Dosimetry

Radiolabelled monoclonal antibodies offer the potential of highly localized uptake for the detection (RIS) and treatment (RIT) of cancer[173]. The ability to quantify the radiation dose delivered to the tumor and normal tissues provides necessary information to identify the non-target organ risk factors during clinical RIS or RIT procedures and predict the effectiveness of radiation treatment of malignant disease[f].

---

[e] Copyright 1984, Oak Ridge Associated Universities, EE Watson, M Stabin and WE Bolch

[f] An extensive literature search and an analysis of monoclonal antibody dosimetry was compiled by the Nuclear Medicine Committee of the American Association of Physicists in Medicine under the Chairmanship of Dr. Barry Wessels. An entire issue of Medical Physics (Issue 20:3, 1993) was devoted to this report and covers such topics as: MIRD theory and calculations for RIT, microdosimetry, pharmacokinetic modelling, experimental and clinical RIT dosimetry and imaging techniques and treatment planning.

Data used to calculate the radiation dose to patients were obtained from the clinical staff at the Cross Cancer Institute (Edmonton) and the Johann Wolgang Goethe University Medical Centre (Frankfurt). Gamma camera measurements of the radioactivity in selected organs and from whole-body images provided information to assess the dose to individual organs. The time-distribution of radioactivity in the patient's blood and the amount excreted in the urine were used to estimate the dose to the urinary bladder wall.

2.8.3.1 Radioimmunoimaging

The in vivo quantitative distribution of a radioactive MAb can be assessed by measuring the radiation emitted from the body post-injection. Several techniques have been applied to this problem, each with their own advantages and limitations, but all are based on predicting the internal distribution from measurements made external to the body[174]. With increasing levels of sophistication these methods include: planar gamma camera imaging, single photon emission computed tomography (SPECT) and positron emission tomography (PET). Each of these methods can be used to estimate the amount of radioactivity in a source organ and are affected to different degrees by 1) scatter and attenuation of the radiation, 2) limited spatial and energy resolution of the instrument, 3) septal penetration in the collimator by high energy photons and 4) statistical noise due to low activity densities in the patient at later imaging times.

Planar gamma camera imaging is the most common method of imaging in nuclear medicine and is the least restrictive on patient time and cost. However, it does suffer from reduced image quality due to its inability to differentiate over-laying activity from an organ of interest. Attempts to quantitate the activity in an organ have been partially successful using the transmission conjugate view method originally introduced by Sorenson[175] to compensate for attenuation of the radiation within the body. The reduction in image resolution due to Compton scattered photons has been addressed with the inclusion of a buildup factor[176] and through the use of a dual energy window[177] to measure both the photopeak and the Compton scatter events.

The problem of differentiating overlaying radioactivity plaguing planar imaging has been addressed with SPECT imaging protocols[178,179]. During a SPECT procedure, the gamma camera is rotated around the patient to acquire different views of the biodistribution of the radiotracer in the subject so that in some of the views the activity in adjacent organs will be superimposed, but in other views, distinct sources can be visualized. After these different projections have been reconstructed[180] the effects of overlaying activity are removed from the transaxial SPECT images.

The multiple views at different angles obtained from a patient also have another benefit; it is possible to combine the series of reconstructed two-dimensional transaxial images to produce a three dimensional image of the distribution of the radiotracer. Using different graphical presentation techniques[181] in conjunction with modern imaging computers, the three-dimensional reconstructed image can be rotated in a "cine mode" on a computer display terminal to assist in the identification of regions of enhanced uptake. Alternately, 3-D surface-rendered images can be produced whereby surfaces with equal activity are joined, again as an identification aid.

Once the regions of uptake have been identified, the activity in the source regions needs to be quantified in order to estimate the radiation dose. The major source of error in quantitation is due to the exponential attenuation of the photons by the patient's body. Several first order correction methods have been proposed to compensate for photon attenuation[182,183], but generally do not deal with measurement ambiguity (i.e. the ability to differentiate between a strong source deep in the body and a weak source near the surface). Still, assuming uniformly attenuating cross-sections and uniform activity distributions, this technique proves adequate.

To compensate for nonuniform attenuation and thereby improve the accuracy of attenuation correction, a 3-D attenuation map of the patient is required. This information may be obtained from X-ray CT images or by collecting a series of transmission images using an external radioactive line-source or flood-source prior to performing the SPECT study[184]. Using this information to quantify the activity in a source region, the error estimates can be reduced to ±10% when patient specific 3-D attenuation maps and build-up functions are utilized. The main disadvantages associated with SPECT imaging are image acquisition times (further increased if attenuation scans are made) and the problems associated with photon attenuation. Long scan times are required in order to accumulate enough counts to accurately reconstruct the transaxial images.

Both of these problems have been addressed with PET imaging procedures. The higher energy photons produced as a result of the annihilation of a positron can travel further without attenuation or scatter; (i.e. 511 keV photons have a 40% transmission factor in 10 cm of water versus approximately 25% for the 140 keV photons emitted by ^{99m}Tc). Imaging times have also been reduced by the inherent design of PET cameras. Entire rings of detectors surround the patient, obviating the need to "step" the camera around the patient, as required in SPECT cameras. Recognizing the time constraints during SPECT protocols, several manufacturers now produce multi-headed SPECT systems. The co-planar nature of the annihilation radiation relaxes the restrictions on the photon-absorbing collimators used in PET compared to planar and SPECT imaging.

The advantages of PET over other imaging modalities are increased spatial resolution and the ability to perform attenuation correction with a high degree of precision producing superior quality images[185,186,187]. PET also has the potential to provide physiological information for the diagnosis of cancer[188] based on altered tissue metabolism and to monitor the effects of therapy on metabolism. PET scanning of an ^{124}I labelled MAb as a method of tumor dosimetry and treatment planning prior to the administration of ^{131}I labelled MAb for the treatment of neuroblastoma has been reported[189,190]. The researchers concluded that the technique showed promise for determination of the radiation absorbed dose for ^{131}I labelled MAb RIT. However, the use of PET instruments in oncological imaging has been limited due to the complexity and expense of the physical facilities required to produce and image MAbs labelled with positron emitting radionuclides.

In order to increase the precision of the absorbed dose calculations for radioimmunoscintigraphy and radioimmunotherapy, accurate, patient-specific biodistribution data are required. Traditional S-factor (MIRD) based methodology ignores information on the shape and position of the activity volume within an organ and assumes the activity to be uniformly distributed over the whole volume of the organ. It also precludes dose calculations to normal tissues that consider activity within adjacent tumors. Sgouros and co-workers have addressed these problems through the development of a patient-specific assessment technique which integrates functional information from SPECT or PET with anatomical information from CT or MRI for three dimensional internal dosimetry treatment planning[191].

In this approach, source-activity volumes were drawn from PET images and assigned a single cumulated activity concentration. A uniform distribution of activity was assumed within each source volume and the spatial activity distribution at a given time represented a good approximation of the spatial cumulated activity distribution. This method used information on the absorbed dose as a function of distance from a point source (point source kernel) generated by a Monte Carlo simulation program (Electron Gamma Shower[192]). An algorithm was designed to convolve the three-dimensional cumulated activity distribution with the point source kernel to give a an isodose contour which is overlaid (fused) on the CT or MRI anatomical image. These contours depict the dose distribution as generated from the actual activity distribution obtained from PET imaging. This technique avoids the traditional S-factor method which assumes that the cumulated activity obtained from the PET or SPECT images is uniformly distributed over the whole volume of the organ.

2.8.3.2 Bladder Contents

The main route of elimination of the MAbs used in this work is via the urinary system. Radiation dose estimates are of particular importance to the kidneys and inner mucosal surface of the urinary bladder wall. Kidney doses can be estimated directly from gamma camera images as described above, however, due to the variable filling and voiding of the radioactive bladder contents, a mathematical model is used to evaluate the dose to the bladder wall. Several bladder models have been published[193,194,195,196] and have attempted to incorporate a number of physiological parameters including: expanding bladder contents, variable urinary input rate, initial volume, first void time and residual volume. MIRD pamphlet 14 addresses these problems and presents a new dynamic urinary bladder model that incorporates these factors[197].

Dose estimates to the bladder wall in this report[198] are based on the standard MIRD phantom[199] in which the bladder is ellipsoid in shape and has a constant volume (202.6 mL or 200g). The bladder wall has a mass of 45.13 g, a constant thickness and varies in size with time. The surface electron dose rate is derived from the approximation that the dose rate at the surface of a large sphere is one-half of the dose rate in an infinite medium that has the same radioactive concentration as within the sphere[200]. The photon dose is derived using Monte Carlo techniques and the cumulated activity in the contents of the bladder is derived using a pharmacokinetic model describing the retention of activity in the whole body. Variable but regularly spaced void intervals are traditionally taken as 2.4 h and 4.8 h corresponding to 10 or 5 equally spaced voiding times over a 24 h period. The bladder wall dose from various source organs, including the bladder contents has been calculated for many radionuclides with this model[201].

The radiation dose to the bladder wall can be obtained using equation (22) above:

$$D\,(r_k \leftarrow r_h)\,/\,A_0 = \tau_h\, S(r_k \leftarrow r_h) \tag{23}$$

where the residence time, τ_h, in the bladder is calculated from

$$\tau_h = \sum_j \alpha_j \left(\frac{1-e^{-\lambda\, T_v}}{\lambda} - \frac{1-e^{-(\lambda_j+\lambda)T_v}}{(\lambda_j+\lambda)} \right) x \left(\frac{1}{1-e^{-(\lambda_j+\lambda)T_v}} \right) \tag{24}$$

and the decay constants, λ are as described for equations (8) and (12), T_v is the regular voiding interval and α_j is the biological coefficient representing the fraction of the administered activity entering the bladder for the j^th component of the kinetic model describing the retention of radioactivity in the body. As the blood represents the compartment transporting the radioactivity to the kidneys, the α_j's were obtained from the pharmacokinetic model that described the disposition of radioactivity in the blood. To compensate for elimination by other mechanisms, the urinary bladder dose was modified by the ratio of the urinary clearance (Cl_u) to the blood clearance (Cl_u). Equation 14 then becomes:

$$D\,(r_k \leftarrow r_h)\,/\,A_0 = Cl_u/Cl_b\,\tau_h\,S(r_k \leftarrow r_h) \tag{25}$$

The principle limitation of this model is that the volume of the bladder contents remains constant with no provision made for dynamic changes in the bladder or the incorporation of other physiologically based variables. However, the original MIRD model[202] is a simpler model to apply and provides comparable dose values to the new model described by SR Thomas and co-workers[203]. They reported a 9% lower dose value than that predicted with the MIRD model used in this study. This difference should not significantly affect the error associated with these dose calculations, which are estimated to be within a factor of two of the actual dose.

2.8.3.3 Remainder of the Body

After the radiation dose had been calculated for those regions of uptake identified by gamma camera imaging there still remained a significant portion of the original activity that was unaccounted for. If the remaining activity is assumed to be distributed uniformly throughout the entire body, the problem reduces to calculating the cumulated activity and S values for the source organ, which in this case would be the "remainder of the body". However, the use of S values for the "total body" would overestimate the dose as this S value is based on the activity being distributed throughout the entire body (the identifiable source regions would be counted twice). To compensate for this effect the S values are modified by subtracting the contributions from the other source regions according to the expression:

$$S\ (r_k \leftarrow RB) = S(r_k \leftarrow TB)(m_{TB}/m_{RB}) - \sum_i S(r_k \leftarrow r_i)(m_i/m_{RB}) \qquad (26)$$

where:

$S\ (r_k \leftarrow RB)$ = modified S value in target region r_k from activity in the remainder of the body (RB)

$S(r_k \leftarrow r_i)$ = S value in target region r_k from activity in source region *i*

m_{TB} = mass of the total body (TB)

m_{RB} = mass of the remainder of the body (mass of the total body - mass of the source organs)

m_i = mass of source organ *i*

Values for patient and source organ masses were obtained from Geigy Scientific Tables, Edition 7, 1970.

3. MATERIALS AND METHODS

This section will describe the monoclonal antibodies used in the clinical and pre-clinical studies. The instrumentation and analytical procedures used in the development of a pharmacokinetic and radiation dosimetric model are discussed in their relation to their application in normal rabbits and cancer patients.

3.1 Monoclonal Antibodies

Four murine derived MAbs and one chimeric MAb directed against various cancers were utilized in this work. Three of these MAbs are still in clinical trails; MAb-174H.64, Phase II trials in Canada and Germany, MAb-B43.13, Phase II/III Trials in Canada and Germany, and MAb-170H.82, Phase III clinical trails in the USA (1995). In vivo applications of the MAb-B80.3 clone have not been developed due to problems with circulating antigen. All four MAbs are summarized below.

3.1.1 MAb-170H.82

The murine derived MAb 170H.82 or Tru Scint® AD™ was developed by Biomira Inc. for the in vivo diagnosis of adenocarcinomas and their metastases. The MAb was derived against a synthetic Thomsen-Freidenreich (TFβ) antigen[204,205] coupled to HSA. However, the exact nature of the natural antigen is still unknown and is under active investigation by Biomira Inc. Preliminary results suggest that the antigen may be related to a member of the cytokeratin family. The TF antigen is a precursor structure of MN blood group antigens and is also expressed by about 90% of human carcinomas[206].

The fusion partner was the FOX-NY myeloma cell line and MAb production was carried out in murine ascites at 2-3 mg/mL with an average hybridoma doubling time of 21.9 hours. The IgG1κ clone was selected on the basis of its in vitro reactivity with human adenocarcinoma tissues of the breast, ovary, endometrium, colon, prostate and some bladder tissues. Immunohistology surveys also revealed that the MAb reacted to most of the glandular epithelial cells, although a pilot study at the Cross Cancer Institute (53 cancer patients) indicated that the MAb localized in tumors and their metastatic sites with no significant uptake in any normal glandular epithelial tissues. Neuroectodermal, hematopoietic and mesenchymal tumors were not found to react with 170H.82.

3.1.1.1 Clinical Trials

Initial clinical trials at the Cross Cancer Institute (CCI) in Edmonton with the ^{99m}Tc-170H.82 MAb have produced encouraging results in the evaluation of locoregional disease in patients with breast cancer. A Phase II study of 53 patients with known or suspected primary or recurrent breast cancer has recently been completed. This group of patients had prior documentation on 80 known sites of primary or local lymph node metastases and imaging results showed true positive uptake in 72 sites (24 breast and 38 lymph node), 8 false negative (2 breast and 6 lymph node) and 4 false positive (2 breast and 2 lymph node). These results indicate a sensitivity of 90% and a positive predictive accuracy of 95%; results that are comparable to, or better than, other results in the literature. A subset of this group of patients was selected for pharmacokinetic and dosimetric modeling.

3.1.2 MAb-174H.64

This MAb was developed at the University of Alberta in 1986. It is a murine derived MAb, directed against an extra-cellular surface component of the cytoskeletal matrix system ectopically expressed on the proliferative compartment of mammalian squamous cell carcinomas; irrespective of the site of origin[207]. The results of immunohistology tests performed by Biomira Inc. showed reactivity with squamous tumors in primary and metastatic locations. Cross reactivity with normal human tissues was limited, showing only weak reactivity with the kidney collecting tubules and hepatocytes.

The immunogen used was Tn-HSA and the MAb appears to recognize cytokeratin bands of approximately 50 and 57 KD. The Tn antigen is a mucin glycoprotein and is an immediate precursor of the blood group MN antigens[208,209]. In most normal human tissues the Tn antigen is usually masked by covalently linked carbohydrates[210] but clinical studies have indicated Tn expression on breast cancer cells[211].

The fusion partner for the murine IgG1 (kappa light chain) was the FOX-NY cell line and the resulting hybridoma was found to have an average doubling time of 17.6 hours. The MAb was produced by sterile acsites production techniques in virus and antibody free Balb/c mice. In order to reduce the HAMA allergic response produced the murine derived MAb[9], Biomira has produced a chimeric form of 174H.64 in which the Fc portion of the antibody has been genetically modified by the insertion of a human Fc fragment. The isotype of the 174H.64 MAb was also changed from an IgG_1 (murine) to an IgG_3 (chimeric). The kinetics of the 174H.64 chimeria were also studied and compared to the murine formulation.

---

[9] A discussion on the HAMA response appears in Chapter II.

3.1.2.1 Clinical Trials

Parallel clinical trials were performed at the CCI and the Johann Wolfgang Goethe University Medical Centre (JWGUMC) in Frankfurt, Germany on patients with squamous cell carcinoma of the head and neck cancer with ^{99m}Tc-174H.64. The murine form of this MAb was studied in 12 patients at the CCI where 15 of 17 known tumor sites were identified giving a positive predictive value of 100% and a sensitivity of 88%. The 2 false negative lesions were a cervical lymph node and oropharyngeal primary. Similar results were obtained at the JWGUMC using a chimeric form of the 174H.64 MAb where a total of 15 patients with head and neck cancer were studied[212]. Besides known lymph node metastases, previously unknown metastatic lymph nodes were detected. A subset of the patients from both institutes were studied to provide data for kinetic modelling.

3.1.3 MAb-80.3

The MAb-B80.3 clone, developed by Biomira Inc., is an IgG1 murine (kappa light chain) MAb directed against prostate specific antigen (PSA) with an affinity of approximately 10^{-10} M. Its fusion partner is the SP2/0 derived hybridoma which has an average doubling time of seven hours. The MAbs used in this study were produced by Biomira Inc. following sterile ascites production techniques in virus and antibody free Balb/c mice. No cross reactivity has yet been found in patients with the exception of weak reactivity in the collecting tubules of the kidney and the liver hepatocytes (2 out of 3 cases showed a weak staining)[h]. It appears that the reactivity on human tissue is limited to prostatic adenomas and carcinomas and that B80.3 behaves like an organ specific antibody.

---

[h] Tru-Scint PR: A synopsis of 99m-Tc-labelled radioimmunopharmaceutical for in vivo diagnosis of prostate cancer, Biomira Inc, MRS-PR-8/91, 1991.

PSA is a naturally occurring antigen that is found in the epithelial cells lining the luminal side of the prostatic acinar and ducts. PSA is also present in high levels in the seminal plasma. It functions as a serine protease belonging to the kallikrein family and is thought to be involved in the thinning of seminal clots by the proteolysis of a major protein in the seminal fluid. It is a small, single-chain glycoprotein with a molecular weight of approximately 33,000 Daltons. In the serum of healthy males, the concentrations of PSA are less than 2.8 μg/L, but range to up to 2,000 to 3,000 μg/L in patients with prostatic cancer. Its metabolic clearance from the serum has been measured[213] and found to have a half-life of 3.15 ± 0.09 days, as calculated in patients after radical prostatectomy.

Patients with prostatic adenocarcinomas and benign prostatic hyperplaysia have elevated PSA levels in their serum and tissues[214]. As PSA is a kallikrein-like protease, complexes with a large excess of serine protease inhibitors in plasma may be expected to form. When PSA is released in its active form into the blood, α_1-antichymotrypsin (ACT) seemed to be the inhibitor with the highest affinity for PSA[215]. This ACT-PSA complex (MW = 100,000 D) was a major form of the PSA in plasma and increased with increasing PSA levels, being over 85% when PSA levels exceeded 1000 μg/L. Sebti and co-workers also found that patients with prostatic cancer had a significantly higher proportion of PSA-ACT than those with benign prostatic hyperplasia.

3.1.3.1 Clinical Trials

A Pilot study completed at the CCI with ^{99m}Tc-B80.3 in 1992 on several patients with prostate cancer had mixed results. The main problem attributed to the poor targeting performance of this MAb was attributed to a circulating form of the target antigen. Due to poor tumor visualization the Pilot study was abandoned.

3.1.4 MAb-B43.13

OVAREX™ (MAb-B43.13[i] clone) is a new product for RIS and immunotherapy for localization and treatment of residual and recurrent ovarian cancer[216]. This MAb specifically recognizes Cancer Antigen 125 (CA 125), a tumor antigen associated with epithelial ovarian cancer[217]. It is a murine IgG1, kappa light chain MAb with an affinity for CA 125 of approximately $1.2 \times 10^{10}\,M^{-1}$.

The CA 125 antigen is a high molecular weight glycoprotein, however it is not a typical mucin due its relatively low carbohydrate composition (24% carbohydrate by weight), low buoyant density and the presence of N-linked and O-linked oligosaccharides[218,219]. Its general structure appears consistent with antigen isolated from a variety of sources, although some size heterogeneity of the denatured subunits and the native aggregated states have been reported.

The CA 125 antigen is expressed in large amounts in tissues and serum of 80% of patients with advanced stage ovarian cancer. Normal sera and both the adult and fetal ovary do not express the antigen; however, CA 125 material has been detected in normal tissues such as the adult pleura, pericardium, peritoneum, fallopian tube, endometrium and endocervix. In pregnancy, the antigen is found in the chorionic membrane, extracts of maternal decidua and abundantly in the amniotic fluid.

---

[i] Marketed by Biomira Research Inc. as OVAREX™.

3.1.4.1 Clinical Trials

A pilot study using MAb-B43.13 was performed at the JWGUMC on six patients with ovarian cancer. Pharmacokinetic and image data were obtained for the purposes of developing a model describing the behavior of this MAb when used as a single dose imaging agent. In a previous study[220] at this institute with MAb-B43.13, 31 lesions were detected in a group of 20 patients with rising CA 125 levels after primary surgery for ovarian cancer. Twenty of these lesions were unknown at the time of imaging.

As of September 1994, approximately 100 patients have received MAb-B43.13 for RIS or therapeutic procedures for ovarian or other CA 125 expressing cancers. Formal studies are currently underway in both Canada and in Germany.

3.2 High Performance Liquid Chromatography

The high performance liquid chromatograph (HPLC) used to measure the different components in the blood and urine was a Waters Millennium 2010 system[i] with a 600E system controller and 486 tunable UV absorbance detector. This system was connected to a 2 x 2 inch Bicron NaI detector via a Berthold LB 5310 Multi-logger and Waters SAT/IN interface module to facilitate the correlation between the peaks detected by the UV monitor (280 nm) and any associated radioactivity. If the radioactivity was too low to be detected by the on-line system, the effluent from the HPLC unit was collected by a fraction collector (typically 1 mL fractions) for subsequent counting in a multisample gamma counter.

---

[i] Millipore Corporation, 34 Maple Street, Milford, MA 01757

A Beckman Ultraspherogel size exclusion column (SEC 2000) was used in conjunction with a standard Beckman guard column for the 170H.82 and B80.3 MAbs. A Waters size exclusion column (TSK 2000) was used with the 174H.64 MAb due to MAb-column interactions resulting in excessive elution times. The buffered aqueous mobile phase consisted of 0.1 M Na H_2PO_4, 0.1 M Na_2SO_4 and 0.05% NaN_3 (pH = 7.2). Flow rates were typically 1 mL/min. Elution time for intact MAbs were approximately 8 to 10 minutes, depending on the antibody being measured.

3.3 Multisample Gamma Counter

The radioactivity associated with patient serum and urine was assayed with an LKB 1282 Compu-gamma multisample gamma counter[k]. All animal and radioimmunoassay samples were counted on a Packard Auto-Gamma 5530 Minaxi instrument[l]. The decay correction capability built into each instrument was used in both machines to decay correct all samples (in the current sample set) to the time when the first sample was counted.

In order to relate the sample counts to the absolute activity (Bq or Ci), both gamma counters were calibrated against a Capintec dose calibrator. The dose calibrator had an associated error of less than 3%. The procedure used to determine the counting efficiency for ^{99m}Tc of the gamma counters follows:

1. Accurately measure a dose of ^{99m}Tc pertechnetate in the dose calibrator (typically 40 MBq).
2. Add the activity to a 1 litre volumetric flask.
3. Make up the volume to 1 litre with water and stir for 15 minutes.

---

[k] LKB Wallac, Turku, Finland .

[l] Packard Instrument Company, Meriden, CT, USA.

4. Pipette aliquots of the activity in triplicate into the same counting vials used for the samples, 0.1 to 1.0 mL, depending on when the standard was prepared.
5. Place the standards in the gamma counter and determine their count-rate using the same instrument conditions (same high voltage and counting windows).
6. Determine the instrument background by counting three vials containing no activity.
7. Counting efficiency = $\dfrac{\text{standard count-rate (cpm)} \times 100\%}{\text{added activity (dpm)}}$

3.4 Gamma camera

Gamma camera images were obtained to provide information on the in vivo distribution of the radiolabelled MAb with time. These data were then be used to augment the information obtained from blood and urine sampling for the purpose of refining the pharmacokinetic and radiation dosimetric model. A pharmacokinetic model could then be developed to include information obtained about the time-activity distribution in different organs based on gamma camera image data.

The patient gamma camera image data obtained for this work were analyzed using a technique based upon the relative organ activity, expressed as a percentage of the whole-body dose. Using rabbits, ROI image data were correlated with the activity measured in the corresponding organ following necropsy.

Time-activity profiles were constructed from the ROI data and used to provide an estimate of the time-course of activity through a selected organ. The following summary describes the protocol used to obtain the biodistribution of the radiolabelled MAb in selected organs. The reader should be aware of the problems associated with these techniques which include: imprecise attenuation coefficients, Compton scatter of photons, and inaccuracies due to overlaying activity from adjacent organs.

3.5 Statistics

All statistical analyses were performed using SPSS for Windows[m] on a 486 - DOS computer. Depending on the homogeneity of the data, either parametric or nonparametric techniques were employed. Unless otherwise stated, a 95% confidence level was used to test for significance.

Analysis of variance, including t-tests, are widely used to compare differences between the means of different data groups. This comparison usually tests the null hypothesis in which the different treatments are proposed to have no effect on some observed variable. If the resulting test was found to be statistically significant, then the null hypothesis was rejected. Generally, a p-value of less than 0.05 is used to conclude that the means were different.

All forms of analysis of variance were based on the assumptions that the data were drawn from normally distributed populations in which the variances were the same, even if the treatments differed. Otherwise nonparametric comparisons between means must be used in which no assumptions about the specific nature of the population were required. Both parametric and nonparametric tests were applied to compare the mean values of a given data set if the sample set was suspect (i.e. variances from the modeling process differed widely or extreme physiological states such as dehydration or weight loss were observed). For those data sets exhibiting wide variations in individual variances, the technique of weighting by the inverse variance, normalized to the number of data points, was employed.

---

[m] SPSS Inc. Release 6.0, SPSS for Windows.

3.6 Software

Initial data collation, radionuclide decay correction and counting efficiency compensation were performed using programs developed with the spreadsheet program, Quattro Pro for Windows[n]. The pharmacokinetic analysis for both the image and blood data was made using a nonlinear least-squares regression program, PCNONLIN[o] and a parameter estimation program, JANA[0]. The program LAGRAN[p] was used to integrate the area under the ROI time-activity curves. Curve analysis of the radioimmunoassy data was accomplished with Table Curve for Windows[q]. All of the figures were produced either by AXUM[r], CoralDRAW[s] or Sigma Plot for Windows[13]. All of the above software was executed on a 486 - DOS computer.

3.7 HAMA

All HAMA testing on patient sera was performed by Biomira Inc. using a technique developed by Connie Sykes and co-workers[221].

---

[n] Borland International Inc. Release 5.0, QPRO for Windows

[o] SCI Software, Release 4.2.

[p] C Ediss, Faculty of Pharmacy and Pharmaceutical Sciences, University of Alberta

[q] Jandel Scientific, San Rafael, CA, 94901

[r] TriMetrix, Inc.Seattle, WA, 98115

[s] Coral Corporation, Ottawa, Canada

4. EXPERIMENTAL METHODOLOGY

4.1 Radionuclide Labelling

All monoclonal antibodies used were supplied from Biomira Inc. as the Tru Scint® SQ™ Monoclonal Antibody Kit (174H.64), the Tru Scint® AD™ Monoclonal Antibody Kit (170H.82), the Tru Scint® PR™ Monoclonal Antibody Kit (B80.3) and the OVAREX™ kit (B43.13 - Biomira Research Inc.). Complete product literature is available upon request from Biomira Inc. and only a summary of the labelling procedure is presented in this document.

The Tru Scint® SQ™ Monoclonal Antibody Kit consisted of 2 mg of MAb 174H.64 (1 mg for the chimeric MAb) in a predispensed sterile, apyrogenic frozen solution in the presence of a suitable reducing agent, saline and buffer complex. Labelling was performed with the addition of sodium pertechnetate ^{99m}Tc USP (1.6 - 2.0 GBq) to directly label the reduced thiol-groups. Reduction of the murine MAb utilized stannous chloride while the chimeric MAb was reduced using a newly developed photoactivation process[t]. Radiochemical purity was monitored by instant thin-layer chromatography (ITLC). A small aliquot of the preparation was spotted onto a 0.5 x 8 cm SG-ITLC strip using methanol:saline (85:15) as the solvent.

The Tru Scint® AD™ Monoclonal Antibody Kit (170H.82) contained 2 mg of predispensed sterile, non-pyrogenic, frozen solution of derivatized MAb 170H.82 in the presence of a suitable reducing agent ($SnCl_2$), saline and a buffer complex. The product contained no antimicrobial preservative. Labelling was performed with the addition of sodium pertechnetate ^{99m}Tc USP (1.6 - 2.0 GBq) to directly label the reduced thiol-groups to produce a slightly acidic pH solution that remained stable for two hours after radiolabelling. Similar quality control measures as the MAb 174H.64 were used to test for radiochemical purity. The 2 mg vials were either combined or split to obtain the proper dosage (patients 1 - 4mg, rabbits < 1 mg).

---

[t] Biomira Inc. - proprietary technique.

Tru Scint® PR™ Monoclonal Antibody Kit (B80.3) contained 2 mg of predispensed sterile, non-pyrogenic, frozen solution of derivatized MAb B80.3 in the presence of a suitable reducing agent, saline and a buffer complex. The product contained no antimicrobial preservative. Labelling was performed with the addition of sodium pertechnetate ^{99m}Tc USP (1.6 - 2.0 GBq) to directly label the reduced thiol-groups to produce a slightly acidic pH solution that remained stable for two hours after radiolabelling. Similar quality control measures as the MAb 174H.64 were used to test for radiochemical purity.

The OVAREX™ Monoclonal Antibody Kit (B43.13) contained 1 mg of predispensed sterile, non-pyrogenic, frozen solution of derivatized MAb 170H.82 in the presence of saline and a buffer complex. The MAb was present in a reduced form using a propietary photoactivation process. The product contained no antimicrobial preservative. Labelling was performed with the addition of sodium pertechnetate ^{99m}Tc USP (1.6 - 2.0 GBq) to directly label the reduced thiol-groups to produce a slightly acidic pH solution that remained stable for two hours after radiolabelling. Similar quality control measures as the MAb 174H.64 were used to test for radiochemical purity.

As with all applications that use radiotracers to measure in vivo physiological parameters, it was important to know the specific activity of the labelled compound in order to make some preliminary assessment as to whether addition of the radionuclide might effect the compound's normal physiological distribution. For example, if there were several radioactive atoms associated with the compound then one might reasonably expect that some of its normal binding sites might have been compromised. However, in the case of a very large molecule, such as a MAb, the addition of several radionuclides can most likely be accomplished with little alteration in its 'normal' kinetics, provided that the label is kept remote from the antigen binding sites (see page 58).

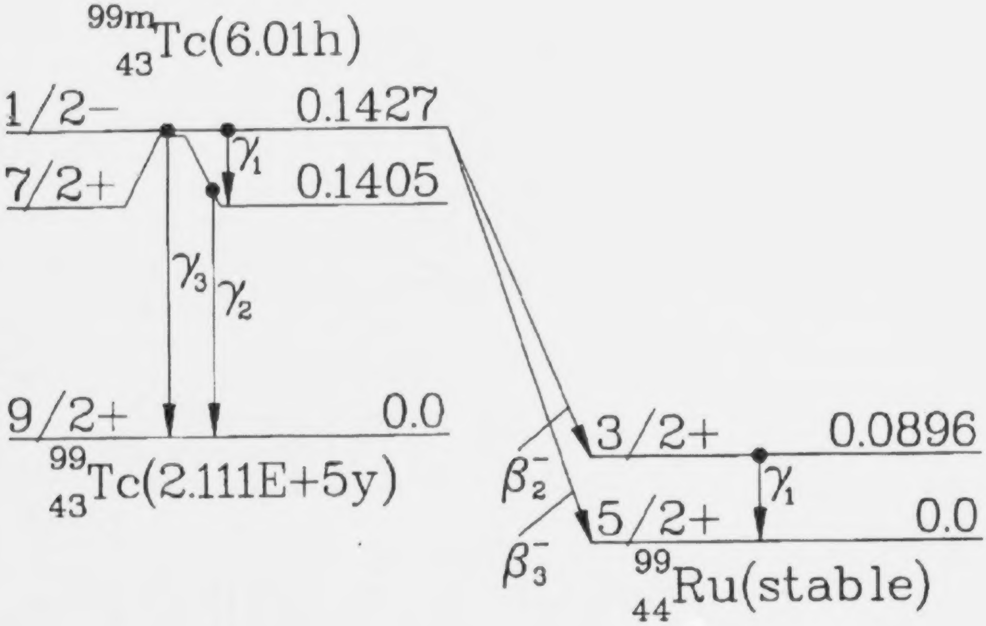

Figure 4: Decay scheme for ^{99m}Tc (from MIRD: Radionuclide Data and Decay Schemes, DA Weber et al, Society of Nuclear Medicine, 1989).

In order to estimate the number of technetium atoms attached to the MAbs (specific activity) used in this study, the following methodology is presented. Since the decay scheme of the metastable radionuclide, ^{99m}Tc, also includes ^{99}Tc, knowing the ratio of ^{99m}Tc to ^{99}Tc is necessary in order to completely assess the specific activity of Tc labelled MAb. Only ^{99m}Tc is suitable for gamma camera imaging as evident from the decay scheme shown in Figure 4. The calculations are shown below for 1 mg of MAb labelled with 1 GBq of ^{99m}Tc. The quantity of ^{99}Tc is estimated for the generator conditions shown.

The number of ^{99m}Tc atoms in 1 GBq is given by equation 27;

$$A = N \lambda \tag{27}$$

where

A = Activity of the radionuclide
N = Number of radioactive atoms
λ = Decay constant of the radionuclide
= 3.21×10^{-5} s^{-1} for ^{99m}Tc.

Solving for N when A = 1 GBq; N = 3.12×10^{13} atoms.

The number of MAb molecules is easily obtained from equation 28.

$$N_{MAb} = (Av \times m) / MW \tag{28}$$

where

N_{MAb} = number of MAb molecules
Av = Avogadros number = 6.02×10^{23}
m = mass of the Mab (g)
MW = molecular weight of the MAb (approx. 150,000 g/mole)

Solving for N_{MAb} when m = 1 mg, we obtain $N_{MAb} = 4.01 \times 10^{15}$ molecules.

The ratio of ^{99m}Tc atoms to MAb molecules is then 7.8×10^{-3}:1 or approximately one MAb molecule in 128 is labelled with ^{99m}Tc.

However, due to the nature of its physical decay scheme, ^{99m}Tc is always associated with ^{99}Tc, where the actual amount is a function of the ^{99}Mo generator and the time elapsed following generator elution. The example illustrated below utilizes similar conditions to those found during the patient clinical trials.

A 24 h ^{99m}Tc generator 'grow-in' period was used and the 1 mg of MAb was labelled with 1 GBq of ^{99m}Tc, 6 h following elution from the generator. The ^{99m}Tc / (^{99m}Tc + ^{99}Tc) ratio or h(t) can be calculated[222] from equation (29). For the purposes of these calculations, ^{99}Tc will be assumed to be stable as its half-life (2.2 x 10^5 y) is long compared to ^{99}Mo and ^{99m}Tc.

$$h(t)=\frac{\lambda_1\left(e^{-\lambda_1 t}-e^{-\lambda_2 t}\right)}{1.162\left(\lambda_2-\lambda_1\right)\left(1-e^{-\lambda_1 t}\right)} \tag{29}$$

where

$h(t)$ = ^{99m}Tc / (^{99m}Tc + ^{99}Tc) ratio

λ_1 = decay constant of ^{99}Mo = 0.01043 h^{-1}

λ_2 = decay constant of ^{99m}Tc = 0.1151 h^{-1}

e = base of the natural log = 2.7183

1.162 = constant (only 86.05% of ^{99}Mo decays to ^{99m}Tc)

t = time (h) elapsed since the last elution

For t = 24 h, $h(t)$ = 0.277 or 277 out of 1000 Tc atoms are ^{99m}Tc.

If the MAb is labelled , 6 h following elution from the generator then one half-life of ^{99m}Tc will have elapsed and $h(t)$ becomes 0.136. From the calculations above, the estimated MAb: ^{99m}Tc ratio was 1:128 but when the total amount of Tc is taken into account this ratio changes to approximately 1:17 or, on the average, one MAb in every 17 has a Tc atom attached to it.

4.2 Radioimmunoimaging

All images were obtained using a Siemens (Frankfurt) or Picker Odyssey 2000 (Edmonton) dual-headed, large-field-of-view gamma camera with low energy all-purpose (LEAP) collimators. The dual-headed arrangement made it possible to collect simultaneous anterior and posterior images (conjugate-views) of the MAb distribution in the patient. Whole-body serial images were obtained for each patient at several times post-injection. The imaging time-points were predicted from pilot studies in patients receiving the ^{99m}Tc labelled MAb (170H.82, 174H.64 or B80.3).

The precision in the development of any type of pharmacokinetic model, whether using quantitative or relative-count imaging protocols, is a function of the amount of data collected, or in this case, the number of patient images. However, due to patient stress and the relatively short half-life of ^{99m}Tc, it was possible to obtain only 3 - 5 images/patient at different times post-injection. This affected the type of model that could be developed, i.e. provision only for a one compartment model owing to the few number of data points. Also larger error terms are generally associated with the kinetic parameters describing a model based on a small number of data points. Thus, due to the inescapable simplifications involved in this method, only the rate constants describing the half-lives of the activity in the ROI's were obtained. These data were then used to determine the biological distribution and elimination phase half-lives for kinetic modeling and radiation dosimetry calculations.

The main assumptions and procedures used in the collection of gamma camera data are summarized below.

1. The first whole-body count contains all the injected activity and represents 100% of the injected dose.
2. The counting efficiency of the gamma camera, photon attenuation and Compton scatter remain constant over the period of the study. No clinical QC data was available to verify that this was indeed the case, but counting efficiency measurements performed over the course of a rabbit study showed less than a 1 % change.
3. Regions-of-interest (ROI) were drawn on the posterior 4 - 6 hour image, and applied to the opposing view. These ROIs were applied to all other images for the that patient.
4. The same operator was used to draw all ROI's to remove inter-operator variability associated with the construction of ROI's.
5. The imaging computer associated with the gamma camera was used to calculate the number of counts and area of each ROI for both anterior and posterior views, as described in the following section.
6. The measurement of activity in a ROI was expressed as a percentage of the administered activity (as measured by the whole-body counts).
7. Values of the amount of activity injected, imaging time, energy window setting, time and date of image acquisition, were recorded for all patients.

4.2.1 Data Processing

The unprocessed data recorded from the gamma camera consisted of the number of counts in each ROI for the anterior and posterior images, the time required to acquire the image and the elapsed time from the injection of the MAb. The data were then corrected for the attenuation and scatter of gamma photons in tissue, and decay corrected to the time of injection as discussed below.

The linear attenuation coefficient was chosen to include scatter and consequently, buildup correction was not employed to directly compensate for scatter. The linear attenuation coefficient $\mu = 0.15\ \text{cm}^{-1}$ is usually chosen to represent the attenuation in tissue of a narrow beam of ^{99m}Tc photons with no scatter component. However, if the linear attenuation coefficient is modified ($\mu = 0.12\ \text{cm}^{-1}$) for a gamma camera energy window of 20% it will include approximately 50% of the scattered photons[223,224]. A 20% window was used to acquire all ROI data and $\mu = 0.12\ \text{cm}^{-1}$ was used in all calculations.

All data analysis was performed using the spreadsheet QPRO for Windows according to the following protocol:

1. The geometric mean counts for each ROI was calculated as:

$$[\{(\text{Anterior}_{\text{cts/px}} - \text{Bkgd}_{\text{cts/px}}) \times (\text{Posterior}_{\text{cts/px}} - \text{Bkgd}_{\text{cts/px}})\}^{1/2}] \times \text{ROI}_{\text{px}} \qquad (30)$$

2. The region chosen to represent the background was selected in the pelvic region away from major blood vessels and other areas of obvious uptake. Variations in area and patient thickness between the background and organ ROI's were taken into account during background subtraction. The thickness of the regions were normalized to that of the central torso and background subtraction was made on a per pixel basis. The volume occupied by the organ-of-interest in the ROI was subtracted from the total volume of the ROI. The background equivalent of that organ volume would then not result in an over subtraction of background activity, leading to the organ counts being underestimated. For example; if the kidney ($\text{Organ}_{\text{vol}}$) represented 20% of the volume of the total ROI volume (ROI_{vol}), then the background (ROI_{Bkgd}) was reduced by multiplying the

background counts ($Bkgd_{cts/px}$) by 0.8 as illustrated in Figure 5 and equation (28).

$$ROI_{Bkgd} = \{Bkgd_{cts/px} \times (ROI_{vol} - Organ_{vol})/ROI_{vol}\} \times ROI_{px} \tag{31}$$

Mean organ dimensions from CT images from several patients were used to estimate organ and torso thickness. The dimensions of rabbit organs were estimated from values measured during necropsy.

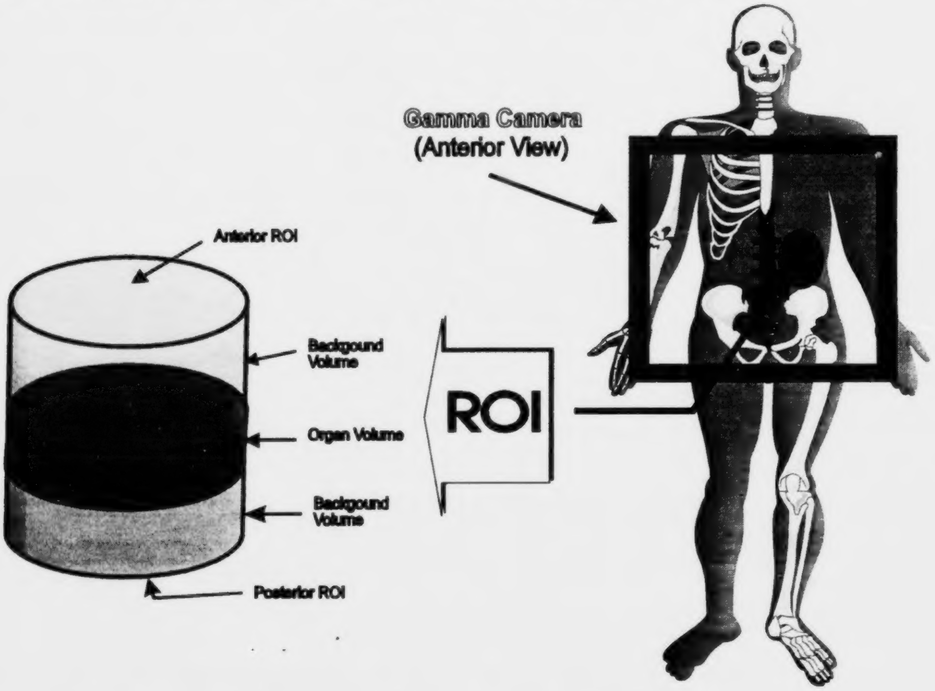
Gamma Camera
(Anterior View)
Anterior ROI
Backgound Volume
Organ Volume
Backgound Volume
Posterior ROI
ROI

Figure 5: Schematic view of a ROI depth-profile.

3. The ROI and whole-body geometric mean counts were modified assuming a uniform attenuation coefficient in the body. A schematic of the gamma camera and patient orientation are shown in Figure 6.

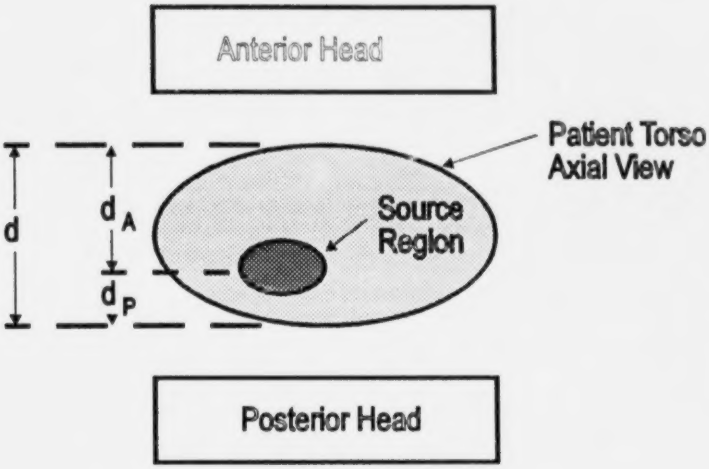
Anterior Head
Patient Torso
Axial View
Source
Region
d
d_A
d_P
Posterior Head

Figure 6: Schematic view of patient - gamma camera orientation.

4. The counts observed in the anterior head of the gamma camera (C_A), corrected for attenuation may be written as:

$$C_A = C_{A_0} e^{-\mu d_A} \tag{32}$$

where:

C_{A_0} = true anterior counts,

$e^{-\mu d_A}$ = correction factor

d_A = distance from the ROI to the anterior surface of the body,

μ = modified linear attenuation coefficient.

Similarly, the counts observed in the posterior head of the gamma camera (C_P), is given by:

$$C_P = C_{P_0} e^{-\mu d_P} \tag{33}$$

where

C_{P_0} = true posterior counts,

d_P = distance from the ROI to the anterior surface of the body,

μ = modified linear attenuation coefficient.

Assuming that the anterior and posterior counts have already been compensated for background, the geometric mean of the observed activity from a ROI is given by:

$$\sqrt{C_A * C_P} = \sqrt{C_{A_0} * C_{P_0} * e^{-\mu d_A} * e^{-\mu d_P}} \qquad (34)$$

From Figure 6 it can be seen that $d = d_A + d_P$ is total patient thickness over the ROI and that rearrangement of Equation (34) gives the expression used to calculate the attenuation-corrected geometric mean counts:

$$\sqrt{C_{A_0} * C_{P_0}} = \frac{\sqrt{C_A * C_P}}{e^{-\mu d/2}} \qquad (35)$$

5. The anterior and posterior geometric mean count data were converted to a percentage of the whole-body counts and then to units of activity (MBq or mCi) based on assumption 1 (above). These data were not decay corrected so that they could be used directly in the calculation of cumulated activity. The whole-body counts were corrected for attenuation based on the mean torso thickness obtained from patient CT data. Mean values from several patients were used when specfic patient measurements were unavailable.

6. A time-activity curve for each ROI was then constructed. The area under the curve was calculated to yield a value for the cumulated activity for each ROI using the computer program Lagran[u].
7. Organ and whole-body radiation doses to patients receiving ^{99m}Tc labelled MAbs were calculated using the classic MIRD formulation[v] as described previously on page 60.

4.2.2 Rabbit Imaging Protocol

The imaging protocol used in the rabbit studies was based upon conjugate-view planar images with the organ activity obtained from appropriate ROI data. Two different methods of imaging were used. The first employed a technique similar to that used for patients as described above, except that absolute organ activity obtained from necropsy was used to convert the relative count data in an ROI to Bq/organ. Absolute organ activity obtained from necropsy was used convert the relative count data in an ROI to Bq/organ following a similar background subtraction routine as used in the patient protocol.

The second method for quantitating organ activity was adapted from a method first described by Thomas and co-workers[225] who used planar conjugate-view imaging for the evaluation of thyroid cancer patients. Hammond and co-workers[226] later reported a less than 10% error in the quantitation of ^{131}I in patients using attenuation corrected geometric-mean data from planar images. These techniques were refined by Eary[227] and co-workers to include the use of a collimated transmission source to obtain an attenuation value for each ROI. The method used in this report was developed by Mr E. Zastre[w] and was based on Eary's technique with the background determination based on an interpolative method developed by Levy and co-workers[228]. All rabbit images were obtained with the same Picker Odyssey 2000 dual-headed, large-field-of-view gamma camera with LEAP collimators.

---

[u] Ediss C, Faculty of Pharmacy and Pharmaceutical Sciences, University of Alberta, Edmonton, Canada.

[v] MIRD Primer for Absorbed Dose Calculations, R Loevinger, TF Budinger and EE Watson, Society of Nuclear Medicine, New York, 1991.

Prior to imaging, all rabbits were anaesthetized following the protocol described below. Images were obtained from the head to the knee of all rabbits unless otherwise noted. Images were acquired continuously from the time of injection to 3 hours post injection in 15 minute intervals and then at 4-6h,10-12h, 18-24h, 30-36h and 46-50h post-injection.

4.2.2.1 Rabbit Blood-Flow

The contributions of normal blood-flow to the organs-of-interest in the MAb studies were estimated using in vivo ^{99m}Tc labelled red cells. Gamma camera image data was obtained from a whole-body scan performed at 15 minutes post-injection. The rabbit was euthanized at the conclusion of this scan and selected organs were removed and assayed in a well-type gamma counter (Table 5). The organ activity expressed as a percentage of the % injected dose per organ at the time of imaging is given in Table 4.

Table 4: Organ activity obtained from quantitative conjugate-view gamma camera imaging of ^{99m}Tc-red cells expressed as a percentage of the injected dose (%ID).

Animal	Heart (%ID)	Liver (%ID)	Rt. Kidney (%ID)	Lt. Kidney (%ID)
SAM17	3.0 ± 0.3	17.2 ± 1.7	4.6 ± 0.5	4.5 ± 0.5

---

[w] Planar conjugate-view imaging using attenuation corrected geometric-mean techniques is part of the current PhD program of E Zastre, University of Alberta.

Table 5: Rabbit tissue sample data for in vivc ^{99m}Tc labelled red cells.

Tissue Sample	SAM17 % inj. dose/organ t = 0.5 h	SAM17 % inj. dose/gm t = 0.5 h
Liver	16.4 ± 0.82	0.108 ± 0.006
Spleen	0.16 ± 0.01	0.156 ± 0.008
Heart	2.9 ± 0.15	0.247 ± 0.013
Right Kidney	4.4 ± 0.22	0.326 ± 0.017
Left Kidney	4.3 ± 0.22	0.308 ± 0.016
Gall Bladder	0.01 ± 0.001	0.151 ± 0.008
Bile	N/A	0.043 ± 0.003
Muscle	N/A	0.004 ± 0.0003
Lung	N/A	0.251 ± 0.013

4.2.3 Patient Imaging Protocol

Following i.v. injection as described in the protocol on page 105, the accumulation of radiolabelled monoclonal antibodies was observed in several organs as identified by gamma camera imaging. Regions of interest (ROI) were drawn around each organ and used to develop time-activity curves for the liver, heart, kidney and a background region. Slight uptake was observed in the spleen of some patients but as this was not universal, the spleen was not included as a source organ.

The imaging protocol used in these studies was based upon conjugate-view planar images with the organ activity expressed as a percent of the whole-body activity, and is described below.

1. Obtain posterior and anterior whole body planar images at: 0.25h, 2-6h, 18-24h, 24-30h and 48 h. Imaging times were based on information from pilot studies performed at the Cross Cancer Institute. LEAP collimators were used for all images.
2. For each time interval, measure the counts and counting period for the whole-body, heart, liver, kidneys, background site and any other regions

where the MAb is observed to localize. A typical whole-body image, with ROI's drawn about these organs is illustrated in Figure 7.

Figure 7: Typical whole-body imaging illustrating the placement of ROI's. This particular image is a 6h anterior view of ^{99m}Tc labelled MAb 170H.82.

3. When calculating the total counts, use the same ROI's for all images. ROI uncertainties can be estimated by redrawing the ROI on one of the images ten times to find the variation in the ROI counts (see analysis of phantom data below, page 108). The same operator should draw all ROI's if possible to reduce inter-operator error.
4. Calculate the geometric mean of the posterior and anterior counts as described above.
5. Background subtraction: Draw an "appropriate" region in the pelvic area (i.e. free from obvious uptake and away from the bladder). Use CT data to estimate the percentage of an organ volume in the ROI in order to compensate background subtraction (for the volume it occupied in the ROI).
6. For each image time, express all ROI counts as a precentage of the whole body counts:

$$\% \text{ ROI} = (\text{ROI}_{\text{organ}} / \text{Whole-body}) \times 100 \qquad (36)$$

7. Normalize data with respect to the initial whole-body image to obtain per cent injected activity values for all ROI's.

4.3 Sampling Methodology

4.3.1 Rabbits

A kinetic study in rabbits was undertaken to: 1) study the in vivo biodistribution of the MAbs in non-tumor bearing animals, 2) study the effects in biodistribution patterns in a species different from that in which the MAbs originated[229] and 3) ensure the adequate availability of data required to develop a pharmacokinetic model.

Non tumor-bearing New Zealand white rabbits were chosen to assess the 'normal' biodistribution of these MAbs as a compromise between animal size and ease of manipulation during data collection. Some of their relevant anatomical and physiological parameters[230] were: body weight 2 - 3 kg, whole-body blood volume of 55.6 - 57.3 mL/kg of body weight, hematocrit of 36.3 ± 3.2, a 24 hour average urine output of 130 mL/kg (but a wide range of 20 - 350 mL/kg) and a torso thickness of 7 - 9.5 cm.

At the time the study was initiated, the only animal data available were from tumor and non-tumor bearing mice[x]. Interspecies variation in the biodistribution of a MAb is generally dependent on the species from which the MAb was obtained and the species in which the MAb is studied[231]. It is also likely that the behavior of murine derived MAbs in patients will generally not follow the same pharmacokinetic patterns as the models developed in mice, thus, a species other than the mouse was chosen to obtain initial estimates for the development of the of the pharmacokinetic model in patients. Although not measured, the study of murine-based MAbs should also reflect the HAMA response, or in this case RAMA response, following the injection of a murine-based foreign protein.

---

[x] Biomira Inc. - Internal studies.

In order to adequately develop a pharmacokinetic model, more data points are required than are typically available from patients. Using an animal model makes frequent sampling and imaging times possible. The relationship between this model and that in patients was explored with the hope of producing a refinement in the patient pharmacokinetic model.

In keeping with the current trend to reduce the number of animals used for research purposes only three rabbits were used per study. If the resulting data was consistent within each test group, no further animals were used. All rabbits were handled in accordance with the "Canadian Council on Animal Care" following those protocols approved by the University of Alberta's "Use of Animals in Research and Teaching Committee - protocol # 91266" and by the Alberta Cancer Board's "Animal Care Committee - protocol # AC92030T".

The imaging protocol used in the rabbit studies was based upon conjugate-view planar images with the organ activity obtained from appropriate ROI data. Prior to the first set of images (3 - 4 hours in length) all rabbits were anaesthetized with a cocktail of Rompun[y] (8 mg/kg), Ketalean[z] (40 mg/kg) and Atravet[aa] 0.5 (mg/kg). This anesthetic dose was administered i.m. with the total dose divided between the left and right thigh muscles. This anesthetic sustained the rabbits in a light surgical plane for approximately 45 - 60 minutes. To maintain this level over the course of the first imaging period, an inhalation anesthetic, Forane[bb] was used in conjunction with a portable anesthetic scavenger (Fluovac). All subsequent images in the imaging protocol were taken after the rabbit had been anaesthetized with Forane gas rather than the anesthetic cocktail as repeated i.m. injections caused local hyperemia due to muscle insult. The animal was sacrificed immediately following the final image with a lethal cardiac injection of Euthanol at 3 mL/rabbit.

---

[y] Rompun: a Xyline based sedative and analgesic containing methylparaben and propylparaben. (Farbenfabriken Bayer (Haver) GmbH)

[z] Ketalean: a rapid-acting general anesthetic containing ketamine hydrochloride. (MTC Pharmaceuticals)

[aa] Atravet: a tranquilizer with acepromazine as the active ingredient. (Ayerst Laboratories)

Images were obtained from the head to the knee of all rabbits unless otherwise noted. Images were acquired continuously from the time of injection to 3 hours post injection in 15 minute intervals and then at 4-6h,10-12h, 18-24h, 30-36h and 44-50h post-injection.

4.3.1.1 Biological sampling

During the first three hour period following MAb injection, 1 mL blood samples were taken from the marginal ear vein, contralateral to the injection ear, through an indwelling, heparinized catheter. All subsequent blood samples were taken using a 1 mL syringe at predetermined time intervals up to 48 h post-injection. All blood samples were collected in 5 mL 'red-top' serum tubes. The samples were then centrifuged at 2000 g for 12 minutes and stored at 4°C. Duplicate 100 μL serum aliquots were prepared and counted in a calibrated gamma counter.

[bb] Forane (isoflurane): an inhalation anesthetic with a low blood-gas solubility coefficient permitting rapid induction and recovery from the anesthetic. Used in conjunction with a portable gas scavenger. (International Market Supply)

The high viscosity of the rabbit's urine[cc] made collection via catheterization impractical. Consequently the urine was collected either during general anesthesia (bladder massage) or from the absorbent cage liner. All samples were counted in a Capentec Dose Calibrator. Samples were obtained up to time-of-death, including urine collected during necropsy.

In order to assess activity excreted through the biliary system fecal samples were collected. This type of measurement is complicated by the fact that rabbits practice nocturnal coprophagy, so that some of this activity may be reabsorbed. However, a lower estimate of excretion via this route of elimination can still be made. Fecal samples were obtained from the animals cage-liner, taking care to avoid those contaminated with urine.

Tissue samples were obtained during necropsy to include organs visualized from gamma camera imaging. Blood was washed from the heart chamber and the surface of the liver to remove its contribution to organ activity. The activity was measured in a calibrated multisample gamma counter and reported as total activity per organ (kBq) and as activity per unit mass of tissue (dpm/gm). The total organ activity was used as a standard to check the planar imaging quantitation technique.

4.3.1.2 Blood-flow Measurements

The contributions to the overall radioactivity in selected organs from normal blood-flow was estimated using erythrocytes labelled in vivo with ^{99m}Tc[232,233,234]. In vivo erythrocyte "tinning" was accomplished by injecting intravenously 1 mg of stannous pyrophosphate into the marginal ear vein and allowed to circulate for 30 minutes. ^{99m}Tc-pyrophosphate was then injected and a whole-body gamma image was taken 15 minutes post-injection. The rabbit was anesthetized as described above, and imaged with the dual-headed Picker gamma camera. At the end of the imaging period, 3 mL of blood was removed via cardiac puncture to aid in determination of the blood volume and radioactivity concentration in the blood. The rabbit was then sacrificed using Euthanyl at 3 mL/rabbit.

[cc] Crystalluria is normal in rabbits.

The same set of organs as those used for the MAb biodistribution studies were collected at necropsy. The heart was divided into sections to expose the chambers and then rinsed with water to dislodge the blood in order to assess the activity in the heart muscle. All other organs were counted as dissected, without further rinsing. The radioactivity in each sample was measured in a calibrated multisample gamma counter and reported as total activity per organ (kBq) and as activity per unit mass of tissue (dpm/gm). The total organ activity was used as a calibration standard to convert the percentage of whole body dose ROI measurements to absolute activity/organ.

4.3.2 Patients

A program to determine the clinical efficacy of selected monoclonal antibodies having application in radioimmunoscintigraphy was undertaken at the Cross Cancer Institute as part of a Pilot, Phase I or a Phase II study[dd]. This work was initiated by a local biotechnology company, Biomira Inc. and the work contained in this report uses data obtained from a subset of the patient groups that were enrolled in the kinetic program. The prime purpose of the kinetic program was to study the in vivo biodistribution of these MAbs and determine dose estimates for RIS procedures.

[dd] Appropriate clinical protocols, ethics approval and patient consent forms are on file at Biomira Inc, Edmonton, Alberta.

Patients aged 18 - 74 yeas of age with confirmed head and neck squamous cell carcinoma (174H.82), breast cancer (170H.82), prostate cancer (B80.3) or ovarian cancer (B43.13) were recruited into the study after obtaining appropriate informed consent. A single dose of 1, 2 or 4mg of the murine derived MAb in 20 mL of saline was administered intravenously over a period of approximately 5 minutes. The chimeric form of MAb-174H.64 and MAb-B43.13 was administered intravenously as a 1 mg (174H.64) or 2 mg (B43.13) dose in 5 mL of saline over a period of 20 - 30 seconds. The injected radioactivity was measured with a dose calibrator.

4.3.2.1 Gamma camera imaging

Planar gamma camera image data (anterior and posterior) were recorded at time intervals prescribed in the appropriate MAb protocols. Data consisted of whole-body counts and selected regions of interest (ROI) including the heart, liver and kidneys. The geometric mean counts were used to calculate ROI activity which was expressed as a percentage of the whole body. The whole-body image taken at the end of infusion of the MAb was assumed to represent 100% of the injected dose. The section on page 92 contains additional details on the methodology used.

4.3.2.2 Biological sampling

Serum and urine data were collected from each patient following a prescribed protocol[ee]. Samples were collected at predetermined times up to 72 hours post-injection and assayed for total radioactivity with a calibrated multi-sample gamma counter. Selected serum samples (up to 8 weeks post-infusion) were also assayed for Human Anti-Mouse Antibody (HAMA) response[ff].

[ee] Canadian Health Protection Branch approved protocol: Biomira 91MD17413 (Head and Neck) add protocol numbers for 170 and B80

The serum samples (5 mL) were collected in the contralateral arm following the prescribed time intervals of: 0.25, 1, 2, 4, 8, 12, 22, 28, 36, 48 and 72 hours post-infusion (not all samples were collected from all patients depending upon individual circumstances). Samples were centrifuged at 2000 G's for 12 minutes and stored at 4°C. At the end of the study, duplicate 0.5 mL aliquots from each serum sample were counted in a calibrated gamma counter. The collection time, sample cpm and instrument counting efficiency were recorded for each sample.

Urine samples were collected in 6 h batches over the length of the study (up to 72 hours post-injection) and stored at 4°C. The volume for each interval was recorded and at the end of the study 1.0 mL aliquots were counted in duplicate in a calibrated gamma counter. The collection time, sample cpm and instrument counting efficiency were recorded for each sample.

A brief protocol follows, describing the blood and serum data-handling methods used to estimate the parameters for a compartmental kinetic model of the radiolabelled MAb.

1. Prepare duplicate 0.5 mL aliquots of the serum or urine (1 mL) collected from each time period.
2. Calibrate the gamma counter using a known amount of activity.
3. Count all samples, noting sample counts per minute, counting efficiency, time and date of analysis.

[ff] TruQuant HAMA Kit, Biomira Inc.

4. Decay correct data to time-of-injection. The spreadsheet QPRO has been successfully utilized for these calculations and its associated graphics package permit a rapid visual check of the data.
5. Calculate dpm/mL (MBq/mL) and % injected dose for each serum time point (QPRO).
6. Calculate dpm/mL (MBq/mL), total activity and % injected dose for each urine time interval (QPRO). The raw data and analytical results from QPRO for all patients and animals discussed in this work are presented in the appendices.
7. The nonlinear fitting program, PCNONLIN was used to fit the serum data (dpm/mL or MBq/mL) to the appropriate compartmental model.
8. The volume of distribution obtained from the model was used in step 5. to calculate the % injected dose. The model can be used to predict whether a significant portion of the MAb will redistribute outside of the blood volume.

4.4 Phantom Studies

A phantom study was performed to estimate the precision of using the count-rate in a region of interest (ROI) drawn around an organ to represent its activity. Two sources of error associated with the utilization of this technique to measure the radionuclide distribution in patients and animals were measured. One attributed to the error in drawing ROI's, and the other related to the problems of overlying activity.

The phantom used in these measurements was the "Organ Scanning Phantom"[gg] duplicating the contours of a man from the diaphragm to the upper pelvis. For this study, separate inserts were used to represent the liver and right and left kidney. The upper portion of the right kidney was positioned to overlap the liver in an effort to mimic the situation observed in the rabbits and patients. A typical posterior image of the phantom is shown in Figure 8 to illustrate the placement of the interior organs. The torso cavity and organs were filled with ^{99m}Tc pertechnetate with the activities shown in Table 6 and imaged at four times up to 30 hours post-filling. A dose calibrator[hh] was used to determine the activity added to the phantom. The gamma camera[ii] used for the phantom images was the same as that used for the animal and patient studies.

To estimate the error associated with the reproducibility of drawing ROI's (heart, liver and kidneys), two techniques were used: 1) wide and narrow ROI's were drawn for each image to estimate the range of error associated with different sizes of an ROI and 2) a "best estimate" for the ROI's were drawn around each organ in the phantom ten times and the mean and standard deviation calculated to estimate reproducibility. The same operator was used to draw all the ROI's for the phantom, animal and patient studies to remove the inter-operator error. Overlapping organ activity was not removed and volume compensated background subtraction[jj] not performed for these tests so as not to introduce errors due to additional data manipulation.

[gg] The Phantom Laboratory, Salem, NY.

[hh] Capintec Inc, Ramsey, NJ.

[ii] Picker International, Bedford OH.

[jj] See section on gamma camera imaging for a description of this technique.

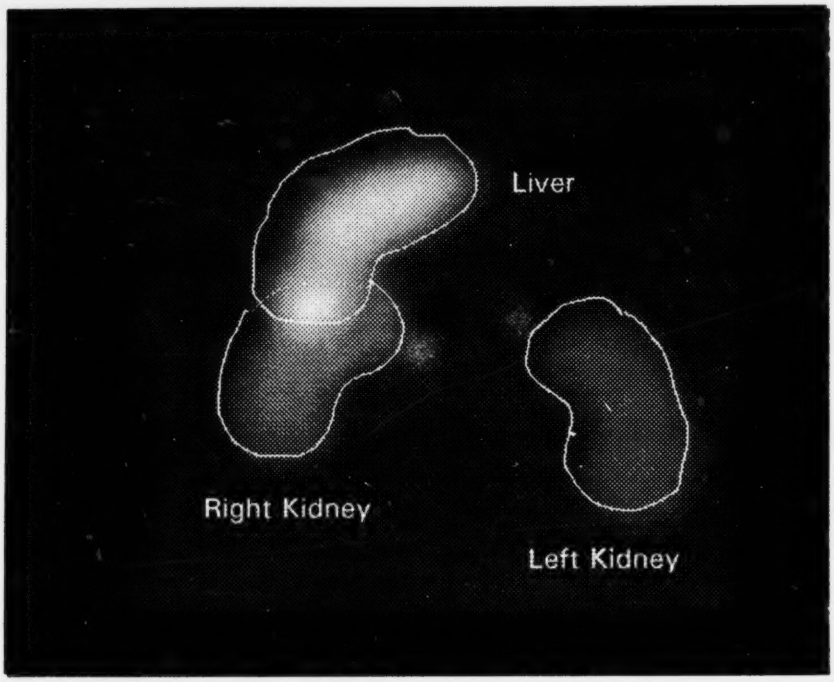

Figure 8: Posterior image of the phantom showing ROI's drawn around the kidneys and liver.

Table 6: Phantom activity expressed in MBq and as a percent of all the activity in the phantom (whole body). The activity was decay corrected to the time of the first image.

Organ	Activity (MBq)	% Whole Body
Liver	1229	20.34
Right Kidney	97	5.39
Left Kidney	102	5.69
Background	365	68.58
Total	1792	100.00

To assess the impact of ROI size on assessing organ activity, two regions were drawn around each organ at the four time periods used in this study. The two sizes used were subjectively chosen to represent the extremes in constructing each ROI; the large size including all of the observed counts (and possibly some of the surrounding background), the narrow region was drawn well inside the observed boundary so as to exclude any of the background area. The data are shown in Table 7 for each imaging time and are expressed as a percentage of the variation from the mean of the wide and narrow regions for each organ.

Table 7: Variation in drawing wide and narrow regions for each phantom organ (expressed as a percentage).

Organ	% Variation Time: Immed	% Variation Time: 12 h	% Variation Time: 23.5 h	% Variation Time: 30.4 h
Liver	34.2	31.4	38.8	30.9
Left Kidney	25.7	22.5	31.1	24.5
Right Kidney	37.5	34.4	36.5	41.2

These data indicate the maximum error that might be attributed to drawing different sizes of ROI's (22.5 to 41.2%). Clearly these regions represent the extremes of drawing ROI's and one might expect to improve on these values by a judicious choice of the ROI boundary.

Another source of error can be attributed to the operator's ability to reproducibly draw a ROI. To measure this error, ROI's were reconstructed ten times on the immediate image. The combined results from the ten trials showing the mean, standard deviation and % error are shown in Table 8. Note, that for all the animal and patient studies performed, a single set of ROI's were drawn on one image and then used for the remainder of that set of images.

Table 8: Error associated with multiple attempts at drawing the same region of interest. The data shown represents the mean of 10 trials of the geometric mean of the ROI's shown in Figure 8.

Results of 10 Repetitions	**Liver counts/ROI**	**Lt Kidney counts/ROI**	**Rt Kidney counts/ROI**	**Whole Body counts/ROI**
Mean:	1838490	557969	872282	15474181
Std Dev:	29996	14721	33188	19050
% Error:	**1.6**	**2.6**	**3.8**	**0.1**

To measure the effects of background subtraction on estimating the activity in a ROI, the following tests were performed on data representing the left and right kidneys. The raw ROI data from the ten repeated ROI-drawing trials on the immediate image were used. The attenuation-corrected[kk] geometric mean was calculated for each trial and expressed as a percentage of the whole body counts. As the phantom provided a uniform attenuation media (water), a linear attenuation coefficient of $\mu = 0.15\ cm^{-1}$ was chosen. Calculations were made for no background subtraction, uniform background subtraction and an "organ-compensated" background subtraction. Uniform background subtraction involved subtracting the background-ROI counts/pixel from the organ-ROI counts/pixel, while the "organ-compensated" background subtraction took into consideration the volume of the organ ROI as explained on page 92. The results, expressed as a percentage of the whole body activity, are presented in Table 9 and demonstrates the ability of the "organ-compensated" background subtraction technique to more closely represent the actual activity for the left kidney which was unencumbered by overlaying activity from another organ (column 4).

[kk] See section on gamma camera imaging for attenuation correction method used.

The effect of overlying activity was estimated by positioning the right kidney such that the upper pole overlapped a portion of the liver when viewed by the gamma camera. The activity for the right kidney was first calculated using the technique described above to obtain the geometric mean counts using the organ-compensated background subtraction technique. Additional regions of interest were drawn to include a no-overlap liver region, a no-overlap right kidney region and the entire region of overlap. The number of pixels and the counts in each region were obtained and the right kidney counts were recalculated by estimating the mean counts/pixel in the liver and subtracting those counts from the right kidney based on the number of pixels in the overlap region. The results are shown in Table 9 expressed as a percent error of the known organ activity.

Table 9: Effects of background subtraction and correction for overlaying activity, expressed as a percentage of the whole body activity

Organ	No Background	Uniform Background	Compensated Background	Overlap Correction	Actual Value
Left Kidney	9.65 ± 0.32 %	3.61 ± 0.10 %	5.23 ± 0.14 %	N/A	5.39 ± 0.16 %
Right Kidney	11.5 ± 0.49 %	5.64 ± 0.21 %	7.24 ± 0.31 %	5.59 ± 0.40%	5.71 ± 0.17 %

Although uniform background subtraction for the right kidney closely approximated that of the actual value, the calculations did not take in account contributions from overlaying liver activity. It was serendipitous that the two effects of "organ-compensated" background subtraction and overlap compensation canceled each other out in this case.

4.5 Radioimmunoassay

The techniques of radioimmunoassay (RIA) were first developed by SA Berson and RS Yalow[235] in the late 1950s for the determination of insulin in human serum. Rosalyn Yalow's contribution in the development of this technique for measuring minute concentrations of biological substances was acknowledged in 1977 when she was awarded the Nobel Prize. Today the method is used extensively in determining a variety of hormones, enzymes, antigens and drugs in quantities as small as (10^{-9} to 10^{-12} M) in human serum. The general term for this method in both immune and nonimmune systems is the "competitive binding assay".

The RIA method of molecular identification is based on the formation of an antibody-antigen complex $\{Ab^* + Ag\}$. Antibodies (Ab) are produced against the molecule to be measured (the antigen or Ag) so that, in the ideal situation, that Ab will only bind to that specific Ag that it was raised against. In general, one component of the assay is labelled with a radioactive marker (e.g. Ab^*) and the other component (Ag) fixed to a surface (usually a test tube) in the RIA kit. An aliquot of serum is then added to the tube where the following reaction takes place:

$$Ab^* + Ag \Leftrightarrow Ag + \{Ab^* + Ag\} \qquad (37)$$

In this example, all the specific antigens in the serum would compete with the Ag bound to the surface of the test tube for the radioactive Ab. Following an incubation period, an inverse relationship will then develop between the amount of radioactivity remaining in the test tube bound to the "fixed Ag", and the amount of Ag present in the patient's serum. A series of standards containing known quantities of the Ag are used to produce a calibration curve to develop an absolute relationship between radioactivity and mass of the Ag being measured.

There are several different types of RIA based on whether the Ag or Ab is labelled with the radiotracer. As it is not always possible (or economical) to isolate purified Ag, an anti-idiotype Ab may used instead of the Ag to produce a sandwich type RIA (see the 170H.82 RIA below). A summary of the RIA procedures used in this work follows.

4.5.1 MAb-170H.82 RIA

An inhibition based RIA was used to quantitate MAb 170H.82 serum levels in both patients and animals. This assay was developed by Biomira Inc. and is described in their Standard Operating Procedure #31, a brief summary of which is presented here.

Sarstedt plastic tubes (5 mL) were coated with 0.5 μg of rabbit, anti-170H.82 MAb (anti-idiotype) in phosphate-buffered saline (PBS) and incubated overnight. The coating solution was aspirated and the tubes blocked with1% BSA and 2% sucrose in PBS. The anti-170H.82 coated tubes were stored at 4°C and were found to be stable for at least 3 months following preparation.

Serum samples (100 μL) were added to the prepared tubes together with 4 ng (in 100 μL PBS) of ^{125}I labelled 170H.82. These samples were then incubated for 1 - 2 hours at room temperature and the contents aspirated and double washed with distilled water. The maximum binding capacity of the tubes was measured by adding 100 μL of 'normal' human (or rabbit) serum (i.e. no 170H.82) with the ^{125}I labelled 170H.82. A series of standards were prepared at the same time with known quantities of MAb-170H.82 (1.0 ng to 64 ng) using 'normal' human (or rabbit) serum as a diluent. Normal mouse serum (0.1%) was added to all samples to reduce non-specific binding of the 170H.82 murine-based MAb.

All tubes were then counted on a Packard Minaxi 5530 gamma counter and data reduction performed using the spreadsheet QPRO The equation of the standard curve and the interpolated value of the unknown serum concentrations were calculated using Table Curve.

4.5.2 MAb-174H.64 RIA

A competition based RIA was used for the quantification of the MAb, 174H.64 as described by Standard Operating Procedure #46 (Biomira Inc.). A summary of this assay is presented here.

Sarstedt plastic tubes (5 mL) were coated with 1.25 μg of goat, anti-174H.64 MAb. The patient's serum (50 μL) was added to the prepared tubes together with 5 ng (in 50 μL PBS) of ^{125}I labelled 174H.64. In an attempt to reduce extrapolation errors, each sample was diluted by two to provide an additional data point to account for the effects of fitting to a shallow slope on the calibration curve. These samples were then incubated overnight and aspirated and double washed with distilled water the following day. The maximum binding capacity of the tubes was measured by adding 50 μL of 1% BSA/PBS (i.e. no MAb 174H.64) with the ^{125}I labelled 174H.64. A series of standards were prepared at the same time with known quantities of 174H.64 (0.5 ng to 64 ng) using 1% BSA/PBS as a diluent. Normal mouse serum (0.1%) was added to all tubes to prevent non-specific binding of the 174H.64 murine-based MAb.

A second procedure was also tested to measure the murine 174H.64 MAb. This test was based on the material supplied in the HAMA kit developed by Biomira Inc. An aliquot of the patient's serum (100 μL) was added to plastic tubes coated with goat anti-mouse antibodies in order to separate the m174H.64 from the patient's serum. Following incubation (1 h) and washing, ^{125}I labelled anti-idiotype MAb (to 174H.64) was added to the tubes. After another 1 h incubation period, the tubes were washed and assayed for total radioactivity. In a similar manner, the chimeric form of

174H.64 was examined using tubes coated with the anti-idiotype to capture the c174H.64, followed by ^{125}I labelled anti-human IgG to measure the amount of c174H.64 in each tube.

All tubes were counted on a Packard Minaxi 5530 gamma counter. Data reduction was performed using the spreadsheet QPRO and the equation of the standard curve and the interpolated value of the unknown serum concentrations were calculated using Table Curve. Unfortunatley, neither of these tests were able to realiably measure MAb-174H.64 in the presence of human or rabbit serum.

4.5.3 MAb-B80.3 RIA

The MAb, B80.3 was measured using a sandwich-type RIA. Serum from the patient was collected at predefined time periods and immediately frozen to prevent the free MAbs from binding to any additional circulating antibody.

The procedure used in the assay was developed by Biomira (Standard Operating Procedure #45). Briefly described, the method uses the MAb, B87.2 which is directed against a different epitope of the PSA antigen in order to fix this antigen on the surface of the assay tube. MAb B87.2 is bound to 5 mL Sarstedt plastic tubes in preparation to performing the assay. The inhibition assay was performed by adding 50 ul of the 'unknown' serum, 50 µL of PSA (120 µg/mL) and 150 µL of ^{125}I-B80 (24 ng) to the coated tubes. The PSA attaches itself to the tube via the B87.2 MAb and then presents itself for competition to either the 'unknown' B80.3 sample or the added ^{125}I-labelled B80.3 in a "sandwich-type" RIA. Following an incubation time of 2 hours at room temperature, the tubes were aspirated and washed twice with distilled water. The activity remaining in the tubes is inversely proportional to the amount of B80.3 present in the sample being tested.

A calibration curve was prepared using known quantities of B80.3 ranging from 1 ng/μL to 100 ng/μL. The RIA data from the gamma counter was processed using the spreadsheet, Quattro PRO to perform the data reduction and error analysis, and the program, Table Curve to obtain the equation representing the best fit of the data. This equation, representing the distribution of the standards, was then utilized to estimate the quantity of the B80.3 in the unknown sample. All standards and unknowns were prepared in triplicate and counted on a multisample gamma-counter (Packard 5530).

4.5.4 CA 125 RIA

Serum values for the tumor associated antigen CA 125 were measured by Biomira Research Inc. The basis for their assay involved a second MAb, B27.1 derived against a different epitope of CA 125. The MAb-B27.1, was fixed to the inside of a 5 mL plastic tube, and following incubation with patient sera and radioidinated B43.13, a classic sandwich-assay procedure was utilized to quantitate CA 125 in U/mL[II].

4.6 Enzyme-Linked Immunosorbent Assay - MAb-B43.13

Analysis of MAb-B43.13 in patient serum was measured by enzyme-linked immunosorbent assay (ELISA). All patient sampling and data analyses were performed by Biomira Research Inc. following Standard Operating Procedure # SP-ANA-007. Their technique may be briefly summarized as follows:

[II] U/mL = units of CA 125 per mL.

1. assay tubes were coated with an anti-mouse IgG_1 (heavy chain specific) antibody,
2. samples, standards or controls were added,
3. following an incubation period and aspiration, horse-radish-peroxidase-conjugated $F(ab')_2$ fragment of anti-mouse IgG_1 (heavy or light chain specific), human absorbed was added to tag the bound MAb-B43.13,
4. a peroxidase substrate solution was added whereby the degree of color formation was proportional to quantity of MAb-B43.13 and finally
5. color development was stopped after a predetermined length of time and the plate containing the standards, controls and patient samples read in a spectrophotometer.

Patient MAb-B43.13 serum levels were determined by comparison against the standards.

4.7 Kinetic Modeling

As discussed in the section on Clinical Data Sources on page 42, the data required for the development of a pharmacokinetic model that describes the in vivo distribution of a radiolabelled MAb can be obtained from at least two sources. If the radiolabel can be shown to remain associated with the MAb, then following the time course of the activity in the patient will produce a valid model. Another source of data for kinetic modeling may be obtained from measurements of the MAb using RIA techniques to evaluate the immunoreactive component in the serum. This will assist the investigator to explore differences between the kinetics of the ^{99m}Tc label and those of the MAb. Additional data sources, such as gamma camera regions of interest, can be used to extend this simple modeling procedure to produce a more complex model to describe active uptake (or elimination) in separate organs.

Several assumptions were made prior to commencing the pharmacokinetic analysis of the radiolabelled MAb, both to simplify the analysis and in recognition of the fact that the only information available was that provided by the ^{99m}Tc label. Due to the short time of infusion (300 seconds for the murine and 30 seconds for the chimeric MAb) an iv bolus-input to the model was used. This was probably a valid assumption as the time course of the drug did not change appreciably during this short time interval. The other assumption was that all the radioactivity measured in the serum was assumed to be associated with the MAb. This implied that any metabolic moiety containing ^{99m}Tc was either excreted or internalized in tissue for sufficient time to allow the ^{99m}Tc to decay. Any transchelation of ^{99m}Tc-labelled MAb that might occur in organs such as the liver and kidneys was assumed to be removed from the general circulation.

5. EXPERIMENTAL RESULTS

No circulating antigens have yet been found for two of the MAbs used in this report[236,237]. The 170H.82 and 174H.64 MAbs are both directed against surface bound antigens. The other two MAbs studied in this report are MAbs B80.3 and B43.13, in which the antigen is both cell-surface bound and in general circulation. This section will include the experimental data obtained for these MAbs in both animal and patient studies.

5.1 MAb-170H.82

Organs demonstrating significant uptake of the MAb, as identified by RIS were noted and their corresponding activity calculated to 1) aid in the development of a multicompartmental model and 2) act as a source organ for radiation dosimetry measurements. Biodistribution patterns in the serum and urine were also measured and the immunoreactive component in the serum was measured using RIA techniques. The molecular weight of the ^{99m}Tc-labelled compound in serum was monitored by HPLC.

A pharmacokinetic model was developed for normal, non-tumor bearing rabbits and used to predict the in vivo biodistribution of MAb 170H.82 in that animal. Excreta were collected from the rabbits and used to estimate clearance profiles. Selected tissue samples were taken at necropsy to assist with image quantitation.

Kinetic data from six patients receiving different MAb dosages were collected and used to estimate the radiation doses received by patients arising from RIS procedures based on the ^{99m}Tc-170H.82 MAb.

5.1.1 Rabbit Kinetics

These data are organized into sections representing serum, excreta, tissue samples and gamma camera image information. All rabbits are uniquely identified by the letters 'SAM' followed by a two digit number.

Table 10: MAb 170H.82 serum activity measured as dpm/mL (1 x 10^6) and as a percentage of the injected dose (% ID) at various time intervals.

ID: SAM04 Dose: 340 MBq			ID: SAM06 Dose: 351 MBq			ID: SAM11 Dose: 406 MBq		
Time (h)	dpm/mL (1×10^6)	% ID	Time (h)	dpm/mL (1×10^6)	% ID	Time (h)	dpm/mL (1×10^6)	% ID
1.30	171	87.3	0.92	193	87.9	0.27	273	98.0
1.55	166	84.9	2.42	180	82.3	1.00	251	90.3
2.47	155	78.9	6.08	119	54.4	2.00	234	84.1
6.38	114	58.1	13.42	85.5	39.1	3.00	215	77.4
10.55	84.2	43.0	22.83	55.8	25.5	7.33	162	58.4
21.97	52.2	23.6	31.50	43.0	19.6	13.00	110	39.5
30.55	36.9	18.8	49.17	24.7	11.3	23.52	67.9	24.4
47.55	20.4	10.4				31.10	47.9	17.2
						44.52	25.1	9.0

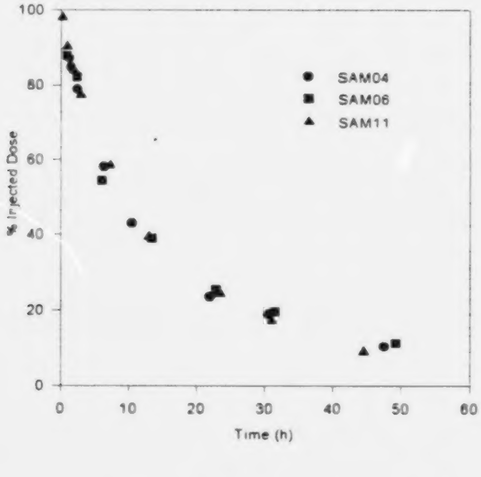

Figure 9: Rabbit serum profile following the iv. bolus administration of 170H.82 MAb.

The serum biodistribution of the radiolabelled MAb is presented in Table 10 and schematically shown in Figure 9 for each of the three rabbits tested. The data are expressed in dpm/mL serum and as a percentage of the injected dose for comparison between rabbits in this study and with the other two MAbs tested.

A pharmacokinetic model was developed to describe the biodistribution of the ^{99m}Tc-labelled compound in serum. The data were best represented by a two compartment model of the form $C(t)=C_1e^{-\lambda_1 t}+C_ze^{-\lambda_z t}$ with the constants describing this equation shown in Table 11 together with the mean and standard deviation. The half-lives are reported rather than the rate-constants in order to compare these data with the other MAbs tested. The rate-constants are easily obtained from the half-lives; where the distribution phase rate-constant, λ_1 is related to the distribution half-life, $T_{½1}$, by

$$\lambda_1 = \ln 2 / T_{½1} \tag{38}$$

A similar relationship exists for the terminal elimination phase rate-constant.

Table 11: Pharmacokinetic parameters representing a two compartment model of the form $C(t)=C_1e^{-\lambda_1 t}+C_ze^{-\lambda_z t}$ following the administration of ^{99m}Tc 170H.82.

Rabbit ID	C_1 % Inj. Dose	C_z % Inj. Dose	$T_{½1}$ (h)	$T_{½z}$ (h)	MRT (h)
SAM04	44.6 ± 2.6	55.2 ± 2.8	3.6 ± 0.4	19.7 ±0.8	25.5 ±0.6
SAM06	48.1 ± 7.4	51.7 ± 7.1	3.5 ±1.1	22.2 ±2.4	28.6 ±2.2
SAM11	28.9 ± 4.1	71.1 ± 4.5	3.3 ± 0.7	15.0 ±0.5	20.3 ±0.4
Mean	40.5 ± 5.9	59.3 ± 6.0	3.5 ± 0.7	19.0 ± 2.1	24.8 ± 2.4

5.1.1.1 Routes of Elimination

Urine and fecal samples were collected as described in the Materials and Methods Section and used to estimate ^{99m}Tc-170H.82 elimination patterns. As the rabbits practice coprophagy, it was difficult to analyze fecal samples; however, no recirculation patterns were observed in the serum kinetics and no bowel activity was observed on the gamma camera images. A limited amount of radioactivity was observed in feces and in the bile collected at necropsy (Table 17). It was therefore assumed that biliary excretion did not play a major role in the elimination of this MAb. Figure 11 documents the ^{99m}Tc activity in the fecal contents.

Renal excretion was found to be the major route of elimination for the ^{99m}Tc label with the data illustrated in Figure 10 (no data was available for SAM04). The labelled metabolites were not identified but were expected to be low molecular weight compounds such as glutathion or cysteine [238,239].

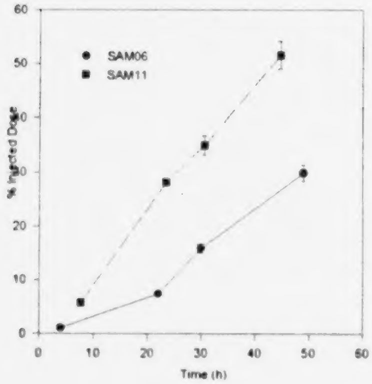

Figure 10: Renal elimination of ^{99m}Tc-170H.82 in rabbits.

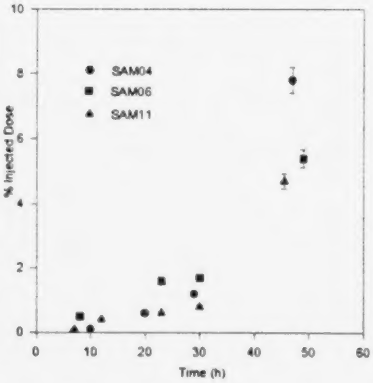

Figure 11: Cummulative fecal elimination of ^{99m}Tc-170H.82 in rabbits.

5.1.1.2 Gamma Camera Imaging

Gamma camera imaging was performed according to the protocol described above in the Experimental Methodology. The purpose of collecting image data was two-fold: 1) to test whether the two-compartment model obtained from the serum data could be expanded to include separate compartments for those organs demonstrating uptake as identified by RIS, and 2) to search for similarities between rabbit and human uptake patterns. If some degree of conformity were found between these two species, then the rabbit model could be applied to predict MAb distribution patterns in patients for future studies. It was also much easier to obtain additional rabbit data to model the biodistribution of ^{99m}Tc-170H.82 in greater detail than was possible in patients.

The image data in Table 12 through Table 14 tabulates the activity as % injected dose (%ID) and %ID/gm for the liver, heart and two kidneys where the time period was the time elapsed in hours post-injection. All values have been corrected for physical decay in order to better represent the biological distribution patterns of the labelled MAb.

Table 12: SAM04 organ activity in obtained from quantitative gamma camera imaging of ^{99m}Tc-170H.82.

Time (h)	Heart		Liver		Left Kidney		Right Kidney	
	%ID	%ID/gm	%ID	%ID/gm	%ID	%ID/gm	%ID	%ID/gm
0.00	13.2 ± 1.3	1.70 ± 0.16	27.1 ± 2.7	0.21 ± 0.02	3.74 ± 0.37	0.24 ± 0.02	3.01 ± 0.30	0.19 ± 0.02
0.25	11.5 ± 1.2	1.49 ± 0.15	30.3 ± 3.0	0.23 ± 0.02	3.58 ± 0.36	0.23 ± 0.02	2.84 ± 0.28	0.18 ± 0.02
0.50	11.5 ± 1.2	1.48 ± 0.15	29.2 ± 2.9	0.22 ± 0.02	3.60 ± 0.36	0.23 ± 0.02	2.84 ± 0.28	0.18 ± 0.02
0.75	11.8 ± 1.2	1.53 ± 0.15	28.5 ± 2.8	0.22 ± 0.02	3.68 ± 0.37	0.23 ± 0.02	3.09 ± 0.31	0.20 ± 0.02
1.00	11.3 ± 1.1	1.46 ± 0.15	29.2 ± 2.9	0.22 ± 0.02	3.80 ± 0.38	0.24 ± 0.02	3.30 ± 0.33	0.21 ± 0.02
1.25	11.3 ± 1.1	1.46 ± 0.15	28.4 ± 2.8	0.22 ± 0.02	4.02 ± 0.40	0.25 ± 0.03	3.48 ± 0.35	0.22 ± 0.02
1.50	11.0 ± 1.1	1.43 ± 0.14	27.3 ± 2.7	0.21 ± 0.02	4.15 ± 0.41	0.26 ± 0.03	3.63 ± 0.36	0.23 ± 0.02
1.75	12.1 ± 1.2	1.57 ± 0.16	26.9 ± 2.7	0.20 ± 0.02	4.28 ± 0.43	0.27 ± 0.03	3.99 ± 0.40	0.26 ± 0.03
2.00	11.4 ± 1.1	1.48 ± 0.15	28.1 ± 2.8	0.21 ± 0.02	4.65 ± 0.47	0.30 ± 0.03	4.28 ± 0.43	0.27 ± 0.03
2.25	10.5 ± 1.1	1.36 ± 0.14	27.9 ± 2.8	0.21 ± 0.02	4.43 ± 0.44	0.28 ± 0.03	3.98 ± 0.40	0.26 ± 0.03
10.70	3.5 ± 0.35	0.45 ± 0.05	15.0 ± 1.5	0.11 ± 0.01	4.11 ± 0.41	0.26 ± 0.03	3.57 ± 0.36	0.23 ± 0.02
21.14	2.5 ± 0.25	0.33 ± 0.03	12.9 ± 1.3	0.10 ± 0.01	2.49 ± 0.25	0.16 ± 0.02	3.88 ± 0.39	0.25 ± 0.02
29.42	2.0 ± 0.20	0.25 ± 0.03	11.0 ± 1.1	0.08 ± 0.01	2.06 ± 0.21	0.13 ± 0.01	3.26 ± 0.33	0.21 ± 0.02
47.01	1.0 ± 0.10	0.13 ± 0.01	6.9 ± 0.7	0.05 ± 0.01	1.43 ± 0.14	0.09 ± 0.01	1.65 ± 0.16	0.11 ± 0.01

Table 13: SAM06 organ activity in obtained from quantitative gamma camera imaging of ^{99m}Tc-170H.82.

Time (h)	Heart		Liver		Left Kidney		Right Kidney	
	%ID	%ID/gm	%ID	%ID/gm	%ID	%ID/gm	%ID	%ID/gm
0.25	5.68±0.57	0.73 ± 0.08	12.9 ±1.3	0.10 ± 0.01	1.78 ±0.18	0.11 ± 0.01	0.51 ± 0.05	0.03 ± 0.003
0.50	8.87±0.89	1.15 ± 0.12	15.8 ±1.6	0.12 ± 0.01	1.80 ±0.18	0.11 ± 0.01	0.54 ± 0.06	0.03 ± 0.003
0.75	5.15±0.52	0.67 ± 0.07	10.8 ±1.1	0.08 ± 0.01	1.89 ±0.19	0.12 ± 0.01	0.59 ± 0.06	0.04 ± 0.004
1.00	5.09±0.51	0.66 ± 0.07	12.4 ±1.3	0.09 ± 0.01	1.78 ±0.18	0.11 ± 0.01	0.66 ± 0.07	0.04 ± 0.004
1.25	5.03±0.51	0.65 ± 0.07	13.4 ±1.4	0.10 ± 0.01	2.14 ±0.22	0.14 ± 0.01	0.75 ± 0.08	0.05 ± 0.005
1.50	5.01±0.50	0.65 ± 0.07	12.3 ±1.3	0.09 ± 0.01	2.04 ±0.21	0.13 ± 0.01	0.90 ± 0.09	0.06 ± 0.006
1.75	4.31±0.43	0.56 ± 0.06	12.4 ±1.3	0.09 ± 0.01	2.03 ±0.21	0.13 ± 0.01	0.92 ± 0.09	0.06 ± 0.006
2.00	4.05±0.41	0.52± 0.06	12.4 ±1.3	0.09 ± 0.01	2.07 ±0.21	0.13 ± 0.01	0.81 ± 0.08	0.05 ± 0.005
2.25	4.17±0.42	0.54 ± 0.06	12.0 ±1.2	0.09 ± 0.01	2.09 ±0.21	0.13 ± 0.01	0.70 ± 0.07	0.04 ± 0.004
2.50	4.15±0.42	0.54 ± 0.06	11.9 ±1.2	0.09 ± 0.01	1.93 ±0.20	0.12 ± 0.01	0.80 ± 0.08	0.05 ± 0.005
2.75	4.05±0.41	0.52 ± 0.06	12.1 ±1.2	0.09 ± 0.01	1.86 ±0.19	0.12 ± 0.01	0.83 ± 0.09	0.05 ± 0.005
3.00	3.91±0.40	0.51 ± 0.05	12.1 ±1.2	0.09 ± 0.01	1.68 ±0.17	0.11 ± 0.01	0.76 ± 0.08	0.05 ± 0.005
7.70	0.87±0.10	0.11 ± 0.01	8.7 ±0.9	0.07 ± 0.01	1.92 ±0.19	0.12 ± 0.01	0.70 ± 0.07	0.05 ± 0.005
13.20	0.96±0.10	0.12 ± 0.01	9.8 ±1.0	0.07 ± 0.01	1.97 ±0.20	0.13 ± 0.01	0.71 ± 0.07	0.05 ± 0.005
22.57	1.40±0.14	0.18 ± 0.02	8.0 ±0.8	0.06 ± 0.01	1.66 ±0.17	0.11 ± 0.01	1.23 ± 0.13	0.08 ± 0.008
29.93	2.61±0.26	0.34 ± 0.04	8.4 ±0.9	0.06 ± 0.01	1.44 ±0.15	0.09 ± 0.01	1.68 ± 0.17	0.11 ± 0.01
49.30	2.83±0.29	0.37 ± 0.04	9.0 ±0.9	0.07 ± 0.01	1.62 ±0.17	0.10 ± 0.01	1.86 ± 0.19	0.12 ± 0.01

Table 14: SAM11 organ activity in obtained from quantitative gamma camera imaging of ^{99m}Tc-170H.82.

Time (h)	Heart		Liver		Left Kidney		Right Kidney	
	%ID	%ID/gm	%ID	%ID/gm	%ID	%ID/gm	%ID	%ID/gm
0.00	4.88 ± 0.49	1.01±0.10	15.3 ± 1.5	0.16 ± 0.02	2.00 ± 0.20	0.20 ± 0.02	0.60 ± 0.06	0.06 ± 0.01
0.17	4.62 ± 0.46	0.96±0.10	15.5 ± 1.6	0.17 ± 0.02	2.09 ± 0.21	0.21 ± 0.02	0.70 ± 0.07	0.07 ± 0.01
0.33	4.45 ± 0.44	0.92±0.09	15.3 ± 1.5	0.16 ± 0.02	2.19 ± 0.22	0.22 ± 0.02	0.81 ± 0.08	0.08 ± 0.01
0.50	4.23 ± 0.42	0.88±0.09	15.1 ± 1.5	0.16 ± 0.02	2.23 ± 0.22	0.22 ± 0.02	0.88 ± 0.09	0.09 ± 0.01
0.67	4.05 ± 0.40	0.84±0.08	15.1 ± 1.5	0.16 ± 0.02	2.34 ± 0.23	0.23 ± 0.02	0.96 ± 0.10	0.09 ± 0.01
0.83	3.90 ± 0.39	0.81±0.08	14.9 ± 1.5	0.16 ± 0.02	2.44 ± 0.24	0.24 ± 0.02	1.03 ± 0.10	0.10 ± 0.01
1.00	3.84 ± 0.38	0.80±0.08	14.5 ± 1.5	0.16 ± 0.02	2.47 ± 0.25	0.24 ± 0.02	1.12 ± 0.11	0.11 ± 0.01
1.17	3.78 ± 0.38	0.79±0.08	14.1 ± 1.4	0.15 ± 0.02	2.49 ± 0.25	0.25 ± 0.02	1.13 ± 0.11	0.11 ± 0.01
1.33	3.89 ± 0.39	0.81±0.08	13.5 ± 1.3	0.14 ± 0.01	2.61 ± 0.26	0.26 ± 0.03	1.13 ± 0.11	0.11 ± 0.01
1.50	3.78 ± 0.38	0.79±0.08	13.3 ± 1.3	0.14 ± 0.01	2.61 ± 0.26	0.26 ± 0.03	1.14 ± 0.11	0.11 ± 0.01
1.67	3.71 ± 0.37	0.77±0.08	13.3 ± 1.3	0.14 ± 0.01	2.67 ± 0.27	0.26 ± 0.03	1.18 ± 0.12	0.12 ± 0.01
1.84	3.73 ± 0.37	0.78±0.08	12.9 ± 1.3	0.14 ± 0.01	2.68 ± 0.27	0.27 ± 0.03	1.23 ± 0.12	0.12 ± 0.01
3.16	4.32 ± 0.43	0.90±0.09	10.9 ± 1.1	0.12 ± 0.01	2.71 ± 0.27	0.27 ± 0.03	1.32 ± 0.13	0.13 ± 0.01
7.11	3.05 ± 0.30	0.63±0.06	14.2 ± 1.4	0.15 ± 0.02	3.49 ± 0.35	0.35 ± 0.03	1.91 ± 0.19	0.19 ± 0.02
12.14	2.42 ± 0.24	0.50±0.05	8.3 ± 0.8	0.09 ± 0.01	3.08 ± 0.31	0.31 ± 0.03	1.73 ± 0.17	0.17 ± 0.02
23.15	1.65 ± 0.17	0.34±0.03	8.2 ± 0.8	0.09 ± 0.01	2.97 ± 0.30	0.29 ± 0.03	2.18 ± 0.22	0.22 ± 0.02
30.65	0.94 ± 0.09	0.20±0.02	6.6 ± 0.7	0.07 ± 0.01	2.69 ± 0.27	0.27 ± 0.03	1.92 ± 0.19	0.19 ± 0.02
44.33	0.67 ± 0.07	0.14±0.01	4.8 ± 0.5	0.05 ± 0.01	1.89 ± 0.19	0.19 ± 0.02	1.85 ± 0.18	0.18 ± 0.02

Pharmacokinetic models were developed for the heart and liver image data. Individual rate-constants were measured from the image data and were found to best fit a one (SAM06) or two (SAM04 AND SAM11) multicompartment model of the same type described by the serum data. The half-lives for the distribution and terminal elimination phases and the mean residence time (MRT) are shown in Table 15. Mean values for the two compartment model are shown in the last row.

Table 15: Organ kinetic parameters from quantitative RIS data of ^{99m}Tc-170H.82 in rabbits.

Rabbit ID	$T_{1/2\,1}$ (h)		$T_{1/2\,z}$ (h)		MRT (h)	
	Heart	Liver	Heart	Liver	Heart	Liver
SAM04	3.3 ± 1.1	3.8 ± 2.2	21.3 ± 4.4	31.8 ± 6.5	25.0± 3.7	43.4 ± 7.5
SAM06	N/A	N/A	26.0 ± 8.8	51.3 ± 2.3	37.5±2.6	74.0 ± 3.3
SAM11	0.3 ± 0.16	1.56 ± 0.5	16.8 ± 0.55	39.8 ± 5.1	24.2±0.75	56.4 ± 7.0
Mean (4&11)	1.80 ± 2.2	2.68 ± 1.6	19.1 ± 3.2	35.8 ± 5.7	24.6± 0.6	49.9 ± 9.2

The kidney kinetics appeared to follow a first-order absorption phase followed by an exponential elimination component. The best fit to the kidneys, as determined by the kinetic-modelling parameter-estimation program JANA, was indeed a first-order absorption phase followed by a single component terminal elimination. Due to varying degrees of bladder and liver overlap in the RIS images of the right kidney, only data from the left kidney was used in the development of a pharmacokinetic model. This was then assumed to represent both kidneys, as no significant differences were observed in the kidneys at necropsy. These data are presented in Table 16 and are represented by kinetic model parameters: absorption phase half-life ($T_{1/2\,a}$), the elimination phase half-life ($T_{1/2\,z}$) and the time to maximum uptake (T_{max}). For those cases when the model was unable to adequately fit a parameter, the term "N/A" was used.

Table 16: Kinetic parameters representing the biodistribution of ^{99m}Tc 170H.82 in the left kidney.

Rabbit ID	$T_{1/2\,a}$ (h)	$T_{1/2\,z}$ (h)	T_{max} (h)
SAM04	0.22 ± 0.06	22.3 ± 2.9	1.46 ± 0.35
SAM06	0.09 ± 0.02	130 ± 35	0.97 ± 0.17
SAM11	0.30 ± 0.13	N/A	1.10 ± 0.30
Mean	0.20 ± 0.11	N/A	1.18 ± 0.25

5.1.1.3 Tissue Sampling

After the final image, a 5 mL blood sample was obtained by cardiac puncture and the animal sacrificed by lethal injection as previously described. Tissue samples were obtained from all rabbits at necropsy and assayed for ^{99m}Tc levels. This information is presented in Table 17 with organ values expressed as % injected dose/gm with the mean and standard deviation for each organ presented in the final column. The mean values for each organ were decay corrected to 48 hours, to facilitate comparison with the other MAbs.

Table 17: Rabbit tissue sample data for ^{99m}Tc-170H.82.

Tissue Sample	SAM04 KBq/gm % ID/gm x 10^{-4} t = 47.5 h	SAM06 KBq/gm % ID/gm x 10^{-4} t = 49.3 h	SAM11 KBq/gm % ID/gm x 10^{-4} t = 45.5 h	Mean ± Std.Dev % ID/gm x 10^{-4} t = 48 h
Liver	2.18	1.65	2.78	2.38 ± 0.71
Spleen	1.25	0.84	2.43	1.32 ± 0.45
Heart	0.92	0.72	1.39	0.91 ± 0.12
Right Kidney	4.94	3.16	9.90	5.23 ± 2.0
Left Kidney	4.88	3.19	10.3	5.32 ± 2.2
Gall Bladder	2.60	2.66	1.96	2.32 ± 0.80
Bile	2.07	2.84	0.66	1.9 ± 1.4
Muscle	0.045	0.085	0.21	0.1 ± 0.06
Lung	N/A	N/A	2.17	N/A

5.1.2 Patient Kinetics

A two-compartment model representing the distribution of ^{99m}Tc labelled 170H.82 was constructed using data obtained from six patients diagnosed with primary or metastatic breast cancer. Approximately 20 mL of normal saline containing 1, 2 or 4 mg of 170H.82 was infused iv into each patient over a period of 5 minutes. Serum samples were collected at selected time intervals up to 48 hours post-injection and urine samples collected in six hour intervals up to 72 hours post injection. All samples were counted in a multi-sample gamma counter and compared against a standard of known activity. The raw-counts obtained from the gamma counter were decay corrected and converted to a per cent of the injected dose using the spreadsheet QPRO. These results are shown in Table 18 to Table 23 and graphically summarized in Figure 12 (serum) and Figure 13 (urine). All reported values are estimated to have an associated error of 10%.

Table 18: Patient data (E196766) following the injection of 1 mg of ^{99m}Tc-170H.82.

ID: E196766 Time (hours)	Serum x 10^6 dpm/mL	% Injected Dose	Urine Time (hours)	Progressive Elimination %
0.33	28.7	97.8	2.2	1.9
10.80	26.2	89.4	8.0	11.1
2.08	25.4	86.5	14.0	14.3
3.67	22.7	77.5	20.0	18.7
5.75	19.6	66.8	26.0	20.2
24.42	11.1	38.0	32.0	23.0
28.25	10.4	35.4	38.0	26.2
48.50	7.0	23.7	50.0	27.1
			56.0	28.2
			62.0	29.4
			73.0	31.9

Table 19: Patient data (E185902) following the injection of 1mg of ^{99m}Tc-170H.82.

ID: E185902 Time (hours)	Serum x 10^6 dpm/mL	% Injected Dose	Urine Time (hours)	Progressive Elimination %
0.27	30.7	97.3	9.10	4.2
1.10	29.4	93.2	15.10	7.1
2.52	29.1	92.1	21.10	8.2
4.18	27.1	85.8	27.10	9.0
6.10	22.9	72.5	33.10	11.1
25.68	14.8	47.0	39.10	12.0
29.43	13.3	42.5	51.10	14.2
49.35	9.2	29.2	57.10	18.8
			63.10	20.0
			71.60	20.8

Table 20: Patient data (E193637) following the injection of 1 mg of ^{99m}Tc-170H.82.

ID: E193637 Time (hours)	Serum x 10^6 dpm/mL	% Injected Dose	Urine Time (hours)	Progressive Elimination %
0.58	26.7	80.5	70.8	4.5
1.33	28.9	87.2	13.08	8.8
2.17	29.2	88.2	19.08	10.8
3.18	26.5	79.8	25.08	13.7
5.95	22.4	67.7	31.08	15.9
23.73	14.8	44.8	37.08	17.5
27.48	13.0	39.1	43.08	18.5
49.15	9.3	28.1	49.08	20.8
			55.08	22.7
			61.08	24.0
			67.08	25.1
			73.08	26.6

Table 21: Patient data (E179268) following the injection of 2mg of ^{99m}Tc-170H.82.

E179268 Time (hours)	Serum x 10^6 dpm/mL	% Injected Dose	Urine Time (hours)	Progressive Elimination %
0.25	38.6	96.1	7.67	8.3
1.25	37.8	94.2	13.67	16.3
2.42	31.4	78.1	25.67	22.9
4.25	27.3	68.0	31.67	25.0
5.60	28.0	69.7	37.67	27.4
23.80	15.9	39.5	49.67	30.2
26.80	14.9	37.0	55.67	32.8
52.00	9.7	24.0	61.67	34.2
			71.67	36.2

Table 22: Patient data (E191358) following the injection of 4 mg of ^{99m}Tc-170H.82.

ID: E191358 Time (hours)	Serum x 10^6 dpm/mL	% Injected Dose	Urine Time (hours)	Progressive Elimination %
0.35	32.0	97.7	8.75	10.0
1.08	29.9	91.4	14.75	14.5
2.17	29.4	89.8	20.75	16.8
4.42	22.9	69.9	26.75	20.9
6.33	22.3	68.0	32.75	23.1
25.42	10.3	31.3	38.75	25.2
28.37	8.3	25.3	44.75	25.7
49.17	4.2	15.8	50.75	28.1
			56.75	29.5
			62.75	30.9
			68.75	31.2
			71.75	32.6

Table 23: Patient data (E192473) following the injection of 4 mg ^{99m}Tc-170H.82.

ID: E192473 Time (hours)	Serum x 10^6 dpm/mL	% Injected Dose	Urine Time (hours)	Progressive Elimination %
0.33	36.6	91.4	7.67	7.3
1.25	37.3	93.1	13.67	16.3
2.08	35.7	89.0	25.67	21.8
3.83	28.6	71.3	31.67	23.6
5.92	24.9	62.3	37.67	26.2
24.75	13.2	33.1	49.67	29.6
28.92	11.5	28.8	55.67	32.1
48.00	8.5	21.3	61.67	34.1
			73.67	36.9

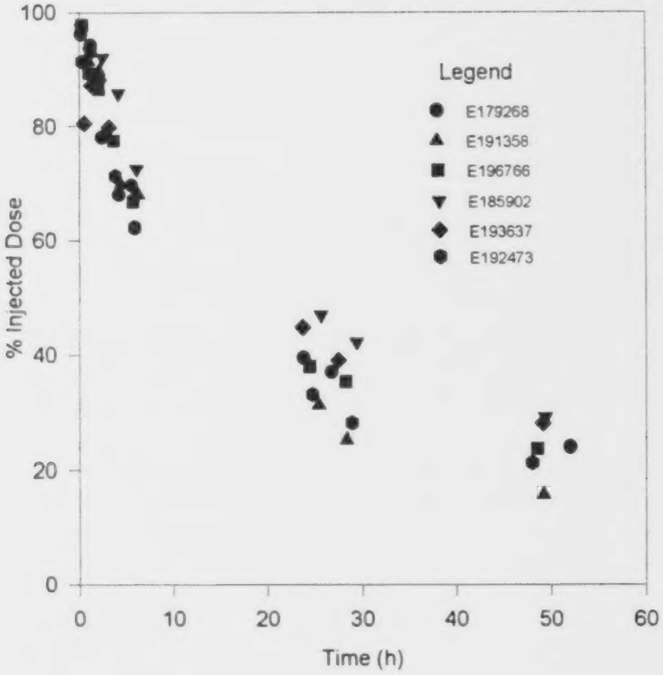

Figure 12: Variation with time of ^{99m}Tc-170H.82 serum levels expressed as a percentage of the injected dose.

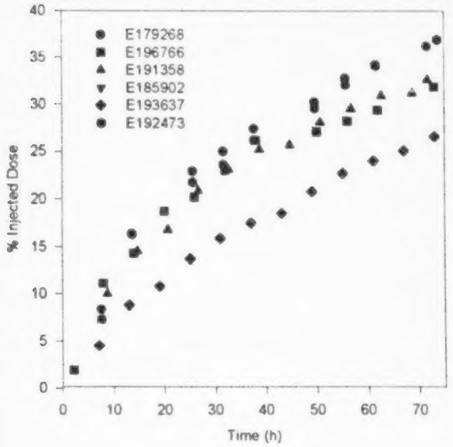

Figure 13: Renal excretion following the i.v. administration of ^{99m}Tc-170H.82.

Several assumptions were made prior to commencing a pharmacokinetic analysis, both to simplify the analysis and in recognition of the fact that the only information used in this model was that provided by the ^{99m}Tc label.

1. Due to the relatively short time interval of infusion (approximately 5 minutes), an iv bolus input to the model was used.
2. All the radioactivity measured in the serum was assumed to be associated with the MAb.
3. Any transchelation of ^{99m}Tc that might occur (liver or kidney) was assumed to be removed from the general circulation.
4. No attempt has been made to resolve the different clearance rates between the serum and urine data. However, one may speculate that this difference is due in part to tissue binding of the transchelated ^{99m}Tc onto cysteine or glutathion.
5. Gamma camera images revealed that patient E191358 (4 mg) had an increased level of ^{99m}Tc liver uptake with a concomitant increase in plasma clearance. As all the other patients in this group

showed no abnormal liver uptake, the last row in Table 24 contains the kinetic summary with this patient removed.

The results from the non-linear fitting analysis of the serum data in Table 18 to Table 23 could be best fit by the two-compartment model of the form:

$$C(t) = C_1 e^{-\lambda_1 t} + C_z e^{-\lambda_z t} \tag{39}$$

as described earlier. The volume of distribution for all data sets was approximately equal to the blood volume, within experimental error.

A summary of parameters representing coefficients from equation 39 that describe the ^{99m}Tc serum kinetics, the plasma clearance and renal clearance are presented in Table 24 together with the average value of the standard error terms. The error terms are only approximate as they are based upon a linearization of a nonlinear model. The half-lives are reported rather than the rate-constants in order to make a more meaningful comparison between the different MAbs tested. Statistical analyses were performed using either SPSS or PCNONLIN.

Table 24: Pharmacokinetic parameters obtained from a two compartment model representing the biodistribution of ^{99m}Tc-170H.82.

Patient ID	Dose (mg)	C_1 (% Inj. dose)	C_z (% Inj. dose)	$t_{½1}$ (h)	$t_{½z}$ (h)	MRT (h)	Plasma Clearance (mL/h)	Renal Clearance (mL/h)
E185902	1	26.5±9.6	73.5±10	5.1±2.9	37.4±6.9	51.7±8.0	66.6±5.3	15.4±0.8
E193637	1	35.4±7.2	64.0±5.9	3.5±1.5	41.4±6.3	57.2±8.0	63.7±4.9	23.6±1.2
E196766	1	39.8±2.8	60.1±2.7	3.8±0.5	36.4±2.3	49.4±2.8	78.8±2.3	33.8±1.7
Mean (1 mg)		**33.9±6.5**	**65.9±6.3**	**4.1±1.6**	**38.4±5.2**	**52.8±6.3**	**69.7±4.2**	**24.3±1.2**
E179268	2	40.6±6.6	59.4±5.7	3.2±0.9	39.6±5.6	54.3±7.1	64.4±4.5	33.4±1.7
E192473	4	60±5.6	49±3.4	4.6±1.3	43.3±12	56.3±14	69.4±8.7	36.3±1.8
E191358	4	51.8±17	48.1±19	5.9±3.0	29.7±9.9	36.9±8.6	116±11	42.5±2.1
Mean (All)		42.4±8.1	59.1±7.8	4.4±1.7	38.0±7.2	51.0±8.1	76.5±6.1	30.8±1.6
Mean All except E191358		**40.5±6.4**	**61.3±5.5**	**4.0±1.4**	**39.6±6.6**	**53.8±8.0**	**68.6± 5.1**	**28.5±1.4**

5.1.2.1 HPLC Analysis

In an attempt to determine whether or not the ^{99m}Tc labelled compound observed in the serum represented intact MAbs, or lower molecular weight fragments, size-exclusion high performance liquid chromatography (SEC-HPLC) radiochromatographic analyses were performed on selected samples. Using the method as described in the Materials and Methods Section, the molecular weight associated with the ^{99m}Tc was estimated using both UV (280 nm) and radioactivity data. An in-line NaI(Tl) radiation detector was used for all radiochromatograms (data points every 5 seconds) except for the 18 hour serum and urine samples, where one minute fractions were collected and analyzed separately in a well-type gamma counter. Data is presented for patient E211438.

The pre-injection ^{99m}Tc-170H.82 labelled kit is shown in Figure 14 where the retention time for the intact MAb was approximately 8.6 minutes for the UV peak and 8.8 minutes for the associated ^{99m}Tc peak. The later UV peaks in Figure 14 are due to the buffers used in the kit. Figure 15 and Figure 16 illustrate serum samples obtained at 1 hour and 18 hours post-injection, respectively. The 1 hour serum sample indicated mainly intact ^{99m}Tc labelled MAb present with a small ^{99m}Tc peak at 14.3 minutes (0.8%). A small amount (≈7%) of aggregated MAb was observed at 7.6 minutes. The early peak in the 18 hour serum sample correlates with that of the intact MAb and the latter two peaks (at 13 and 15 minutes) had similar retention times as those observed in the 18 hour urine radiochromatogram (Figure 17). These two low molecular weight ^{99m}Tc peaks observed in the 18 hour serum sample accounted for approximately 55% of the total radioactivity. Although a 24 hour sample from another patient revealed similar low molecular weight ^{99m}Tc peaks, they only accounted for 8% of the total radioactivity.

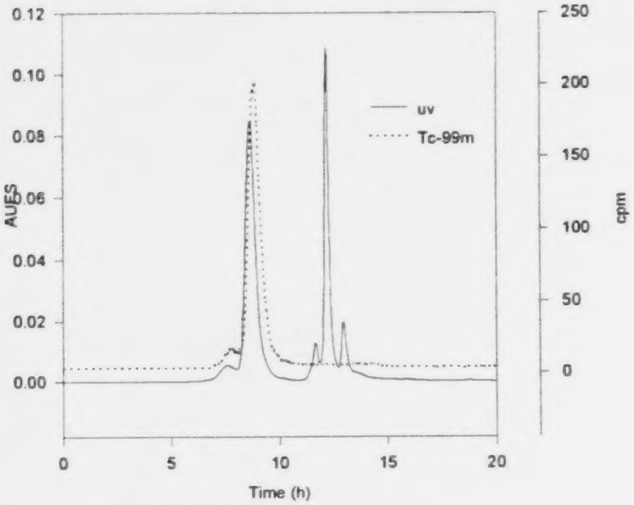

Figure 14: HPLC of ^{99m}Tc labelled MAb 170H.82; pre-injection kit.

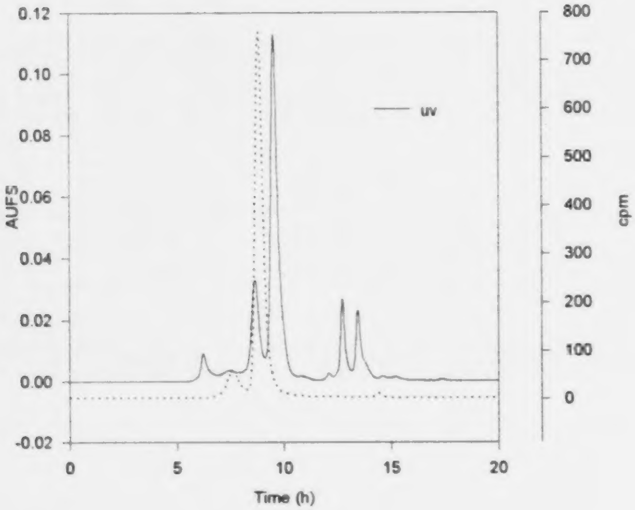

Figure 15: HPLC of ^{99m}Tc labelled MAb 170H.82; serum - 1 hr post-injection.

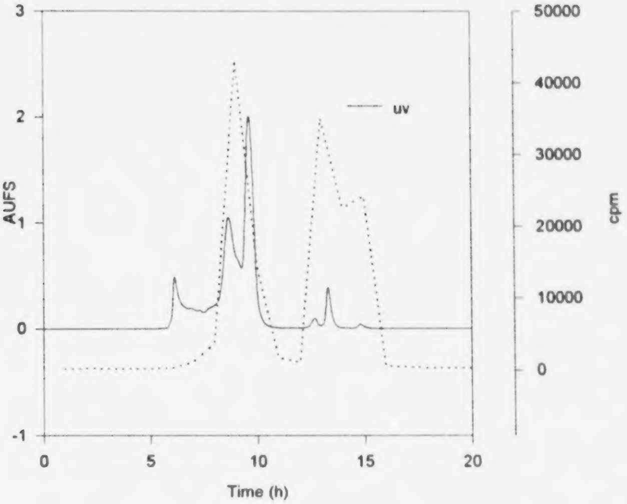

Figure 16: HPLC of ^{99m}Tc labelled MAb 170H.82; serum - 18 hr post-injection.

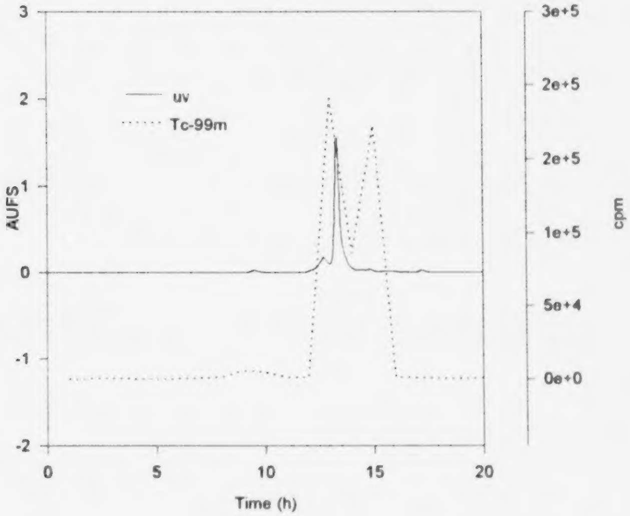

Figure 17: HPLC of ^{99m}Tc labelled MAb 170H.82; urine - 18 hr post-injection.

In an attempt to verify the existence these ^{99m}Tc labelled lower molecular weight compounds observed in the 18 - 24 hour serum samples, instant thin-layer chromatography (ITLC: 85% methanol, 15% water) was used to estimate ^{99m}Tc-labelled protein-bound fractions in a 23 hour serum sample from a third patient. While the majority of the labelled material remained at the origin as expected for a labelled protein, as much as 20% of the activity was observed both at the 6-7 cm mark and at the solvent front (12 cm run length).

5.1.2.2 Radioimmunoassay:MAb-170H.82

The pharmacokinetics described above are based upon the assumption that the ^{99m}Tc is bound to the MAb and that one can infer the serum kinetics of the MAb by radioactivity measurements. However, it has been postulated that the ^{99m}Tc label is transchelated in the body, principally by the kidneys and liver[240]. It thus becomes necessary to obtain an independent assessment of the radiolabelled MAb.

The radioimmunoassay (RIA) technique (described in the previous chapter) was adapted from an assay developed by Biomira Inc. and was used to quantitate the MAb in the serum. This technique relied only on binding of the immunoreactive component of the MAb and so could be applied over a much longer time interval following injection. Typically, data were obtained from patients up to two to three months post-injection. Table 25 contains data from two patients, where the serum MAb-170H.82 levels have been normalized to the highest concentration, which was taken to represent 100% of the injected dose.

Table 25: Patient RIA data following the i.v. administration of ^{99m}Tc-170H.82.

ID: E193637 Time (hours)	Serum 170 % Inj Dose	ID: E185902 Time (hours)	Serum 170 % Inj Dose
0.6	88.0 ± 13.2	0.3	100.0 ± 17.1
1.3	100.0 ± 20.8	1.1	86.2 ± 21.2
2.2	75.9 ± 26.1	2.5	92.9 ± 8.0
3.2	59.5 ± 24.8	4.2	79.3 ± 22.4
5.9	78.3 ± 13.5	6.1	75.9 ± 5.9
23.7	61.6 ± 8.7	25.7	56.7 ± 20.8
27.5	51.7 ± 9.0	29.4	49.8 ± 4.5
49.2	38.3 ± 6.9	49.3	36.9 ± 7.0
504	17.0 ± 2.0	192.3	6.2 ± 2.1
912	2.7 ± 1.8	384.3	1.0 ± 0.6

In order to visualize the relationship between the RIA and ^{99m}Tc label, data are presented graphically in Figure 18 for the two patients described in Table 25. The data are plotted only over the time period where the RIA and ^{99m}Tc data overlap (0 to 50 h).

The RIA data were analyzed with PCNONLIN and found to yield a two or three-compartment model with a bolus-type input. The appropriate kinetic constants are shown in Table 26. As illustrated in Figure 18, the radioactivity data and RIA data are in agreement with each other where their sampling times overlap.

Table 26: Pharmacokinetic parameters obtained from the 170H.82 RIA data.

Patient ID	t½$_1$	t½$_2$	t½$_z$	MRT
E185902	0.31 ± 0.21	29.3 ± 3.3	76.6 ± 3.5	83.8 ± 0.7
E193637	0.61 ± 0.96	225 ± 23	N/A	322 ± 33

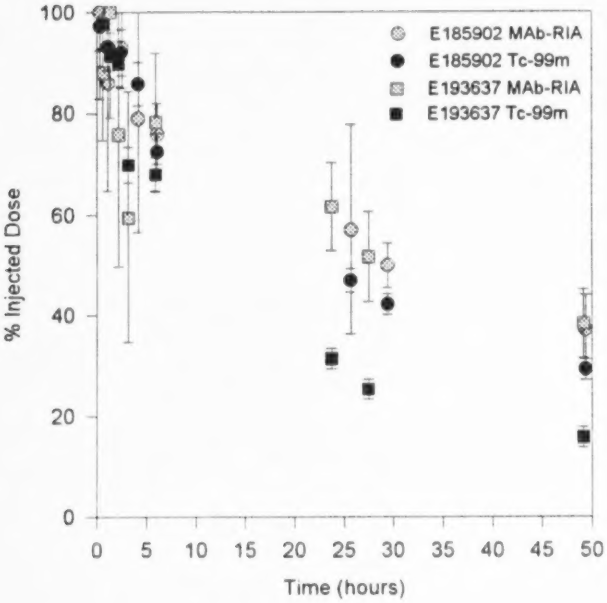

Figure 18: Serum ^{99m}Tc-170H.82 overlaid with the immunoreactive component of the MAb as identified by RIA.

5.1.2.3 Dosimetry

Standard MIRD formulations, as discussed in detail in previous sections, were used to estimate the radiation dose to patients receiving 1 mg, 2 mg and 4 mg doses of ^{99m}Tc labelled monoclonal antibody, 170H.82. The accumulation of the radiolabelled monoclonal antibodies were observed in several organs as identified by gamma camera imaging. Regions of interest (ROI) were drawn around these organs and used to develop time-activity curves for the liver, heart and kidney. The radiation dose was calculated using Quattro Pro for Windows using as source organs: the liver, kidneys, heart, the 'remainder of the body', and a dynamic bladder model. A summary of these data are reproduced in the table below.

Table 27: Mean radiation dose estimates following the administration of ^{99m}Tc-170H.82 for each target organ over all dosage levels.

Target Organs	(1 mg) E185902 mrad/mCi	(1 mg) E196766 mrad/mCi	(1 mg) E193637 mrad/mCi	(2 mg) E179268 mrad/mCi	(4 mg) E191358 mrad/mCi	(4 mg) E192473 mrad/mCi	Combined Mean mrad/mCi
Adrenals	42.0	39.2	43.1	45.7	45.2	43.9	43.2 ± 2.4
Brain	19.4	16.8	19.2	17.9	18.2	19.9	18.6 ± 1.1
Breasts	20.8	18.0	21.4	19.7	20.5	20.4	20.1 ± 1.2
GB Wall	49.4	44.2	51.0	53.1	53.4	50.7	50.3 ± 3.4
LLI	29.3	27.7	30.4	30.4	29.4	33.7	30.1 ± 2.0
Sml Int	32.3	29.6	32.8	33.0	32.5	35.0	32.5 ± 1.7
Stomach	33.6	30.0	34.1	33.4	33.8	34.4	33.2 ± 1.6
ULI	34.0	30.9	34.5	34.7	34.4	36.3	34.1 ± 1.8
Heart Wall	99.8	84.4	113.3	90.2	105.1	79.7	95.4 ± 12.
Kidney	107.5	143.2	110.0	175.0	145.4	145.9	137.8 ± 25.4
Liver	94.3	82.2	101.2	110.9	113.3	93.4	99. ± 11.7
Lungs	33.7	29.3	35.0	32.7	34.2	32.6	32.9 ± 2.0
Muscle	24.0	21.6	24.4	23.8	23.8	25.2	23.8 ± 1.2
Ovaries	31.5	29.6	32.7	32.6	31.7	35.6	32.3 ± 2.0
Pancreas	42.1	38.2	43.2	44.1	44.2	43.2	42.5 ± 2.3
Red Marr	27.1	24.3	27.4	26.8	26.8	28.3	26.8 ± 1.3
Bone Surf	43.1	38.3	43.5	42.0	42.4	44.6	42.3 ± 2.2
Skin	15.5	13.7	15.5	14.9	15.0	16.0	15.1 ± 0.8
Spleen	31.9	30.1	32.2	33.7	32.9	34.0	32.4 ± 1.4
Thymus	33.5	28.8	35.1	30.9	33.1	31.4	32.1 ± 2.2
Thyroid	24.4	21.1	24.3	22.6	23.1	24.8	23.4 ± 1.4
UB Wall	48.7	83.7	74.6	103.1	77.6	118.4	84.4 ± 24.
Uterus	31.7	32.0	34.1	35.8	33.4	39.7	34.4 ± 3.0
Tot Body	27.3	24.7	28.0	27.7	27.8	28.6	27.4 ± 1.4

5.2 MAb-m174H.64

Biodistribution patterns for both the murine and chimeric forms of the ^{99m}Tc-174H.64 MAb were measured in rabbits and patients. A pharmacokinetic model was developed for normal, non-tumor bearing rabbits and used to predict the in vivo biodistribution of ^{99m}Tc-174H.64 in that animal. Excreta were collected from the rabbits and used to estimate clearance profiles. Selected tissue samples were taken at necropsy to assist with image quantitation and aid in the development of a dosimetric model.

Serum ^{99m}Tc data from three patients, receiving 2 mg of the murine ^{99m}Tc-174H.64 and seven patients receiving the 1 mg chimeric form were collected and the results analyzed and compared with the rabbit data. There was insufficient image data for the murine and chimeric forms of the ^{99m}Tc-174H.64 to develop a radiation dosimetric model.

5.2.1 Rabbit Kinetics

The data are organized into sections representing serum, excreta, tissue samples and gamma camera image information. All rabbits are uniquely identified by the letters 'SAM' followed by a two digit number. Rabbit kinetics for the chimeric form of this MAb are presented in the following section.

Table 28: MAb 174H.64 serum activity in rabbits measured as dpm/mL (1 x 10^6) and as a percentage of the injected dose (% ID) at various time intervals.

ID: SAM12 Dose: 379 MBq			ID: SAM13 Dose: 403 MBq			ID: SAM14 Dose: 306 MBq		
Time (h)	dpm/mL (1×10^6)	% ID	Time (h)	dpm/mL (1×10^6)	% ID	Time (h)	dpm/mL (1×10^6)	% ID
0.33	266	97.5	0.15	215	98.1	0.52	196	90.7
1.00	219	80.5	0.57	187	85.3	1.02	196	90.6
2.42	199	73.2	1.15	175	79.6	2.10	169	78.1
3.42	181	66.3	2.23	172	78.1	3.10	158	73.0
6.17	130	47.7	3.15	158	72.0	5.47	119	55.3
11.67	76.3	28.0	5.82	118	53.5	10.18	71.5	37.7
21.47	46.8	17.2	10.73	75.0	34.2	21.77	44.6	20.7
25.58	40.4	14.8	20.57	42.0	19.1	29.25	31.7	14.7
29.80	33.0	12.1	29.28	27.9	12.7	48.85	16.6	7.7
45.13	17.4	6.4	46.63	16.0	7.3			

The serum biodistribution of the radiolabelled MAb is presented in Table 28 and schematically shown in Figure 19 for each of the three rabbits tested. The data is expressed in dpm/mL serum and as a percentage of the injected dose for comparison between rabbits in this study and with the other two MAbs tested.

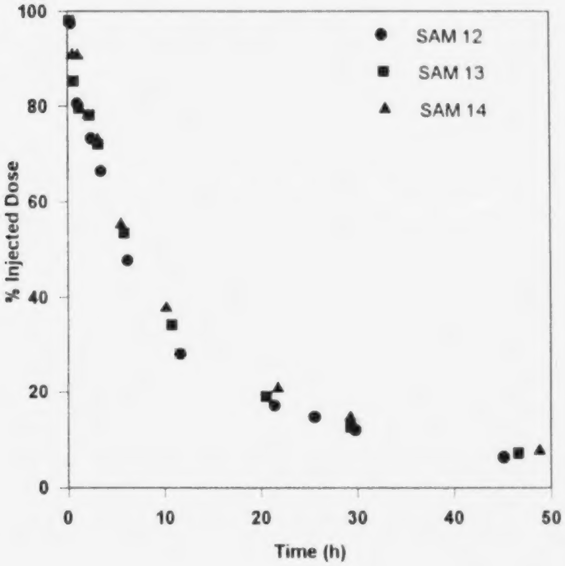

Figure 19: Rabbit serum profile following the iv. bolus administration of ^{99m}Tc 174H.64 MAb.

A pharmacokinetic model was developed to describe the biodistribution of the ^{99m}Tc-labelled compound in serum. The data were best represented by a two compartment model of the form $C(t) = C_1 e^{-\lambda_1 t} + C_2 e^{-\lambda_2 t}$ with the constants describing this equation shown in Table 29 together with the mean and standard deviation. The half-lives are reported rather than the rate-constants to aid in the comparison between the different MAbs tested.

Table 29: Pharmacokinetic parameters representing a two compartment model of the form $C(t) = C_1 e^{-\lambda_1 t} + C_2 e^{-\lambda_2 t}$ following the administration of ^{99m}Tc 174H.64.

Rabbit ID	C_1 dpm/mL	C_2 dpm/mL	$T_{1/2 1}$ (h)	$T_{1/2 2}$ (h)	MRT (h)
SAM12	28.9 ± 4.1	71.1 ± 4.4	3.4 ± 0.55	17.6 ± 1.7	20.4 ± 1.2
SAM13	70.4 ± 6.3	25.0 ± 7.0	5.1 ± 0.74	25.7 ± 5.9	26.4 ± 4.0
SAM14	61.2 ± 3.4	38.2 ± 3.7	3.9 ± 0.57	20.0 ± 1.6	23.8 ± 1.2
Mean	53.5 ± 21.8	44.8 ± 23.8	4.1 ± 0.87	21.1 ± 4.2	23.5 ± 3.0

5.2.1.1 Routes of Elimination

Urine and fecal samples were collected as described previously and used to estimate ^{99m}Tc-174H.64 elimination patterns. As the rabbits practice coprophagy it was difficult to analyze fecal samples; however, no recirculation patterns were observed in the serum kinetics and no bowel activity was observed on the gamma camera images. A limited amount of radioactivity was observed in the feces and in the bile collected at necropsy (Table 34) but was not significant when compared with the overall amount of activity injected. It was therefore assumed that biliary excretion did not play a major role in the elimination of this MAb. Figure 20 illustrates the ^{99m}Tc activity in the fecal contents. Figure 11 documents the ^{99m}Tc activity in the fecal contents.

Renal excretion was found to be the major route of elimination for the ^{99m}Tc label (Figure 21). The labelled metabolites were not identified but were expected to be low molecular weight compounds, possibly glutathion or cysteine.

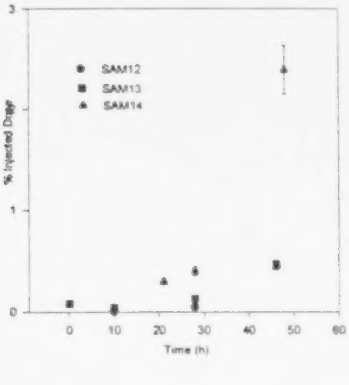

Figure 20: Cumulative fecal elimination of ^{99m}Tc labelled MAb 174H.64 in rabbits.

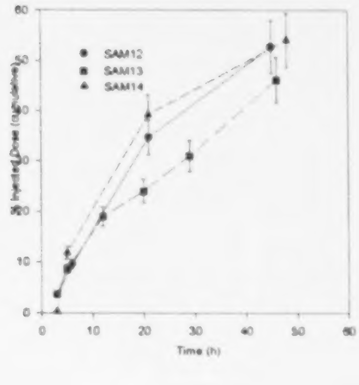

Figure 21: Cumulative urine excretion of ^{99m}Tc labelled MAb 174H.64 in rabbits.

5.2.1.2 Gamma Camera Imaging

Gamma camera imaging was performed according to the protocol described above in the Experimental Methodology section. The purpose of collecting image data was two-fold: 1) to test whether the two-compartment model obtained from the serum data could be expanded to include separate compartments for those organs demonstrating uptake as identified by RIS, and 2) to search for similarities between rabbit and human uptake patterns. If some degree of conformity were found between these two species, then the rabbit model could be applied to predict MAb distribution patterns in patients for future studies. The image data in Table 30 through Table 32 tabulates the activity as the % injected dose (%ID) and %ID/gm for the liver, heart and two kidneys over the time period of the study, where the time is measured in hours post-injection. All values have been corrected for physical decay in order to represent the biological distribution patterns of the labelled MAb.

Table 30: SAM 12 organ activity obtained from quantitative RIS of ^{99m}Tc-174H.64 expressed as a percentage of the injected dose (%ID).

Time (h)	Heart		Liver		Left Kidney		Right Kidney	
	%ID	%ID/gm	%ID	%ID/gm	%ID	%ID/gm	%ID	%ID/gm
0.35	7.30 ± 0.7	1.71 ± 0.17	24.1 ± 2.4	0.29 ± 0.03	1.76 ± 0.2	0.25 ± 0.02	1.97 ± 0.2	0.28 ± 0.03
0.52	6.63 ± 0.7	1.55 ± 0.15	24.0 ± 2.4	0.29 ± 0.03	1.97 ± 0.2	0.28 ± 0.03	2.22 ± 0.2	0.32 ± 0.03
0.68	5.93 ± 0.6	1.39 ± 0.14	23.6 ± 2.4	0.28 ± 0.03	2.10 ± 0.2	0.29 ± 0.03	2.43 ± 0.2	0.35 ± 0.03
0.85	6.90 ± 0.7	1.61 ± 0.16	23.2 ± 2.3	0.28 ± 0.03	1.90 ± 0.2	0.27 ± 0.03	2.29 ± 0.2	0.33 ± 0.03
1.02	5.37 ± 0.5	1.26 ± 0.13	22.7 ± 2.3	0.27 ± 0.03	2.37 ± 0.2	0.33 ± 0.03	2.79 ± 0.3	0.40 ± 0.04
1.18	5.13 ± 0.5	1.20 ± 0.12	22.0 ± 2.2	0.26 ± 0.03	2.81 ± 0.3	0.39 ± 0.04	3.05 ± 0.3	0.44 ± 0.04
1.35	4.91 ± 0.5	1.15 ± 0.11	21.2 ± 2.1	0.25 ± 0.03	3.04 ± 0.3	0.42 ± 0.04	3.26 ± 0.3	0.46 ± 0.05
1.52	4.84 ± 0.5	1.13 ± 0.11	21.0 ± 2.1	0.25 ± 0.03	3.12 ± 0.3	0.44 ± 0.04	3.36 ± 0.3	0.48 ± 0.05
1.68	4.69 ± 0.5	1.09 ± 0.11	20.2 ± 2.1	0.25 ± 0.02	3.37 ± 0.3	0.47 ± 0.05	3.59 ± 0.4	0.51 ± 0.05
1.85	4.46 ± 0.5	1.04 ± 0.10	20.8 ± 2.1	0.25 ± 0.02	3.66 ± 0.4	0.51 ± 0.05	3.85 ± 0.4	0.55 ± 0.05
2.02	4.27 ± 0.4	1.00 ± 0.10	20.5 ± 2.0	0.25 ± 0.02	3.63 ± 0.3	0.51 ± 0.05	3.81 ± 0.4	0.54 ± 0.05
2.18	4.09 ± 0.4	0.95 ± 0.10	20.2 ± 2.0	0.24 ± 0.02	3.20 ± 0.3	0.45 ± 0.04	3.26 ± 0.3	0.47 ± 0.05
3.19	3.57 ± 0.4	0.83 ± 0.08	12.3 ± 1.2	0.15 ± 0.01	3.57 ± 0.4	0.50 ± 0.05	3.98 ± 0.4	0.57 ± 0.06
5.84	3.58 ± 0.4	0.84 ± 0.08	10.4 ± 1.0	0.12 ± 0.01	4.03 ± 0.4	0.56 ± 0.06	3.22 ± 0.3	0.46 ± 0.05
10.93	1.75 ± 0.2	0.41 ± 0.04	8.0 ± 0.8	0.10 ± 0.01	3.63 ± 0.4	0.51 ± 0.05	3.91 ± 0.4	0.56 ± 0.06
21.42	1.49 ± 0.2	0.35 ± 0.03	6.5 ± 0.7	0.08 ± 0.01	4.34 ± 0.4	0.61 ± 0.06	4.21 ± 0.4	0.60 ± 0.06
29.77	1.02 ± 0.1	0.24 ± 0.02	5.6 ± 0.6	0.07 ± 0.01	3.27 ± 0.3	0.46 ± 0.05	4.09 ± 0.4	0.58 ± 0.06
44.62	0.86 ± 0.1	0.20 ± 0.02	4.4 ± 0.5	0.06 ± 0.01	3.35 ± 0.3	0.47 ± 0.05	3.13 ± 0.3	0.45 ± 0.04

Table 31: SAM 13 organ activity in obtained from quantitative RIS of ^{99m}Tc-174H.64 expressed as a percentage of the injected dose (%ID).

Time (h)	Heart		Liver		Left Kidney		Right Kidney	
	%ID	%ID/gm	%ID	%ID/gm	%ID	%ID/gm	%ID	%ID/gm
0.00	5.50 ± 0.5	3.11 ± 0.31	17.4± 1.7	0.21 ± 0.02	3.11 ± 0.31	0.43 ± 0.04	2.37 ± 0.24	0.34 ± 0.03
0.17	5.35 ± 0.5	3.05 ± 0.31	16.7 ± 1.7	0.20 ± 0.02	3.05 ± 0.31	0.43 ± 0.04	2.61 ± 0.26	0.37 ± 0.04
0.33	5.04 ± 0.5	3.21 ± 0.32	16.5 ± 1.6	0.20 ± 0.02	3.21 ± 0.32	0.45 ± 0.04	2.84 ± 0.28	0.40 ± 0.04
0.50	4.88 ± 0.5	3.33 ± 0.33	16.0 ± 1.6	0.19 ± 0.02	3.33 ± 0.33	0.47 ± 0.05	2.94 ± 0.29	0.42 ± 0.04
0.67	5.11 ± 0.5	3.46 ± 0.35	15.5 ± 1.5	0.18 ± 0.02	3.46 ± 0.35	0.48 ± 0.05	3.05 ± 0.30	0.43 ± 0.04
0.83	5.16 ± 0.5	3.56 ± 0.36	15.0 ± 1.5	0.18 ± 0.02	3.56 ± 0.36	0.50 ± 0.05	3.10 ± 0.31	0.44 ± 0.04
1.00	4.97 ± 0.5	3.67 ± 0.37	14.9 ±1.5	0.18 ± 0.02	3.67 ± 0.37	0.51 ± 0.05	3.18 ± 0.32	0.45 ± 0.05
1.17	4.65 ± 0.5	3.76 ± 0.38	14.6 ± 1.5	0.17 ± 0.02	3.76 ± 0.38	0.53 ± 0.05	3.33 ± 0.33	0.48 ± 0.05
1.33	4.45 ± 0.4	3.91 ± 0.39	14.3 ± 1.4	0.17 ± 0.02	3.91 ± 0.39	0.55 ± 0.05	3.43 ± 0.34	0.49 ± 0.05
1.50	4.35 ± 0.4	0.09 ± 0.41	13.9 ± 1.4	0.17 ± 0.02	4.09 ± 0.41	0.57 ± 0.06	3.48 ± 0.35	0.50 ± 0.05
1.67	4.31 ± 0.4	4.17 ± 0.42	13.5 ± 1.4	0.16 ± 0.02	4.17 ± 0.42	0.58 ± 0.06	3.47 ± 0.35	0.49 ± 0.05
1.84	4.34 ± 0.4	3.99 ± 0.40	12.8 ± 1.3	0.15 ± 0.02	3.99 ± 0.40	0.56 ± 0.06	3.25 ± 0.33	0.46 ± 0.05
3.02	4.08 ± 0.4	2.98 ± 0.30	12.0 ± 1.2	0.14 ± 0.01	2.98 ± 0.30	0.42 ± 0.04	4.48 ± 0.45	0.64 ± 0.06
5.17	4.69 ± 0.5	2.83 ± 0.28	7.3 ± 0.7	0.09 ± 0.01	2.83 ± 0.28	0.40 ± 0.04	3.94 ± 0.39	0.56 ± 0.06
10.05	2.30 ± 0.2	4.31 ± 0.43	9.2 ± 0.9	0.11 ± 0.01	4.31 ± 0.43	0.60 ± 0.06	3.50 ± 0.35	0.50 ± 0.05
20.28	0.93 ± 0.1	3.87 ± 0.39	7.0 ± 0.70	0.08 ± 0.01	3.87 ± 0.39	0.54 ± 0.05	4.08 ± 0.41	0.58 ± 0.06
27.89	0.93 ± 0.1	3.71 ± 0.37	6.3 ± 0.6	0.08 ± 0.01	3.71 ± 0.37	0.52 ± 0.05	3.22 ± 0.32	0.46 ± 0.05
46.09	0.97 ± 0.1	2.79 ± 0.28	5.1 ± 0.5	0.06 ± 0.01	2.79 ± 0.28	0.39 ± 0.04	3.45 ± 0.34	0.49 ± 0.05

Table 32: SAM 14 organ activity obtained from RIS of ^{99m}Tc-174H.64 expressed as a percentage of the injected dose (%ID).

Time (h)	Heart		Liver		Left Kidney		Right Kidney	
	%ID	%ID/gm	%ID	%ID/gm	%ID	%ID/gm	%ID	%ID/gm
0.00	5.54± 0.5	1.59 ± 0.16	13.6 ± 14	0.18 ± 0.02	1.80 ± 0.18	0.20 ± 0.02	0.52 ± 0.15	0.18 ± 0.02
0.17	5.02 ± 0.0	1.44 ± 0.14	13.4 ± 1.4	0.17 ± 0.02	2.00 ± 0.20	0.22 ± 0.02	0.68 ± 0.17	0.19 ± 0.02
0.33	4.65 ± 0.5	1.33 ± 0.13	13.3 ± 1.3	0.17 ± 0.02	2.26 ± 0.23	0.25 ± 0.03	1.88 ± 0.19	0.22 ± 0.02
0.50	4.47 ± 0.5	1.28 ± 0.13	12.7 ± 1.3	0.17 ± 0.02	2.61 ± 0.26	0.29 ± 0.03	2.19 ± 0.22	0.25 ± 0.03
0.67	4.22 ± 0.4	1.21 ± 0.12	12.4 ± 1.2	0.16 ± 0.02	3.01 ± 0.30	0.33 ± 0.03	2.61 ± 0.26	0.30 ± 0.03
0.83	4.06 ± 0.4	1.16 ± 0.12	12.0 ± 1.2	0.16 ± 0.02	3.32 ± 0.33	0.37 ± 0.04	2.88 ± 0.29	0.33 ± 0.03
1.00	3.99 ± 0.4	1.14 ± 0.11	11.6 ± 1.2	0.15 ± 0.02	3.61 ± 0.36	0.40 ± 0.04	3.21 ± 0.32	0.37 ± 0.04
1.17	3.90 ± 0.4	1.12 ± 0.11	11.3 ± 1.1	0.15 ± 0.01	3.88 ± 0.39	0.43 ± 0.04	3.51 ± 0.35	0.40 ± 0.04
1.33	3.83 ± 0.4	1.10 ± 0.11	10.9 ± 1.1	0.14 ± 0.01	4.14 ± 0.41	0.46 ± 0.05	3.75 ± 0.38	0.43 ± 0.04
1.50	3.82 ± 0.4	1.10 ± 0.11	10.3 ± 1.0	0.13 ± 0.01	4.36 ± 0.44	0.48 ± 0.05	3.97 ± 0.40	0.46 ± 0.05
1.67	3.79 ± 0.4	1.09 ± 0.11	9.9 ± 1.0	0.13 ± 0.01	4.02 ± 0.40	0.45 ± 0.04	3.72 ± 0.37	0.43 ± 0.04
1.83	3.85 ± 0.4	1.10 ± 0.11	9. 7 ± 1.0	0.13 ± 0.01	3.79 ± 0.38	0.42 ± 0.04	3.37 ± 0.34	0.39 ± 0.04
3.08	3.32 ± 0.3	0.95 ± 0.10	9.1 ± 0.9	0.12 ± 0.01	3.55 ± 0.36	0.39 ± 0.04	3.42 ± 0.34	0.39 ± 0.04
5.08	3.14 ± 0.3	0.90 ± 0.09	11.9 ± 1.2	0.16 ± 0.02	3.68 ± 0.37	0.41 ± 0.04	3.58 ± 0.36	0.41 ± 0.04
10.38	1.96 ± 0.2	0.56 ± 0.06	6.0 ± 0.6	0.08 ± 0.01	3.14 ± 0.31	0.35 ± 0.03	3.63 ± 0.36	0.42 ± 0.04
21.20	1.43 ± 0.2	0.41 ± 0.04	8.0 ± 0.8	0.10 ± 0.01	3.26 ± 0.33	0.36 ± 0.04	3.57 ± 0.36	0.41 ± 0.04
28.63	1.00 ± 0.1	0.29 ± 0.03	6.3 ± 0.6	0.08 ± 0.01	3.36 ± 0.34	0.37 ± 0.04	2.23 ± 0.22	0.26 ± 0.03
48.19	0.4 ± 0.04	0.12 ± 0.01	4.8 ± 0.5	0.06 ± 0.01	2.55 ± 0.25	0.28 ± 0.03	2.47 ± 0.25	0.28 ± 0.03

Pharmacokinetic models were developed for the heart and liver image data. However, the kidney activity rose to a maximum within 30 minutes of injection and remained there for the length of the study so that further modelling was not possible. Individual rate-constants were measured from the image data and were found to best fit a two multicompartment model of the same type described by the serum data. The half-lives for the distribution and terminal elimination phases and the mean residence time (MRT) are shown in Table 33.

Table 33: Organ kinetic parameters from quantitative RIS data of ^{99m}Tc-m174H.64 in rabbits.

Rabbit ID	$T_{1/2\,1}$ (h)		$T_{1/2\,z}$ (h)		MRT (h)	
	Heart	Liver	Heart	Liver	Heart	Liver
SAM12	2.1 ± 0.6	2.2 ± 0.37	28.8 ± 6.6	47.5 ± 12	36.1± 7.8	62.2 ± 16
SAM13	3.2 ± 0.8	1.8 ± 0.21	35.3 ± 7.2	46.2 ± 3.5	46.1± 8.1	64.8± 4.8
SAM14	0.49 ± 0.13	0.76 ± 0.23	14.7 ± 0.41	50.1 ± 6.7	21.0±0.5	71.8± 9.5
Mean	1.59 ± 0.74	1.93 ± 1.36	26.3 ± 10.5	47.9 ± 2.0	34.4± 13	66.3± 5.0

5.2.1.3 Tissue Sampling

After the final image, a 5 mL blood sample was obtained by cardiac puncture and the animal sacrificed by lethal injection. Tissue samples were obtained for all rabbits at necropsy and assayed for ^{99m}Tc levels. This information is presented in Table 34 with organ values given in units of % injected dose/gm to facilitate a comparison between the rabbits. The mean and standard deviation for each organ (corrected to 48 h post-injection) is presented in the final column for comparison with the other MAbs tested.

Table 34: Rabbit tissue sample data for ^{99m}Tc-174H.64.

Tissue Sample	**SAM12** % inj. dose/gm t = 45.3 h	**SAM13** % inj. dose/gm t = 46.7 h	**SAM14** % inj. dose/gm t = 48.8 h	**Mean ± Std.Dev** % inj. dose/gm @ t = 48
Liver	2.93E-04	2.76E-04	2.23E-04	2.33 ± 0.16E-04
Spleen	4.02E-04	5.02E-04	2.67E-04	3.40 ± 0.80E-04
Heart	1.16E-04	1.27E-04	9.09E-05	9.82 ± 0.12E-05
Right Kidney	2.33E-03	1.78E-03	1.02E-03	1.45 ± 0.30E-03
Left Kidney	2.27E-03	1.87E-03	1.00E-03	1.46 ± 0.31E-03
Gall Bladder	3.09E-04	2.79E-04	3.92E-04	2.99 ± 0.11E-04
Bile	1.39E-04	1.16E-04	5.30E-04	2.61 ± 0.28E-04
Muscle	1.78E-05	2.34E-05	9.80E-06	1.46 ± 0.49E-05
Lung	1.96E-04	1.64E-04	1.42E-04	1.47 ± 0.08E-04

5.2.2 Patient Kinetics

Phase I and II clinical evaluations of the murine form of ^{99m}Tc-labelled MAb 174H.64 were undertaken at the Cross Cancer Institute in Edmonton to evaluate its application in patient staging of primary, metastatic and recurrent disease. As part of this study, human kinetics and dosimetry were determined. Concomitantly, a pilot study at the Johann Wolfgang Goethe University Medical Centre in Frankfurt, Germany evaluated the chimeric form of this MAb[148]. Data from these two sites were used to determine the pharmacokinetics of the two different forms of this MAb to test the null hypothesis that "there is no difference between kinetic models describing disposition of radioactivity for the in vivo distribution of the murine and chimeric ^{99m}Tc - 174H.64 MAb".

A two-compartment model representing the in vivo distribution of ^{99m}Tc labelled 174H.64 was constructed using data obtained from three patients at the Cross Cancer Institute in Edmonton with head and neck cancer. Approximately 20 mL of normal saline containing 2 mg of 174H.64 was infused iv into each patient over a period of 5 minutes. Serum samples were collected at selected time intervals up to 48 hours post-injection and urine samples collected in six hour intervals up to 72 hours post injection. All samples were counted in a multi-sample gamma counter and compared against a standard of known activity. The raw-counts obtained from the gamma counter were decay corrected and converted to a percentage of the injected dose using the spreadsheet QPRO. The serum data reflecting total radioactivity for patients M1 to M3 are shown in Table 35 to Table 37 and illustrated in Figure 22. A estimated 10% error (composed of sampling and counting errors) is associated with the serum and urine data.

Table 35: Patient M1 data following the injection of 2 mg of Tc-99m labelled m 174H.64 MAb.

Patient M1 Time (hours)	Serum x 10^6 dpm/mL	% Injected Dose	Urine Time (hours)	Progressive Elimination %
0.08	32.9	100.0	N/A	N/A
0.17	32.1	97.6		
0.25	31.5	96.0		
0.50	30.6	93.0		
1.25	29.5	89.7		
4.67	21.4	65.2		
18.43	11.0	33.4		
20.5	10.1	30.8		
23.17	9.1	27.6		
26.85	7.2	21.8		
32.50	5.6	16.9		
42.55	4.0	12.1		

Table 36: Patient M3 data (head and neck cancer) following the injection of 2 mg of Tc-99m labelled m-174H.64 MAb.

Patient M3 Time (hours)	Serum x 10⁶ dpm/mL	% Injected Dose	Urine Time (hours)	Progressive Elimination %
0.08	27.3	100	6	8.5
1.08	25.6	93.3	12	14.6
3.58	18.8	68.7	24	24.1
10.58	13.9	50.8	30	28.3
25.33	6.7	24.4	36	31.6
30.08	5.3	19.5		
49.17	3.0	11.0		

Table 37: Patient M2 data (head and neck cancer) following the injection of 2 mg of Tc-99m labelled m-174H.64 MAb.

Patient M2 Time (hours)	Serum x 10⁶ dpm/mL	% Injected Dose	Urine Time (hours)	Progressive Elimination %
0.08	19.3	65.9	7.67	2.2
0.20	28.7	98.3	13.67	4.8
0.52	28.1	96.3	19.67	6.2
0.58	25.9	88.6	25.67	6.9
0.70	29.2	100.0	31.67	8.5
1.00	26.5	90.6	37.67	11.0
2.75	24.6	84.3	43.67	11.9
5.50	19.3	66.1	49.67	12.7
22.67	8.8	30.2		
24.08	8.5	29.1		
28.67	8.0	27.4		
46.83	4.3	14.8		
51.08	3.8	13.0		

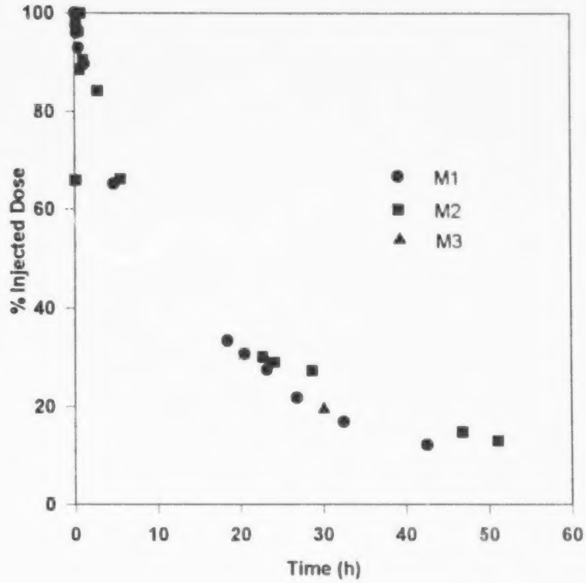

Figure 22: Patient serum radioactivity profile following the iv. administration of 2 mg of m-174H.64 MAb.

The serum data (Table 35 to Table 37) were analyzed with PCNONLIN using the same assumptions as listed on page 133 (assumptions 1 - 4 for MAb 170H.82) and are best described by a two compartment model of the form:

$$C(t) = C_1 e^{-\lambda_1 t} + C_z e^{-\lambda_z t} \quad (40)$$

A summary of parameters representing the coefficients from equation 40, describing the ^{99m}Tc serum kinetics, and the plasma and renal clearance are presented in Table 38 together with the average value of the standard error terms. The error terms are only approximate as they are based upon a linearization of a nonlinear model. The half-lives are reported rather than the rate-constants in order to make a more meaningful comparison between the different MAbs tested. Statistical analyses were performed using either SPSS or PCNONLIN.

Table 38: Pharmacokinetic parameters representing a two compartment model of the form $C(t) = C_1 e^{-\lambda_1 t} + C_z e^{-\lambda_z t}$

Patient ID	Dose (mg)	C1 (%ID)	Cz (% ID)	$t_{1/2}1$ (h)	$T_{1/2}z$ (h)	MRT (h)	Plasma Clearance (mL/h)	Renal Clearance (mL/h)
M1	2	27.4±4.3	72.2±4.1	2.4±0.8	16.2± 0.7	22.3±0.7	134±2.0	N/A
M2	2	44.0±0.5	60.5±5.1	3.4±1.0	23.1±1.6	30.5±1.5	140±3.2	21.7±1.1
M3	2	29.0±9.8	71.2±9.8	3.3±1.7	25.5±4.2	35.1±4.7	89.2±5.5	17.1±0.9
Mean		33.5 ± 9.2	68.3 ± 6.8	3.1 ± 0.6	21.5 ± 4.7	29.1 ± 6.3	121 ± 3.6	19.4 ±1.0

5.3 MAb-c174H.64

5.3.1 Rabbit Kinetics

The serum biodistribution data of the chimeric form of this radiolabelled MAb are presented in Table 39 and schematically shown in Figure 23 for each of the two rabbits tested. The data is expressed in dpm/mL serum and as a percentage of the injected dose (%ID) for comparison between rabbits in this study and with the other two MAbs tested.

Table 39: MAb c174H.64 serum activity in rabbits measured as dpm/mL (1×10^6) and as a percentage of the injected dose (% ID) at various time intervals.

ID: SAM30 Dose: 477 MBq			ID: SAM31 Dose: 439 MBq		
Time (h)	dpm/mL (1×10^6)	% ID	Time (h)	dpm/mL (1×10^6)	% ID
0.50	286	96.6	0.60	169	94.2
1.22	232	78.2	1.18	155	86.3
1.98	207	69.9	2.25	122	68.1
3.32	167	56.3	3.37	104	57.8
7.77	102	34.4	7.38	73	40.7
12.0	73	24.8	16.1	38	21.0
21.0	43	14.5	25.1	20	11.1
28.1	27	9.2	39.3	11	6.1
44.7	14	4.8			

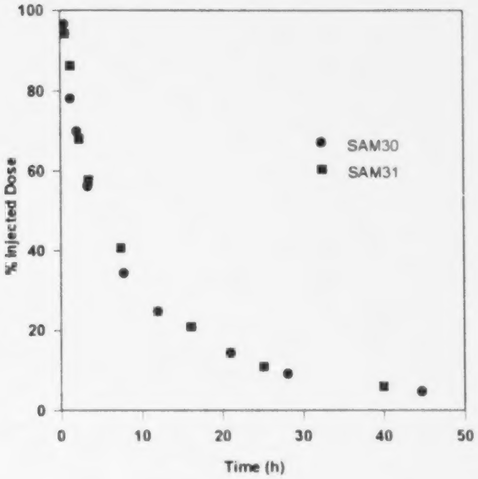

Figure 23: Rabbit serum profile following the iv. bolus administration of ^{99m}Tc c174H.64 MAb.

The same pharmacokinetic model ($C(t) = C_1 e^{-\lambda_1 t} + C_z e^{-\lambda_z t}$) that was used to fit the murine form of the MAb was found to best describe the biodistribution of the ^{99m}Tc-labelled compound in serum. The constants describing this equation are shown in Table 40 together with the mean and standard deviation. The half-lives are reported rather than the rate-constants to simplify the comparison between the different MAbs tested.

Table 40: Pharmacokinetic parameters representing a two compartment model of the form $C(t) = C_1 e^{-\lambda_1 t} + C_z e^{-\lambda_z t}$ following the administration of ^{99m}Tc c174H.64.

Rabbit ID	C_1 dpm/mL	C_z dpm/mL	$T_{½1}$ (h)	$T_{½z}$ (h)	MRT (h)
SAM30	63.2 ± 5.2	36.6 ± 4.5	2.7 ± 0.5	14.9 ± 1.1	17.6 ± 0.8
SAM31	59.5 ± 9.9	39.7 ± 11	3.0 ± 0.9	14.1 ± 1.9	16.6 ± 1.2
Mean	61.4 ± 7.6	38.2 ± 7.7	2.8 ± 0.7	14.5 ± 1.5	17.0 ± 1.0

5.3.1.1 Routes of Elimination

Urine and fecal samples were collected and used to estimate ^{99m}Tc-c174H.64 elimination patterns. As the rabbits practice coprophagy it was difficult to analyze fecal samples; however, no recirculation patterns were observed in the serum kinetics and no bowel activity was observed on the gamma camera images. A limited amount of radioactivity was observed in feces and in the bile collected at necropsy (Table 44) but was not significant when compared with the overall amount of activity injected and it was therefore assumed that biliary excretion did not play a major role in the elimination of this MAb. Figure 24 illustrates the ^{99m}Tc activity in the fecal contents.

Renal excretion was found to be the major route of elimination for the ^{99m}Tc label with the data illustrated in Figure 25. The labelled metabolites were not identified but were expected to be low molecular compounds such as glutathion or cysteine.

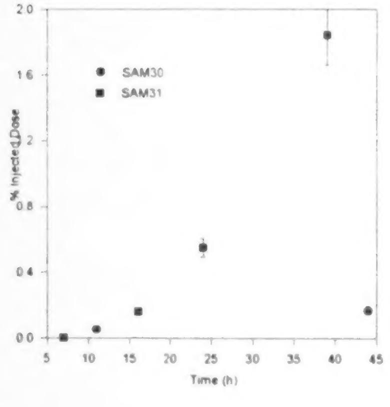

Figure 24: Cumulative fecal elimination of ^{99m}Tc labelled MAb c174H.64 in rabbits.

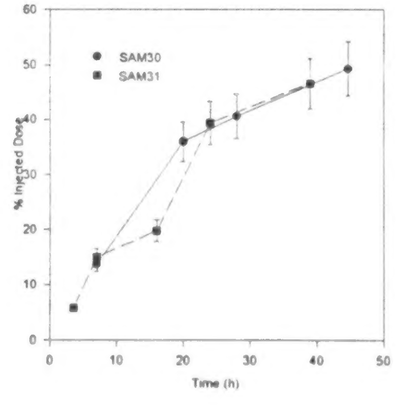

Figure 25: Cumulative urine excretion of ^{99m}Tc labelled MAb c174H.64 in rabbits.

5.3.1.2 Gamma Camera Imaging

Gamma camera imaging was performed according to the protocol described above in the Experimental Methodology section. The purpose of collecting image data was two-fold:

1. to test whether the two-compartment model obtained from the serum data could be expanded to include separate compartments for those organs demonstrating uptake as identified by RIS, and
2. to search for similarities between rabbit and human uptake patterns for the murine form of this MAb as well MAbs 170H.82 and B80.3. If some degree of conformity were found between these two species then the rabbit model could be applied to predict MAb distribution patterns in patients for future studies.

Table 41: SAM 30 organ activity obtained from quantitative gamma camera imaging of ^{99m}Tc-c174H.64 expressed as a percentage of the injected dose (%ID).

Time	Heart		Liver		Left Kidney		Right Kidney	
(h)	%ID	%ID/gm	%ID	%ID/gm	%ID	%ID/gm	%ID	%ID/gm
0.08	4.78 ± 0.7	1.02 ± 0.15	14.2 ± 2	0.17 ± 0.03	2.06 ± 0.3	0.27 ± 0.04	3.80 ± 0.6	0.50 ± 0.08
0.60	4.37 ± 0.7	0.93 ± 0.14	14.8 ± 2	0.18 ± 0.03	2.53 ± 0.4	0.33 ± 0.05	4.98 ± 0.7	0.66 ± 0.10
0.77	4.28 ± 0.6	0.91 ± 0.14	14.6 ± 2	0.17 ± 0.03	2.76 ± 0.5	0.36 ± 0.05	5.26 ± 0.8	0.70 ± 0.10
0.93	4.32 ± 0.6	0.92 ± 0.14	14.8 ± 2	0.18 ± 0.03	3.11 ± 0.5	0.41 ± 0.06	5.66 ± 0.8	0.75 ± 0.11
1.10	4.10 ± 0.6	0.88 ± 0.13	15.2 ± 2	0.18 ± 0.03	3.40 ± 0.6	0.44 ± 0.07	6.03 ± 0.9	0.80 ± 0.12
1.27	3.98 ± 0.6	0.85 ± 0.13	14.8 ± 2	0.18 ± 0.03	3.49 ± 0.6	0.46 ± 0.07	6.11 ± 0.9	0.81 ± 0.12
1.43	3.77 ± 0.6	0.81 ± 0.12	14.6 ± 2	0.17 ± 0.03	3.58 ± 0.6	0.47 ± 0.07	6.16 ± 0.9	0.82 ± 0.12
1.60	3.72 ± 0.6	0.80 ± 0.12	14.5 ± 2	0.17 ± 0.03	3.77 ± 0.6	0.49 ± 0.07	6.19 ± 0.9	0.82 ± 0.12
1.77	3.70 ± 0.6	0.80 ± 0.12	14.3 ± 2	0.17 ± 0.03	4.08 ± 0.6	0.53 ± 0.08	6.40 ± 0.9	0.85 ± 0.13
1.93	3.83 ± 0.6	0.82 ± 0.12	14.1 ± 2	0.17 ± 0.03	4.44 ± 0.7	0.58 ± 0.09	6.72 ± 1	0.89 ± 0.13
2.10	3.49 ± 0.6	0.75 ± 0.11	14.2 ± 2	0.17 ± 0.03	4.83 ± 0.7	0.63 ± 0.09	7.13 ± 1	0.94 ± 0.14
2.27	3.50 ± 0.6	0.75 ± 0.11	14.0 ± 2	0.17 ± 0.02	5.12 ± 0.8	0.67 ± 0.10	7.22 ± 1	0.96 ± 0.14
2.43	3.35 ± 0.6	0.72 ± 0.11	13.9 ± 2	0.16 ± 0.02	5.32 ± 0.8	0.70 ± 0.10	7.50 ± 1	0.99 ± 0.15
2.63	2.61 ± 0.5	0.56 ± 0.08	11.6 ± 2	0.14 ± 0.02	5.38 ± 0.8	0.70 ± 0.11	5.68 ± 0.8	0.75 ± 0.11
7.85	1.84 ± 0.3	0.39 ± 0.06	9.1 ± 1.5	0.11 ± 0.02	5.41 ± 0.8	0.7[illegible] ± 0.11	4.55 ± 0.7	0.60 ± 0.09
12.00	1.50 ± 0.3	0.32 ± 0.05	7.7 ± 1.5	0.09 ± 0.01	5.19 ± 0.8	0.68 ± 0.10	4.41 ± 0.7	0.58 ± 0.09
20.60	1.09 ± 0.2	0.23 ± 0.03	7.1 ± 1.5	0.08 ± 0.01	4.26 ± 0.6	0.56 ± 0.08	4.15 ± 0.7	0.55 ± 0.08
28.17	0.73 ± 0.1	0.16 ± 0.02	5.9 ± 1	0.07 ± 0.01	4.37 ± 0.6	0.57 ± 0.09	3.39 ± 0.6	0.45 ± 0.07
44.02	0.74 ± 0.1	0.16 ± 0.02	5.2 ± 1	0.06 ± 0.01	3.37 ± 0.6	0.44 ± 0.07	3.26 ± 0.5	0.43 ± 0.06

Table 42: SAM 31 organ activity obtained from quantitative gamma camera imaging of ^{99m}Tc-c174H.64 expressed as a percentage of the injected dose (%ID).

Time (h)	Heart		Liver		Left Kidney		Right Kidney	
	%ID	%ID/gm	%ID	%ID/gm	%ID	%ID/gm	%ID	%ID/gm
0.07	6.57 ± 0.9	0.71 ± 0.11	13.8 ± 2	0.11 ± 0.02	0.93 ± 0.2	0.06 ± 0.01	1.70 ± 0.3	0.11 ± 0.02
0.35	7.67 ± 1	0.83 ± 0.12	13.9 ± 2	0.11 ± 0.02	1.12 ± 0.2	0.07 ± 0.01	2.24 ± 0.4	0.14 ± 0.02
0.52	7.34 ± 1	0.79 ± 0.12	13.7 ± 2	0.11 ± 0.02	1.33 ± 0.2	0.08 ± 0.01	2.41 ± 0.4	0.15 ± 0.02
0.68	7.07 ± 1	0.76 ± 0.11	13.6 ± 2	0.10 ± 0.02	1.47 ± 0.2	0.09 ± 0.01	2.52 ± 0.4	0.16 ± 0.02
0.85	6.71 ± 0.9	0.72 ± 0.11	13.6 ± 2	0.10 ± 0.02	1.66 ± 0.3	0.10 ± 0.02	2.68 ± 0.5	0.17 ± 0.03
1.02	6.46 ± 0.9	0.70 ± 0.10	13.3 ± 2	0.10 ± 0.02	1.89 ± 0.3	0.12 ± 0.02	2.89 ± 0.5	0.19 ± 0.03
1.18	6.25 ± 0.9	0.68 ± 0.10	13.2 ± 2	0.10 ± 0.02	2.20 ± 0.4	0.14 ± 0.02	3.21 ± 0.6	0.21 ± 0.03
1.35	5.97 ± 0.9	0.65 ± 0.10	13.3 ± 2	0.10 ± 0.02	2.58 ± 0.4	0.16 ± 0.02	3.55 ± 0.6	0.23 ± 0.03
1.52	5.83± 0.8	0.63 ± 0.09	13.6 ± 2	0.10 ± 0.02	2.76 ± 0.5	0.17 ± 0.03	3.71 ± 0.7	0.24 ± 0.04
1.68	5.83 ± 0.8	0.63 ± 0.09	13.6 ± 2	0.10 ± 0.02	2.83 ± 0.5	0.17 ± 0.03	3.78 ± 0.7	0.24 ± 0.04
1.85	5.66 ± 0.8	0.61 ± 0.09	13.6 ± 2	0.10 ± 0.02	2.93 ± 0.5	0.18 ± 0.03	3.88 ± 0.7	0.25 ± 0.04
2.02	5.75 ± 0.8	0.62 ± 0.09	13.3 ± 2	0.10 ± 0.02	2.97 ± 0.5	0.18 ± 0.03	3.92 ± 0.7	0.25 ± 0.04
2.18	5.76 ± 0.8	0.62 ± 0.09	13.2 ± 2	0.10 ± 0.02	3.05 ± 0.5	0.19 ± 0.03	4.05 ± 0.7	0.26 ± 0.04
3.00	3.38 ± 0.5	0.37 ± 0.05	10.9 ± 1.5	0.08 ± 0.01	4.23 ± 0.6	0.26 ± 0.04	4.24 ± 0.8	0.27 ± 0.04
7.48	2.86 ± 0.8	0.31 ± 0.05	10.3 ± 1.5	0.08 ± 0.01	4.49 ± 0.7	0.28 ± 0.04	3.90 ± 0.7	0.25 ± 0.04
15.88	1.49 ± 0.2	0.16 ± 0.02	8.8 ± 1.5	0.07 ± 0.01	3.79 ± 0.6	0.23 ± 0.03	3.66 ± 0.7	0.23 ± 0.04
25.15	1.03 ± 0.2	0.11 ± 0.02	7.2 ± 1.5	0.06 ± 0.01	3.77 ± 0.6	0.23 ± 0.03	3.41 ± 0.6	0.22 ± 0.03
39.43	0.59 ± 0.1	0.06 ± 0.01	6.2 ± 1	0.05 ± 0.01	2.95 ± 0.5	0.18 ± 0.03	2.94 ± 0.5	0.19 ± 0.03

The image data in Table 41 and Table 42 tabulates the activity as % injected dose (%ID) and %ID/gm for the liver, heart and both kidneys, where the time period is the time in hours post-injection.

Pharmacokinetic models were developed for the heart and liver gamma camera image data. Individual rate-constants were measured and found to best fit a one compartment model with a bolus input for the liver and a two compartment model for the heart (bolus input). The half-lives for the distribution ($T_{½1}$) and terminal elimination phases ($T_{½z}$) and the mean residence time (MRT) are shown in Table 43 for ^{99m}Tc-c174H.64. The development of a pharmacokinetic model for the kidneys was not possible due to the unchanging nature of the activity over the time period studied.

Table 43: Kinetic parameters of selected organs from quantitative RIS data of 99mTc-c174H.64 in rabbits (2 compartment model, bolus input).

Rabbit ID	$T_{1/2\,1}$ (h)		$T_{1/2\,2}$ (h)		MRT (h)	
	Heart	Liver	Heart	Liver	Heart	Liver
SAM30	2.5 ± 0.36	N/A	37.0 ± 5.9	25.7 ± 2.2	47.6± 7.3	37.0± 3.2
SAM31	2.0 ± 0.45	N/A	16.5 ± 2.0	31.3 ± 2.0	20.2± 1.9	45.3± 2.8
Mean	2.25 ± 0.35	N/A	26.8 ± 14.5	28.5 ± 4.0	33.9± 19	41.1± 5.9

5.3.1.3 Tissue Sampling

After the final image, a 5 mL blood sample was obtained by cardiac puncture and the animal sacrificed by lethal injection as described above. Tissue samples were obtained from all rabbits at necropsy and assayed for ^{99m}Tc levels. This information is presented in Table 34 with organ values given in units of % injected dose/gm to facilitate a comparison between the rabbits. The mean and standard deviation for each organ is presented in the final column, decay corrected to 48 hours, for comparison with the other MAbs tested.

Table 44: Rabbit tissue sample data for ^{99m}Tc-c174H.64.

Tissue Sample	SAM30 % inj. dose/gm t = 44.7 h	SAM31 % inj. dose/gm t = 39.9 h	Mean ± Std.Dev % inj. dose/gm @ t = 48
Liver	3.60E-04	4.71E-04	2.16 ± 0.42E-04
Spleen	3.19E-04	5.58E-04	2.19 ± 0.02E-04
Heart	9.44E-05	1.38E-04	5.95 ± 0.71E-05
Right Kidney	2.50E-03	1.87E-03	1.22 ± 0.68E-03
Left Kidney	2.55E-03	1.80E-03	1.23 ± 0.73E-03
Gall Bladder	4.23E-04	7.71E-04	2.97 ± 0.10E-04
Bile	1.47E-04	1.34E-03	3.13 ± 3.0E-04
Muscle	1.43E-05	1.22E-05	7.27 ± 3.5E-06
Lung	2.84E-04	2.27E-04	1.42 ± 0.74E-04

5.3.2 Patient Kinetics

Kinetic data were obtained from seven patients diagnosed with head and neck cancer at the JWGUMC, Frankfurt, Germany. The serum data reflecting total radioactivity for each patient (C1 to C7) are presented in Table 45 through Table 51 and are illustrated in Figure 26. These data were analyzed with JANA and PCNONLIN and were found to fit the same type of model representing the murine form of the MAb. The parameters describing this model are presented in Table 52 together with an estimate of the standard error. Weighting factors proportional to the inverse variance were used to weight the data in an attempt to compensate for the nonhomogeneity between patients. The error associated with the serum and urine radioactivity measurements was estimated to be less than 10%.

Table 45: Patient data (head and neck cancer) following the injection of 1 mg of Tc-99m labelled c-174H.64 MAb.

Patient C1 Time (hours)	Serum x 10^6 dpm/mL	% Injected Dose	Urine Time (hours)	Progressive Elimination %
0.25	19.0	99.5	6.2	8.9
0.50	17.3	90.8	12.2	16.2
1.33	15.9	83.4	18.2	19.9
2.25	15.4	80.4	24.2	23.0
5.50	10.9	57.2	30.2	26.6
12.0	6.8	35.7	36.2	31.2
18.5	5.8	30.3		
43.0	1.7	19.6		

Table 46: Patient data (head and neck cancer) following the injection of 1 mg of Tc-99m labelled c-174H.64 MAb.

Patient C2 Time (hours)	Serum x 10^6 dpm/mL	% Injected Dose	Urine Time (hours)	Progressive Elimination %
0.25	24.5	100.3	5.7	1.8
0.42	22.8	93.3	11.7	9.2
3.33	18.7	76.5	19.7	12.8
5.25	15.6	63.9	23.7	18.6
10.42	10.6	43.4	29.7	20.7
24.58	6.49	26.6	35.7	21.9
29.67	5.59	22.9	41.7	25.4
			47.7	26.7

Table 47: Patient data (head and neck cancer) following the injection of 1 mg of Tc-99m labelled c-174H.64 MAb.

Patient C3 Time (hours)	Serum x 10^6 dpm/mL	% Injected Dose	Urine Time (hours)	Progressive Elimination %
0.08	27.3	100	6	8.5
1.08	25.6	93.3	12	14.6
3.58	18.8	68.7	24	24.1
10.58	13.9	50.8	30	28.3
25.33	6.7	24.4	36	31.6
30.08	5.3	19.5		
49.17	3.0	11.0		

Table 48: Patient data (head and neck cancer) following the injection of 1 mg of Tc-99m labelled c-174H.64 MAb.

Patient C4 Time (hours)	Serum x 10^6 dpm/mL	% Injected Dose	Urine Time (hours)	Progressive Elimination %
.08	14.3	100	7	8.5
.25	13.3	93.1	19	21.3
1.03	12.1	84.3	31	25.1
4.37	9.4	65.7	37	29.5
19.28	4.8	33.2		
26.28	3.5	24.6		
42.87	2.0	14.1		

Table 49: Patient data (head and neck cancer) following the injection of 1 mg of Tc-99m labelled c-174H.64 MAb.

Patient C5 Time (hours)	Serum x 10^6 dpm/mL	% Injected Dose	Urine Time (hours)	Progressive Elimination %
0.63	18.7	100	6	7.2
1.38	18.7	96.4	12	16.9
4.13	14.3	76.5	18	22.8
24.47	4.19	26.2	24	28.4

Table 50: Patient data (head and neck cancer) following the injection of 1 mg of Tc-99m labelled c-174H.64 MAb.

Patient C6 Time (hours)	Serum x 10^6 dpm/mL	% Injected Dose	Urine Time (hours)	Progressive Elimination %
0.50	28.5	100	N/A	N/A
1.50	27.7	97.2	N/A	N/A
5.25	22.4	78.6	N/A	N/A
24	10.4	36.4	N/A	N/A
47.42	4.8	17	N/A	N/A

Table 51: Patient data (head and neck cancer) following the injection of 1 mg of Tc-99m labelled c-174H.64 MAb.

Patient C7 Time (hours)	Serum x 10^6 dpm/mL	% Injected Dose	Urine Time (hours)	Progressive Elimination %
0.50	23.6	100	12	11.1
2.17	19.0	80.6	30	12.6
4.25	14.7	62.3	36	21.3
5.42	13.2	55.8		
22.75	5.6	23.8		
46.75	2.6	11.0		

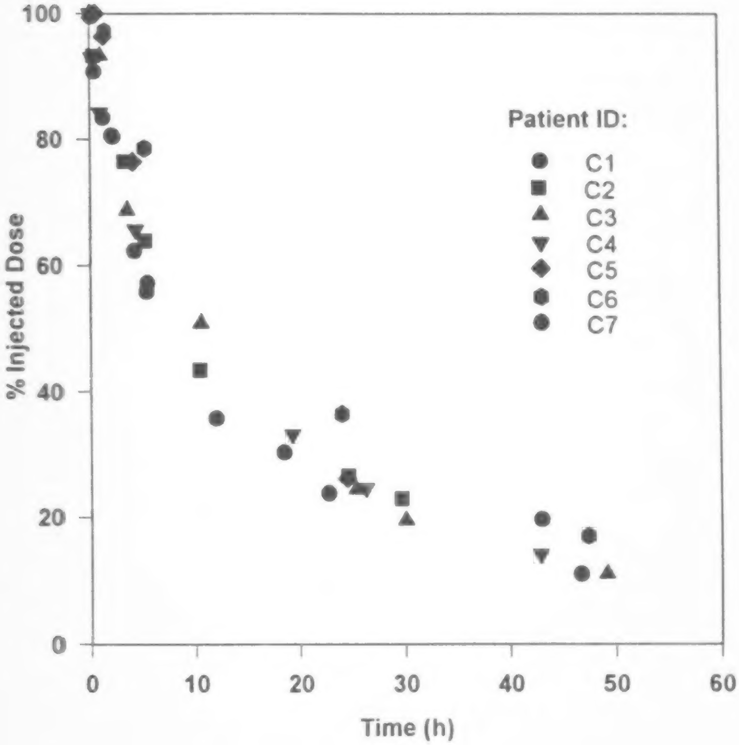

Figure 26: Patient serum profile following the iv. administration of 1 mg of c-174H.64 MAb.

Although the data from patient C5 is incomplete for the purposes of contributing to the development of a pharmacokinetic model, it was reported as it did not substantially differ from the serum data of the other patients in this group as illustrated in Figure 26. However, C5's effect on the mean kinetic values was removed from the last row in Table 52. The values in this last row will be used for comparison with the other MAbs used in this study. Although not reported in this table, the volume of distribution in this group of patients was approximately equal to the blood volume.

Table 52: Pharmacokinetic parameters representing a model of the form: $C(t) = C_1 e^{-\lambda_1 t} + C_z e^{-\lambda_z t}$. # Data are ill-conditioned

Patient ID	C_1 (% ID)	C_z (% ID)	$T_{½1}$ (h)	$T_{½z}$ (h)	MRT (h)	Plasma Clr (mL/h)	Renal Clr (mL/h)
1	61.6 ± 6.7	40.6 ± 7.4	3.5 ± 0.9	41.2 ± 11.6	53.2 ± 13.8	201 ± 6	79 ± 4
2 #	65.9 ± 19	35.0 ± 20	4.8 ± 1.6	45.6 ± 52.3	55.9 ± 63.8	102 ± 60	45 ± 3
3	30.9 ± 12	71.6 ± 12	2.2 ± 1.5	17.1 ± 2.4	23.6 ± 2.5	112 ± 11	50 ± 3
4	32.7 ± 5.0	64.9 ± 4.6	2.4 ± 0.7	19.3 ± 1.2	26.4 ± 1.3	102 ± 2	79 ± 4
6	35.7 ± 18	68.2 ± 20	6.6 ± 3.4	23.4 ± 4.2	30.7 ± 2.8	93 ± 3	N/A
7	59.8 ± 1.4	48.6 ± 1.1	2.7 ± 0.1	21.8 ± 0.4	27.8 ± 0.4	180 ± 1	52 ± 3
Weighted Mean	44.4 ± 15	59.0 ± 12	2.7 ± 0.2	22.5 ± 1.3	27.6 ± 1.2	159 ± 16	61 ± 8

5.4 MAb-B80.3

Biodistribution patterns of the murine form of the ^{99m}Tc-B80.3 MAb were measured in rabbits and patients. Rabbit organs demonstrating significant uptake of the MAb, as identified by RIS, were noted and their corresponding activity calculated to aid in the development of a multicompartmental model. Biodistribution of the ^{99m}Tc label in the serum and urine was measured. However, no reliable RIA method was found for analyzing the ^{99m}Tc-B80.3 in serum due to circulating PSA, so that the immunoreactive component in the serum was not measured.

A pharmacokinetic model based on serial serum measurements was developed for normal, non-tumor bearing rabbits and used to predict the in vivo biodistribution of ^{99m}Tc-B80.3. Excreta were collected from the rabbits and used to estimate clearance profiles. Selected tissue samples were taken at necropsy to assist with image quantitation.

Kinetic data from two patients, receiving 2 mg of ^{99m}Tc-B80.3 were collected and the results analyzed and compared with the rabbit data. Patients were selected to study the effects of circulating PSA on the kinetics and to assess the serum clearance of the MAb as the concentration of PSA increased. Consequently, one the patients was selected with a high serum PSA level (2500 ng/mL) and the other, a low PSA level (10 ng/mL). Insufficient image data was available from the two patients to perform a kinetic analysis and consequently, no dosimetry data were available.

5.4.1 Rabbit kinetics

The data are organized into sections representing serum, excreta, tissue samples and gamma camera image information. In order to assess the effect of circulating antigen (PSA) on the B80.3 pharmacokinetics in patients the following sets of experiments were performed using nontumor-bearing rabbits.

In the first set of rabbits, a single iv bolus dose of ^{99m}Tc labelled B80.3 (0.5 mg) was injected into the marginal ear vein of the rabbit and a kinetic profile was developed using serum, urine, fecal and gamma camera image data. A second set of rabbits were then tested to study the effects of a circulating B80.3/PSA complex. The complex was prepared by incubating the labelled ^{99m}Tc-B80.3 with a two-fold molar excess of PSA in a normal phosphate buffered solution (pH = 7.4) for one hour at 37°C. The complexed MAb and any remaining free PSA (to mimic circulating Ag in patients) was injected into the rabbit.

The serum biodistribution data of the free ^{99m}Tc-B80.3 MAb are presented in Table 53 and in Table 54 for the ^{99m}Tc-B80.3/PSA complex. The data are expressed in dpm/mL serum and as a percentage of the injected dose for comparison between the rabbits in this study and with those using the other two MAbs tested.

Table 53: ^{99m}Tc-B80.3 serum activity measured as dpm/mL (1 x 10^6) and as a percentage of the injected dose (% ID) at various time intervals.

ID: SAM07 Dose: 384 MBq			ID: SAM08 Dose: 340 MBq			ID: SAM10 Dose: 363 MBq		
Time (h)	dpm/mL (1×10^6)	% ID	Time (h)	dpm/mL (1×10^6)	% ID	Time (h)	dpm/mL (1×10^6)	% ID
0.28	188	99.6	0.32	255	99.2	0.05	234	99.0
1.20	173	91.4	0.98	199	87.7	0.88	213	90.1
2.20	156	82.6	1.98	193	85.1	1.88	208	87.9
3.12	151	80.1	2.98	180	79.4	2.88	108	76.2
7.21	112	59.2	7.82	124	54.4	6.13	137	58.1
12.28	82.2	43.5	12.32	95.3	41.9	11.80	97.3	41.2
20.62	52.3	27.7	22.00	58.9	25.9	21.85	57.7	24.4
29.78	40.1	21.2	30.28	47.8	21.0	29.60	43.6	18.5
44.62	25.3	13.4	45.65	31.3	13.8	46.15	25.2	10.7

Table 54: ^{99m}Tc-B80.3/PSA complex serum activity measured as dpm/mL (1 x 10^6) and as a percentage of the injected dose (% ID) at various time intervals.

ID: SAM09 Dose: 236 MBq			ID: SAM 15 Dose: 280 MBq			ID: SAM 16 Dose: 310 MBq		
Time (h)	dpm/mL (1×10^6)	% ID	Time (h)	dpm/mL (1×10^6)	% ID	Time (h)	dpm/mL (1×10^6)	% ID
0.42	142	93.3	0.12	187	98.3	0.35	221	92.6
1.12	128	84.3	0.62	169	89.3	1.63	201	84.2
1.87	123	80.4	1.12	154	81.1	2.23	193	81.0
2.95	109	71.8	1.95	132	69.4	4.48	143	59.8
6.12	76.9	50.4	2.95	126	66.2	9.13	87.3	36.6
10.45	52.1	34.2	7.25	75.0	39.5	19.65	44.8	18.8
19.78	34.8	22.9	11.95	52.6	27.7	26.97	27.0	11.3
28.20	23.4	15.3	21.78	34.1	18.0	50.53	10.9	4.6
43.70	12.4	8.2	30.12	26.5	14.0			
			46.83	12.1	6.4			

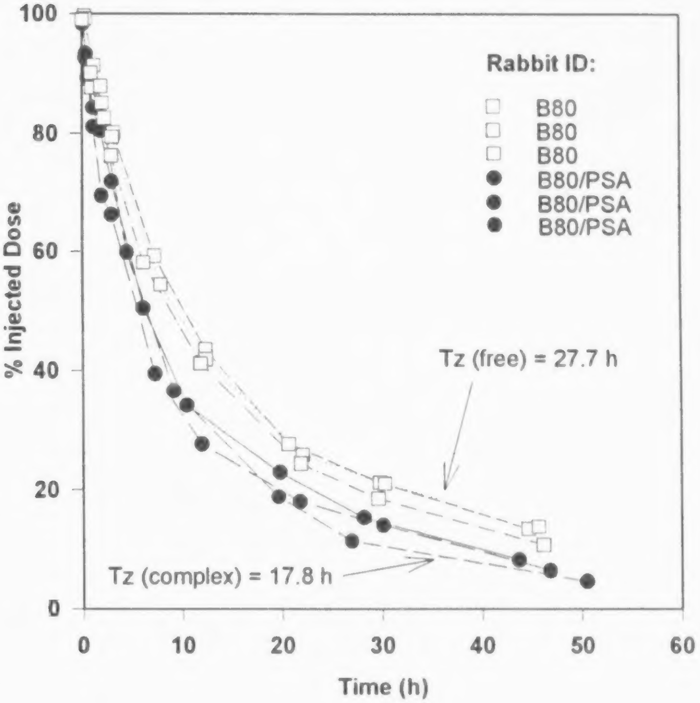

Figure 27: Serum biodistribution of ^{99m}Tc-B80.3 and ^{99m}Tc-B80.3/PSA illustrating the different clearance rates.

A pharmacokinetic model was developed to describe the biodistribution of the ^{99m}Tc-B80.3 in serum. The data were best represented by a two compartment model of the form $C(t) = C_1 e^{-\lambda_1 t} + C_z e^{-\lambda_z t}$ with the constants describing this equation shown in Table 55 together with the mean and standard error. The biodistribution of the ^{99m}Tc-B80.3/PSA complex can also be represented by a two compartment model of the same form. The data describing the constants of this pharmacokinetic model are listed in Table 56. The half-lives are reported in both tables rather than the rate-constants in order to make a more meaningful comparison between the different MAbs tested. The serum profiles from the free, and complexed B80.3 have been overlaid and are presented in Figure 27 to graphically illustrate the altered kinetic profiles.

Table 55: ^{99m}Tc-B80.3 pharmacokinetic parameters representing a two compartment model of the form $C(t) = C_1 e^{-\lambda_1 t} + C_z e^{-\lambda_z t}$.

Rabbit ID	C_1 % ID	C_z % ID	$T_{1/2\,1}$ (h)	$T_{1/2\,z}$ (h)	MRT (h)	Plasma Clr (mL/h)	Renal Clr (mL/h)
SAM07	61 ± 7.0	40 ± 7.7	5.6 ± 0.8	28 ± 4.9	33 ± 4.1	5.8 ± 0.3	2.6 ± 0.3
SAM08	64 ± 6.7	36 ± 7.4	5.5 ± 0.8	32 ± 6.5	37 ± 5.9	4.1 ± 0.3	1.6 ± 0.2
SAM10	57 ± 5.2	43 ± 5.7	4.8 ± 0.7	23 ± 2.3	27 ± 1.8	5.1 ± 0.1	1.7 ± 0.2
Mean	61 ± 3.5	40 ± 3.3	5.3 ± 0.5	28 ± 4.5	32 ± 5.0	5.0 ± 0.9	2.0 ± 0.6

Table 56: ^{99m}Tc-B80.3/PSA pharmacokinetic parameters representing a two compartment model of the form $C(t) = C_1 e^{-\lambda_1 t} + C_z e^{-\lambda_z t}$.

Rabbit ID	C_1 % ID	C_z % ID	$T_{1/2\,1}$ (h)	$T_{1/2\,z}$ (h)	MRT (h)	Plasma Clr (mL/h)	Renal Clr (mL/h)
SAM09	53 ± 4.4	48 ± 4.4	3.0 ± 0.5	17.2 ± 1.1	21.5 ± 0.9	6.6 ± 0.1	3.4 ± 0.3
SAM15	91 ± 16	10 ± 17	2.4 ± 0.4	17.0 ± 1.0	21.4 ± 0.9	6.9 ± 0.1	3.2 ± 0.3
SAM16	72 ± 7.6	27 ± 8.8	4.6 ± 0.9	19.1 ± 3.3	19.6 ± 1.5	6.2 ± 0.2	3.3 ± 0.3
Mean	72 ± 19	29 ± 9	3.3 ± 1.1	17.8 ± 1.2	20.8 ± 1.1	6.6 ± 0.4	3.3 ± 0.1

5.4.1.1 Routes of Elimination

Urine and fecal samples were collected and used to estimate ^{99m}Tc-B80.3 elimination patterns. As the rabbits practice coprophagy it was difficult to analyze fecal samples; however, as before, no recirculation patterns were observed in the serum kinetics and no bowel activity was observed on the gamma camera images for either the free or complexed form of the MAb. Even though a limited amount of radioactivity was observed in the feces and bile collected at necropsy (Table 66 and Table 67), it was not a significant when compared with the amount of activity injected. It was, therefore; assumed that biliary excretion did not play a major role in the elimination of the MAb. Figure 29 documents the ^{99m}Tc activity in the fecal contents for B80.3 and the PSA/B80.3 complex.

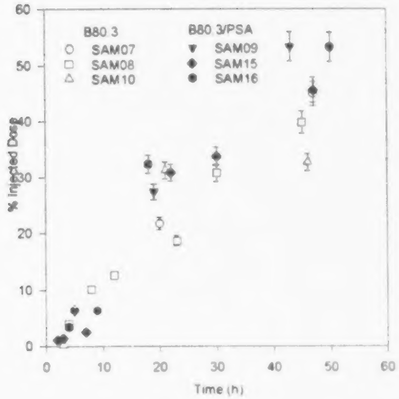

Figure 28: Renal elimination of ^{99m}Tc labelled B80.3 and B80.3/PSA in rabbits.

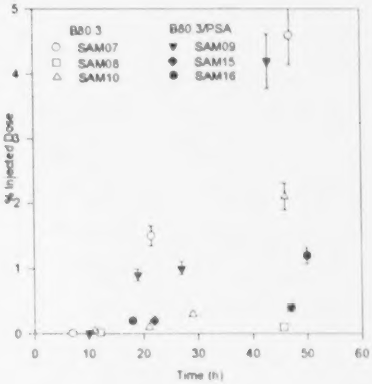

Figure 29: Fecal elimination of ^{99m}Tc labelled B80.3 and B80.3/PSA in rabbits.

Renal excretion was found to be the major route of elimination for the ^{99m}Tc label as illustrated in Figure 28 for B80.3 and PSA/B80.3. The labelled metabolites were not identified but were expected to be low molecular compounds such as glutathion or cysteine.

5.4.1.2 Gamma Camera Imaging

Gamma camera imaging was performed according to the protocol described in the Materials and Methods Section. The purpose of collecting image data was three-fold: 1) to test whether the two-compartment model obtained from the serum data could be expanded to include separate compartments for those organs demonstrating uptake as identified by RIS,

2) to search for similarities between rabbit and human uptake patterns and 3) search for different organ distribution patterns between the free and the complexed form of MAb B80.3. The image data in Table 57 through Table 59 tabulates the activity as the % injected dose (%ID) and %ID/gm for the liver, heart and two kidneys where the time period was the time elapsed in hours post-injection. Table 60 through Table 62 contains the image data from the three rabbits imaged with the B80.3/PSA complex. The right kidney is artificially high for SAM 9 due to overlaying bladder activity (11hr).

Table 57: SAM 7 organ activity obtained from quantitative gamma camera imaging of ^{99m}Tc-B80.3 expressed as a percentage of the injected dose (%ID).

Time (h)	Heart		Liver		Left Kidney		Right Kidney	
	%ID	%ID/gm	%ID	%ID/gm	%ID	%ID/gm	%ID	%ID/gm
0.27	5.4 ± 0 .5	1.01 ± 0.10	14.6 ± 0.5	0.15 ± 0.01	2.3 ± 0.2	0.28 ± 0.03	0.9 ± 0.1	0.12 ± 0.01
0.43	5.2 ± 0.5	0.97 ± 0.10	14.5 ± 1.5	0.15 ± 0.01	2.4 ± 0.2	0.30 ± 0.03	1.0 ± 0.1	0.13 ± 0.01
0.60	5.1 ± 0.5	0.94 ± 0.09	14.3 ± 1.4	0.14 ± 0.01	2.6 ± 0.3	0.32 ± 0.03	1.1 ± 0.1	0.14 ± 0.01
0.77	4.9 ± 0.5	0.91 ± 0.09	13.9 ± 1.4	0.14 ± 0.01	2.7 ± 0.3	0.34 ± 0.03	1.3 ± 0.1	0.15 ± 0.02
0.93	4.8 ± 0.5	0.89 ± 0.09	13.5 ± 1.4	0.14 ± 0.01	2.9 ± 0.3	0.36 ± 0.04	1.4 ± 0.1	0.17 ± 0.02
1.10	4.6 ± 0.5	0.86 ± 0.09	12.9 ± 1.3	0.13 ± 0.01	3.1 ± 0.3	0.38 ± 0.04	1.6 ± 0.2	0.19 ± 0.02
1.27	4.5 ± 0.5	0.83 ± 0.08	12.3 ± 1.2	0.12 ± 0.01	3.3 ± 0.3	0.41 ± 0.04	1.8 ± 0.2	0.22 ± 0.02
1.43	4.4 ± 0.4	0.82 ± 0.08	12.1 ± 1.2	0.12 ± 0.01	3.4 ± 0.3	0.42 ± 0.04	2.0 ± 0.2	0.24 ± 0.02
1.60	4.3 ± 0.4	0.79 ± 0.08	12.1 ± 1.2	0.12 ± 0.01	3.5 ± 0.4	0.43 ± 0.04	2.1 ± 0.2	0.26 ± 0.03
1.77	4.0 ± 0.4	0.74 ± 0.07	12.1 ± 1.2	0.12 ± 0.01	3.5 ± 0.4	0.44 ± 0.04	2.3 ± 0.2	0.28 ± 0.03
1.93	3.8 ± 0.4	0.71 ± 0.07	11.9 ± 1.2	0.12 ± 0.01	3.6 ± 0.4	0.45 ± 0.05	2.3 ± 0.2	0.28 ± 0.03
2.10	3.9 ± 0.4	0.72 ± 0.07	11.6 ± 1.2	0.12 ± 0.01	3.6 ± 0.4	0.44 ± 0.04	2.2 ± 0.2	0.27 ± 0.03
3.06	3.8 ± 0.4	0.71 ± 0.07	12.9 ± 1.3	0.13 ± 0.01	3.6 ± 0.4	0.45 ± 0.04	1.9 ± 0.2	0.23 ± 0.02
6.76	3.2 ± 0.3	0.60 ± 0.06	10.8 ± 1.1	0.11 ± 0.01	3.0 ± 0.3	0.36 ± 0.04	3.3 ± 0.3	0.40 ± 0.04
11.47	2.3 ± 0.2	0.42 ± 0.04	10.6 ± 1.1	0.11 ± 0.01	2.2 ± 0.2	0.27 ± 0.03	2.8 ± 0.3	0.34 ± 0.03
20.26	1.6 ± 0.2	0.29 ± 0.03	7.2 ± 0.7	0.07 ± 0.01	2.8 ± 0.3	0.34 ± 0.03	2.9 ± 0.3	0.35 ± 0.04
29.23	1.1 ± 0.1	0.20 ± 0.02	5.5 ± 0.6	0.06 ± 0.01	2.9 ± 0.3	0.36 ± 0.04	2.4 ± 0.2	0.30 ± 0.03
44.62	0.7 ± 0.1	0.12 ± 0.01	5.5 ± 0.6	0.06 ± 0.01	3.0 ± 0.3	0.37 ± 0.04	2.4 ± 0.2	0.29 ± 0.03

Table 58: SAM 8 organ activity obtained from quantitative gamma camera imaging of ^{99m}Tc-B80.3 expressed as a percentage of the injected dose (%ID).

Time	Heart		Liver		Left Kidney		Right Kidney	
(h)	%ID	%ID/gm	%ID	%ID/gm	%ID	%ID/gm	%ID	%ID/gm
0.13	4.43 ± 0.44	0.93 ± 0.09	17.5 ± 1.7	0.23 ± 0.02	0.95 ± 0.29	0.33 ± 0.03	1.04 ± 0.10	0.13 ± 0.01
0.29	4.26 ± 0.43	0.89 ± 0.09	17.5 ± 1.7	0.23 ± 0.02	2.83 ± 0.28	0.32 ± 0.03	1.25 ± 0.13	0.15 ± 0.02
0.46	4.01 ± 0.40	0.84 ± 0.08	16.9 ± 1.7	0.22 ± 0.02	2.97 ± 0.30	0.33 ± 0.03	1.44 ± 0.14	0.18 ± 0.02
0.63	3.81 ± 0.38	0.80 ± 0.08	17.2 ± 1.7	0.22 ± 0.02	3.29 ± 0.33	0.37 ± 0.04	1.57 ± 0.16	0.19 ± 0.02
0.79	3.88 ± 0.39	0.81 ± 0.08	16.6 ± 1.7	0.22 ± 0.02	3.26 ± 0.33	0.37 ± 0.04	1.71 ± 0.17	0.21 ± 0.02
0.96	3.50 ± 0.35	0.74 ± 0.07	16.3 ± 1.6	0.21 ± 0.02	3.40 ± 0.34	0.38 ± 0.04	1.83 ± 0.18	0.23 ± 0.02
1.13	3.52 ± 0.35	0.74 ± 0.07	16.2 ± 1.6	0.21 ± 0.02	3.53 ± 0.35	0.40 ± 0.04	1.97 ± 0.20	0.24 ± 0.02
1.29	3.29 ± 0.33	0.69 ± 0.07	15.3 ± 1.5	0.20 ± 0.02	3.69 ± 0.37	0.41 ± 0.04	2.11 ± 0.21	0.26 ± 0.03
1.46	3.25 ± 0.32	0.68 ± 0.07	15.3 ± 1.5	0.20 ± 0.02	3.84 ± 0.38	0.43 ± 0.04	2.22 ± 0.22	0.27 ± 0.03
1.63	3.18 ± 0.32	0.67 ± 0.07	15.3 ± 1.5	0.20 ± 0.02	3.99 ± 0.40	0.45 ± 0.04	2.34 ± 0.23	0.29 ± 0.03
1.80	3.11 ± 0.31	0.65 ± 0.07	15.2 ± 1.5	0.20 ± 0.02	4.10 ± 0.41	0.46 ± 0.05	2.48 ± 0.25	0.31 ± 0.03
1.96	3.06 ± 0.31	0.64 ± 0.06	14.9 ± 1.5	0.20 ± 0.02	4.20 ± 0.42	0.47 ± 0.05	2.53 ± 0.25	0.31 ± 0.03
3.05	2.92 ± 0.29	0.61 ± 0.06	16.3 ± 1.6	0.21 ± 0.02	4.00 ± 0.40	0.45 ± 0.04	3.28 ± 0.33	0.41 ± 0.04
7.15	3.82 ± 0.38	0.80 ± 0.08	13.5 ± 1.3	0.18 ± 0.02	2.98 ± 0.30	0.34 ± 0.03	3.54 ± 0.35	0.44 ± 0.04
12.13	2.20 ± 0.22	0.46 ± 0.05	11.3 ± 1.1	0.15 ± 0.01	3.84 ± 0.38	0.43 ± 0.04	3.99 ± 0.40	0.49 ± 0.05
21.90	1.56 ± 0.16	0.33 ± 0.03	10.9 ± 1.1	0.14 ± 0.01	2.82 ± 0.28	0.32 ± 0.03	4.49 ± 0.45	0.55 ± 0.06
30.09	1.47 ± 0.15	0.31 ± 0.03	7.5 ± 0.7	0.10 ± 0.01	3.42 ± 0.34	0.38 ± 0.04	2.88 ± 0.29	0.36 ± 0.04
44.76	0.86 ± 0.09	0.18 ± 0.02	6.8 ± 0.7	0.09 ± 0.01	3.20 ± 0.32	0.36 ± 0.04	3.05 ± 0.30	0.38 ± 0.04

Table 59: SAM 10 organ activity obtained from quantitative gamma camera imaging of ^{99m}Tc-B80.3 expressed as a percentage of the injected dose (%ID).

Time	Heart		Liver		Left Kidney		Right Kidney	
(h)	%ID	%ID/gm	%ID	%ID/gm	%ID	%ID/gm	%ID	%ID/gm
0.00	3.85 ± 0.39	0.80 ± 0.08	16.3 ± 1.6	0.17 ± 0.02	2.21 ± 0.22	0.22 ± 0.02	2.59 ± 0.26	0.26 ± 0.03
0.17	3.85 ± 0.38	0.80 ± 0.08	15.7 ± 1.6	0.17 ± 0.02	0.31 ± 0.23	0.23 ± 0.02	0.78 ± 0.28	0.28 ± 0.03
0.33	3.71 ± 0.37	0.77 ± 0.08	15.6 ± 1.6	0.17 ± 0.02	2.63 ± 0.26	0.26 ± 0.03	3.00 ± 0.30	0.30 ± 0.03
0.50	4.14 ± 0.41	0.86 ± 0.09	15.1 ± 1.5	0.16 ± 0.02	2.74 ± 0.27	0.27 ± 0.03	3.15 ± 0.31	0.31 ± 0.03
0.67	3.65 ± 0.36	0.76 ± 0.08	15.5 ± 1.5	0.17 ± 0.02	2.93 ± 0.29	0.29 ± 0.03	0.31 ± 0.33	0.33 ± 0.03
0.83	3.42 ± 0.34	0.71 ± 0.07	15.3 ± 1.5	0.16 ± 0.02	3.10 ± 0.31	0.31 ± 0.03	3.48 ± 0.35	0.34 ± 0.03
1.00	3.48 ± 0.35	0.72 ± 0.07	14.8 ± 1.5	0.16 ± 0.02	3.19 ± 0.32	0.32 ± 0.03	3.63 ± 0.36	0.36 ± 0.04
1.17	3.51 ± 0.35	0.73 ± 0.07	14.5 ± 1.4	0.16 ± 0.02	3.31 ± 0.33	0.33 ± 0.03	3.50 ± 0.35	0.35 ± 0.03
1.33	3.40 ± 0.34	0.71 ± 0.07	14.4 ± 1.4	0.15 ± 0.02	3.40 ± 0.34	0.34 ± 0.03	3.93 ± 0.39	0.39 ± 0.04
1.50	3.36 ± 0.34	0.70 ± 0.07	14.6 ± 1.5	0.16 ± 0.02	3.49 ± 0.35	0.35 ± 0.03	4.11 ± 0.41	0.41 ± 0.04
1.67	3.31 ± 0.33	0.69 ± 0.07	14.8 ± 1.5	0.16 ± 0.02	3.59 ± 0.36	0.36 ± 0.04	4.23 ± 0.42	0.42 ± 0.04
1.84	3.29 ± 0.33	0.68 ± 0.07	15.0 ± 1.5	0.16 ± 0.02	3.64 ± 0.36	0.36 ± 0.04	0.95 ± 0.39	0.39 ± 0.04
3.02	2.71 ± 0.27	0.56 ± 0.06	15.9 ± 1.6	0.17 ± 0.02	3.65 ± 0.37	0.36 ± 0.04	4.26 ± 0.43	0.42 ± 0.04
5.97	2.78 ± 0.28	0.58 ± 0.06	11.4 ± 1.1	0.12 ± 0.01	3.58 ± 0.36	0.35 ± 0.04	4.30 ± 0.43	0.43 ± 0.04
11.28	1.76 ± 0.18	0.37 ± 0.04	9.3 ± 0.9	0.10 ± 0.01	4.47 ± 0.45	0.44 ± 0.04	4.21 ± 0.42	0.42 ± 0.04
21.47	1.18 ± 0.12	0.25 ± 0.02	7.0 ± 0.7	0.07 ± 0.01	4.00 ± 0.40	0.40 ± 0.04	3.74 ± 0.37	0.37 ± 0.04
45.57	0.82 ± 0.08	0.17 ± 0.02	5.6 ± 0.6	0.06 ± 0.01	2.70 ± 0.27	0.27 ± 0.03	2.55 ± 0.26	0.25 ± 0.03

Table 60: SAM 9 organ activity obtained from quantitative gamma camera imaging of ^{99m}Tc-B80.3/PSA complex expressed as a percentage of the injected dose (%ID).

Time	Heart		Liver		Left Kidney		Right Kidney	
(h)	%ID	%ID/gm	%ID	%ID/gm	%ID	%ID/gm	%ID	%ID/gm
0.27	6.6 ± 0.7	1.55 ± 0.15	20.0 ± 2.0	0.18 ± 0.02	1.7 ± 0.2	0.29 ± 0.03	3.2 ± 0.3	0.16 ± 0.02
0.43	6.0 ± 0.6	1.41 ± 0.14	20.1 ± 2.0	0.18 ± 0.02	2.0 ± 0.2	0.29 ± 0.03	3.2 ± 0.3	0.18 ± 0.02
0.60	6.0 ± 0.6	1.41 ± 0.14	21.5 ± 2.2	0.19 ± 0.02	2.4 ± 0.2	0.34 ± 0.03	3.7 ± 0.4	0.22 ± 0.02
0.77	6.0 ± 0.6	1.41 ± 0.14	20.3 ± 2.0	0.18 ± 0.02	2.6 ± 0.3	0.38 ± 0.04	4.1 ± 0.4	0.24 ± 0 .02
0.93	5.9 ± 0.6	1.40 ± 0.14	21.0 ± 2.1	0.19 ± 0.02	2.9 ± 0.3	0.39 ± 0.04	4.3 ± 0.4	0.27 ± 0.03
1.10	5.5 ± 0.5	1.30 ± 0.13	21.2 ± 2.1	0.19 ± 0.02	3.1 ± 0.3	0.40 ± 0.04	4.4 ± 0.4	0.29 ± 0.03
1.27	5.6 ± 0.6	1.31 ± 0.13	21.2 ± 2.1	0.19 ± 0.02	3.3 ± 0.3	0.41 ± 0.04	4.5 ± 0.5	0.31 ± 0.03
1.43	5.3 ± 0.5	1.25 ± 0.12	21.8 ± 2.2	0.19 ± 0.02	3.4 ± 0.3	0.41 ± 0.04	4.5 ± 0.5	0.32 ± 0.03
1.60	5.0 ± 0.5	1.18 ± 0.12	22.0 ± 2.2	0.20 ± 0.02	3.6 ± 0.4	0.42 ± 0.04	4.6 ± 0.5	0.33 ± 0.03
1.77	5.0 ± 0.5	1.19 ± 0.12	22.2 ± 2.2	0.20 ± 0.02	3.7 ± 0.4	0.42 ± 0.04	4.6 ± 0.5	0.34 ± 0.03
1.93	5.1 ± 0.5	1.20 ± 0.12	20.9 ± 2.1	0.19 ± 0.02	3.6 ± 0.4	0.42 ± 0.04	4.7 ± 0.5	0.34 ± 0.03
2.10	5.2 ± 0.5	1.23 ± 0.12	21.0 ± 2.1	0.19 ± 0.02	3.6 ± 0.4	0.41 ± 0.04	4.5 ± 0.5	0.33 ± 0.03
3.06	5.1 ± 0.5	1.21 ± 0.12	26.3 ± 2.6	0.23 ± 0.02	4.3 ± 0.4	0.43 ± 0.04	4.7 ± 0.5	0.40 ± 0.04
6.76	3.7 ± 0.4	0.87 ± 0.09	21.1 ± 2.1	0.19 ± 0.02	5.8 ± 0.6	0.44 ± 0.04	4.9 ± 0.5	0.54 ± 0.05
11.47	3.6 ± 0.4	0.84 ± 0.08	20.7 ± 2.1	0.18 ± 0.02	4.8 ± 0.5	1.09 ± 0.11	*12.0 ± 1.2*	0.44 ± 0.04
20.26	2.2 ± 0.2	0.52 ± 0.05	18.3 ± 1.8	0.16 ± 0.02	5.7 ± 0.6	0.34 ± 0.03	3.7 ± 0.4	0.53 ± 0.05
29.23	1.3 ± 0.2	0.31 ± 0.03	14.3 ± 1.4	0.13 ± 0.01	4.3 ± 0.4	0.42 ± 0.04	4.6 ± 0.5	0.40 ± 0.04
44.62	1.2 ± 0.1	0.27 ± 0.03	12.7 ± 1.3	0.11 ± 0.01	3.2 ± 0.3	0.30 ± 0.03	3.3 ± 0.3	0.30 ± 0.03

Table 61: SAM 15 organ activity obtained from quantitative gamma camera imaging of ^{99m}Tc-B80.3/PSA complex expressed as a percentage of the injected dose (%ID).

Time	Heart		Liver		Left Kidney		Right Kidney	
(h)	%ID	%ID/gm	%ID	%ID/gm	%ID	%ID/gm	%ID	%ID/gm
0.17	1.5 ± 0.2	0.41 ± 0.04	19.8 ± 2.0	0.27 ± 0.03	0.9 ± 0.1	0.14 ± 0.01	1.0 ± 0.1	0.15 ± 0.01
0.33	4.1 ± 0.4	1.14 ± 0.11	16.3 ± 1.4	0.22 ± 0.02	1.3 ± 0.1	0.20 ± 0.02	1.1 ± 0.1	0.18 ± 0.02
0.50	4.0 ± 0.4	1.11 ± 0.11	16.8 ± 1.7	0.23 ± 0.02	1.5 ± 0.2	0.23 ± 0.02	1.3 ± 0.1	0.21 ± 0.02
0.67	4.0 ± 0.4	1.11 ± 0.11	18.5 ± 1.9	0.25 ± 0.03	1.8 ± 0.2	0.28 ± 0.03	1.6 ± 0.2	0.25 ± 0.03
0.83	4.4 ± 0.5	1.21 ± 0.12	17.3 ± 1.8	0.24 ± 0.02	1.4 ± 0.2	0.22 ± 0.02	1.2 ± 0.1	0.19 ± 0.02
1.00	3.5 ± 0.4	0.98 ± 0.10	19.6 ± 2.0	0.27 ± 0.03	2.0 ± 0.2	0.30 ± 0.03	1.5 ± 0.2	0.23 ± 0.02
1.17	3.6 ± 0.5	1.00 ± 0.10	19.7 ± 2.0	0.27 ± 0.03	1.8 ± 0.2	0.28 ± 0.03	1.9 ± 0.2	0.29 ± 0.03
1.33	2.7 ± 0.3	0.76 ± 0.08	20.1 ± 2.0	0.28 ± 0.03	2.1 ± 0.2	0.31 ± 0.03	1.9 ± 0.2	0.30 ± 0.03
1.50	3.1 ± 0.3	0.87 ± 0.09	19.8 ± 2.0	0.27 ± 0.03	2.3 ± 0.2	0.34 ± 0.03	1.7 ± 0.2	0.27 ± 0.03
1.67	3.0 ± 0.3	0.82 ± 0.08	19.1 ± 1.9	0.26 ± 0.03	2.6 ± 0.3	0.39 ± 0.04	2.4 ± 0.3	0.37 ± 0.04
1.83	2.9 ± 0.3	0.79 ± 0.08	19.1 ± 1.9	0.26 ± 0.03	2.5 ± 0.3	0.38 ± 0.04	2.6 ± 0.3	0.40 ± 0.04
2.00	2.5 ± 0.3	0.62 ± 0.06	17.7 ± 1.8	0.24 ± 0.02	2.6 ± 0.3	0.39 ± 0.04	2.3 ± 0.2	0.36 ± 0.04
2.50	2.0 ± 0.2	0.56 ± 0.06	18.8 ± 1.9	0.26 ± 0.03	2.8 ± 0.3	0.43 ± 0.04	3.2 ± 0.3	0.50 ± 0.05
7.00	2.2 ± 0.2	0.60 ± 0.06	20.4 ± 2.0	0.28 ± 0.03	2.8 ± 0.3	0.42 ± 0.04	3.0 ± 0.3	0.47 ± 0.05
12.00	1.7 ± 0.2	0.47 ± 0.05	21.2 ± 2.1	0.29 ± 0.03	3.3 ± 0.3	0.50 ± 0.05	4.1 ± 0.4	0.64 ± 0.06
22.00	1.3 ± 0.2	0.35 ± 0.03	20.8 ± 2.1	0.28 ± 0.03	3.8 ± 0.4	0.57 ± 0.06	3.4 ± 0.3	0.52 ± 0.05
30.00	1.2 ± 0.1	0.33 ± 0.03	16.5 ± 1.7	0.23 ± 0.02	3.2 ± 0.3	0.49 ± 0.05	2.6 ± 0.3	0.41 ± 0.04
46.00	1.4 ± 0.2	0.39 ± 0.04	12.3 ± 1.3	0.17 ± 0.02	2.0 ± 0.2	0.30 ± 0.03	2.2 ± 0.2	0.34 ± 0.03

Table 62: SAM 16 organ activity obtained from quantitative gamma camera imaging of ^{99m}Tc-B80.3/PSA complex expressed as a percentage of the injected dose (%ID).

Time (h)	Heart		Liver		Left Kidney		Right Kidney	
	%ID	%ID/gm	%ID	%ID/gm	%ID	%ID/gm	%ID	%ID/gm
0.00	3.36±0.34	0.85 ± 0.08	0.0 ± 0.0	0.00 ± 0.00	2.10 ± 0.21	0.28 ± 0.03	0.75 ± 0.07	0.10 ± 0.01
0.16	3.62 ± 0.36	0.92 ± 0.09	18.6 ± 1.9	0.24 ± 0.02	2.27 ± 0.23	0.31 ± 0.03	0.70 ± 0.07	0.09 ± 0.01
0.32	3.57 ± 0.36	0.90 ± 0.09	19.5 ± 1.9	0.25 ± 0.03	2.23 ± 0.22	0.30 ± 0.03	0.68 ± 0.07	0.09 ± 0.01
0.48	3.54 ± 0.35	0.90 ± 0.09	20.3 ± 2.0	0.27 ± 0.03	2.31 ± 0.23	0.31 ± 0.03	0.76 ± 0.08	0.10 ± 0.01
0.64	3.23 ± 0.32	0.82 ± 0.08	20.5 ± 2.1	0.27 ± 0.03	2.43 ± 0.24	0.33 ± 0.03	0.91 ± 0.09	0.12 ± 0.01
0.80	3.01 ± 0.30	0.76 ± 0.08	20.6 ± 2.1	0.27 ± 0.03	2.58 ± 0.26	0.35 ± 0.03	1.06 ± 0.11	0.14 ± 0.01
0.96	3.07 ± 0.31	0.78 ± 0.08	20.9 ± 2.1	0.27 ± 0.03	2.86 ± 0.29	0.39 ± 0.04	1.24 ± 0.12	0.16 ± 0.02
1.12	2.92 ± 0.29	0.74 ± 0.07	20.9 ± 2.1	0.27 ± 0.03	3.10 ± 0.31	0.42 ± 0.04	1.43 ± 0.14	0.19 ± 0.02
1.28	2.89 ± 0.29	0.73 ± 0.07	21.0 ± 2.1	0.27 ± 0.03	3.15 ± 0.31	0.43 ± 0.04	1.48 ± 0.15	0.19 ± 0.02
1.44	2.67 ± 0.27	0.68 ± 0.07	21.0 ± 2.1	0.27 ± 0.03	3.12 ± 0.31	0.42 ± 0.04	1.41 ± 0.14	0.19 ± 0.02
1.60	2.92 ± 0.29	0.74 ± 0.07	21.9 ± 2.2	0.29 ± 0.03	3.24 ± 0.32	0.44 ± 0.04	1.46 ± 0.15	0.19 ± 0.02
1.77	2.89 ± 0.29	0.73 ± 0.07	21.9 ± 2.2	0.29 ± 0.03	3.28 ± 0.33	0.44 ± 0.04	1.55 ± 0.15	0.20 ± 0.02
2.91	2.84 ± 0.28	0.72 ± 0.07	20.8 ± 2.1	0.27 ± 0.03	2.99 ± 0.30	0.40 ± 0.04	1.57 ± 0.16	0.21 ± 0.02
3.92	2.44 ± 0.24	0.62 ± 0.06	24.7 ± 2.5	0.32 ± 0.03	2.34 ± 0.23	0.32 ± 0.03	1.47 ± 0.15	0.19 ± 0.02
9.28	1.80 ± 0.18	0.46 ± 0.05	23.3 ± 2.3	0.30 ± 0.03	2.88 ± 0.29	0.39 ± 0.04	6.44 ± 0.64	0.85 ± 0.09
18.07	0.97 ± 0.10	0.25 ± 0.02	19.8 ± 2.0	0.26 ± 0.03	0.17 ± 0.32	0.43 ± 0.04	2.70 ± 0.27	0.36 ± 0.04
27.15	0.80 ± 0.08	0.20 ± 0.02	15.5 ± 1.6	0.20 ± 0.02	2.79 ± 0.28	0.38 ± 0.04	2.17 ± 0.22	0.29 ± 0.03
48.22	0.28 ± 0.03	0.07 ± 0.01	9.2 ± 0.9	0.12 ± 0.01	1.73 ± 0.17	0.23 ± 0.02	2.86 ± 0.29	0.38 ± 0.04

Pharmacokinetic models were developed for the heart and liver image data. Individual rate-constants were measured from the image data and were found to fit a variety of models ranging from a one or two compartment model with a bolus input to a one compartment model with a first order input for the liver B80.3/PSA. The half-lives for the distribution ($T_{1/2\,1}$) and terminal elimination phases ($T_{1/2\,z}$) and the mean residence time (MRT) are shown in Table 63 for ^{99m}Tc-B80.3 and in Table 64 for the ^{99m}Tc-B80.3/PSA complex.

Table 63: Organ kinetic parameters from quantitative RIS data of ^{99m}Tc labelled B80.3 MAb in rabbits (bolus input).

Rabbit ID	$T_{1/2\,1}$ (h)		$T_{1/2\,z}$ (h)		MRT (h)	
	Heart	Liver	Heart	Liver	Heart	Liver
SAM07	0.93 ± 0.24	0.50 ± 0.39	16.9 ± 0.7	34.1 ± 3.7	23.7± 0.9	48.9± 5.3
SAM08	0.50 ± 0.13	0.87 ± 0.45	24.1 ± 1.1	37.7 ± 3.3	34.4± 1.5	54.2± 4.7
SAM10	N/A	N/A	19.7 ± 1.5	28.6 ± 2.4	28.4± 2.2	41.3± 3.5
Mean	0.72 ± 0.30	0.69 ± 0.26	20.2 ± 3.63	33.5 ± 4.6	28.8± 5.4	48.1± 6.5

Table 64: Organ kinetic parameters from quantitative RIS data of ^{99m}Tc labelled B80.3/PSA complex in rabbits (bolus input).

Rabbit ID	$T_{1/2\,1}$ (h)		$T_{1/2\,z}$ (h)		MRT (h)	
	Heart	Liver	Heart	Liver	Heart	Liver
SAM09	1.8 ± 1.1	0.71 ± 2.5	20.8 ± 2.3	62.2 ± 11	29.0± 2.8	89.7 ± 16
SAM15	0.97 ± 0.26	0.77 ± 4.3	31.4 ± 9.5	135 ± 100	43.8 ± 13	195± 143
SAM16	0.55 ± 0.30	0.69 ± 4.7	14.0 ± 0.55	48.2 ± 2.4	20.0± 0.7	69.5±18
Mean	1.18 ± 0.88	0.70 ± 0.01	17.4 ± 4.8	55.2 ± 9.9	24.5± 6.4	79.6±14

As the liver kinetics also appeared to follow a first-order absorption phase followed by an exponential elimination component a second model was constructed to represent the data. The best fit to the liver for this type of model was determined to be a first-order absorption phase followed by a single component terminal elimination. These data are presented in Table 65 and are represented by kinetic model parameters: absorption phase half-life ($T_{1/2\,a}$), the elimination phase half-life ($T_{1/2\,z}$) and the time to maximum uptake (T_{max}).

The development of a pharmacokinetic model for the kidney was not possible for either the free or complexed MAb due to the unchanging nature of the activity over the time period studied.

Table 65: Kinetic parameters representing the biodistribution ^{99m}Tc labelled B80.3/PSA complex in the rabbit liver (first-order input).

Rabbit ID	$T_{1/2\,a}$ (h)	$T_{1/2\,z}$ (h)	T_{max} (h)
SAM09	0.084 ± 0.015	57.5 ± 4.5	0.80 ± 0.11
SAM15	0.070 ± 0.022	106 ± 39	0.73 ± 0.20
SAM16	0.070 ± 0.018	45.1 ± 6.1	0.65 ± 0.14
Mean	0.07 ± 0.01	69.5 ± 32	0.73 ± 0.0.8

5.4.1.3 Tissue Sampling

After the final image, a 5 mL blood sample was obtained by cardiac puncture and the animal sacrificed by lethal injection. Tissue samples were obtained from all rabbits at necropsy and assayed for ^{99m}Tc levels. This information is presented in Table 66 for the ^{99m}Tc-B80.3 and in Table 67 for the ^{99m}Tc-B80.3/PSA with organ values expressed as % injected dose/gm to facilitate a comparison between the rabbits. The mean and standard deviation for each organ is presented in the final column, decay corrected to 48 hours, for comparison with the other MAbs tested.

Table 66: Rabbit tissue sample data for ^{99m}Tc-B80.3 in % injected dose/gm at time-of death.

Tissue Sample	SAM 7 KBq/gm % ID/gm x 10^{-4} t = 44.6 h	SAM 8 KBq/gm % ID/gm x 10^{-4} t = 45.6 h	SAM 10 KBq/gm % ID/gm x 10^{-4} t = 46.2 h	Mean ± Std.Dev % ID/gm x 10^{-4} t = 48 h
Liver	3.02	4.79	2.97	2.70 ± 0.85
Spleen	4.35	4.89	3.27	3.14 ± 0.56
Heart	1.84	1.83	1.75	1.35 ± 0.01
Right Kidney	15.5	20.2	14.1	12.4 ± 2.6
Left Kidney	15.7	19.3	13.4	12.1 ± 2.3
Gall Bladder	2.67	4.68	3.06	2.62 ± 0.08
Bile	1.75	2.33	1.32	1.34 ± 0.04
Muscle	0.29	0.29	0.22	0.20 ± 0.002
Lung	3.18	2.22	2.97	2.08 ± 0.36

Table 67: Rabbit tissue sample data for ^{99m}Tc-B80.3/PSA.

Tissue Sample	SAM 9 KBq/gm % ID/gm x 10^{-4} t = 43.7 h	SAM 15 KBq/gm % ID/gm x 10^{-4} t = 46.85 h	SAM 16 KBq/gm % ID/gm x 10^{-4} t = 50.6 h	Mean ± Std.Dev % ID/gm x 10^{-4} t = 48 h
Liver	5.97	7.46	3.51	4.95 ± 1.5
Spleen	3.30	3.33	1.74	2.42 ± 0.5
Heart	1.50	0.92	0.83	0.83 ± 0.07
Right Kidney	15.2	14.5	7.09	10.5 ± 1.9
Left Kidney	15.0	14.6	7.15	10.5 ± 2.0
Gall Bladder	5.60	2.38	1.55	2.52 ± 0.8
Bile	3.42	2.18	0.42	1.52 ± 0.8
Muscle	0.21	0.12	0.07	0.11 ± 0.02
Lung	1.51	1.53	0.78	1.1 ± 0.2

5.4.2 Patient kinetics

Gamma camera images obtained from patients with prostate cancer showed high liver uptake and poor tumor imaging, thought to be due in part to the high levels of circulating antigen. It was also expected that the biodistribution of the MAbs in these patients might be altered from the distribution pattern observed for the other MAbs (170H.82 and 174H.64) for which there was no circulating antigen. In an attempt to measure this effect, two patients were selected, one with a low level of PSA (10 ng/mL) and another with a high level (2500 ng/mL).

Table 68: Patient data (E201981) following the injection of 2 mg of ^{99m}Tc-B80.3, PSA: 10 ng/mL.

ID: E201981 Time (hours)	Serum x 10^6 dpm/mL	% Injected Dose	Urine Time (hours)	Progressive Elimination %ID
0.08	24.0	99.9	6	1.6
0.60	23.7	98.4	12	6.2
3.60	18.5	76.9	18	7.9
22.73	11.6	48.0	24	10.8
43.73	6.64	27.6	30	13.2
70.15	2.86	11.9	36	15.1
			42	17.4
			48	18.7
			54	20.4
			60	21.8
			66	23.7
			72	25.0

Approximately 20 mL of normal saline containing 2 mg of ^{99m}Tc-B80.3 was infused iv to each patient over a period of 5 minutes. Serum samples were collected at selected time intervals up to 48 hours post-injection and urine samples collected in six hour intervals up to 72 hours post injection. All samples were counted in a multi-sample gamma counter and compared against a standard of known activity. The raw-counts obtained from the gamma counter were decay corrected and converted to a per cent of the injected dose using the spreadsheet QPRO. These results are shown in Table 68 and Table 69 and graphically summarized in Figure 30 and Figure 31.

Table 69: Patient data (E127971) following the injection of 2 mg of ^{99m}Tc-B80.3, PSA: 2500nl/mL.

ID: E127971 Time (hours)	Serum x 10^6 dpm/mL	% Injected Dose	Urine Time (hours)	Progressive Elimination %
0.27	33.6	97.3	N/A	N/A
0.88	30.2	87.5		
3.63	22.2	64.2		
5.72	20.8	60.2		
7.97	15.8	45.6		
9.97	14.2	41.1		
18.72	10.1	29.2		
21.30	8.5	27.6		
23.72	9.4	27.3		
26.72	8.1	23.5		
43.72	4.7	13.8		

The serum data were analyzed with PCNONLIN and used to develop a two compartment model ($C(t) = C_1 e^{-\lambda_1 t} + C_2 e^{-\lambda_2 t}$) or a one compartment model ($C(t) = C_1 e^{-\lambda_1 t}$). A two-compartment model representing the distribution of ^{99m}Tc-B80.3 was constructed using data obtained from the patient with the high level of PSA; however, there was insufficient data to adequately fit a two compartment model to the patient with the low PSA value. A one compartment model was used in this case. A summary of parameters representing coefficients of these models, the ^{99m}Tc serum kinetics, the plasma clearance and renal clearance are presented in Table 70, together with the standard error terms. The error terms are only approximate as they are based upon a linearization of a nonlinear model. The volume of distribution for all data sets was approximately equal to the blood volume within experimental error. The half-lives of the two compartments are reported rather than the rate-constants in order to make a more meaningful comparison between the different MAbs tested. It was not considered appropriate to calculate mean values for the kinetic parameters listed in Table 70 due to the wide disparity in PSA levels.

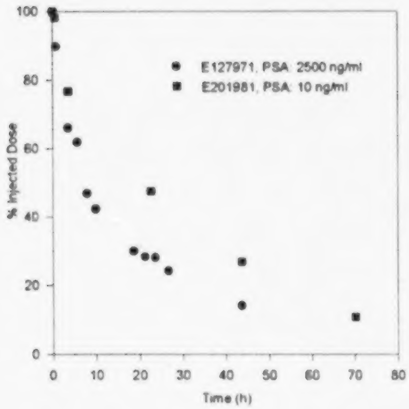

Figure 30: Variation with time of ^{99m}Tc-B80.3 serum levels expressed as a percentage of the injected dose.

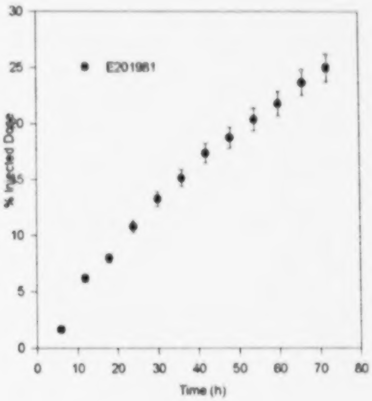

Figure 31: Renal excretion following the i.v. administration of ^{99m}Tc-B80.3.

Table 70: Pharmacokinetic parameters representing the biodistribution of ^{99m}Tc-B80.3. The standard error term is shown for each data point.

Patient ID	PSA ng/mL	C_1 (% ID)	C_2 (% ID)	$t_{½1}$ (h)	$T_{½z}$ (h)	MRT (h)	Plasma Clearance (mL/h)	Renal Clearance (mL/h)
E201981	10	N/A	N/A	N/A	23.5 ± 0.8	33.9 ± 1.2	110 ± 3.3	32.5 ± 1.6
E127971	2500	47.4 ±5.2	52.8 ±4.2	2.6 ± 0.4	22.6 ± 1.6	29.9 ± 1.7	164 ± 4.5	N/A

5.4.2.1 Radioimmunoassay

The assay was tested on human serum that had no measurable quantity of PSA. The reliability of the RIA was tested through the addition of known quantities of B80.3 to the serum to represent those levels expected in patient samples . However, all of the patients in this study had varying and elevated levels of PSA in their blood. Subsequent RIA analysis of this group of patients was not possible as the RIA utilized PSA as part of its assay[mm]. Although several alternate methods of separating the PSA from patient serum were attempted, (affinity and size exclusion chromatography, and precipitation with PAGE)[nn] they met with limited success and proved ineffective when combined with the RIA to measure B80.3 content in serum.

5.5 MAb-B43.13

Organs demonstrating significant uptake of the MAb as identified by RIS were noted and their corresponding activity calculated to 1) aid in the development of a multicompartmental model and 2) act as a source organ for radiation dosimetry measurements. Biodistribution patterns in the serum and urine were also measured.

5.5.1 Patient Kinetics

Kinetic data was collected from six patients with ovarian cancer receiving 2 mg of ^{99m}Tc-B43.13. These data were also used to estimate the radiation doses received by patients arising from RIS procedures based on the ^{99m}Tc-B43.13 MAb. In addition to the ^{99m}Tc data, ELISA techniques were used to determine the MAb-B43.13 content in serum and an RIA procedure estimated the serum CA 125 content.

[mm] Developed by Biomira Inc to monitor the immunoreactivity of the B80.3 MAb in a phosphate buffered solution.

[nn] Post-doctoral work of Dr. Matina Stathaki

5.5.1.1 Kinetic Modeling

A two-compartment model representing the distribution of ^{99m}Tc labelled MAb-B43.13 was constructed using data obtained from six patients diagnosed with ovarian cancer. Approximately 5 mL of normal saline containing 2 mg of MAb-B43.13 was injected iv into each patient over a period of 1 minutes. Serum samples were collected at selected time intervals up to 72 hours post-injection and urine samples collected in six hour intervals up to 72 hours post injection. All samples were counted in a single-sample gamma counter and compared against a standard of known activity. The raw-counts obtained from the gamma counter were decay corrected and converted to a percentage of the injected dose using the spreadsheet QPRO. These results are shown in Table 72 to Table 76 and graphically summarized in Figure 32 (serum) and Figure 33 (urine). All reported values are estimated to have an associated error of 10%.

Table 71: Patient serum and urine data (OVAREX-Gy-01-002) following the IV injection of 2 mg of ^{99m}Tc-B43.13.

Ovarex-002 Time (h)	Serum x 10^6 dpm/mL	% Injected Dose	Collection Time (h)	Urine (% ID)
0.47	18.0	90.7	6.75	5.5
1.83	13.8	69.8	10.75	13.5
3.53	12.1	61.1	18.75	14.8
4.25	10.1	51.1	24.75	18.6
22.25	6.0	30.0		

Table 72: Patient serum and urine data (OVAREX-Gy-01-001) following the IV injection of 2 mg of ^{99m}Tc-B43.13.

Ovarex-001 Time (h)	Serum x 10^6 dpm/mL	% Injected Dose	Collection Time (h)	Urine (% ID)
0.33	22.7	103.7	6.00	0.7
1.25	19.8	90.5	12.00	1.5
2.93	17.5	79.8	18.00	7.1
6.27	14.8	67.7	24.00	14.5
22.58	8.8	40.0	30.00	19.5
45.85	5.4	24.6	36.00	20.3
69.67	3.8	17.1	42.00	22.8
			48.00	24.2
			54.00	27.1
			60.00	28.7
			66.00	30.3
			72.00	31.2

Table 73: Patient serum and urine data (OVAREX-Gy-01-003) following the IV injection of 2 mg of ^{99m}Tc-B43.13.

Ovarex-003 Time (h)	Serum x 10^6 dpm/mL	% Injected Dose	Collection Time (h)	Urine (% ID)
0.10	18.2	99.9	6.27	11.0
0.45	17.0	92.9	12.27	18.1
1.98	15.3	83.9	18.27	23.1
6.48	11.0	60.2	24.27	25.5
22.40	6.3	34.6	30.27	28.9
45.27	3.7	20.2	36.27	29.6
			42.27	34.3
			48.27	35.5
			54.27	38.8
			60.27	42.0
			66.27	45.2
			72.27	47.5

Table 74: Patient serum and urine data (OVAREX-Gy-01-004) following the IV injection of 2 mg of ^{99m}Tc-B43.13.

Ovarex-004 Time (h)	Serum x 10^6 dpm/mL	% Injected Dose	Collection Time (h)	Urine (% ID)
0.32	13.6	101.3	6.15	8.2
0.98	11.8	87.7	12.15	9.3
5.40	9.1	67.6	18.15	17.9
23.43	4.8	35.6	24.15	20.1
48.15	2.5	18.2	30.15	21.3
71.35	1.7	12.5	36.15	22.1
			42.15	24.6
			48.15	27.4
			54.15	28.8
			60.15	30.0
			66.15	31.5
			72.15	32.8

Table 75: Patient serum and urine data (OVAREX-Gy-01-005) following the IV injection of 2 mg of ^{99m}Tc-B43.13.

Ovarex-002 Time (h)	Serum x 10^6 dpm/mL	% Injected Dose	Collection Time (h)	Urine (% ID)
0.25	19.2	98.5	6.17	5.9
0.50	18.5	95.0	12.17	14.3
1.00	17.3	88.9	18.17	14.3
4.17	14.2	72.6	24.17	22.7
5.75	11.6	59.7	30.17	25.2
22.75	6.6	33.9	36.17	27.0
45.25	4.3	22.1	42.17	30.7
			48.17	32.1

Table 76: Patient serum and urine data (OVAREX-Gy-01-006) following the IV injection of 2 mg of ^{99m}Tc-B43.13.

Ovarex-002 Time (h)	Serum x 10^6 dpm/mL	% Injected Dose	Collection Time (h)	Urine (% ID)
0.33	16.3	95.2	6.50	8.0
1.08	13.0	75.7	12.50	17.5
4.50	8.1	47.4	18.50	22.4
19.83	4.2	24.7	24.50	25.3
44.95	2.4	13.7	30.50	28.5
			36.50	30.3
			42.50	32.8
			48.50	34.2

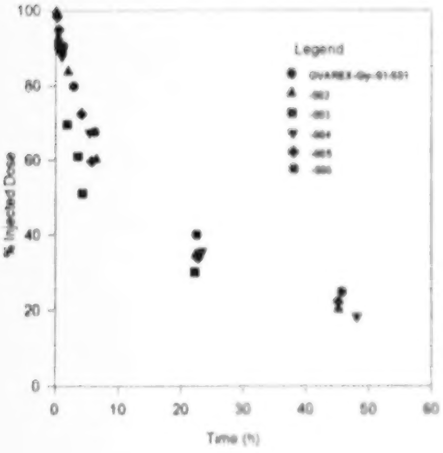

Figure 32: Biodistribution of ^{99m}Tc-B43.13 in patient serum.

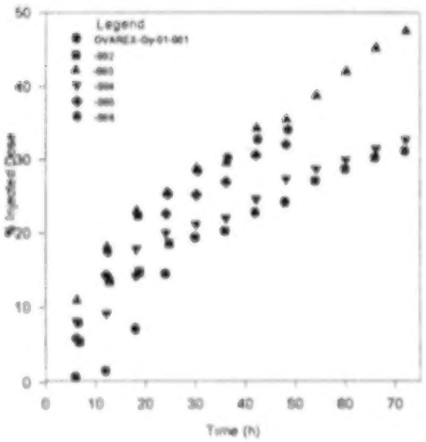

Figure 33: Urine elimination of ^{99m}Tc-B43.13 in patients.

Several assumptions were made prior to commencing a pharmacokinetic analysis, both to simplify the analysis and in recognition of the fact that the only information used in this model was that provided by the ^{99m}Tc label.

1. Due to the relatively short time interval of infusion (approximately 1 minute), an iv bolus input to the model was used.
2. All the radioactivity measured in the serum was assumed to be associated with the MAb.
3. Any transchelation of ^{99m}Tc that might occur (liver or kidney) was assumed to be removed from the general circulation.
4. No attempt has been made to resolve the different clearance rates between the serum and urine data. However, one may speculate that this difference is due in part to tissue binding of the transchelated ^{99m}Tc onto cysteine or glutathion. Alternately,

CA125-MAb immunoconjugates formed in the serum are likely to be removed by the RES, particularily the spleen as observed in the gamma camera images.

The results from the non-linear fitting analysis of the serum data could be best fit by a two-compartment model of the form: $C(t) = C_1 e^{-\lambda_1 t} + C_z e^{-\lambda_z t}$ as described earlier. The volume of distribution for all data sets was approximately equal to the blood volume within experimental error.

A summary of parameters representing coefficients from this equation that describe the ^{99m}Tc serum kinetics, the plasma clearance and renal clearance are presented in Table 77 together with the average value of the standard error terms. The error terms are only approximate as they are based upon a linearization of a nonlinear model. The half-lives are reported rather than the rate-constants in order to make a more meaningful comparison between the different MAbs tested. The mean and standard deviation data for each column are shown in the final row. Statistical analyses were performed using either SPSS or PCNONLIN.

Table 77: Model parameter values representing the serum biodistribution of ^{99m}Tc-B43.13.

OVAREX-	C_1 (% ID)	C_z (% ID)	$t_{½1}$ (h)	$t_{½z}$ (h)	MRT (h)	Plasma Clearance (mL/h)	Renal Clearance (mL/h)	Renal / Plasma
001	45 ± 5	55 ± 5	4.0 ± 1.0	39.9± 3.5	53.6 ± 3.9	76.5 ± 2.5	31.6 ± 3.2	0.41
002	51 ± 32	48 ± 38	1.7 ± 2.1	31.3 ± 49	42.9 ± 65	132 ± 119	57.3 ± 5.7	0.43
003	42 ± 4	57 ± 4	3.4 ± 0.5	30.1± 1.9	40.5 ± 2.2	125 ± 3.1	83.4 ± 8.3	0.67
004	42 ± 11	57 ± 11	3.6 ± 1.9	30.9± 5.9	41.5 ± 6.3	155 ± 11	61.2 ± 6.1	0.39
005	50 ± 6	50 ± 6	3.8 ± 0.8	39.1± 7.2	51.8 ± 8.7	103 ± 8.5	55.3 ± 5.5	0.54
006	60 ± 6	40 ± 4	1.8 ± 4	29.1± 3.4	38.6 ± 4.1	192 ± 8.9	94.4 ± 9.4	0.49
Mean	48 ± 3	51 ± 3	3.1 ± 0.4	33.4± 2.0	44.8 ± 2.6	131 ± 16	63.9 ± 22.3	0.49 ±0.1

5.5.1.2 ELISA: MAb-B43.13

The pharmacokinetics described above are based upon the assumption that the ^{99m}Tc is bound to the MAb and that one can infer the serum kinetics of the MAb by radioactivity measurements. However, the ^{99m}Tc label may be transchelated in the body, principally by the kidneys and liver[239]. This effect not withstanding, measurements of serum radioactivity may still be valid if the transchelated ^{99m}Tc remains primarily bound in the tissue until it decays. Similarly, if the ^{99m}Tc-B43.13/CA 125 immunoconjugate is removed by the RES, and the ^{99m}Tc does not re-enter blood circulation, measurements of serum radioactivity will still reflect the biodistribution of the radiolabelled MAb. It thus becomes necessary to obtain an independent assessment in order to validate the assumption: "The biodistribution of ^{99m}Tc-B43.13 can be estimated from serum radioactivity measurements".

The ELISA data were obtained directly from Biomira Research Inc. Their technique detected the presence of B43.13 in serum, independent of the radiolabel. The data were obtained over the same time period as the ^{99m}Tc data. Table 79 contains data from selected patients where the serum MAb-B43.13 levels have been normalized to the highest concentration, which was taken to represent 100% of the injected dose.

Table 78: Patient ELISA data expressed as a percentage of the injected dose at selected times post injection of ^{99m}Tc-MAb-B43.13.

OVAREX-003		OVAREX-004		OVAREX-005		OVAREX-006	
Time (h)	% ID	Time (h)	% ID	Time (h)	% ID	Time (h)	% ID
0.10	100	0.32	100	0.25	87.7	0.33	100
0.45	77.7	5.40	73.6	0.50	100.0	1.08	92.7
1.98	62.4	23.43	45.6	1.00	80.6	4.50	82.9
6.48	36.9	48.15	21.0	4.17	71.8	19.83	45.5
22.40	14.0	71.35	15.8	22.75	52.7	44.95	27.7
45.27	7.5			45.25	39.5		

In order to visualize the relationship between the ELISA and ^{99m}Tc data for this MAb, this information is presented graphically in Figure 34 for the patients described in Table 79.

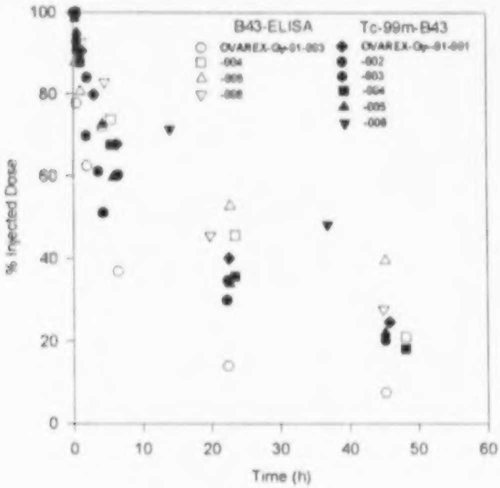

Figure 34: Serum ^{99m}Tc-B43.13 overlaid with the immunoreactive component of the MAb as identified by ELISA.

The ELISA data were analyzed with PCNONLIN and found to yield either a one or two-compartment model with a bolus-type input. The appropriate kinetic time constants are shown in Table 80.

Table 79: Pharmacokinetic parameters obtained from MAb-B43.13 ELISA data.

Patient ID	t½$_1$	t½$_2$	MRT
OVAREX-003	3.0 ± 0.8	26.0 ± 7.7	29.7 ± 7.2
OVAREX-004	2.1 ± 3.3	27.2 ± 5.7	38.5 ± 6.9
OVAREX-005	0.3 ± 0.09	47.7 ± 3.5	68.4 ± 5.1
OVAREX-006	N/A	21.0 ± 2.4	30.3 ± 3.5

5.5.1.3 RIA: CA125

The presence of circulating antigen was explored through the measurement of CA 125 levels in four of the six patients studied with ^{99m}Tc-MAb-B43.13 and are presented in Table 80. Serum CA 125 levels were measured by Biomira Research Inc. for the same group of patients discussed above. Patient 003 had the highest CA 125 concentration and also the highest urine elimination (47.5 %ID at 72h) with a concommitant high renal to plasma clearance ratio (Table 77).

Table 80: CA 125 levels following the injection of ^{99m}Tc-MAb-B43.13.

Patient 003		Patient 004		Patient 005		Patient 006	
Time (h)	CA 125(U/mL)	Time (h)	CA 125(U/mL)	Time (h)	CA 125(U/mL)	Time (h)	CA 125(U/mL)
0.0	760.8	0.0	68.6	0.0	66.0	0.0	73.0
0.1	210.7	0.3	2.1	0.3	6.6	0.3	21.6
0.5	240.9	1.0	3.4	0.5	0	1.1	22.6
2.0	144.3	5.4	0	1.0	0	4.5	10.9
6.5	277.1	23.4	0.7	4.2	2.8	19.8	6.1
22.4	307.6	48.2	4.6	22.8	5.2	45.0	1.0
45.3	323.8	71.7	2.1	45.3	4.0		
69.3	362.9						

5.5.1.4 Dosimetry

Standard MIRD schema as discussed in detail in previous sections was used to estimate the radiation dose to patients receiving 2 mg doses of ^{99m}Tc labelled monoclonal antibody, B43.13. The accumulation of the radiolabelled monoclonal antibodies were observed in several organs as identified by gamma camera imaging. Regions of interest (ROI) were drawn around these organs and used to develop time-activity curves for the liver, spleen, heart and kidney. The results from six patients are presented in the table below. The radiation dose was calculated using Quattro Pro for Windows using as source organs: the liver, spleen, kidneys, heart, the 'remainder of the body', and a dynamic bladder model. A summary of this data provided is reproduced in the table below.

Table 81: Mean radiation dose estimates following the administration of ^{99m}Tc-MAb-B43.13 for the target organs listed in the first column.

Target Organs	OVAREX-Gy-01-001 mrad/mCi	OVAREX-Gy-01-002 mrad/mCi	OVAREX-Gy-01-003 mrad/mCi	OVAREX-Gy-01-004 mrad/mCi	OVAREX-Gy-01-005 mrad/mCi	OVAREX-Gy-01-006 mrad/mCi	**Combined Mean** mrad/mCi
Adrenals	41.5	52.4	36.9	42.4	44.0	46.8	44.0 ± 5.3
Brain	19.0	19.4	17.1	17.6	18.9	19.4	18.6 ± 1.0
Breasts	19.9	21.0	18.7	18.7	20.7	20.2	19.9 ± 1.0
GB Wall	48.3	58.5	43.6	50.0	51.4	60.5	52.0 ± 6.4
LLI	31.5	34.9	29.0	29.8	31.9	35.0	32.0 ± 2.5
Sml Int	32.9	37.3	29.6	31.8	33.5	36.1	33.6 ± 2.8
Stomach	33.7	38.1	31.1	33.1	35.4	35.1	34.4 ± 2.4
ULI	34.2	38.8	30.8	33.3	35.0	38.2	35.1 ± 3.0
Heart Wall	86.2	90.0	94.9	76.8	100.9	66.0	85.8 ± 13
Kidney	118.2	235.9	73.4	131.6	120.5	116.5	133 ± 54
Liver	89.7	118.5	83.2	102.7	102.0	141.2	106 ± 21
Lungs	32.1	35.1	30.6	30.9	34.2	33.5	32.7 ± 1.8
Muscle	24.0	26.5	22.0	23.0	24.6	25.7	24.3 ± 1.7
Ovaries	33.4	37.2	30.9	31.7	34.0	37.0	34.0 ± 2.6
Pancreas	42.7	51.5	39.5	43.7	46.1	46.3	45.0 ± 4.0
Red Marr	26.9	29.8	24.3	25.7	27.4	28.4	27.1 ± 1.9
Bone Surf	42.5	46.3	38.7	40.5	43.4	44.9	42.7 ± 2.8
Skin	15.3	16.3	13.9	14.5	15.5	16.1	15.3 ± 0.9
Spleen	71.8	96.6	88.9	95.6	105.0	32.6	81.8 ± 27
Testes	22.6	24.7	20.9	21.2	22.8	25.1	22.9 ± 1.7
Thymus	31.3	32.5	30.4	28.8	33.2	29.4	30.9 ± 1.7
Thyroid	23.7	24.4	21.6	22.0	23.8	24.1	23.3 ± 1.2
UB Wall	102.4	146.8	106.8	102.0	111.7	159.4	121 ± 25
Uterus	36.6	42.6	34.4	35.0	37.6	43.5	38.3 ± 3.9
Tot Body	27.3	31.0	25.0	26.7	28.3	30.1	28.1 ± 2.2

6. DISCUSSION OF RESULTS

This chapter is organized in a manner to first determine whether intra-group differences exist between the MAbs grouped according to the presence (MAb-B43.13 and MAb-B80.3) or absence (MAb-170H.82 and MAb-174H.64) of circulating antigen. Corroborating data obtained from HPLC, ITLC, ELISA and RIA analyses of patient serum is shown to indicate that the kinetics obtained from the ^{99m}Tc radiolabel reflect those of the MAb. After the group biodistribution patterns were identified, an inter-group comparison was made. A section discussing the merits of expanding the basic two compartment model and a discussion on the radiation dosimetry of these ^{99m}Tc labelled MAbs conclude this section.

Rabbit studies were performed to assess the different biodistribution patterns of the MAbs in a species different from that in which the MAbs were derived. Where appropriate, these comparisons are correlated with available patient data. Dosimetric evaluations based on the rabbit data are compared with patient data for the 170H.82 MAb in the appropriate section.

6.1 Monoclonal Antibodies With No Circulating Antigen

This section will look for similarities in the biodistribution patterns of the ^{99m}Tc labelled 170H.82 and 174H.64 MAbs by testing the general form of the null hypothesis that *"There is no difference between the pharmacokinetic models that describe the biodistribution of the 170H.82 and 174H.64 MAbs"*. Individual kinetic parameters reflecting different aspects of the biodistribution of these MAbs were tested for significance through an appropriate modification of this general null hypothesis.

A statistical analysis of the ^{99m}Tc data was performed using either parametric or nonparametric tests, depending on sample variance. Homogeneity in sample variances[oo] was tested for each group to insure the validity of unpaired t-tests or simple factorial analysis of variance (ANOVA). If nonhomogeneity was found in the sample variance then appropriate nonparameteric tests were performed. A 95% confidence level was used for all tests of significance.

Rabbit serum and organ data was also compared using unpaired t-tests or ANOVA analyses. There was insufficient gamma camera image data available from the 174H.64 patient study to draw any statistical conclusions from variations in organ uptake values during RIS of the two MAbs. Observations unique to a particular MAb were discussed separately under the heading for that MAb. For MAb 170H.82, in which dosimetry figures were available, the suitability of using a rabbit model is discussed.

6.1.1 Rabbit Kinetics: MAb-170H.82 vs MAb-174H.64

The biodistribution of both the ^{99m}Tc labelled 170H.82 and the murine and chimeric forms of 174H.64 MAb was measured in normal, non-tumor bearing New Zealand White rabbits. Individual data from these experiments was summarized in the Experimental Section and only their interrelationships based on serum, RIS and tissue samples will be discussed here.

The serum clearance data are shown in Figure 35. The error bars (5% error) are about the same size as the symbols and so were not included for the sake of clarity. The two-compartment pharmacokinetic model parameters that describe these data are summarized in Table 82.

[oo] Levine's test for equalitiy of variance.

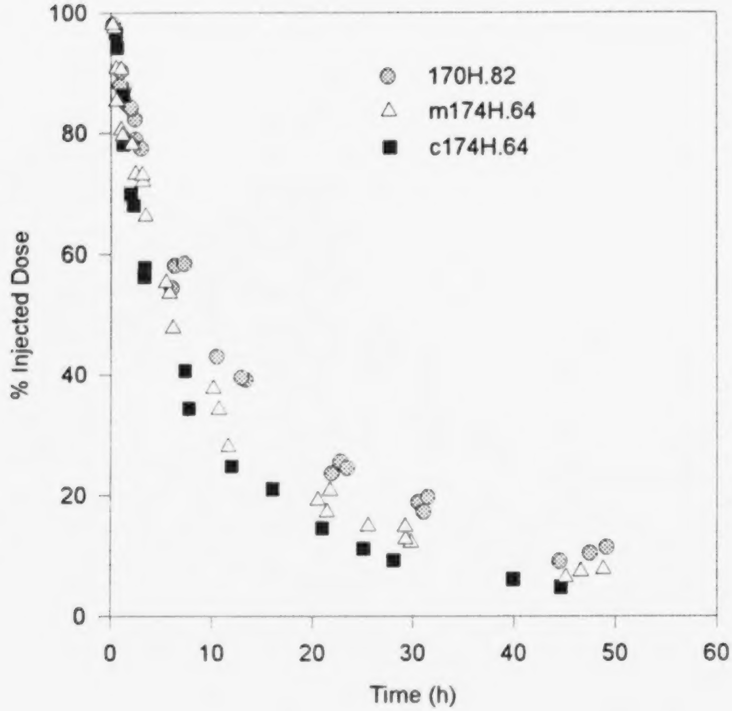

Figure 35: Serum biodistribution of ^{99m}Tc labelled 170H.82 and 174H.64 in rabbits.

The data listed in the two rows under the heading; Parametric Tests, in the table below show the statistical results of a comparison between these three MAbs. The second last row (t-test, c vs. m) contains p-values for an unpaired t-test between the chimeric and murine forms of MAb 174H.64 and the last row (f-test, all) contains the values from a single factorial ANOVA comparing the three MAbs (170H.82, m174H.64 and c174H.64) with each other. Data from this limited data set revealed no significant differences between the serum models at the 95% confidence level $(p<0.05)$.

Table 82: Comparison of the serum kinetic parameters representing ^{99m}Tc labelled 170H.82 and 174H.64 in rabbits.

MAb	C_1 % Inj. Dose	C_2 % Inj. Dose	$T_{\frac{1}{2}1}$ (h)	$T_{\frac{1}{2}2}$ (h)	MRT (h)
170H.82	40.5 ± 5.9	59.3 ± 6.0	3.5 ± 0.7	19.0 ± 2.1	24.8 ± 2.4
m174H.64	53.5 ± 21.8	44.8 ± 23.8	4.1 ± 0.87	21.1 ± 4.2	23.5 ± 3.0
c174H.64	61.4 ± 7.6	38.2 ± 7.7	2.8 ± 0.7	14.5 ± 1.5	17.0 ± 1.0
Statistical Test	**Parametric Tests**				
t-test, c vs. m	0.104	0.123	0.175	0.139	0.271
f-test, all	0.375	0.394	0.272	0.213	0.108

An attempt was made to model the biodistribution of these MAbs in organs identified visually by RIS. The heart, liver and left kidney were chosen as they were easily identified in all the rabbit images and also easily distinguished in patient RIS images. The various rabbit-organ models and their associated parameters are summarized in Table 83. Only the half-lives and mean residence time are presented due to the different types of models used to fit the data.

No significant difference was found in the two-compartment model that described the distribution in the heart and liver for either of the murine based MAbs or for the heart model representing all three of the MAbs. Although a one-compartment model was the best fit for the c174H.64 liver data, no significant difference was found between the terminal elimination phase and the mean residence time when compared to the murine forms of MAbs 170H.82 and 174H.64.

The only kidney data that could be modelled was that for MAb-170H.82. It was found to follow a first-order absorption phase followed by a single exponential elimination component. The ^{99m}Tc-m and c-174H.64 kidney concentration was approximately constant over the time period studied. There may have been a rate-limiting process, such as the transchelation of the ^{99m}Tc or other metabolic process, occurring in the kidney that might explain the relatively constant concentration of ^{99m}Tc. Due to the nature of the data, the comparison of kinetic liver models were not pursued further.

Table 83: A comparison of the kinetic models describing the biodistribution of the ^{99m}Tc labelled MAbs 170H.82 and 174H.64.

MAb	**$T_{1/2\,1}$(h)**		**$T_{1/2\,2}$ (h)**		**MRT (h)**	
	Heart	**Liver**	**Heart**	**Liver**	**Heart**	**Liver**
170H.82	1.80 ± 2.2	2.68 ± 1.6	19.1 ± 3.2	35.8 ± 5.7	24.6 ± 0.6	49.9 ± 9.2
m174H.64	1.59 ± 0.74	1.93 ± 1.36	26.3 ± 10.5	47.9 ± 2.0	34.4 ± 12.6	66.3 ± 5.0
c174H.64	2.25 ± 0.35	N/A	26.8 ± 14.5	28.5 ± 4.0	33.9 ± 19.4	41.1 ± 5.9
t-test, m vs. c	0.378	N/A	0.972	0.057	0.978	0.243
f-test all	0.950	0.499	0.721	0.181	0.706	0.199

Following euthanasia, tissue samples were taken from all the rabbits at the conclusion of the final image. To facilitate a comparison between the different MAbs, these data have been normalized to represent organ activity at 48 hours post-injection, as discussed in the experimental section. The accumulation of ^{99m}Tc in those organs selected at necropsy were compared in the last two columns of Table 84.

An unpaired t-test was used to compare differences between the murine and chimerized forms of MAb 174H.64. The results appear in column 5 (t-test, m vs. c) and show higher uptake in muscle tissue (heart and chest muscle) for the murine MAb. As no significant difference was found between the muscle or heart values for the murine forms of MAbs 170H.82 and 174H.64; this could imply that the elevated muscle uptake was related to the murine portion of the MAb, possibly the Fc region.

Organ uptake for all three MAbs were compared using a simple factorial ANOVA. The results appear in the last column of Table 84 (f-test, all) and reveal significant differences in the mean data for the heart and spleen.

These differences were explored using unpaired t-tests performed between the different MAb groups. The significance in the f-value in the spleen activity was isolated and found to be due to differences in the murine forms of 170H.82 and 174H.64 (p=0.033). It was noted that the chimeric 174H.64 spleen uptake was also higher than MAb-70H.82. This difference might possibly be attributed to the formation of an immune complex (or metabolic product) that localized in the spleen. A t-test using the kidney data from the murine forms of 170H.82 and 174H.64 disclosed a lower uptake in the 170H.82 MAb (p-value of 0.018 for the right kidney and p=0.019 for the left kidney). This lower value observed at 48 hours may be attributed to that fact that the activity in the kidneys of the 170H.82 group did not remain constant as was the case for the 174H.64 MAb but was observed to fall after the initial absorption phase.

Table 84: A comparison between rabbit tissue samples obtained at necropsy.

Tissue Sample	**170H.82** % ID/gm x 10^{-4}	**m174H.64** % ID/gm x 10^{-4}	**c174H.64** % ID/gm x 10^{-4}	**t-test m vs. c 174H.64**	**f-test, all**
Liver	2.38 ± 0.71	2.33 ± 0.16	2.16 ± 0.42	0.647	0.268
Spleen	1.32 ± 0.45	3.40 ± 0.80	2.19 ± 0.02	0.111	**0.017**
Heart	0.91 ± 0.12	0.98 ± 0.12	0.59 ± 0.07	**0.018**	**0.024**
Right Kidney	5.23 ± 2.0	14.5 ± 3.0	12.2 ± 6.8	0.706	0.072
Left Kidney	5.32 ± 2.2	14.6 ± 3.1	12.3 ± 7.3	0.718	0.085
Gall Bladder	2.32 ± 0.80	2.99 ± 0.11	2.97 ± 0.10	0.949	0.609
Bile	1.9 ± 1.4	2.61 ± 0.28	3.13 ± 3.0	0.865	0.849
Muscle	0.1 ± 0.06	0.15 ± 0.49	0.07 ± 0.04	**0.037**	0.123

6.1.2 Patient Kinetics: MAb-170H.82 vs MAb-174H.64

The serum data for the six murine-170H.82[pp], three murine and five chimeric 174H.64 patients are presented together in Figure 36 with their individual model coefficients and kinetic parameters summarized in Table 85. The error bars (5% error) are approximately the same size as the data points and have been removed from Figure 36 for clarity.

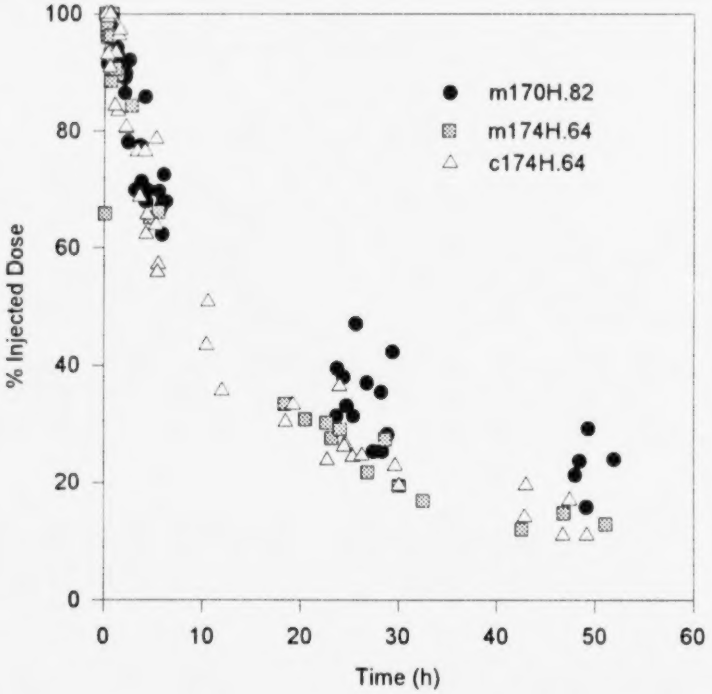

Figure 36: Biodistribution of ^{99m}Tc-170H.82 and ^{99m}Tc-174H.64 in patient serum.

[pp] No significant difference was found between the different dosages of MAb 170H.82. See the following section.

The data in the last two rows of Table 85 show the statistical results of a comparison between these three MAbs in patients. The second last row (t-test, c vs. m) contains p-values for an unpaired t-test between the chimeric and murine forms of MAb 174H.64 and the last row (f-test, all) contains the values from a single factorial ANOVA comparing the three MAbs (170H.82, m174H.64 and c174H.64) with each other.

The results from this limited data set revealed several significant differences at the 95% confidence level. Results from the simple factorial ANOVA show several differences between the 170H.82 and 174H.64 MAbs. The 170H.82 MAb has a slower wash-out as manifested by longer distribution and terminal elimination phases half-lives, a longer mean residence time and a lower plasma clearance. The results of the unpaired t-test indicate no significant difference between the two forms of MAb 174.H64. No value was reported for a renal clearance comparison between the murine and chimeric forms of MAb 174H.64 as Levine's test for equality of variance failed (i.e. parametric tests require that samples be drawn from populations with the same variance).

Table 85: A statistical comparison of the pharmacokinetic parameters representing biodistribution of ^{99m}Tc-170H.82 (murine) and ^{99m}Tc-174H.64 (murine and chimeric) in patient serum.

MAb	Statistic	C1 (%ID)	Cz (%ID)	$t_{\frac{1}{2}}1$ (h)	$T_{\frac{1}{2}}z$ (h)	MRT (h)	Plasma Clearance (mL/h)	Renal Clearance (mL/h)
170H.82		40.5 ± 12	61.2± 8.8	4.0 ± 0.8	39.6 ± 2.8	53.8 ± 3.2	68.6 ± 6.1	28.5 ± 1.4
m174H.64		33.5± 9.2	68.0± 6.5	3.0 ± 0.6	21.5 ± 4.7	29.3 ± 6.5	121 ±2 7.8	19.4 ± 3.3
c174H.64		44.4 ± 15	59.0 ± 12	2.7 ± 0.2	22.5 ± 1.3	27.6 ± 1.2	159 ± 16	61 ± 8
c vs. m	t-test	0.262	0.243	0.630	0.584	0.658	0.566	N/A
all	f-test	0.525	0.489	0.492	0.003	0.001	0.0124	0.002

Due to the apparent wide range in the variances of the model, parameters describing the serum distribution of the c174H.64 MAb (page 162) and the fact that Levine's test for equality of variance failed, several non parametric statistical tests were performed to test whether any significant differences existed between the murine and chimeric forms of 174H.64. P-values were obtained for the following tests of sample means: 1) Mann-Whitney U test, 2) Kolmogorov-Smirnov 2-sample test and 3) Wald-Wolfowitz runs test and are respectively reported in Table 86. As with the parametric test (t-test, c vs. m) no difference was found in the two compartment pharmacokinetic model representing the serum distribution of the murine and chimeric forms MAb 174H.64. It should be noted however, that the greatest restriction in this comparison was the small size of the data sets.

Table 86: A non-parametric comparison of the serum kinetic parameters (p-values) representing ^{99m}Tc labelled c174H.64 and m174H.64 in patients.

Statistic	C1 (%ID)	Cz (%ID)	$t_{\frac{1}{2}}1$ (h)	$T_{\frac{1}{2}}z$ (h)	MRT (h)	Plasma Clearance (mL/h)	Renal Clearance (mL/h)
Mann-Whitney	0.180	0.297	1.000	0.882	0.882	0.060	0.655
Kolmogorov-Smirnov	0.336	0.336	0.979	0.979	0.979	0.139	0.925
Wald-Wolfowitz	0.345	0.345	0.881	0.881	0.881	0.133	0.929

6.1.3 Monoclonal Antibody Dose

The effects of varying the dose levels were tested on a limited number of patients enrolled in the kinetic trials of the Phase II 170H.82 study. Three patients received 1 mg, one received 2 mg and two patients received 4 mg. The serum biodistribution for each patient is shown in Figure 12 and the kinetic parameters listed in Table 24. Although there was not enough data to test for significance, a comparison of the mean and standard deviation data for the three 1 mg doses with the corresponding values for the 2 and 4 mg dose did not reveal any obvious differences.

6.2 Monoclonal Antibodies With Circulating Antigen

The existence of a secreted or shed cell-surface antigen is generally considered an obstacle for RIS and RIT procedures. Circulating antigen can result in diminished tumor to nontumor uptake ratios, clinically adverse circulating MAb-antigen complexes and possibly false diagnoses due to accumulation of the antigen at nontumor sites.

Some of the early anti-CEA RIS programs observed that the circulating radiolabel was associated with a high molecular weight compound[241,242]. Surprisingly, many of these complexes are not cleared by the liver or spleen but appear to remain in circulation and may not even interfere with the successful imaging of tumors. The B72.3 MAb discussed above on page 25, has been successfully used in imaging colorectal cancer even though the TAG-72 antigen was present at elevated levels in about 60% of all patients[243]. It has been suggested that the MAb may have a higher affinity for the cellular bound antigen compared to the soluble blood borne antigen[244].

Even though some MAbs appear to retain their ability to localize at tumor sites in the presence of circulating antigen, this did not appear to be the case with the B80.3 MAb. Qualitatively[qq], high liver uptake was observed within 3 - 6 hours after injection and tumor localization was poor. As neither conjugate-view or whole-body gamma camera images were available for patients, only the similarities between the rabbit and patient pharmacokinetic models representing the serum biodistribution patterns of ^{99m}Tc labelled B80.3 were explored.

[qq] Counts per ROI were not available for this group of B80.3 patients

Patient kinetic data for the B43.13 MAb were obtained for both the ^{99m}Tc-labelled MAb and the MAb itself from ELISA measurements. Dosimetry estimates were calculated using RIS techniques. These data are discussed and compared with the other MAbs used in this report in the appropriate section below.

6.2.1 MAb-B80.3

The biodistribution in rabbits of ^{99m}Tc labelled B80.3 and B80.3/PSA complex was compared using serum and gamma camera image data. The serum data is summarized in Table 87, where the last row contains the t-test results and indicate no significant difference between these groups. There was insufficient patient data available to perform a statistical comparison with the rabbit model but patient data is included in Table 87 and Figure 37 to provide a visual comparison with the rabbit values.

Note that even though the patient with the low PSA serum concentration appears to have a longer elimination phase half-life (Figure 37), it was similar to the patient with the high PSA value (Table 87). The slopes of these terminal elimination phases are approximately parallel and are just displaced vertically. This implies that a greater concentration of the MAb is present in this final elimination phase for the "low" PSA patient compared to that of the patient with the high value of the PSA. The effect of the high levels of circulating antigen appear to cause a more rapid removal of the B80.3 from the serum as a result of B80.3/PSA complex formation. Although detailed image ROI data was not available, this statement was supported by the fact that higher liver and spleen uptake was observed in the patient with the high PSA levels. Note that a 1 mg MAb injection corresponds to a PSA:MAb ratio of approximately 150:1 for

PSA levels of 10ng/mL and 37,000:1 for 2500ng/mL, assuming a PSA distribution volume of 3L (serum).

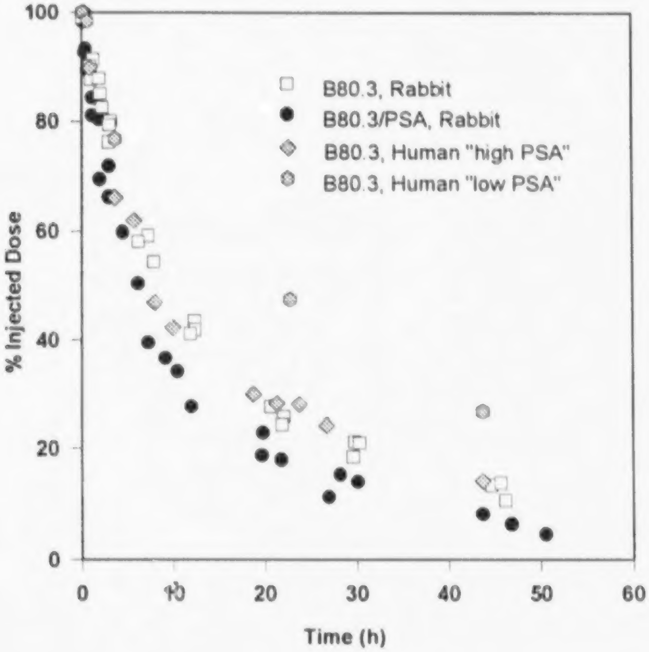

Figure 37: Serum biodistribution of ^{99m}Tc labelled B80.3 in patients and rabbits.

Table 87: A comparison of ^{99m}Tc-B80.3 serum kinetics in rabbits and patients.

MAb	C_1 % Inj. Dose	C_z % Inj. Dose	$T_{\frac{1}{2}1}$ (h)	$T_{\frac{1}{2}z}$ (h)	MRT (h)
B80 Rabbit	61 ± 3.5	40 ± 3.3	5.3 ± 0.5	28 ± 4.5	32 ± 5.0
B80/PSA Rabbit	72 ± 19	29 ± 19	3.3 ± 1.1	18 ± 1.2	21 ± 1.1
Patient: low PSA	N/A	N/A	N/A	23.5 ± 0.8	33.9 ± 1.2
Patient: high PSA	47.4 ±5.2	52.8 ±4.2	2.6 ± 0.4	22.6 ± 1.6	29.9 ± 1.7
Statistical Test	**Parametric Tests**				
t-test, rabbits	0.411	0.411	0.081	0.055	0.053

The model parameters representing rabbit heart and liver ^{99m}Tc activity obtained from gamma camera image data are presented in Table 88. Again no significance was found between these models. An alternative model was constructed for the liver of the B80.3/PSA group of rabbits as the liver data appeared to follow a first-order absorption phase. These data are also presented in Table 88 (row 3 - absorption). There was indicate no significant difference between the terminal elimination phases (t_z) of either liver model. Data from SAM15 was excluded from the calculation of the mean T_z values for the two groups due to the poor fit to the model.

This was the only group of rabbits for which an initial absorption-phase model of the liver was predicted (using the pharmacokinetic parameter estimation program, JANA). Inspection of the liver image data in Table 60 through Table 62 would indicate that the absorption model is probably a better choice than the two compartment iv bolus model. The absorption-phase model predicted a time-to-maximum uptake of approximately 45 minutes which contradicts one of the premises of the iv bolus model, that of "instantaneous uptake". The unchanging nature of the kidney data for both the B80.3 and B80.3/PSA rabbit groups did not permit the development of either a linear or nonlinear kinetic model.

Table 88: A comparison between ^{99m}Tc labelled B80.3 and B80.3/PSA heart and liver models in rabbits.

MAb	$T_{½\,1}$ (h)		$T_{½\,z}$ (h)		MRT (h)	
	Heart	**Liver**	**Heart**	**Liver**	**Heart**	**Liver**
1) B80.3	0.72 ± 0.30	0.69 ± 0.26	20.2 ± 3.63	33.5 ± 4.6	28.8 ± 5.4	48.1 ± 6.5
2) B80.3/PSA	1.18 ± 0.88	0.70 ± 0.01	17.4 ± 4.8	55.2 ± 9.9	24.5 ± 6.36	79.6 ± 14.3
3) Absorption	N/A	N/A	N/A	51.3 ± 8.8	N/A	N/A
t-test, 1 vs. 2	0.594	0.949	0.560	0.163	0.513	0.164
f-test all	N/A	N/A	N/A	0.058	N/A	N/A

Differences in organ uptake between the free ^{99m}Tc-B80.3 MAb and the ^{99m}Tc-B80.3/PSA MAb/Ag complex were measured from tissue samples collected during necropsy and decay corrected to 48 hours post-injection. These data are presented in Table 89 and indicate higher heart and chest muscle uptake in those rabbits receiving uncomplexed MAb. The enhanced muscle uptake in those rabbits receiving the free MAb may be due to a low affinity receptor for this MAb in muscle tissue. A comparison of B80.3 muscle uptake with MAbs 170H.82 and 170H.64 appear in the next section.

Table 89: Rabbit tissue sample data for ^{99m}Tc-B80.3 presented as the % injected dose/gm (% ID/gm) at 48 h post-injection.

Tissue Sample	**B80.3** % ID/gm x 10^{-4}	**B80.3/PSA** % ID/gm x 10^{-4}	**t-test**
Liver	2.70 ± 0.85	5.49 ± 2.4	0.099
Spleen	3.14 ± 0.56	2.66 ± 0.09	0.181
Heart	1.35 ± 0.01	0.90 ± 0.12	**0.002**
Right Kidney	12.4 ± 2.6	11.5 ± 3.8	0.360
Left Kidney	12.1 ± 2.3	11.5 ± 3.9	0.409
Gall Bladder	2.62 ± 0.08	2.7 ± 0.66	0.898
Bile	1.34 ± 0.04	1.67 ± 0.98	0.769
Muscle	0.20 ± 0.002	0.12 ± 0.024	**0.005**

6.2.2 MAb-B43.13

The serum biodistribution of ^{99m}Tc-Mab-B43.13 in patients was measured and was found to fit a two compartment model, similar to that for the other Mabs tested. ELISA data describing the biodistribution of MAb-B43.13, independent of the ^{99m}Tc label, was found to fit a similar model. The kinetic parameters describing these models, including dosimetric estimates obtained from gamma camera images were presented in the previous chapter.

Over the time period studied, there appeared to be little difference between MAb-B43.13 as measured by ELISA, compared to the ^{99m}Tc-labelled MAb-B43.13 (Figure 34). However, in order to explore the significance of these data, the kinetic parameters representing the time distribution of both the B43.13 and the ^{99m}Tc label were compared using an unpaired t-test, with the p-values reported in Table 90. No significant difference was found between the distribution-phase half-life, the terminal elimination-phase half-life or the mean residence times. Differences in the serum kinetic model and the radiation doses will be explored in the next section.

Table 90: T-test values comparing ^{99m}Tc-MAb-B43.13 and MAb-B43.13 kinetics.

t-test	$t\frac{1}{2}_{1}$	$t\frac{1}{2}_{z}$	MRT
^{99m}Tc-B43.13 vs. B43.13	0.253	0.653	0.763

The circulating antigen, CA125, was quantified for a subgroup of these patients and presented in Table 80. It was observed that the CA 125 levels dropped after injection in all cases. One explaination for this drop could be due to the formation MAb-B43.13/CA 125 complexes, which are cleared from the circulation by the RES. This was confirmed by RIS where a spleen uptake of ^{99m}Tc-MAb-B43.13 was observed in all six patients.

6.3 InterMAb Kinetic Comparison

A comparison between MAbs 170H.82, 174H.64, B43.13 and B80.3 labelled with ^{99m}Tc was performed to test whether a single serum-based pharmacokinetic model could describe the in vivo distribution of these MAbs. The serum data for these patients are presented visually in Figure 38 and the parameters that describe the two-compartment model representing their biodistribution are shown in Table 91. Two loosely grouped data sets can be visualized in Figure 38; 1) MAb 170H.82 and the "low" PSA, B80.3 patient and 2) the B43.13, 174H.64 MAbs (murine and chimeric) and the B80.3 patient with the high level of circulating antigen.

Table 91: Pharmacokinetic parameters describing the serum distribution of ^{99m}Tc labelled 170H.82, 174H.64, B43.13 and B80.3 in patients.

MAb	C_1 %ID	C_z %ID	$T_{\frac{1}{2}1}$ (h)	$T_{\frac{1}{2}z}$ (h)	MRT (h)
m-170H.82	40.5 ± 12	61.2± 8.8	4.0 ± 0.8	39.6 ± 2.8	53.8 ± 3.2
m-174H.64	33.5± 9.2	68.0± 6.5	3.0 ± 0.6	21.5 ± 4.7	29.3 ± 6.5
c-174H.64	44.4 ± 15	59.0 ± 12	2.7 ± 0.2	22.5 ± 1.3	27.6 ± 1.2
m-B43.13	48.3 ± 2.8	51.2 ± 2.7	3.1 ± 0.4	33.4 ± 2.0	44.8 ± 2.6
B80.3,high PSA	47.4 ±5.2	52.8 ±4.2	2.6 ± 0.4	22.6 ± 1.6	29.9 ± 1.7
B80.3, low PSA	N/A	N/A	N/A	23.5 ± 0.8	33.9 ± 1.2
Statistical Test	**Parametric Test**				
t-test, 170 vs. 174	0.654	0.351	0.261	**< 0.001**	**< 0.001**
t-test, 170 vs. B43.13	0.249	0.880	0.548	**0.028**	**0.017**
t-test, 174 vs. B43.13	0.142	**0.047**	0.695	**0.013**	**0.008**

As there was no difference in the models describing the murine and chimeric 174H.64 MAbs, these data were pooled and compared against the parameters describing the serum disposition of MAbs 170H.82 and B43.13. The results are presented in Table 91 and indicate that there was a significant difference in the terminal elimination phase and the mean residence times for the ^{99m}Tc labelled: 1) 170H.82 versus 174H.64 Mabs, 2) B43.13 versus 170H.82 and 3) B43.13 versus 174H.64. In order of ascending biological elimination half-lives, the MAbs may be ranked as 174H.64, B43.13 and 170H.82. Due to the limited data sets describing the B80.3 MAbs, these data were not included in the statistical comparison.

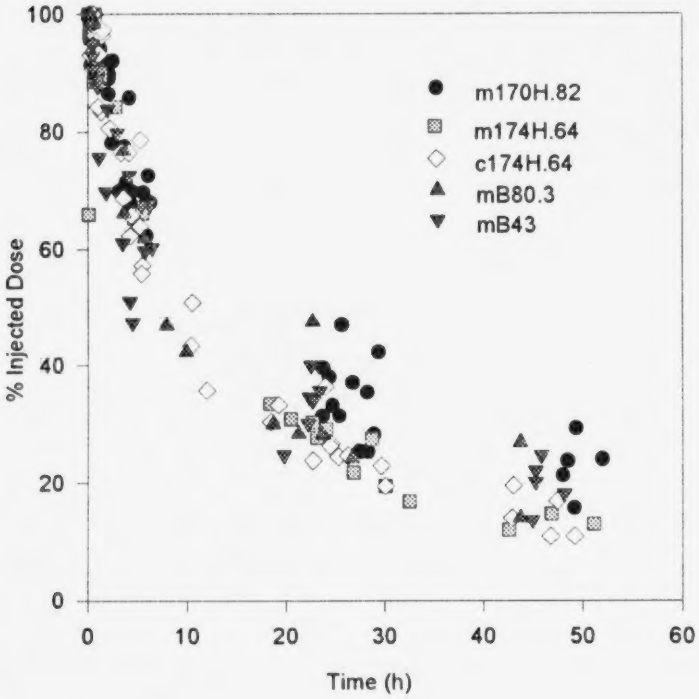

Figure 38: Serum data representing the biodistribution of ^{99m}Tc labelled 170H.82, 174H.64, B43.13 and B80.3 in patients.

This difference was explored in rabbits for the 170H.82, 174H.64 and B80.3 Mabs to test the validity of the rabbit model in predicting the biodistribution of these MAbs patient serum. The ANOVA results for a comparison between MAb groups are shown in the second-last row (f-test, all) of Table 92 and indicate a significant difference in the distribution, terminal elimination phase and mean residence times that describe these models. This difference was isolated to the free B80.3 MAb as shown by the ANOVA results in the last row of this table (f-test, -B80.3). The free ^{99m}Tc labelled B80.3 had a longer serum residence time compared to the other MAbs.

Table 92: Pharmacokinetic parameters describing the serum distribution of ^{99m}Tc labelled 170H.82, 174H.64 and B80.3 in rabbits.

MAb	C_1 % Inj. Dose	C_z % Inj. Dose	$T_{1/2 1}$ (h)	$T_{1/2 z}$ (h)	MRT (h)
m-170H.82	40.5 ± 5.9	59.3 ± 6.0	3.5 ± 0.7	19.0 ± 2.1	24.8 ± 2.4
m-174H.64	53.5 ± 21.8	44.8 ± 23.8	4.1 ± 0.87	21.1 ± 4.2	23.5 ± 3.0
c-174H.64	61.4 ± 7.6	38.2 ± 7.7	2.8 ± 0.7	14.5 ± 1.5	17.0 ± 1.0
B80.3	61 ± 3.5	40 ± 3.3	5.3 ± 0.5	28 ± 4.5	32 ± 5.0
B80.3/PSA	72 ± 19	29 ± 19	3.3 ± 1.1	18 ± 1.2	21 ± 1.1
Statistical Test	**Parametric Test**				
f-test, all	0.198	0.246	**0.024**	**0.016**	**0.007**
f-test, -B80.3	0.214	0.258	0.382	0.207	0.081

The difference in the rabbit serum model was explored by observing the 48 hour tissue distribution for all the MAbs tested. The ANOVA results are shown in Table 93 and show significant differences for the heart (B80.3 and c174H.64), muscle (B80.3), spleen (170H.82) and liver (B80.3/PSA). These differences were isolated from the group by performing individual f-tests on the whole data set with the suspected group removed. An explanation for some of these differences might include: 1) The longer residence times for B80.3 might be due in part to the increased uptake in the peripheral tissues (muscle); the heart muscle also exhibited increased uptake for this group. 2) The high liver uptake of the B80.3/PSA complex could possibly have been due to the liver actively removing this complex from the serum, as noted by the decreased residence time for the B80.3/PSA compared to the free B80.3 MAb. 3) The reduced muscle and cardiac uptake of c174H.64 MAb may be explained by the differences in the Fc portion of the MAb. There may have been a weak-affinity receptor in muscle tissue for the murine-coded Fc region on the other Mabs.

Table 93: A comparison of ^{99m}Tc activity in selected tissues at 48 hours post-injection for MAbs 170H.82, 174H.64 and B80.3.

Tissue Sample	**170H.82** %ID/gm x 10^{-4}	**m174H.64** %ID/gm x 10^{-4}	**c174H.64** % ID/gm x 10^{-4}	**B80.3** % ID/gm x 10^{-4}	**B80.3/PSA** % ID/gm x 10^{-4}	**f-test All**
Liver	2.38 ± 0.71	2.33 ± 0.16	2.16 ± 0.42	2.70 ± 0.85	**5.49 ± 2.4**	**0.010**
Spleen	**1.32 ± 0.45**	3.40 ± 0.80	2.19 ± 0.02	3.14 ± 0.56	2.66 ± 0.09	**0.009**
Heart	0.91 ± 0.12	0.98 ± 0.12	**0.59 ± 0.07**	**1.35 ± 0.01**	0.90 ± 0.12	**< 0.001**
Right Kidney	5.23 ± 2.0	14.5 ± 3.0	12.2 ± 6.8	12.4 ± 2.6	11.5 ± 3.8	0.055
Left Kidney	5.32 ± 2.2	14.6 ± 3.1	12.3 ± 7.3	12.1 ± 2.3	11.5 ± 3.9	0.067
Gall Bladder	2.32 ± 0.80	2.99 ± 0.11	2.97 ± 0.10	2.62 ± 0.08	2.7 ± 0.66	0.856
Bile	1.9 ± 1.4	2.61 ± 0.28	3.13 ± 3.0	1.34 ± 0.04	1.67 ± 0.98	0.784
Muscle	0.1 ± 0.06	0.15 ± 0.49	0.07 ± 0.04	**0.20 ± 0.002**	0.12 ± 0.03	**0.012**

6.4 Kinetic Modeling

The practicality of expanding the serum-based rabbit kinetic model using organ image data was explored and the influence of organ blood-flow on the activity observed in the gamma camera images was taken into account during the modelling process. Observations and interrelations between serum radioactivity, RIA and HPLC patient data were explored. The suitability of the rabbit model in assessing patient kinetics and radiation dosimetric models was investigated.

In the Experimental section, a rabbit pharmacokinetic model was developed to represent the biodistribution of ^{99m}Tc labelled 170H.82 in the serum and selected organs as identified by RIS. The two-compartment serum model appeared to be related to blood-flow, as highly perfused organs such as the liver and kidneys were observed to reach rapid equilibrium with the blood as confirmed by RIS (5 second dynamic images). This implied that the blood and all readily accessible fluids and tissues could be treated kinetically as a common homogeneous 'central compartment'. The second compartment contained those tissues that were poorly perfused. Even though the MAb levels may change at different rates, these rates are generally very similar and could not be differentiated based solely on serum data. Consequently, these poorly perfused tissues were lumped together into a single 'peripheral compartment'.

The effect of blood-flow on an organ-based kinetic model was estimated using ^{99m}Tc labelled blood cells. A rabbit red blood-cell labelling experiment (page 104) was performed to estimate the blood-flow in each of the organs identified by RIS as approximately 3% of the injected dose in the heart, 16% in the liver and 4 - 5% in each kidney. As the heart RIS kinetic data was representative of the blood (Table 95), liver/heart and kidney/heart ratios were calculated with time to illustrate how these organs deviate from the two compartment serum model (Table 94). A constant ratio would be expected if these organs were from the same compartment. The first row of this table shows the expected ratio based only on blood flow from the red blood-cell (rbc) labelling data.

Table 94: Organ/heart ratios for RIS data.

SAM04			SAM06			SAM11		
Time (h)	Liver	Kidney	Time (h)	Liver	Kidney	Time (h)	Liver	Kidney
rbc	5.7	1.5	rbc	5.7	1.5	rbc	5.7	1.5
0.00	2.1	0.28	0.25	2.3	0.31	0.00	3.1	0.41
0.25	2.6	0.31	0.50	1.8	0.20	0.17	3.4	0.45
0.50	2.5	0.31	0.75	2.1	0.37	0.33	3.4	0.49
0.75	2.4	0.31	1.00	2.4	0.35	0.50	3.6	0.53
1.00	2.6	0.34	1.25	2.7	0.43	0.67	3.7	0.58
1.25	2.5	0.36	1.50	2.5	0.41	0.83	3.8	0.63
1.50	2.5	0.38	1.75	2.9	0.47	1.00	3.8	0.64
1.75	2.2	0.35	2.00	3.0	0.51	1.17	3.7	0.66
2.00	2.5	0.41	2.25	2.9	0.50	1.33	3.5	0.67
2.25	2.7	0.42	2.50	2.9	0.46	1.50	3.5	0.69
10.70	4.3	1.17	2.75	3.0	0.46	1.67	3.6	0.72
21.14	5.1	0.98	3.00	3.1	0.43	1.84	3.5	0.72
29.42	5.6	1.06	7.70	10.0	2.21	3.16	2.5	0.63
47.01	7.1	1.47	13.20	10.3	2.06	7.11	4.7	1.15
			22.57	5.7	1.18	12.14	3.4	1.27
			29.93	3.2	0.55	23.15	5.0	1.80
			49.30	3.2	0.57	30.65	7.0	2.86
						44.33	7.2	2.82

Within experimental error, the initial organ uptake was related mainly to blood-flow indicating no significant first-pass uptake effect. These data indicated increased uptake in the liver and kidney with time that could not be predicted soley by the blood content of that organ. These uptake patterns were not entirely unexpected as the liver and kidneys are major metabolic sites for the transchelation of the ^{99m}Tc from the MAb. The increased activity in the kidneys could also be related to its role as the main route of ^{99m}Tc excretion.

One of the goals of these experiments was to try and expand this two compartment model and to identify some of its components. The liver, heart and kidneys were identified from gamma camera images as major organs of ^{99m}Tc uptake. Separate compartments for the liver and kidney were considered important as these organs are the major biotransformation sites where transchelation of the ^{99m}Tc from the MAb may be expected to occur (see Chapter 2). In addition, the kidneys also served as the main route of elimination for the metabolized MAb. The observed heart activity was most likely related to blood flow from the highly perfused heart tissue and the contents of the heart chambers. A model describing the disposition of ^{99m}Tc-170H.82 with time in the heart was developed to confirm this supposition.

Other smaller compartments having important roles in the biodistribution or pharmacodynamic behaviour of the MAbs almost surely exist. For instance, only small quantities of a MAb may be required to provoke an immune response which may provide a beneficial aid for therapy. The selection of these three organs was not meant to down-play the importance of other compartments, only that these were the main organs identified with the analytical techniques available.

For example, differences in the biodistribution of ^{99m}Tc labelled MAb-170H.82 in rabbits for selected organs were reflected in the half-lives ascribed to the different compartments of the associated models and their mean residence times. Serum model parameters are presented in Table 11, the heart and liver models in Table 15 and kidneys in Table 16 (Experimental section). As expected the serum and heart models do not significantly differ from each other as shown by the results of an unpaired t-test in Table 95. However, the coefficients representing the liver model were significantly different from the serum and could be used to develop a third compartment. The kidney RIS data was best fit by a first order absorption phase followed by a single component terminal-elimination phase. Although there was insufficient data to test for significance using the kidney data, the data indicate a fourth compartment could be added to the model on the basis that the kidney ^{99m}Tc-MAb-170H.82 data was described by a different model. A model incorporating these compartments could be illustrated by the schematic diagram shown in Figure 39. A biliary compartment was added as some activity was found in the bile at necropsy.

Table 95: Comparison between the serum and organ time-dependent kinetic model coefficients (p-values for an unpaired t-test).

Organ	**$t_{½}1$**	**$T_{½}z$**	**MRT**
Heart vs. Serum	0.466	0.520	0.465
Liver vs. Serum	0.610	**0.047**	0.056

However, even though it is tempting to model these data to such a mulicompartment model, one should not lose site of the initial goals of these experiments. That is, to develop a pharmacokinetic model that describes the biodistribution of the ^{99m}Tc labelled MAb. If the activity in the liver and kidneys were mainly associated with a transchelated product (unrelated to the MAb or its metabolic products) then these compartments should not be included in a model intended to represent the biodistribution intact ^{99m}Tc-

MAb. A simple 2 compartment model is sufficient, if it describes the MAb distribution adequately, and the multicompartmental model in Figure 39 is appropriate only if intact ^{99m}Tc- MAbs are indentified in each compartment. It is not appropriate when a process such as transchelation "tags" a different molecule, such as cysteine or glutathione, especially if the model is to represent the biodistribution of the MAb. Thus even though it is tempting to fit the data to such a multicompartmental model, the two-compartment model probably best suits these data.

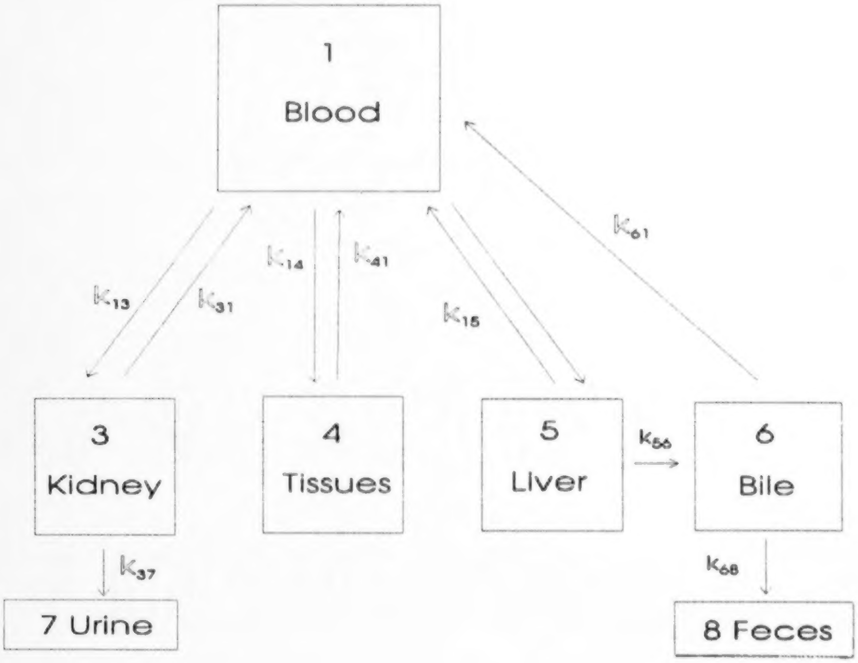

Figure 39: Possible kinetic model for ^{99m}Tc labelled 170H.82.

Radioimmunoassay data were used to assess the kinetics of the immunoreactive component in serum and were presented in a previous section (page 138). Although there was insufficient data to perform a statistical analysis between RIA and ^{99m}Tc models, a visual inspection of

Figure 18 would seem to indicate a more rapid loss of ^{99m}Tc compared to that of the immunoreactive component of the MAb. This deviation was evident at sampling time greater than 18 hours post-injection and is in agreement with the HPLC and ITLC data (page 135 and paragraph below) where a second, ^{99m}Tc-labelled low molecular weight peak appeared at approximately the same time. Even though the data sets were limited in size, the mean residence times for the immunoreactive component in serum (84 to 322 hours, Table 26) were longer than those observed for the ^{99m}Tc based model (49 to 79 hours, Table 24).

Size exclusion HPLC analysis of the radioactive component of the patient sera revealed that the majority of the activity was associated with the intact MAb during early imaging times (less than 12 hours). Although a small, lower molecular weight radioactive peak was observed, it was only a few percent of the injected dose and was attributed in part to the free ^{99m}Tc pertechnetate from the kit that was injected with the MAb. However, at longer times post-injection (18 to 24 hours), an ingrowth of a low molecular weight radioactive peak was observed with a retention time similar to that of the radioactive peak observed in a urine sample. This low molecular weight peak was confirmed by ITLC but was not explicitly identified. Possible explanations for the formation of this lower molecular weight peak might include: ex vivo serum stability[rr], low-affinity MAb labelling (page 43) or metabolism in an organ other than the kidney (such as the liver) and subsequent release back into the circulatory system, or renal reabsorption of a metabolic product.

Serum kinetics observed for this group of patients do not appear to support a reabsorption process as no reabsorption peak was noted during the terminal elimination phase (Figure 12). If such were the case, the 10 -

---

[rr] Tests at Biomire Inc. have indicated ^{99m}Tc labelled product is stable in serum.

55 %ID of the lower molecular weight peak should be easily visualized. However, if this were a genuine effect of the medium to long-term in vivo MAb stability, the following generalized circumstances might offer one explanation. The MAb is either metabolized or transchelated in the liver or kidney and is released back into the blood pool. This ^{99m}Tc labelled low-molecular weight compound would normally be cleared by the kidneys. However, if the kidneys were operating in a rate-limited mode (following Michaelis-Menten kinetics) then the low molecular weight compound would tend to increase with time in the serum.

This theory was explored in the rabbit model as more gamma camera image data was available. A visual inspection the kidney data (Table 12 through Table 14) and the relatively poor fit to the absorption model for the 170H.82 rabbit kidneys might suggest that these data could represent a rate limiting process. If the ^{99m}Tc labelled compound were eliminated in a nonlinear fashion then the capacity-limited process could be described by the Michaelis-Menten equation:

$$-\frac{dC}{dt} = \frac{V_m C}{K_m + C}, \tag{41}$$

where

$\frac{dC}{dt}$ is the rate of decline (biological elimination) of the ^{99m}Tc label (C),

V_m is the theoretical maximum rate of the elimination process and

K_m is Michaelis constant.

This same rabbit ^{99m}Tc kidney kinetic profile was also observed for the 174H.64 MAb, the kidney kinetic profile (Table 30 through Table 32, Table 41 and Table 42) and both the free and complexed form of B80.3 (Table 57 through Table 62). However, as the concentration of the kidney ^{99m}Tc levels did not appreciably change over the duration of the rabbit studies, it was not possible to develop this model other than to note that the kidney activity in all the rabbits was fairly constant at 3 to 4 %ID over the 48 hour study period. An attempt to fit these data to a nonlinear model by PCNONLIN was unsuccessful.

6.5 Dosimetry

The ability to predict the radiation dose to patients receiving ^{99m}Tc labelled MAb 170H.82 for RIS procedures from rabbit studies was tested to determine the viability and accuracy of such predictions. Although mouse data was not available, it was thought that the kinetics in a species other than mice might more closely represent that in humans. The murine-based MAb would then be a foreign protein to both rabbits and humans and similar clearance patterns might be expected.

A general picture of these clearance patterns can be visualized by overlaying the serum distribution of patients with that of the rabbits (Figure 40). The first step was to discover whether there were any significant differences between the models representing the serum distribution.

The same type of two compartment model was found to best fit the serum radioactivity data for MAb 170H.82 in both rabbits and humans. Their respective model coefficients are summarized in Table 96, with the p-values from an unpaired t-test reported in the final row of this table. The fraction of the injected MAb in each compartment (C_1 and C_z) and distribution phase half-life were in excellent agreement with each other. The faster rabbit serum clearance observed in Figure 40 was shown to be statistically different than that in patients as shown by the longer patient elimination components; ($t_{½}z$) and MRT. As calculations of the radiation dose contain a biological component representing the clearance of activity, it was expected that the faster rabbit clearance might result in a lower radiation dose estimate.

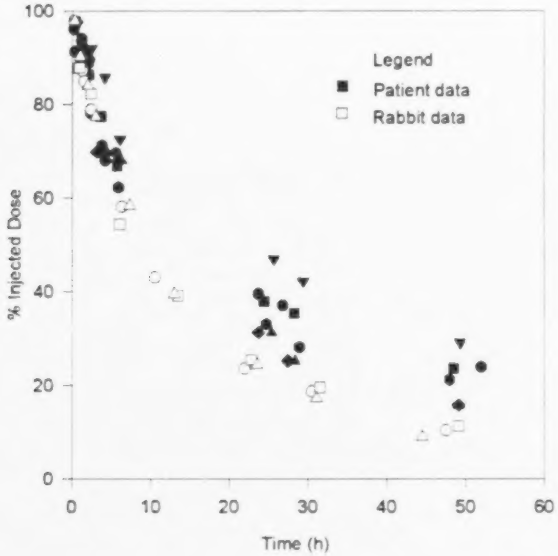

Figure 40: A comparison between patient and rabbit ^{99m}Tc-170H.82 serum data.

Table 96: A comparison of serum kinetic model parameters in patients and rabbits for ^{99m}Tc-170H.82.

MAb	**C1 (%ID)**	**Cz (%ID)**	**$t_{1/2}1$ (h)**	**$t_{1/2}z$ (h)**	**MRT (h)**
Patients	40.5 ± 12	61.2± 8.8	4.0 ± 0.8	39.6 ± 2.8	53.8 ± 3.2
Rabbits	40.5 ± 5.9	59.3 ± 6.0	3.5 ± 0.7	19.0 ± 2.1	24.8 ± 2.4
t-test	0.993	0.808	0.183	**0.002**	**0.001**

The radiation dose in patients was calculated from gamma camera image data using the liver, heart, kidneys and "remainder of the body" as source organs and a dynamic bladder model for dose estimates to the bladder wall (as discussed in previous sections). The dose was calculated from tables of

S-values for the Standard Reference Woman obtained from the software package MIRDOSE2 and from estimates of the cumulated activity obtained by integrating the area under the time-activity curve for each target organ.

The cumulated activity could also be obtained from measurements of organ residence time as discussed in the Background and Literature Review chapter. This method of calculating the cumulated activity was used in conjunction with MIRDOSE2 to estimate the radiation dose in patients due to the activity observed in the corresponding rabbit source organs. As described in an earlier chapter, the general formula for the radiation dose, D was:

$$D\ (r_k \leftarrow r_h) = \tilde{A}_h S(r_k \leftarrow r_h) \qquad (11)$$

where the cumulated activity was given by

$$\tilde{A}_h = 1.443\ A_h T_{eff} \qquad (16)$$

The effective half-life (T_{eff}) contains both the physical and biological elimination components.

Radiation dose estimates to the standard reference woman model were calculated using rabbit kinetic data and the computer program MIRDOSE2. The heart, liver, kidneys and 'remainder of the body' were used as source organs; the same organs as used in calculating the radiation dose to patients. The following assumptions were made for these calculations. Estimates for the fraction of the activity in each source organ were obtained from gamma camera image data. The biological half-lives for the heart, liver and kidneys were obtained from the terminal elimination phases of the gamma camera model data, and the 'remainder of the body' half-life from the serum terminal elimination phase. Source organ contributions as expressed as a percentage of the injected dose and the corresponding biological half-life respectively were: heart (5%, 19 hours), liver (15%, 36 hours), kidneys (3%, no biological clearance) and the 'remainder of the body' (77%, 19 hours). No bladder model was used due to the difficulty in measuring urine output. The results of these dose estimates are shown in Table 97 and compared against the mean value obtained from patients.

Radiation dose estimates for six breast cancer patients were calculated using standard MIRD schema as discussed previously. A comparison (Table 97) with the product insert for OncoScint CR/OV[ss] (MAb B72.3) showed that the average absorbed dose was higher for the ^{111}In labelled OncoScint as that produced from the ^{99m}Tc labelled 170H.82. These results should agree reasonably well with each other after the shorter half-life and different decay characteristics of ^{99m}Tc were taken into account. The rabbit data would be in agreement with the patient dosimetry data when the faster rabbit clearance and lack of a bladder model are taken into account.

Radiation dosimetry estimates were also made for the ^{99m}Tc-labelled B43.13 (Table 97). A visual inspection for ^{99m}Tc labelled Mabs 170H.82 and B43.13 revealed differences between two of the target organs; the urinary bladder wall and the spleen. An unequal t-test yielded values of 0.026 for the bladder wall and 0.006 for the spleen. At the 95% level of significance, the estimated dose to both of these target organs differ from one another. One possible cause for this difference might be due to effect of circulating antigen in the case of B43.13 where the complexed MAb/Ag is removed from the blood by the spleen. The higher renal clearance for ^{99m}Tc-B43.13 (64.4 ± 18 mL/h) compared to ^{99m}Tc-170H.82 (28.5 ± 1.4 mL/h) was a significant cause for the observed increase in the radiation dose to the urinary bladder wall for ^{99m}Tc-B43.13.

[ss] CYTOGEN Corp, Princeton, NJ

Table 97: ^{99m}Tc-170H.82 radiation dose estimates based on human and rabbit data. ^{111}In OncoScint data shown for comparison.

Target Organ	^{99m}Tc-170H.82 Rabbit (mrad/mCi)	^{99m}Tc-170H.82 Human (mrad/mCi)	^{99m}Tc-B43.13 Human (mrad/mCi)	^{111}In OncoScint Human (mrad/mCi)
Adrenals	26	44	44	900
Brain	11	19	20	N/A
Breasts	12	20	20	N/A
GB Wall	32	51	52	N/A
LLI	16	30	32	500
Sml Int	19	33	34	600
Stomach	20	33	35	640
ULI	20	34	35	620
Heart Wall	47	96	86	640
Kidney	70	138	133	1940
Liver	70	99	106	3000
Lungs	19	33	33	980
Muscle	14	24	25	N/A
Ovaries	18	33	34	580
Pancreas	26	43	45	740
Red Marr	16	27	27	2400
Bone Surf	25	43	43	N/A
Skin	9	15	16	320
Spleen	18	33	82	3200
Thymus	18	32	31	N/A
Thyroid	14	24	24	300
UB Wall	17	85	121	560
Uterus	17	35	39	540
Tot Body	16	28	28	540

7. CONCLUSIONS

The central theme of this work was the comparison of the biodistribution between selected MAbs in patients and rabbits and the effects of circulating serum antigens on that distribution. The serum biodistribution patterns for ^{99m}Tc labelled MAbs-170H.82, 174H.64, B43.13 and B80.3 were measured to test whether a single serum-based pharmacokinetic model could be used to describe their behavior. These data were supplemented with information on organ uptake obtained from gamma camera images and from tissue samples from the rabbit studies.

Based on these results, a pharmacokinetic model was developed for all the ^{99m}Tc labelled MAbs. Radiation dose estimates were calculated for two of these Mabs (170H.82 and B43.13). The rabbit model was found to be useful for its ability to estimate the ^{99m}Tc radiation dose for the MAb-170H.82 and MAb-B43.13 group of patients. Future projects based on some of the questions raised during the course of this work are outlined at the conclusion of this chapter.

7.1.1 Two-Compartment Model

The serum kinetic model that best fit the patient data sets for all four MAbs tested was a bolus-input, two-compartment model with elimination from the central compartment. No significant difference was found between the MAb's distribution-phase half-lives, however their elimination-phase half-lives and mean residence times were significantly different at the 95% confidence-level for the small group of patients tested. ^{99m}Tc-MAb-174H.64 cleared the quickest and ^{99m}Tc-MAb-170 had the longest clearance time.

A limited comparison of three dosages of the 170H.82 MAb (1 mg, 2 mg and 4 mg) revealed no differences in the serum based kinetic model describing the biodistribution. This was not entirely unexpected, as the mass difference (only 4 x) was not that great.

7.1.2 Circulating versus Non Circulating Antigen: No Significant Difference

A statistical comparison (t-test) revealed no differences between ^{99m}Tc labelled MAbs-170H.82 and 174H.64 (no circulating antigen) versus ^{99m}Tc labelled MAb-B43.13 (circulating antigen). Significant differences were found in the the terminal elimination phase and mean residence time, if MAb-B43.13 was compared separately with each of the MAbs in the 'no circulating' antigen group. However, this difference was probably due to the inherent biodistribution patterns of the individual MAbs rather than the affects of circulating antigen, as the terminal elimination phase and mean residence time of MAb-B43.13 lay between that of the other two MAbs. There was insufficient MAb-B80.3 patient data to include in this comparison.

7.1.3 Dosimetry Concordance

Subsequently, all the patients in this dosage range were included in radiation dosimetry estimates for the ^{99m}Tc labelled 170H.82 MAb. These data compared favorably with dose calculations based on the ^{99m}Tc-170H.82 rabbit data, indicating the suitability of the rabbit model for calculations of radiation dose. ^{99m}Tc-MAb-B43.13 patient radaition dose estimates were similar to those observed for ^{99m}Tc-MAb-170H.82.

A separate study was performed to look for model differences between the murine and chimeric forms of ^{99m}Tc labelled MAb-174H.64. No difference was isolated for the limited patient data set tested. This work was presented at the 8th International Symposium on Radiopharmacology in Gent (1993)[245].

In summary, this work has demonstrated that a simple, reproducible animal model can be utilized to compare and contrast the biodistribution characteristics of five different ^{99m}Tc labelled monoclonal antibodies. The model is sufficiently robust to show meaningful differences in kinetic modeling of the antibodies and to provide an understanding of these differences when the MAbs are used in the clinical setting. In addition, this model was shown to provide reliable estimates for patient radiation dosimetry when compared with other clinical data. The multiphase protocol developed to estimate the pharmacokinetics and radiation dosimetry for these Mabs could be adapted to evaluate other noval radiopharmaceuticals.

7.2 Future Research

As a result of this work, several interesting observations were made which could require further evaluation to determine significance and may lead to improved clinical strategies.

7.2.1 Variations in ^{99m}Tc-MAb-170H.82 Liver Uptake

One of the patients, E191358 who had received a 4 mg dose of MAb-170H.82 was excluded from the above comparison of dosage levels due to abnormalities in her RIS images. High liver uptake of the ^{99m}Tc-MAb-170H.82 was observed within 3 hours and continued to rise throughout the study. An analysis of the kinetic model showed a concomitant increase in blood clearance with the high liver uptake (Table 24).

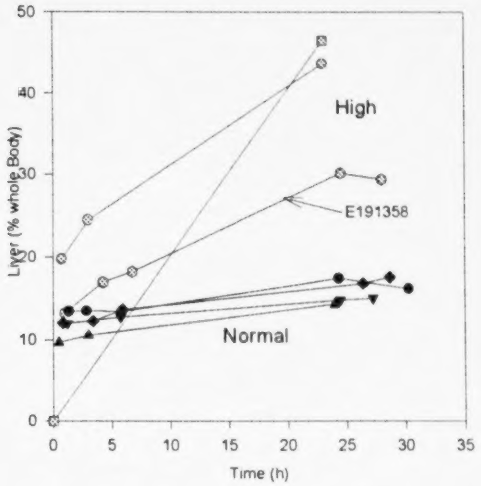

Figure 41: High liver uptake expressed as a percentage injected dose.

Although not part of the kinetic study, high liver uptake was observed in about 8% of the breast cancer patients studied with ^{99m}Tc-MAb-170H.82. Several possible causes were sought to explain this effect. The amount of antibody infused did not appear to be a factor as the effect was also observed at the 1 mg dose. Figure 41 illustrates this effect in seven patients receiving ^{99m}Tc-170H.82 by plotting the liver activity, expressed as a percentage of the whole-body counts, as a function of time post-injection. The liver activity from patient E191358 is overlaid in this figure.

Poor liver function was ruled out following normal liver-function test results, based on measurements of the patient's serum. A HAMA response by the patient also could have caused the high liver uptake if the liver were to remove the MAb-immune-complex from the serum. However, the HAMA levels for all the patients in this clinical trial were within the normal range. Other signs of immune system activity were explored by measuring the serum levels of the IL2 receptor (IL2r). Although inconclusive, these results did show that the serum IL2r levels were all in the high-normal range for this group of patients. Even though the causes of high liver uptake have not yet been discovered, the effect itself may be of prognostic value. These patients will be periodically evaluated to monitor their disease status.

As the liver function[tt] for this group of patients was within the normal range, one may speculate that this increased uptake might be due to metabolic products from the ^{99m}Tc-170H.82 complexes trapped within the liver. Further research is planned to discover if there is a prognostic value in identifying this group patients.

7.2.2 Pharmacodynamic Modelling of MAb-B43.13

During the last five years of clinical research performed by Biomira with MAb-B43.13, many patients (with ovarian cancer) unexpectedly exhibited tumor regression and improved longevity[246,247]. Further studies by Biomira have indicated that this therapeutic effect appeared to be related to the induction of the patient's endogenous anti-idiotype response following repeated administration of ^{99m}Tc-MAb-B43.13[248].

^{99m}Tc-MAb-B43.13 and B43.13 pharmacokinetics have been measured as part of this work and, as an extension, it would be interesting to attempt to model patient response against parameters such as the amount of MAb injected, time intervals between injection, the development of HAMA, and CA 125 levels, to name a few. The utilization of a neural network would permit the experimenter to input several, independently-weighted but interrelated factors in order to isolate and optimize those parameters which most effect patient outcome. The subsequent development of an appropriate model could then assist the physician in predicting the best dosage and dosage intervals in order to optimize a therapeutic response.

[tt] Standard blood profile.

8. REFERENCES

---

[1] Saha GP; Fundamentals of Nuclear Pharmacy, Springer-Verlage, New York, pp109-140, 1992.

[2] Francis MD and Fogelman I; ^{99m}Tc diphosphonate uptake mechanism in bone, In *Bone Scanning and Clinical Practise*, London, Springer-Verlag, 7-18, 1987.

[3] Srivastava SC and Straub RF; Blood cell labeling with ^{99m}Tc: progress and perspectives, *Semin Nucl Med*, 20:41, 1990.

[4] R. H. Mannan, V. V. Somayaji, J. Lee, J. R. Mercer, J. D. Chapman and L. I. Wiebe, "Radioiodinated 1-(-5-Iodo-5-Deoxy-β-D-Arabinofuranosyl)-2-nitroimidazole (Iodoazomycin Arabinoside: IAZA), A Novel Marker of Tissue Hypoxia", *J. Nuc. Med.*, 32:1764, 1991.

[5] R. H. Mannan, J. R. Mercer, L. I. Wiebe, V. V. Somayaji and J. D. Chapman, "Radioiodinated 1-(2-Fluoro-4-Iodo-2,4-Dideoxy-β-L-Xylopyranosyl)-2-Nitroimidazole: A Novel Probe for the Non-Invasive Assessment of Tumor Hypoxia", *Radiation Research.*, 132:368, 1992.

[6] R. B. Moore, J. D. Chapman, J. R. Mercer, R. H. Mannan, L. I. Wiebe, A. J. McEwan and M. S. McPhee, "Measurement of PDT-Induced Hypoxia in Dunning Prostate Tumors by Iodine-123-Iodoazomycin Arabinoside", *J. Nuc. Med.*, 34:405, 1993.

[7] Sampson CB; Textbook of Radiopharmacy, Theory and Practice, Gordon and Breach Science Publ., 2nd Edition, 1994.

[8] MacLean GD, McEwan AJ, Noujaim AA et al Two novel monoclonal antibodies have potential for gynecological cancer imaging, *Antibody Immuno Radiopharm*, 4:297-308, 1991.

[9] Longenecker BM, Rahman A, Leighh JB et al, Monoclonal antibody against a cryptic monoclonal antibody against a cryptic carbohydrate antigen of murine and human lymphocytes. 1. Antigen expression in non-cryptic unsubstituted form on certain murine lymphomas, on a spontaneous murine mammary carcinoma and on several human adenocarcomas, *Int J Cancer*, 33:123-129, 1984.

[10] Goldenberg DM and Larson SM; Radioimmunodetection in cancer indentification, *J Nucl Med*, 33:803-814, 1992.

[11] Khaw B-A, Strauss H and Narula J; Magic bullets: from muskets to smart bombs, *J Nucl Med*, 34:2264-2268, 1993.

[12] Goldenberg DM; New developments in monoclonal antibodies for cancer detection and therapy, *CA Cancer J Clin*, 44:43-64, 1994.

---

[13] Order SE, Sleeper AM, Stillwagon GB, Klien JL and Leichner PK; Radiolabeled antibodies: results and potential in cancer therapy, Cancer Res (suppl), 50:1011s-1013s, 1990.

[14] Goldenberg DM *Immunodiagnosis and immunodetection in colorectal cancer*, Caner Bull (Huston) 30:213-218, 1978.

[15] Order SE, Sleeper AM, GB Stillwagon Klein JL and Leichner PK; Radiolabelled antibodies: results and potential in cancer therapy, *Cancer Res* (suppl) 50:1011s-1013s, 1990.

[16] Khaw BA, Yasuda T, Gold HK, et al; *Acute myocardical infarct imaging with In-111-labelled monoclonal antimyosin*, J Nucl Med, 28:1671-1678, 1987.

[17] Oster ZH, Srivastava SC, Som P, et al; *Thrombus radioimmunoscintigraphy: an approach using monoclonal antiplatelet antibody*, Proc Natl Acad Sci USA, 82:3465-3468, 1985.

[18] Lochner JT, Seybold K, Andres RY, et al; *Imaging of inflamatory and infectios lesions after injection of radiolabelled monoclonal antigranulocyte antibodies*, Nucl Med Commun, 7:659-660, 1986.

[19] Ehrlich P and Herter CA; Ueber Einige Verwendungen der Napthochinosulfosaure, *Z Physiol Chem*, 61:379-392, 1904.

[20] Cuatrecasas P; Protein purification by affinity chromatography. Derivation of agrose and polyamide beads, *J Biol Chem*, 245:3059-3065, 1970.

[21] Order SE, Monoclonal antibody: potential role in radiation therapy and oncology, *Int J Radiat Oncol Biol Phys*, 8:1193-1201, 1981.

[22] Order SE, Vriesendorp HM, Klein JL and Leichner PK; A phase I study of 90-yttrium antiferritin: dose escalation and tumor dose, *Antibody Immunoconj Radiopharm*, 1:163-167, 1988.

[23] Leonard DF, Mounier M, et al; efficacy of five enzyne immunoassays for antibody to HIV in detecting antibody to HTLV-IV, *Lancet*, 1:324-325, 1987.

[24] Batzer FG; Test kits for ovulation and pregnancy, *Contempory OB/GYN*, 28:7-16, 1986.

[25] Papsidero LD, Croghan GA, Asirwatham J, et al; Immunohistochemical demonstration of prostate-specific antigen in metastases with the use of monoclonal antibody F5, *Amer J Pathol*, 451-454, 1985.

[26] Papsidero LD, Croghan GA, Asiratham J, et al; Immunohistochemical demonstration of prostate-specific antigen in metatases with the use of monoclonal antibody F5, *Amer J Pathol*, 451-454, 1985.

[27] Muirhead M, Martin P, Toruk-Strob, et al; Use of antibody-ricin A chain conjugate to deplete neoplastic cells from human bone marrow, *Blood*, 62:327-332, 1983.

---

[28] Ramsy NK and Kersey JH; Bone marrow purging using monoclonal antibodies, *J Clin Immunol*, 8:81-88, 1988.

[29] Filopovich AH Vallera D, Youle R, et al; Ex vivo depletion with immunotoxins in allogenic bone-marrow transplantation: the pilot clinical study for the prevention of graft-versus-host disease, *Transplantation Proc*, 17:442-444,1985.

[30] Coleman, R.M.; Lombard, MF; Sicard, R.E. and Rencricca N.J. Elements of humoral immunity, in "Fundamental Immunology" William C. Brown Publishers, Dubuque, Iowa, pp 129-161, 1989.

[31] Perkins AC and Pimm; Immunoscintigraphy: Practical Aspects and Clinical Applications, Wiley-Liss, New York, pp 177-188, 1991.

[32] Hilschmann N and Craig LC; Amino acid sequence studies with Bence-Jones proteins, *Proc Natl Acad Sci (USA)*, 53:1403, 1965.

[33] Bier OG, da Silva WD, Gotze D and Mota I; in Fundamentals of Immunolgy, Springer-Verlag, New York, pp 105, 1986.

[34] Bier OG, da Silva WD, Gotze D and Mota I; in Fundamentals of Immunolgy, Springer-Verlag, New York, pp 221-222, 1986.

[35] Covell, D.G.; Barbet, J.; Holton, O.D.; Black, C.D.V.; Parker, R.J.; Weinstein, J.N.; Pharmacokinetics of Monoclonal Immunoglobulin G1, F(ab')2, and Fab' in Mice, *Cancer Res*, 46:3969-3978, 1986.

[36] Morell A, Terry WD and Waldman TA; *Metabolic properties of IgG subclass in man*, J Clin Invest, 49:673-680, 1970.

[37] Turner, M.; Molecules which recognize antigen, Roitt, I.M.; Brostoff, J. and Male, D.K.; eds. "Immunology", Gower Medical Publishing, London, 5.1-5.12, 1989.

[38] Kohler G, Milstein C, Continuous cultures of fused cells secreting antibodies of predefined specificity, *Nature* 256:495-497, 1975.

[39] DePinho RA, Fieldman RB and Scharff MD; Monoclonal antibodies: A new technology for producing serologic reagents, *New Engl J Med*, 304:1344-1349, 1981.

[40] Schook LB(ed); Monoclonal Antibody Production Techniques and Applications, Marcel Dekker, New York , 1986.

[41] Kagan JM and Fahey JL; *Tumor immunology*, J Amer Med Assoc, 258:2988-2992, 1987.

[42] Zimmerman U and Vienken J; *Electric field induced cell fusion*, J Membrane Biol, 62:165-185, 1982.

---

[43] Bogard WC, Dean RT, Deo Y, et al; Practical considerations in the production, purification and formulation of monoclonal antibodies for immunoscintigraphy and immunotherapy, *Semin Nucl Med*, 19:202-220, 1989.

[44] Levy JA, Lee HM Kawahata, et al; Purification of monoclonal antibodies from mouse ascites eliminates contaminating infectious mouse type C viruses and nucleic acids, *Clin Exp Immunol*, 131:1201-1204, 1984.

[45] Operation Manual: An operation manual for control of production, preclinical toxicology and and Phase I trials of anti-tumor antibodies and drug antibody conjugates; *Br J Cancer*, 54:557-568, 1986.

[46] Reynolds JC, Del Vecchio S, Sukahara H, Lora ME, Carrasuillo JA, Neuman RD and Larson SM; *Anti-murine antibody response to mouse monoclonal antibodies: Clinical findings and implications*, Nucl Med Biol, 16:121-125, 1989.

[47] De Jagger R, Abdel-Nabi H, Serafini A, Pecking A, Klein JL, Hanna MG Jr; Current status of immunodection with radiolabeled human monoclonal antibodies, *Semin Nucl Med* 23:165-179, 1993.

[48] Morrison SL, Johnson MJ, Herenberg LA, et al; Chimeric human antibody molecules: mouse antigen binding domains with human constant region domains, *Proc Natl Acad Sci (USA)*, 81:6851-6855, 1984.

[49] Boulianne GL Hozumi N and Shulman MJ; Production of functional chimeric mouse/human antibody, *Nature*, 312:643-646, 1984.

[50] Serafini AN; from monoclonal antibodies to peptides and molecular recognition units: an overview, *J Nucl Med* 34:533-536, 1993.

[51] Zalutsky MR (ed); Antibodies in Radiodiagnosis and Therapy, CRC PressBoca Raton, FL, 1989.

[52] Pressman D and Korngold L; The in vivo localization of anti-Wagner osteogenic sarcoma antibodies, *Cancer* 6:7619, 1953.

[53] Gold P and Freeman SE; Demonstration of tumor specific antigen in human colonic carcinomata by immunological tolerance and absroption techniques, *J Exp Med*, 121:439, 1965.

[54] MAch JP, Carrel S, Forni M, Ritchard J, Donath A and Alberto P; Tumor localization of radiolabelled antibodies against carcinoembryonic antigen in patients with carcoma, *N Engl J Med*, 5:303 1980.

---

[55] Goldenberg DM, DeLand FH, Kim EE, et al; Use of radiolabelled antibodies to carcinoembryonic antigen for the detection and localization of diverse cancers by external photoscanning, *N Engl J Med*, 298:1384, 1978.

[56] Halpern SE, Hagan PL, Garver PR, et al; Stability, characterization and kinetics of In-111 labelled monoclonal antitumor antibodies in normal animals and nude mouse-human tumor models, *Cancer Res*, 43:5347, 1983.

[57] Morrsison RT, Lyster DM, Alcorn L, Rhodes BA, Breslow K and Burchiel SW; Radioimmunoimaging with Tc-99m monoclonal antibodies: clinical studies, *Int J Nucl Med Biol*, 11:1984, 1984.

[58] Goldenberg DM, Kim EE, DeLand FH, et al; Clinical studies of the immunodetection of tumors containing alpha-fetoprotein, *Cancer*, 45:497-501,1980.

[59] Goldenberg DM, Kim EE, DeLand FH, et al; Radioimmunodetection of cancer with radioactive antibodies to carcinoembryonic antigen, *Cancer Res*, 40:2984-2992, 1980.

[60] Riva P, Moscatelli G, Paganelli G, Benini S and Siccardi A; Antibody guided diagnosis: an Italian experience on CEA-expresing tumors, *Int J Cancer* (suppl), 2:114-120, 1988.

[61] Schlom, J.; Basic principles and applications of monoclonal antibodies in the management of carcinomas: The Richard and Hinda Rosenthal Foundation Award Lecture, *Cancer Res*, 46:3225-3238, 1986.

[62] Ghosh BC and Ghosh L; Tumor Markers and Tumor Associated Antigens, McGraw-Hill, **1992**.

[63] Hellstrom I, Brown JP and Hellstrom KE; Melanoma-associated anitgen p97 continues to tbe expressed after prolonged exposure of cells to specific antibody, *Int J Cancer*, 31:553, 1983.

[64] Ritz J, Pesando JM, Notis-McConarty J and Schlossman SF; Modulation of human acute lymphoblastic leukemia antigen induced by monoclonal antibody in vitro, *J Immunol* 125:1506, 1980.

[65] Sharkey RM, Goldenberg DM, Goldenberg H, et al; Murine monoclonal antibodies against carcinoembryonic antigen: immunological, pharmaco-kinetic and targeting properties in humans, *Cancer Res*, 50:2823-2831, 1990.

[66] Doerr RJ, Abdel-Nabi H, Baker JM, etal; Detection of primary colorectal cancer with indium-111 monoclonal antibody b72.3, *Arch Surg*, 125:1601-1605, 1990.

[67] Bale, W.F.; Contreras, M.A.; Grady, E.D.; Factors influencing localization of labeled antibodies in tumors, *Cancer Res*, 40:2965-2972, 1980.

---

[68] Khaw BA, Klibanov A, O'Donnell SM, et al; Gamma imaging with negatively charge-modified monoclonal antibody: modification with synthetic polymers, *J Nucl Med*, 32:1742-1751, 1991.

[69] Goodwin DA, Meares CF, Watanabe, et al; Pharmacokinetics of pretargeted monoclonal antibody 2D12.5 and ^{88}Y-Janus-2-(p-nitrobenzyl)-1-4,7,10-tetraazacyclododdecanetetra-acetic acid (DOTA) in BALB/c mice with KHJJ mouse adenocarcinoma: A model for ^{90}Y therapy, *Cancer Res*, 54:5937-5946, 1994.

[70] Ritschel WA; in Handbook of Basic Pharmacokinetics, Drug Intelligence Publications Inc., Hamilton IL, p 132-136, 1986.

[71] DeNardo GL and de Nardo SJ; Perspectives on the future of radioimmunodiagnosis and radioimmunotherapy of cancer in Burchiel SW and Rhodes BA (eds) Radioimmunoimaging and Radioimmunotherapy, Elsevier science Publ, New York, pp 41-62, 1983.

[72] Nuti M, Teramoto YA, Mariani-Constantini R, Horan Hand P, Colcher D and Schlom; A monoclonal antibody (B72.3) defines patterns of distribution of a noval tumor-associated antigen in human mamary carcinoma cell population, *Int J Cancer*, 29:539-545, 1982.

[73] Johnson VG, Schlom J, Paterson AJ, Bennett J, Magnani JL and Colcher D; Analysis of a human tumor-associated glycoprotein (TAG-72) identified by monoclonal antibody B72.3, *Cancer Res*, 46:850-857, 1986.

[74] Stramignoni D, Bowen R, Atkinson BF and Schlom J; Differential reactivity of monoclonal antibodies with human adenocarcinomas and adenomas, *Int J Cancer*, 31:543-552, 1983.

[75] Nuti M, Teramoto YA, Mariani-Costantini R, Horan-Hand P, Colcher D and Schlom J; A monoclonal antibody (B72.3) defines patterns of distribution of a novel tumor associated antigenin human mammary carcinoma cell population, *Int J Cancer*, 29:539-545, 1982.

[76] Thor A, Gorstein F, Ohuchi N, Szpak CA, Johnston WW and Schlom J; Tumor associated glycoprotein (TAF-72) in ovarian carcinomas defined by monoclonal antibody B72.3, *J Natl Cancer Inst*, 76:995-1006, 1986.

[77] Ohuchi N, Simpson J, Colcher D and Schlom J; Complementation of anti-CEA and anti-TAG-72 monoclonal antibodies in reactivity to to human gastric adenocarcinomas, *Int J Cancer*, 40:726-733, 1987.

[78] Colcher D, Esteban JA, Carrasquillo, et al; Quantitative analysis of selective radiolabeled monoclonal antibody localization in metastatic lesions of colorectal cancer patients, *Cancer Res*, 47:1185-1189, 1987.

---

[79] Thor A, Ohuchi N, Szpak CA, Johnston WW and Schlom J; The distribution of oncofetal antigen TAG-72 recognized by monoclonal antibody B72.3, *Cancer Res*, 46:3118-3124, 1986.

[80] Schlom J, Colcher D, Roselli M, et al; Tumor targeting with monoclonal antibody B72.3, *Nucl Med Biol*, 16:137-142, 1989.

[81] Colcher D, Esteban J, Carrasquillo JA, et al; Complementation of intra-cavitary and intravenous administration of a monoclonal antibody (B72.3) in patients with carcinoma, *Cancer Res*, 47:4218-4224, 1987.

[82] Weinstein JN, Immunolymphoscintigraphy and other nonintravenous applications of monoclonal antibodies, in Zalutsky MR (ed); Antibodies in Radiodiagnosis and Therapy, CRC PressBoca Raton, FL, p 153-168, 1989.

[83] Sgouros G, Graham MC, Divgi CR, Larson SM and Scheinberg; Modeling and dosimetry of monoclonal antibody M195 (anti CD33) in acute myelogenous leulemia, *J Nucl Med*, 34:422-430, 1993.

[84] Gibaldi, M; and Perrier, D; Pharmacokinetics, Second edition, Marcel Dekker, Inc, New York, 1982.

[85] Levy G, Tsuchiya and Amsel LP; Limited capacity for salicyl phenolic glucuronide formation and and its effect on the kinetics of salicylate in man, *Clin Pharmacol Ther*, 13:258, 1972.

[86] Koizumi, M.; DeNardo, G.L.; DeNardo, S.J.; Hays, M.T.; Hine, H.H.; Scheibe, P.O.; Peng, J.S.; Macey, D.J.; Tonami, N. and Hisada, K.; Multicompartmental analysis of the kinetics of radioiodinated MoAb in patients with cancer, *J Nucl Med*, 27:1243-1254, 1986.

[87] Holton, O.D.; Black, C.D.V.; Parker, R.J.; Covell, D.G.; Barbet, J.; Sieber, S.M.; Talley, M.J.; Weinstein, J.N.; Biodistribution of Monoclonal IgG1, F(ab')2, and Fab' in Mice After Intravenous Injection, *J Immun*, 139:3041-3049, 1987.

[88] Shani, J.; Mohd, S.; Wolf, W.; Walker, L.E.; Compartmental biodistribution of a monoclonal antibody against human lung adenocarcoma grown in athymic mice, *Nucl Med Biol*, 16:33-40, 1989.

[89] Covell, D.G.; Barbet, J.; Holton, O.D.; Black, C.D.V.; Parker, R.J.; Weinstein, J.N.; Pharmacokinetics of Monoclonal Immunoglobulin G1, F(ab')2, and Fab' in Mice, *Cancer Res*, 46:3969-3978, 1986.

[90] Zalutsky, M.R.; Bast, R.C.; Knapp, R.C.; Pharmacokinetics of a radioiodinated monoclonal antibody F(ab')2 fragment in a xenograft model with circulating antigen, *Nucl Med Biol*, 16:405, 1989.

---

[91] Manaka, R.C.; Schumitzky, A. and Wolf, W.; Symbolic program for structural identification of linear pharmacokinetic systems, *Comput Progr Biomed*, 13:203-216, 1981.

[92] Shani, J.; Wolf, W.; Chanachai, W.; Mohd, S.; Reisfeld, R.A. and Walker, L.E.; Labelling and comparative biodistribution of the MoAb KS1/4 in nude mice bearing human lung adenocarcoma, *Int J Nucl Med Biol*, 13:379-382; 1986.

[93] J Folkman; Tumor angiogenesis in Cancer Medicine, JF Holland et al eds, Lea and Febiger, 1993.

[94] Jain RK, Bariers to drug delivery in solid tumors, Sci Amer, 59-65, July 1994.

[95] Scheinberg DA and Strand M; Leukemic cell targeting and therapy by monoclonal antibody ina mouse model system, *Cancer Res*, 44:1002-1007, 1982.

[96] Himmelsbach, M.; Wahl, R.L.; Studies on the Metabolic Fate of 111-In-labeled Antibodies, *Nucl Med Biol*, 16:839-845, 1989.

[97] Britton, K.E.; ranowska, M.; Nimmon, C.C.; Crowther, M.; Mather, S.; Bomanji, J. and Sheppard, J.; Monitoring the in vivo behaivor of immunoglobulins with radiotracers: Imaging approaches and data processing techniques, *Nucl Med Biol*, 16:105-109, 1989.

[98] Otsuka, F.L. and Welch, M.J.; Methods to label monoclonal antibodies for use in tumor imaging, Nucl Med Biol, 14:243-249, 1987.

[99] DeNardo, S.J.; Peng, J.-S.B.; DeNardo, G.L.; Mills, S.L.; 28. Embleton MJ, Drug-targeting by monoclonal antibodies, *Br J Cancer* 55:227-231, 1987.

[100] Hnatowich DJ; Recent developments in the radiolabeling of antibodies with iodine, indium and technetium, *Semin Nucl Med*, 20:80-91, 1990.

[101] Hnatowich DJ, Virzi F and Doherty PW; DTPA coupled antibodies labelled with yttrium-90, *J Nucl Med*, 26:503, 1985.

[102] Hnatowich DJ, Mardirossian, Rusckowski M, Fogarasi M, Virzi F and Winnard Jr P; *Directly and indirectly Technetium-99m-labeled antibodies - a comparison of in vitro and animal invivo properties*, J Nucl Med, 34:109-119, 1993.

[103] Eary JF, Krohn KA, Kishore R and WB Nelp; Radiochemistry of halogenated antibodies in Antibodies in Radiodiagnosis and Therapy, Zalutsky MR (ed), CRC PressBoca Raton, FL, pp 83-102, 1989.

[104] Eckelman WC and Paik CH; Labeling antibodies with metals in Antibodies in Radiodiagnosis and Therapy, Zalutsky MR (ed), CRC PressBoca Raton, FL, pp 103-128, 1989.

[105] Hnatowich DJ; Recent developments in the radiolabeling of antibodies with iodine, indium and technetium, *Semin Nucl Med*, 20:80, 1990.

---

[106] Paik CH, Murphy PR, Eckelman WC Volkert WA and Reba RC; Optimization of the the DTPA mixed-anhydride reaction with antibodies at low concentration, *J Nucl Med*, 24:932, 1983.

[107] Walker FW, Parrington JR and Feiner F; Nuclides and Isotopes - 14th Edition, General Electric Co, 1989.

[108] Rhodes BA, Zamora PO, Newell KD and Valdez EF; Technetium-99m labeling of murine monoclonal antibody fragments, *J Nucl Med*, 27:685-693, 1986.

[109] Rhodes BA, Zamora PO, Newell KD, et al; Technetium-99m labeling of murine monoclonal antibody fragments, *J Nucl Med*, 27:685-693, 1986.

[110] Thakur ML, DeFulvio J, Richard MD and Park CH; Technetium-99m labeled monoclonal antibodies: evaluation of reducing agents, *Nucl Med Biol*, 18:227-233, 1991.

[111] Paik CH, Phan LNB, Hong, et al; The labelling of high affinity sites of anitobodies with Tc-99m, *Int J Nucl Med Biol*, 12:3, 1985.

[112] Schwartz A and Steinstrasser A; A novel approach to Tc-99m labeled monoclonal antibodies, *J Nucl Med*, 28:721, 1987.

[113] Schwarz A and Steinstraver A; A novel appraoch to Tc=99m-labeled monoclonal antibodies, *J Nucl Med*, 28:721 (abstr), 1987.

[114] Pak YK, Dean RT, Mattis J, et al; Tc-99m antimyosin infarct-avid scintigraphy: Improved results with a new instant kit labrling technique for routine use, (Abstr, Suppl 2), *Circulation*, 76:2013, 1987.

[115] Kuhlmann, L. and Steinstrasser A; Effect of TPA to antibody ratio on chemical, immunological and biological properties of the In-111 labelled fab$_2$ fragment of the monoclonal antibody 431/31, *Nucl Med Biol*, 6:617-627, 1988.

[116] Meares, C.F. and Wensel, T.G.; Metal chelates as probes of biological systems, *Acc Chem Res*, 17:202-209, 1984.

[117] Zhang ZM, BallingerJR, Sheldon K and Boxen I; Evaluation of reduction-mediated labelling of antibodies with technetium-99m, *Nucl Med Biol*, 19:607-609, 1992.

[118] Wolf, W. and Shani, J.; Criteria for the selection of the most desirable radionuclide for radiolabelling of monoclonal antibodies, *Int J Nucl Med Biol*, 13:319-324, 1986.

[119] Hoffman, E.J.; The positron tomograph: basic principles of the instrument and its images, in "Principles of Radionuclide Emission Imaging", D.E. Kuhl ed, Pergamon Press, New York, pp201-226, 1983.

[120] Strauss LG and Conti PS; The applications of PET in clinical oncology; *J Nucl Med* 32, 623-648, 1991.

---

[121] Vinerhoets FJG, Snow BJ, Schulzer M, et al; Reproducibility of fluorine-18-6-fluorodopa positron emission tomography in normal human subjects, *J Nucl Med*, 35:18-24, 1994.

[122] Wilson CB, Snook DE, Dhokia B, Taylor CV, Watson IA, Lammertsma AA, Lambrecht R, Waxman J, Jones T and Epenetos AA; Quantitative measurement of monoclonal antibody distribution and blood flow using positron emission tomography and 124iodine in patients with breast cancer, *Int J Cancer*, 47:344-347, 1991.

[123] Anderson CJ, Connett JM, Schwarz SW, Rocque PA, Guo LW, Philpott GW, Zinn KR, Meares CF and Welch MJ;
Copper-64-labeled antibodies for PET imaging, *J Nucl Med*, 33:1685-1691, 1992.

[124] Westera G, Reist HW, Buchegger F, Heusser CH, Hardman N,Pfeiffer A, Sharma HL, von Schulthess GK and Mach JP; Radioimmuno positron emission tomography with monoclonal antibodies: a new approach to quantifying in vivo tumour concentration and biodistribution for radioimmunotherapy, *Nucl-Med-Commun*, 12:429-437, 1991.

[125] Muasner LF and Srivastava SC; Selection of radionuclides for radiotherapy, *Med Phys*, 20:503-509, 1993.

[126] Clark LP, Cullom SJ, Shaw R, Reece C, Penney BC King MA and Silbiger M; Bremsstrahlung imaging using the gamma camera: Factors affecting attentuation, *J Nucl Med*, 33:161-166, 1992.

[127] Breitz HB, Weiden PL, Vanderheyden J-L, et al; Clinical experience with rhenium-186-labeled monoclonal antibodies for radioimmunotherapy: Results of phase I trials, J Nucl Med, 15:911-916, 1990.

[128] Covell, D.G.; Barbet, J.; Holton, O.D.; Black, C.D.V.; Parker, R.J.; Weinstein, J.N.; Pharmacokinetics of Monoclonal Immunoglobulin G1, F(ab')2, and Fab' in Mice, *Cancer Res*, 46:3969-3978, 1986.

[129] Roitt I, Brostoff, J and Male D; in Immunology, 2nd Edition, Gower Medical Publishing, pp 5.1-7.10, 1989.

[130] Tjandra JJ, Ramadi L and McKenzie IFC; Development of human anti-murine antibody (HAMA) response in patients, *Immunol Cell Biol*, 68:367-376, 1990.

[131] Larson SM, Brown JP, Wright JP, Carrasquillo JA, Hellstrom I, and Hellstrom KE, Imaging of melanoma with I-131-labelled monoclonal antibodies, *J Nucl Med*, 24:123-129, 1983.

[132] Del Vecchio S, Reynolds JC, Carrasquillo JA, Lora ME, and Larson SM; Human anti-murine antibody (HAMA) concentration and HAMA-murine antibody (antibody-antibody) complexes, *J Nucl Med*, 28, p614, 1987.

---

[133] Reynolds JC, Del Vecchio S, sakahara H, Lora ME, Carrasquillo JA, Newman RD and Larson SM, Anti-murine antibody response to mouse monoclonal antibodies: clinical findings and implications, *Nucl Med Biol*, 16:121-125, 1989.

[134] Pimm MV, Perkins AC, Armitage AC and Baldwin RW, The characteristics of blood-borne radiolabels and the effect of anti-mouse IgG antibodies on localization of radiolabelled monoclonal antibody in cancer patients, *J Nucl Med* 26:1011-1023, 1985.

[135] Hosono M, Endo K, Sakahara H, Watanabe Y, Saga T, Nakai T, Kawai C, Matsumori A, Yamada T, Watanabe T and Konishi J; Human/Mouse chimeric antibodies show low reativity with human anti-murine antibodies (HAMA), *Br J Cancer*, 65:197-200, 1992.

[136] Schroff RW, Foon KA, Beatty SM, Oldham RK and Morgan AC; Human anti-murine immunoglobulin responses in patients receiving monoclonal antibody therapy, *Cancer Res*, 879, 1985.

[137] Senekowitsch R, Bauer R, Schrock R, Langhammer HR and Pabst HW, Influence of human anti-mouse antibodies (HAMA) on the radioimmunological determination of tumor markers, *Nuklearmedizin*, 26, p262, 1987.

[138] Zimmer AM, Rosen ST, Spies SM Goldman-Leiken R, Kazikiewicz JM, Silverstein EA and Kaplan EH, Radiotherapy of patients with cutaneous T-cell lymphoma using iodine-131-labelled monoclonal antibody: analysis of retreatment following plasmapheresis, *J Nucl Med*, 29:164-180, 1988.

[139] Hosono M, Endo K, Sakahara H, Watanabe Y, Saga T, Nakai T, Kawai C, Matsumori A, Yamada T, Watanabe T and Konishi J; Human/Mouse chimeric antibodies show low reativity with human anti-murine antibodies (HAMA), *Br J Cancer*, 65:197-200, 1992.

[140] Miller RA, Oseroff AR, Stratte PT and Levy R, Monoclonal antibody therapeutic trials in seven patients with T-cell lymphoma. *Blood*, 62:988-995, 1983.

[141] Shawler DL, Bartholomew RM, Smith LM and Dillman RO, Human immune response to multiple injections of murine monoclonal IgG, *J Immunol*, 135:1530-1535, 1985.

[142] Jerne NK; Toward a network theory of the immune system, *Ann Immunol* (Institut Pasteur), 125C:373, 1974.

[143] Baum RP, Niesen A, Hertel A, Nancy A, Hess H, Donnerstag B, Sykes T, Sykes C, Suresh MR, Noujaim AA, and Hor G; Activating anti-idiotypic human anti-mouse antibodies for immunotherapy of ovarian carcinoma, *Cancer* (suppl) 73:1121-1125, 1994.

[144] Madiyalakan R, Sykes TR, Dharampaul S, Sykes CJ, Baum RP, Hor G and Noujaim AA; Anti-idiotype induction therapy: evidence for the induction of immune response through the

---

idiotype network in patients with ovarian cancer after administration of anti-CA125 murine monoclonal antibody B43.13.13, *Hybridoma*, in press.

[145] Larson, S.M.; A tentative biological model for the localization of radiolabelled antibody in tumor: the importance of immunoreactivity, *Nucl Med Biol*, 13:393-399, 1986.

[146] McEwan AJ, MacLean GD, Hooper HR, Sykes T; McQuarrie SA; Golberg L; Bodnar DM; Lloyd SL; Noujaim AA; MAb 170H.82: an evaluation of a novel panadenocarcinoma monoclonal antibody labelled with 99Tcm and with 111In, *Nucl-Med-Commun*, 13:11-19, 1992.

[147] Ding L, Samuel J, MacLean GD, Noujaim-AA, Diener E, Longenecker BM; Effective drug-antibody targeting using a novel monoclonal antibody against the proliferative compartment of mammalian squamous carcinomas, *Cancer-Immunol-Immunother,* 32:105-109, 1990.

[148] Turner CJ, Sykes TR, Longenecker BM and Noujaim AA; Comparative radiolabeling and distribution of a tumour-directed monoclonal antibody, *Int-J-Rad-Appl-Instrum-B*, 15:701-706, 1988.

[149] Baum RP, Adams S, Kiefer, J, et al; A novel Tc-99m labeled monoclonal antibody (174H.64) for staging head and neck cancer by immuno-SPECT, *Acta Oncol*, 32:747-751, 1993.

[150] Roit I, Brostoff J and Male D; Immunology, 2nd Edition, Gower Medical Publishing, New york, pp5.3-5.6, 1989.

[151] Melchers F; Possible roles of the carbohydrate groups in biological functios of the glocoproteins, immunoglobin M and G, in Kent (ed), Membrane-Mediated Information, Vol 2, Elsevier, New York, pp39-56, 1973.

[152] Zuckier LS, Rodriguez LD and Scharff MD; Immonologic and pharmacologic conceptes of monoclonal antibodies, *Semin Nucl Med*, 19:166-186, 1989.

[153] Thornberg RW, Day JF, Baynes, et al; Carbohydrate mediated clearance of immune complexes from the circulation. A role for galactose residues in hepatic uptake of IgG-antigen complexes, *J Biol Chem*, 255:6820-6825, 1980.

[154] Greiner JW, Gaudagni F, Noguchi P, Colcher S, Fisher BP, Schlom J; Recombinant interferon enhances monoclonal antibody-targeting of carcinoma lesions in vivo; *Science* 235:895-898, 1987.

[155] Mach, J.-P.; Chatal, J.-F.; Lumbroso, J.-D.; Buchegger, F.; Forni, M.; Ritschard, J.; Berche, C.; Douillard, J.-Y.; Carrel, S.; Herlyn, M.; Steplewski, Z.; Koprowski, H.; Tumor localization in patients by radiolabeled monoclonal antibodies against colon carcinoma, *Cancer Res*, 43:5593-5600, 1983.

---

[156] Strand S-E, Zanzonico P and Johnson TK; Pharmacokinetic modelling, *Med Phys*, 20:515-527, 1993.

[157] Stickney DR, Slater JB Kirk GA, Ahlem C, Chang CH and Frinke HM; Bifunctional antibody: ZCE/CHA Indium-111 BLEDTA-IV clinical imaging in colorectal carcinoma, *Antibody, Immunoconjugates and Radiopharmaceuticals*, 2:1-13, 1989.

[158] Mach J-P, Buchegger F, Forni M, et al; Use of radiolabelled monoclonal anti-CEA antibody for the detection of human carcinomas by external photoscanning and tomoscintigraphy, *Immunol Today* 2:239-249, 1981.

[159] Wilbur DS; Radiohalogenation of proteins: anoverview of radionuclides, labeling methods and reagents for conjugate labeling, *Bioconjugate Chem*, 3:433-470, 1992.

[160] Wu C, Rusckowski M and Hnatowich DJ; Stability of Tc-99m directly labelled to antibodies (abstr), *J Nucl Med* 32:1099, 1991.

[161] John E, Thakur ML, Wilder S, Alauddin MM and Epstein AL; Technetium-99m-labeled monoclonal antibodies: influence of technetium-99m binding sites, *J Nucl Med*, 35:876-881, 1994.

[162] Zamora PO, Mercer-Smith JA, Marek MJ, Schulte LD ad Rhodes BA; Similarity of copper and Tc-99m binding sites in human IgG, *Nucl Med Biol*, 19:797-802, 1992.

[163] Brown BA, Comeau RD, Jones PL, Libertore FA, Neacy WP, Sans H and Gallagher BM; Pharmacokinetics of the monoclonal antibody B72.3 and its fragments labelled with I-125 or In-111, *Cancer Res*, 47:1149-1154, 1987.

[164] EE Watson, MG Stabin and JA Siegel; MIRD Formulation, *Med Phys* 20:511-514, 1993.

[165] R Loevinger, TF Budinger and EE Watson; *MIRD Primer for Absorbed Dose Calculations,* Society of Nuclear Medicine, New York, NY, 1988.

[166] Howell RW; The MIRD schema: From organ to cellular dimensions, *J Nucl Med*, 35:531-533, 1994.

[167] Loevinger R and Berman M; A revised schema for calculating the absorbed dose from biologically distributed radionuclides, MIRD Pamphlet No.1 (revised), Society of Nuclear Medicine, New York, 1976.

[168] Howell RW, Rao DV and Sastry KSR; Macroscopic dosimetry for radioimmunotherapy: nonuniform activity distributions in solid tumors, *Med Phys*, 16:66-74, 1989.

[169] Weber DA, Eckerman KF, Dillman LT and RymanJC; MIRD: Radionuclide Data and Decay Schemes, Society of Nuclear Medicine, New York, NY, 1989.

---

[170] Synder WS, Ford MR and Warner GG; Estimates of Specific Absorbed Fractions for Photon Sources Uniformly Distributed in Various Organs of a Heterogeneous Phantom, MIRD Pamphlet No. 5, Revised Society of Nuclear Medicine, New York, NY, 1978.

[171] Snyder WS, Ford MR and Warner GG et al; *"S"* Absorbed Dose per Unit Cumulated Activity for Selected Radionuclides and Organs, MIRD Pamphlet No. 11, Society of Nuclear Medicine, New York, NY, 1978.

[172] Weber DA, Eckerman KF, Dillman LT and RymanJC; MIRD: Radionuclide Data and Decay Schemes, Society of Nuclear Medicine, New York, NY, 1989.

[173] Humm JL; Dosimetric aspects of radiolabelled antibodies for tumor therapy, *J Nucl Med*, 27:1490-1497, 1986.

[174] Leichner PK, Koral KF, Jaszcak RJ, Green AJ, Chen GTY and Roeske JC; An overview of imaging techniques and physical aspects of treatment planning in radioimmunotherapy, *Med Phys* 20:569-577, 1993.

[175] Sorenson JA; *Quantitative measurement of radioactivity in vivo by whole-body counting*, in Instrumentation in Nuclear Medicine, edited by Hine GJ and Sorenson JA, Academic Press, New York, 1974.

[176] Wu RK and Siegel JA; Absolute quantitation of radioactivity using the buildup factor, *Med Phys*, 11:189-192, 1984.

[177] Koral KF, Swailem FM, Clinthorne NH, Rogers WL and Tsui BMW; Dual-energy window compton scatter correction: Scatter multiplier required for quantification, *J Nucl Med*, 31:798-799 (abst), 1990.

[178] English RJ and Brown SE, SPECT Single-Photon Emission Computed Tomography: A Primer, 2nd Edtion, Society of Nuclear Medicne, New York, 1990.

[179] Kuhl DE; Principles of Radionuclide Emission Imaging, Pergammom Press, Oxford, England, 1983.

[180] Soussaline F, The single-photon tomograph, In: Principles of Radionuclide Imaging, Kuhl DE (ed), Pergamon Press, Oxford, England, 153-184, 1983.

[181] English RJ and Brown SE; SPECT Single Photon Emission Computed Tomography: A Primer, 2nd edition, Society of Nuclear Medicine, New York, 1990.

[182] Chang LT; A method for attenuation correcetion in radionuclide computed tomography, *IEEE Trans Nucl Sci*, NS-25:638-643, 1978.

[183] Sorenson JA; *Methods for quantitative measurement of radioactivity in vivo by whoel-body counting*, In: Instrumnetation in Nuclear Medicine, Vol 2, Hine GJ and Sorenson JA, eds, Academic Press, New York, 311-348, 1974.

---

[184] Ljungberg M and Strand S-E; Attenuation correction in SPECT based on transmission studies and Monte Carlo simulations of build-up functions, *J Nucl Med*, 31:493-500, 1990.

[185] Brownell GL, Correia JA and Zamenhof RG; *Positron instrumentaion*. in Recent Advances in Nuclear Medicine, edited by Lawerence JH and Budinger TF, Grune and Stratton, New York, 1985.

[186] Phelps ME, Hoffman EJ, Huang SC and Kuhl DE, ECAT: A new computerized tomographic imaging system for positron-emitting radiopharmaceuticals, *J Nucl Med*, 19:635-647, 1978.

[187] Phelps ME, Hoffman EJ, Mullani NA and Ter-Pogossian MM; Application of annihilation coincidence detection to transaxial reconstruction tomography, *J Nucl Med*, 16:210-224, 1975.

[188] Strauss LG and Conti PS; The application of PET in clinical oncology, *J Nucl Med*, 32:623-648, 1991.

[189] Larson SM, Pentlow KS, Volkow NC, et al; PET scanning of I-124-3F8 as a noval method of tumor dosimetry during treatment planning for radioimmunotherapy in a child with neuroblastoma, *Antib Immunoconj Radiopharm*, 4:34 1991.

[190] Pentlow KS, Graham MC Lambrecht RM Cheung N-K V and Larson SM; Quantitative imaging of I-124 using positron emssion tomography with application to radioimmunodiagnosis and radimmunotherapy, *Med Phys*, 18:357-366, 1991.

[191] Sgouros G, Chiu S, Pentlow KS, et al; Three-Dimensional Imaging for Radioimmunotherapy Treatment Planning; *J Nucl Med*, 34:1595-1601, 1993.

[192] Ma CM and Nahum AE; Calculation of absorbed dose ratiosusing correlated Monte Carlo sampling, *Med Phys*, 20:1189-1199, 1993.

[193] Chen C-T, Harper PV and Lathrop KA, Radiation absorbed dose to the Bladder from 2-FDG and other radiopharmaceuticals, *J Nucl Med*, 25:92-93 1984.

[194] Chen C-T, Harper PV and Lathrop KA; A simple dynamic model for calculating radiation absorbed dose to the bladder wall, in 4th International Radiopharmaceutical Dosimetry Synposium, Oak Ridge, TN, CONF-851113-(DE86010102), Nov 5-8, 1985.

[195] Snyder WS and Ford MR; Estimation of dose to the urinary bladder and to the gonads, In Radiopharmaceutival Dosimetry Symposium, Oak Ridge, TN, 313-350, April 26-29, 1976.

[196] Diffey B, Hilson A; Absorbed dose to the bladder from 99m-Tc-DTPA, (letter), *Br J Radiol*, 49:196-198, 1976.

---

[197] Thomas SR, MG Stabin, CT Chen and RC Samaratunga; MIRD pamphlet no. 14: A dynamic urinary bladder model for radiation dose calculations, *J Nucl Med*, 33:783-802, 1992.

[198] Cloutier RJ, SA Smith, EE Watson, et al, Dose to the fetus from radionuclides in the bladder, *Health Phys*, 25:147-161, 1973.

[199] Synder WS, MR Ford and GG Warner; Estimates of Specific Absorbed Fractions for Photon Sources Uniformly Distributed in Various Organs of a Heterogeneous Phantom, MIRD Pamphlet No. 5, Revised Society of Nuclear Medicine, New York, NY, 1978. *Note: same as ref 8, will modify later.*

[200] Loevinger R, EM Japha and GL Brownell; Discrete radioisotope sources. In: GJ Hine and GL Brownell eds. Radiation Dosimetry. New York: Academic Press; 693-799, 1956.

[201] Snyder WS, Ford MR, Warner GG and Watson SB; A tabulation of dose equivalent per microcurie-day for source and target organs of an adult for various radionuclides, ORNL 5000, Oak Ridge TN: Oak Ridege National Laboratory, 1975.

[202] RJ Cloutier, SA Smith, EE Watson, et al, Dose to the fetus from radionuclides in the bladder, *Health Phys*, 25:147-161, 1973.

[203] SR Thomas, MG Stabin, CT Chen and RC Samaratunga; MIRD pamphlet no. 14: A dynamic urinary bladder model for radiation dose calculations, J *Nucl Med*, 33:783-802, 1992.

[204] Longenecker BM, Willans DJ, MacLean GD, Selvaraj S, Greenberg A, Suresh MR and Noujaim AA; Monoclonal antobodies and synthetic tumor associated glycoconjugates to study the expression of Thomsen-Friedenreich (TF)-like and Tn-like antigens on human cancers; *J Natl Cancer Inst*, 78:489-496, 1987.

[205] Longenecker BM, MacLean GD, McEwan AJB, Sykes TR, Henningson C, Suresh MR and Noujaim AA, Synethetic Thomsen-Friedenreich antigens for the production of adenocacinoma monoclonal antobodies and generation of anti-carcinoma T-cells, in Reading CL, Hakomri S and Marcus DM (eds), Altered Glycosylation in Tumor Cells, UCLA Symposium on Molecular and Cellular Biology, Alan R Liss Press, NewYork, Vol, 79, 307-320, 1988.

[206] Samuel J, Noujaim AA, MacLean GD Suresh MR and Longenecker BM; Analysis of human tumor associated Thomsen-Friedenreich antigen, *Cancer Research*, 50:4801-1808, 1990.

---

[207] Samuels J, Noujaim AA, Willans DJ, Brezinska GS, Haines DM and Longenecker BM; A novel marker for basal (stem) cells of mammalian stratified squamous epithelia and squamous cell carcinomas, *Cancer Res* 49, 2465-2470, 1989.

[208] Springer GF, Taylor CR, Howard DR, et al; Tn, a carcinoma-associated antigen, reacts with anti-Tn of normal human sera, *Cancer*, 55:561-569, 1985.

[209] Springer GF; T and Tn: general carcinoma autoantigens, *Science*, 224:1198-1206, 1984.

[210] Springer GF and Desai PR; Common precursors of human blood group MN specificities, *Biochem Biophys Res Commun*, 61:470-475, 1974.

[211] Springer GF, Desai PR and Banatwala I; Blood group MN antigens and precursors in normal and maliganant human breast glandular tissue, *J Natl Cancer Inst*, 54:335-339, 1975.

[212] Baum RP, Nieson A, Golberg L, McQuarrie SA, Sykes T, Sykes C, Adams S, Boniface G, McEwan AJB, MacLean GD, Noujaim AA and G Hor, A novel human chimeric antibody (Tc-99m c-174) for the staging of head and neck cancer, (abstr). *European J Nucl Med,* ___.

[213] Oesterling JE, Chan DW, Epstein JI, Kimball AW Jr, Bruzek DJ, Rock RC, Brendler CB and Walsh PC; Prostate specific antigen in the preoperative and postoperative evaluation of localized prostatic cancer treated with radical prostatectomy, *J Urol*, 139:766-772, 1988.

[214] Stamey TA, Yang N, Hay AR, McNeal JE, Freiha FS and Redwine E; Prostate specific antigen as a serum marker for adenocarcinoma of the prostate, *N Engl J Med*, 317:909-916, 1987.

[215] Stenman U-H, Leinonen J, Alfthan H, Ranniko S, Tuhkanen K, Alfthan O; A complex between Prostate-specific antigen and alpha1-antichymotripsin is the major form of prostate -specific antigen in serum of patients with prostatic cancer: assay of the complex improves clinical sensitivity for cancer, *Cancer Res*, 51:222-226, 1991.

[216] R.P. Baum, A. Hertel, T. Baew-Christow, A.A. Noujaim, G. Hör; A novel Tc-99m labeled monoclonal antibody against CA 125 (B43.13.13) for radioimmunodetection of ovarian cancer - initial results, *Eur J Nucl Med*, 18:535, 1991.

[217] Hertel A, Baum RP, Neisen and AA Noujaim; A novel Tc-99m-labelled monoclonal antibody against CA 125 for early detection of ovarian cancer recurrences - first clinical results, *J Nucl Med*, 33:904, 1992.

[218] Kobayashi H, Ohi H, Moniwa N, Shinohara H and Terao T; characterization of CA 125 antigen identified by monoclonal antibodies that recognize different isotopes, *Clin Biochem*, 25:391-397, 1993.

---

[219] Farghaly SA; Tumor markers in gynecologic cancer (review), *Gynecol Obstetric Invest*, 34:65-72, 1992.

[220] R.P. Baum, A. Hertel, T. Baew-Christow, A.A. Noujaim, G. Hör. A novel Tc-99m labeled monoclonal antibody against CA 125 (B43.13.13) for radioimmunodetection of ovarian cancer - initial results. In: Nuclear Medicine - Nuclear Medicine in Research and Practice, H.A.E. Schmidt and R. Höfer (Eds), Schattauer, Stuttgart, pp 670-672 (1992).

[221] Sykes CJ, Sykes TR, McEwan AJ, MacLean GD, Armstrong K and Noujaim AA, Immunoradiometric assay for the detection of circulating antibodies to murine monoclonal antibodies in humans (HAMA), Proceedings from the International Symposium on Radiopharmacology, Maddelena DJ, Snowdon GM and Boniface GR (Eds), 179-184, 1990.

[222] Lamson M, Hoffe CE and Ice RD; Practical generator kinetics, *J Nucl Med Technol*, 4, 21-27, 1976.

[223] Harris CC, Greer KL, Jaszczak RJ, Floyd Jr CE, Fearwow EC and Coleman RE; 99m-Tc attenuation coefficients in water-filled phantoms determined with gamma cameras, *Med Phys*, 11:687, 1984.

[224] Bailey DL, Hutton BF and Walker PJ, Improved SPECT using simultaneous emission and transmission tomography, *J Nucl Med*, 28:844, 1987.

[225] Thomas SR, Maxon HR, Kernakes JG and Saenger, Quantitative external counting counting technniques enabling improved diagnostic and therapeutic decisions in patients with well-differentiated thyroid cancer, *Radiology*, 122:731-737, 1972.

[226] Hammond ND, Moldofsky PJ, Beardsley MR and Nulhern CB; External imaging techniques for quantitation of distribution of 131-I $F(ab')_2$ fragments of monoclonal antibody in humans, Med Phys, 11:778-783, 1984.

[227] Eary JF, Frederick L, Applelbaum LE and Brown P; Preliminary validation of the opposing view method for quantitative gamma camera imaging, *Med Phys*, 16:382-387, 1989.

[228] Levy WC, Cerqueira MD, Matsuoka DT, Harp GD, Sheehan FH and Stratton JR; Four radionuclide methods for determination of left ventricular volume determination: comparison of manual and new automated technique, *J Nucl Med*,33:763-770, 1992.

[229] Spiegelberg. H.L. and Weigle, W.O.; The catabolism of homologous and heterologous 7S gamma globulin fragments, *J Exp Med* 121:323, 1965.

[230] Weisbroth SH, Flatt RE and Kraus AL; The Biology of the Rabbit, Academic PressInc, New York, 1974.

[231] SpiegelbergHL and Weigle WO; The catabolism of homologous and heterologous 7S gamma globulin fragments, *J Exp Med* 121:323, 1965.

---

[232] Pavel DG, Zimmer M and Patterson VN; In vivo labeling of red blood cells with Tc-99m: a new appraoch to blood pool visualization, *J Nucl Med*, 18:305-308, 1977.

[233] Callahan RJ, Froelich JW, Mckusick KA, Leppo j and Strauss HW; A modified method for the in vivo labling of red blood cells with 99mTc, *J Nucl Med*, 23:315-318, 1982.

[234] Kelly MJ, Cowie AR, Antonino A, Barton H and Kalff V; an assessment of factors which influence the effectiveness of the modified in vivo Tc-99m-erythrocyte labeling technique in clinical use; *J Nucl Med*, 33:2222-2225, 1992.

[235] Yalow RS; Radioimmunoassay, a probe for the fine structure of biologic systems, *Science*, 200:1236, 1978.

[236] Tru-Scint SQ: A Synopsis, ^{99m}Tc-Labelled Radioimmunopharmaceutical for in vivo Diagnosis of Squamous Cancers of Lung, Cervix Head and Neck, Biomira Inc, Edmonton, Canada, MRS-SQ-8/91,1991.

[237] Tru-Scint AD: A Synopsis, ^{99m}Tc-Labelled Radioimmunopharmaceutical for in vivo Diagnosis of Squamous Cancers, Biomira Inc, Edmonton, Canada, MRS-AD-8/91,1991.

[238] Xue LY; Studies on the Mechanisms of Biodisposition of Directly-Labelled ^{99m}Tc-Antibodies, PhD Thesis, University of Alberta, 1994.

[239] Mardirossian G, Bushe H and Hnatowich DJ; Pharmacokinetic modelling of Tc-99m labeled antibody in patients, *J Nucl Med* (abstr), 33:958, 1992.

[240] Hnatowich DJ, Mardirossian G, Rusckowski, et al; Directly and indirectly technetium-99m labeled antibodies - a comparison of in vitro and animal in vivo properties, *J Nucl Med*, 34:109-119, 1993.

[241] Mach J-P, Buchegger F, Forni M; Use of radiolabelled monoclonal anti-CEA antibody for the detection of human carcinomas by external photoscanning and tomoscintigraphy, Immonol Today, 2:239-249, 1981.

[242] Hnatowich DJ, Gionet M, Rusckowski M, et al, Pharmacokinetics of In-11 labeled OC-125 antibody in cancer patients compared with the 19-9 antibody, *Cancer Res*, 47:6111-6117, 1987.

[243] Colcher D, Esterban JM, Carrasquillo JA, Sugarbaker P, Reynolds JC, Bryant G, Larson SM and Schlom J; Quantitative analyses of of selective radiolabelled monoclonal antibody localization in metastatic lesions of colorectal cancer patients, *Cancer Res*, 47:1185-1189, 1987.

[244] Bosslet K, Streinstraser A, Schwartz A, Harthus HP, Lubenm G, Kulmann L and Sedlacek HH; Quantitative considerations supporting the irrelevance of circulating serum CEA for the

---

immunoscintigraphic visualization of CEA expressing carcinoma, *Eur J Nucl Med*, 14:523-528, 1988.

[245] McQuarrie SA, McEwan AJB, Noujaim AA, Baum, Niesen A, Golberg L and Golberg K; Phamacokinetic comparison of the murine and chimeric forms of the 99mTc-labelled 174H.64 monoclonal antibody, *J Nucl Biol Med*, 37:158, 1993.

[246] Baum RP, Noujaim AA, Nanci, et al; Clinical course of ovarian cancer patients under repeated stimulation of HAMA using OC 125 and MAb-B43.13, *Hybridoma*, 12:583, 1993.

[247] Baum RP, Neisen A, Hertel A, et al; Activating anti-idiotype human anti-mouse antibodies for immunotherapy of ovarian carcinoma, *Cancer* (suppl) 73:1121-1125, 1994.Baum RP, Noujaim AA, Nanci A, et al; Clinical course of ovarian cancer patients under repeated stimulation of HAMA using OC 125 and MAb-B43.13, *Hybridoma* 12:583, 1993.

[248] Madiyalakan R, Sykes TR, Dharampaul S, Sykes CJ, Baum RP Hor G and Noujaim AA; Anti-idiotype induction therapy: evidence for the induction of immune response through the idiotype network in patients with ovarian cancer after administration of anti-Ca 125 murine monoclonal antibody B43.13, *Hybridoma*, in press.